Eta Electroproduction in the Region of the Isospin One Half, Spin One Half 1535 MeV Baryon Resonance

by

Richard Allen Thompson

B.S., Univeristy of Wyoming, 1992

Submitted to the Graduate Faculty of
Arts and Sciences in partial fulfillment
of the requirements for the degree of
Doctor of Philosophy

University of Pittsburgh

2000

UNIVERSITY OF PITTSBURGH

FACULTY OF ARTS AND SCIENCES

This dissertation was presented by

Richard Allen Thompson

It was defended on

March 13, 2000

and approved by

Wilfred Cleland

James Mueller

John Norton

Frank Tabakin

Steven A. Dytman

Committee Chairperson

Eta Electroproduction in the Region of the Isospin One Half, Spin One Half 1535 MeV Baryon Resonance

Richard Allen Thompson, Ph.D.

University of Pittsburgh, 2000

The results of an experiment to measure the η meson electroproduction cross section are presented. The measurement is made from a center of mass total energy W from the 1.487 GeV ηp threshold to 1.635 GeV and a virtual photon four momentum squared Q^2 of 0.5 $GeV^2$to 1.5 GeV^2. The measurement was performed at the CEBAF Large Acceptance Spectrometer at the Thomas Jefferson National Accelarator Facility during February and March of 1998. A partial wave fit indicates that there are processes contributing to the cross section other than the excitation of the IJ^P $\frac{1}{2}\frac{1}{2}^-(1535)$ bound state baryon. This data, along with all previous published η electroproduction data, are fit to extract baryon resonance parameters of the $\frac{1}{2}\frac{1}{2}^-(1535)$. There is some indication of a Q^2 dependence to the width of the resonance, allthough the data are not conclusive. The excitation amplitude $A^p_{1/2}(Q^2)$ is determined from this and all previous published η electroproduction data.

Acknowledgements

I extend my sincerest gratitude to my advisor, Steven Dytman. He provided me with many unique opportunities to develop as a scientist, as well as the guidance to perform the research presented in this thesis. My thanks to Jim Mueller for discussions and explanations on issues too many to enumerate. Kui Young Kim and Haluk Denizli made important contributions on understanding systematic errors. Adam Fineman developed code to help us visualize the acceptance of CLAS. The dedication and hard work of the Hall B students and staff at Jefferson Lab made the detector and reconstruction come together. Simon Taylor and Kostantin Loukachine made invaluable contributions to calibrations and reconstruction code, and were invaluable friends. Very special thanks to Joe Manak, who enlightened me on software development. His countless contributions to the the reconstruction software project, often in the face of bitter resistance, were critical to the building of a successful reconstruction code. His friendship, though, I value most.

Let this work be a celebration of my friends and family: of my mother, who gave me my start in life and my love of nature, and of my father who gave me my start in science and my love of life, of my sister and her husband who kept me from starving in college, and of Linda who was by my side through it all and believed in me.

Table of Contents

List of Tables

List of Figures

Chapter 1

Introduction

This thesis presents the results and analysis details of a measurement of the η electroproduction differential cross section taken at the Thomas Jefferson National Accelerator Facility (JLab) in February and March of 1998. The η mesons are detected via the $ep \rightarrow epX$ missing mass. The data is in the region of the IJ^P $\frac{1}{2}\frac{1}{2}^-(1535)$ baryon resonance, a total center of mass energy W from the 1.487 threshold to $1.90GeV$ and a virtual photon momentum transfer Q^2 from 0.50 to 1.50 GeV^2. The center of mass η decay angular coverage is virtually complete. The cross sections are used to study properties of the $\frac{1}{2}\frac{1}{2}^-(1535)$.

In this chapter, the motivation for the experiment is presented along with a review of the currently published data and analysis. Chapter 2 presents the apparatus of the CEBAF Large Acceptance Spectrometer (CLAS) used to make the measurement and Chapter 3 contains considerable details of the construction of one of the detectors. The reconstruction of the data from the CLAS to obtain identified particles and momenta are presented in Chapter 4. In Chapter 5, the analysis of the reconstructed data to obtain absolute cross sections is presented. The results of the measurement, including an extraction of $\frac{1}{2}\frac{1}{2}^-(1535)$ baryon resonance properties, are presented in Chapter 6, along with some studies to understand the potential systematic errors.

1.1 Motivation

The motivation for this study is to make a significant improvement on the data from which the nature and properties of the IJ^P $\frac{1}{2}\frac{1}{2}^-(1535)$ and other baryon resonances are determined. Baryon resonances are labelled by their isospin I, spin J, and parity P as IJ^P. This convention will be used throughout this thesis. The improved angular coverage of this experiment allows the determination of more multipole parameters than was previously possible. The $\frac{1}{2}\frac{1}{2}^-(1535)$ is a state that has been the focus of considerable interest and debate, even as it is listed as a "4-star" resonance ("existence is certain, and

properties are at least fairly well explored" [12]). The interest in this state lies primarily in that its structure is remarkably different from other baryon resonances. The debate, which comes about primarily because it lies only about $50MeV$ above the threshold for η production, is in the experimental determination of its properties.

The underlying theory of strong interaction physics is believed to be Quantum Chromodynamics (QCD). Contrary to the case of electroweak physics, QCD is inherently a nonpertubative theory at the low energies where ordinary matter resides and has hence proven unamenable to analytic solutions. The low energy test of QCD lies in the ability of effective theories which are inspired by it to produce results that are consistent with those observed in nature. These effective theories exploit the fundamental symmetries and degrees of freedom of QCD, but are formulated in a manner such that the theory is solvable.

The primary tests of QCD to date have been in deep inelastic scattering. At these scales, the strong coupling α is less than 1 and pertubative approaches are successful. But at low, nonpertubative, energies, baryon resonance physics provide an arena for testing QCD. These low energy investigations will test not only the degrees of freedom and symmetries of QCD, but the details of the strong force interaction between quarks.

A fundamental test of a theory that seeks to explain the nature of matter at a basic level, like QCD, is in its ability to reproduce and predict the spectroscopy of the bound states of that matter. The stable ground state particles of strong physics that compose ordinary matter are the proton and neutron, and their excited states are baryon resonances. Baryon resonances are characterized by their spin, isospin and parity quantum numbers, their resonance masses and widths, and their decay modes. These are determined from the energy dependence of the excitation and the decay final state and its angular distribution.

Fig. 1.1 shows the inclusive excitation spectra $ep \rightarrow eX$ along with the masses of known baryon resonances and illustrates that the picture is, in general, quite complicated. The excited states of the proton are broad and overlapping, making the extraction of their resonance parameters very difficult. A multipole decomposition and analysis that properly addresses the effects of the coupling between different decay channels is necessary[1].

This situation is considerably simplified when there is a final state that is populated by only a single resonance. Such is believed to be the case with the ηp final state and the $\frac{1}{2}\frac{1}{2}^{-}(1535)$ resonance. The branching fraction of the $\frac{1}{2}\frac{1}{2}^{-}(1535)$ to ηp is $30-55\%$ [12], while the only other resonance with a measured branching fraction into the ηp channel greater that 1% is the $\frac{1}{2}\frac{1}{2}^{-}(1650)$. The simplification is in that there are

[1]Such an analysis is not within the scope of this thesis. See instead [33] and the references therein.

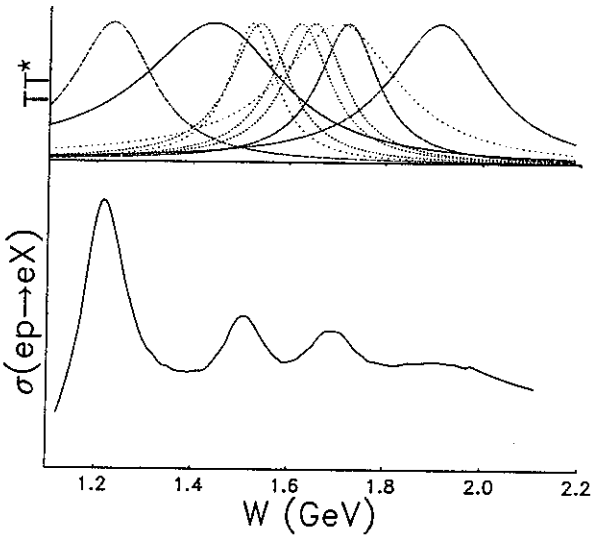

Figure 1.1: The general shape of the cross section for inclusive electron scattering shown with the Breit Wigner amplitudes of known baryon resonances. Only the 4 star baryon resonances with spin less than $\frac{5}{2}$ are shown. The Breit Wigner amplitudes for each resonance, TT^*, are normalized to a common scale for illustrative purposes. Each resonance curve is drawn in a line style that reflects its quantum numbers.

no longer overlapping states. Moreover, production of η mesons that does not proceed through a baryon resonance (t-channel processes) appears to be quite small [32].

However, observation in the ηp final state does not simplify the coupled channel issue. Unitarity dictates that as the strength in other channels varies (as happens in the πN channel across other resonances that overlap the $\frac{1}{2}\frac{1}{2}^-(1535)$), the cross section in the ηN channel must have corresponding variations in order to preserve probability. Hence the cross section from which baryon resonance parameters are often extracted is invariably sensitive to coupled channel effects. For this reason, the emphasis of this analysis is not on the extraction of $\frac{1}{2}\frac{1}{2}^-(1535)$ resonance parameters, but rather on the production of high quality angular distribution data that drives full coupled-channel analyses. The investigation presented in this thesis is a natural complement to other work [33] done by the Strong Physics Group here at the University of Pittsburgh in constructing coupled channel models alluded to above. The motivation for studying the $\frac{1}{2}\frac{1}{2}^-(1535)$ is not in that it is a state from which it is easy to extract resonance parameters (for coupled channels effects will always be important), but rather that there are interesting physics issues associated with it.

Constituent Quark Models (CQM) have had considerable success in reproducing the excited baryon spectrum as well as the dynamical features of resonance formation [10]. In the CQM, a phenomenological model for the interaction between quarks is used to construct wavefunctions of the ground state nucleons and their excited states. In

the CQM, an excited state arises that has the quantum numbers and approximate mass of the experimentally observed $\frac{1}{2}\frac{1}{2}^-(1535)$. The $\frac{1}{2}\frac{1}{2}^-(1535)$ of the CQM is an $l = 1$ orbital excitation of the proton with the orbital angular momentum and spin angular momentum coupled to give a total spin of $\frac{1}{2}$. Once the wavefunctions are determined in the CQM, electromagnetic transition amplitudes can be calculated as $\langle N^*|H_{em}|N\rangle$ where $|N\rangle$ represents the ground state nucleon, $|N^*\rangle$ the excited state, and H_{em} the electromagnetic interaction. However, the dependence of the production amplitude on the photon momentum transfer Q^2 is not well explained for the $\frac{1}{2}\frac{1}{2}^-(1535)$, while it is for other states. Specifically, the $\frac{1}{2}\frac{1}{2}^-(1535)$ production amplitude does not fall off as fast in Q^2 as other resonances, and as some CQM models predict, as shown in Fig. 1.2.

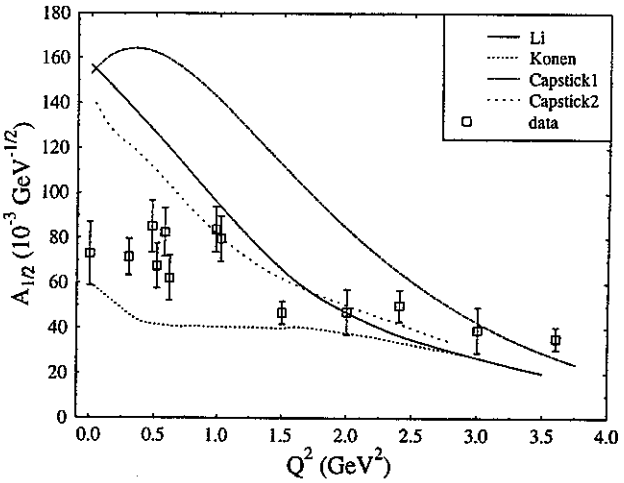

Figure 1.2: The $\frac{1}{2}\frac{1}{2}^-(1535)$ proton excitation amplitude $A^p_{1/2}(Q^2)$. This amplitude is labelled for the total helicity of the $\gamma_v p$ system. The data are from [2], [3], [4], [6], [7], [8], and [26], The theoretical models are from constituent quark models of Li and Close [13], Konen and Weber [23], and Capstick and Keister [10]. The models for the curves labelled "Li" and "Capstick1" are non-relativistic, whereas the others are based on relativistic models. For other N^* resonances, the experimental measurement fall off faster with Q^2 and are more consistent with theoretical calculations.

The very existence of the $\frac{1}{2}\frac{1}{2}^-(1535)$ as a baryon resonance is at issue. Three recent investigations are given as examples. In one recent study, an enhancement in the $e^-p \rightarrow e^-p\eta$ cross section that is consistent with the observed photoproduction cross section arises, not as a qqq excited state, but as a quasi-bound state of $K - \Sigma$ [20]. In another study, Höhler [18], who employs speed plot techniques, argues that there is no resonance signal for the $\frac{1}{2}\frac{1}{2}^-(1535)$, just an enhancement due to the threshold production

of the stable η in an S-wave state. And finally, Denschlag et. al. [15] used a non-relativistic Lee model and make a conclusion very similar to Höhler's.

The model of Kaiser et. al. [20] is a coupled channels effective Lagrangian approach that exploits the chiral symmetry of the strong interaction. The degrees of freedom are the interactions between the baryon and pseudoscalar meson octet. There are 9 free parameters, which are fit to πp, γp, and low energy $K^- p$ scattering data. Their fit yields an interaction between the kaon and sigma that is strongly attractive and results in a resonant structure with properties similar to the $\frac{1}{2}\frac{1}{2}^-(1535)$: quantum numbers $I(J^P)$ of $\frac{1}{2}\frac{1}{2}^-$, a mass of $1.557GeV$ and a width of $179MeV$. Due to the large uncertainty in the experimentally extracted parameters of the $\frac{1}{2}\frac{1}{2}^-(1535)$, this is not inconsistent with observation.

The technique used by Höhler to analyze baryon resonance parameters is known as speed plots. It is based on the calculation of the time delay between the arrival of the incident wave packet, and the departure of the final state wave packets. The signal of a resonance is then a peak in the time delay at the resonance mass. The method is known as speed plot because the time delay is determined from the rate of change of partial wave amplitudes with respect to W as $\frac{d\delta(W)}{dW}$, where δ is the phase of the amplitude defined through $T = |T|e^{i\delta}$. This technique identifies 16 of the 17 4-star resonances listed in the 1996 Review of Particle Properties [12], but a resonance peak in the S11 channel for the 4-star $\frac{1}{2}\frac{1}{2}^-(1535)$ is not seen. There is only a peak at the ηN threshold of $1.487GeV$ which is interpreted as the time delay which is caused by the production of the long-lived η in an S-wave.

Denschlag [15] employed a simple, non-relativistic model with the explicit intent of investigating the interplay between threshold and resonance effects near a threshold. By fitting a few parameters of the model to partial wave analyses and total cross sections, they demonstrated that the qualitative features of the $\frac{1}{2}\frac{1}{2}^-(1535)$ are reproducible without introducing a resonance.

There are certainly problems with the three studies mentioned above and they should be by no means taken as definitive proof that the $\frac{1}{2}\frac{1}{2}^-(1535)$ is not a baryon resonance. If the $\frac{1}{2}\frac{1}{2}^-(1535)$ is a $K - \Sigma$ molecule as Kaiser et. al. speculate, one might expect the spatial extent of the wavefunction to be large, but the slow falloff of the $\frac{1}{2}\frac{1}{2}^-(1535)$ production amplitude $A^p_{1/2}(Q^2)$ with Q^2 suggests just the opposite. An analysis by them of $A_{1/2}(Q^2)$ would help to clarify this. The speed plot technique of Höhler does not seem to treat threshold properly. In fact, a speed plot analysis of a Breit Wigner resonance close to threshold (discussed below) would reveal no resonance peak.

The existence of the $\frac{1}{2}\frac{1}{2}^{-}(1535)$ so close to threshold introduces some interesting experimental issues as well. The amplitude representing the production of an unstable resonance state and its decay into a channel X is commonly parameterized with a Breit-Wigner form. The relativistic form is

$$T = \frac{M\Gamma^*}{M^2 - W^2 - iM\Gamma(W)}, \tag{1.1}$$

where M is the mass of the resonance, Γ^* is the width of the state at $W = M$, and Γ is the energy dependent total resonance width, which is a sum over all the possible final states:

$$\Gamma(W) = \sum_i \Gamma_i(W) \tag{1.2}$$

The proper threshold dependence to the amplitude of a state with angular momentum l is $|\vec{q}|^l$ (where $|\vec{q}|$ is the momentum of the outgoing meson in the center of mass frame) and is often realized by an energy dependence of $\Gamma_i(W)$:

$$\Gamma_i(W) = \Gamma_i^* \frac{|\vec{q}|}{|\vec{q}_{(W=M)}|} \tag{1.3}$$

for $l = 0$. The cross section is given by $|T|^2$ times a phase space factor.

For a resonance near threshold, the energy dependence of the width is so strong that $|T|^2$ may show no peak. Fig. 1.3 shows the real and imaginary parts of a Breit-Wigner amplitude formulated as above with $M = 1.525 \rightarrow 1.575GeV$ and $\Gamma^* = 0.150GeV$. As is illustrated, the magnitude of the amplitude for $M = 1.525GeV$ decreases monotonically from threshold without a resonant peak. As the mass of the resonance moves away from threshold, the effect of the energy dependent width is less and a peak in $|T|^2$ appears. The phase space factor that relates $|T|^2$ to the cross section goes to zero at threshold, so there is by necessity a peak in the cross section.

Another experimental issue that is associated with the threshold issue is that of extracting η yields from $ep \rightarrow epX$ missing mass peaks. The kinematic limit on M_X is $W - M_p$, where M_p is the mass of the proton. In this experiment, the typical η peak width was $\sigma = 7MeV$, which means that the kinematic limit begins to encroach on the η peak (and its radiative tail) around $W = 1.50GeV$. The accurate extraction of η yields requires a careful treatment of this. This issue is discussed in detail in Chapter 5.

1.2 Formalism

In this section the standard kinematic conventions of meson electroproduction, along with the definitions of cross sections and a common multipole expansion, are presented for reference.

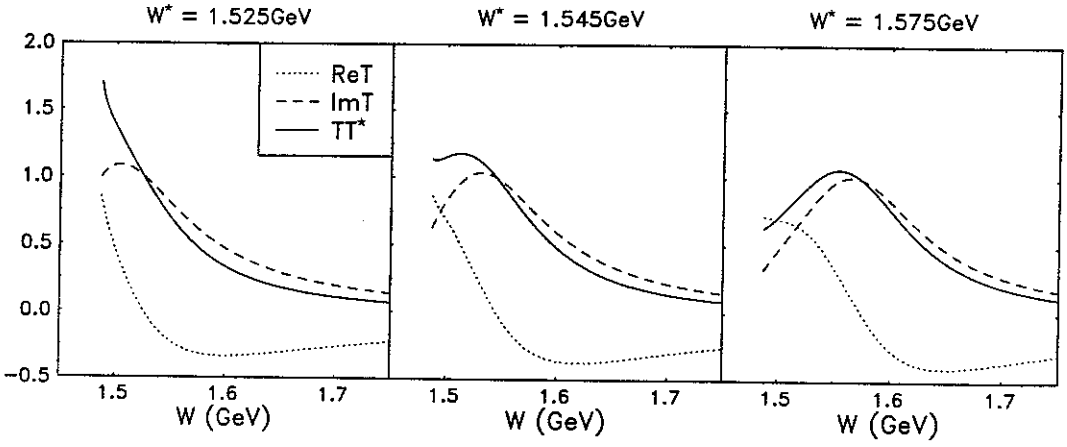

Figure 1.3: The effect of the energy dependent width on the amplitude. For a resonance that is far from threshold (right), there is a classic signature of a resonance: the imaginary part of the amplitude goes through zero rapidly, the real part peaks, and $|T|^2$ shows a resonant structure. When a resonance is close to threshold (left), the energy dependence of the width may be so strong that there is no peak in $|T|^2$. The resonant nature is obscured close to threshold.

1.2.1 Kinematics

Fig. 1.4 is a diagram of $e^- p \to e^- p\eta$ identifying the momenta of the reaction. Meson electroproduction is characterized in terms of the invariants W and Q^2 (which of course can be evaluated in any frame). W is the invariant mass of the intermediate state (labelled by its momentum p^*_W in Fig. 1.4) and is given by

$$W^2 = (p_\gamma + p_i)^2 \tag{1.4}$$

and Q^2, the invariant of the virtual photon momentum transfer is given by

$$Q^2 = -(k_i - k_f)^2 \tag{1.5}$$

The $ep \to epX$ missing mass is evaluated as

$$M_X^2 = (p_W - p_f)^2 \tag{1.6}$$

The energy of the incident and scattered electrons in the laboratory frame are often denoted by E and E', respectively. The electron scattering angle in the laboratory will be denoted by $\theta_{e'}$

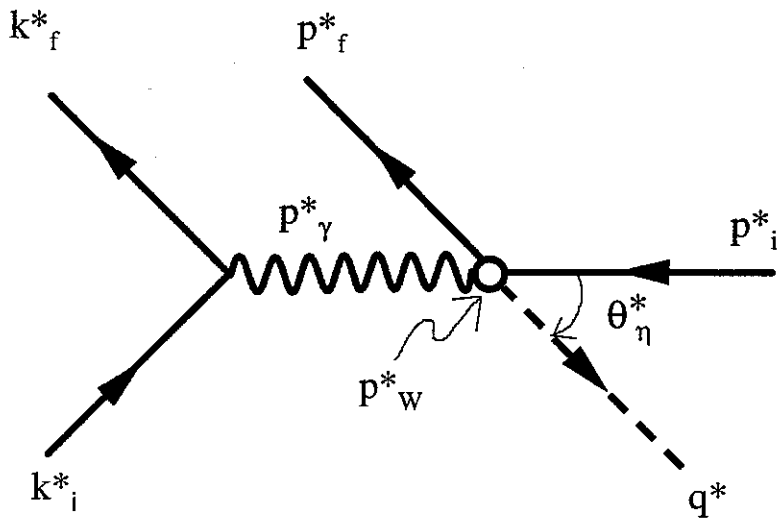

Figure 1.4: A diagram of $e^- p \to e^- p\eta$ identifying the momenta of the reaction. The reaction is depicted in the center of mass system, where the resonance is at rest. The meson decay polar angle is define relative to the virtual photon momentum, and the azimuthal angle is defined relative the the lepton plane such that the situation shown here is $\phi_\eta^* = 180°$.

1.2.2 Cross Sections and Multipoles

The η electroproduction cross section in the laboratory frame is given in the standard convention [17] by

$$\frac{d^5\sigma}{dE' d\Omega_{e'} d\Omega_\eta^*} = \Gamma_\gamma(E, E', \theta_{e'}) \frac{d^2\sigma}{d\Omega_\eta^*} \tag{1.7}$$

where Γ_γ is the flux of virtual photons.

When the unit element of electron phase space is taken to be $dW dQ^2$, the above formula is transformed via the Jacobian

$$dE' d(cos\theta_{e'}) = \frac{W}{2M_p E E'} dW dQ^2 \tag{1.8}$$

to

$$\frac{d^2\sigma}{d\Omega_\eta^*}\left(W, Q^2\right) = \frac{M_p E E'}{\pi W \Gamma_\gamma(W, Q^2)} \cdot \frac{d^4\sigma}{dW dQ^2 d\Omega_\eta^*}. \tag{1.9}$$

It is the quantity $\frac{d^4\sigma}{dW dQ^2 d\Omega_\eta^*}$ that is directly measured in the experiment, and the above equation is the transformation from it to the desired cross section.

The virtual photon flux is given by

$$\Gamma_\gamma(W, Q^2) = \frac{\alpha}{2\pi^2} \frac{E' K}{E Q^2} \frac{1}{1-\epsilon} \tag{1.10}$$

The quantity K is the equivalent real photon energy and it will be used throughout this thesis. It is the energy that would be required of a real photon in order to excite a proton

to a resonance of mass W.

$$K = \frac{W^2 - M_p^2}{2M_p} \tag{1.11}$$

ϵ is the degree of longitudinal polarization of the virtual photon and is given by

$$\epsilon = \left[1 + 2\left(1 + \frac{p_\gamma^2}{Q^2}\right) tan^2\left(\frac{\theta_{e'}}{2}\right)\right]^{-1} \tag{1.12}$$

The cross section $\frac{d^4\sigma}{dW dQ^2 d\Omega_\eta^*}$ is determined from the number of counts N in a bin via

$$\frac{d^4\sigma}{dW dQ^2 d\Omega_\eta^*} = \frac{N}{C \cdot \mathcal{L} \cdot \Delta} \tag{1.13}$$

where C is a correction factor that accounts for acceptance and radiative effects, $\mathcal{L}$ is the luminosity integrated over the time for which the measurement is taken, and Δ is the product of the bin widths $\Delta = \Delta W \cdot \Delta Q^2 \cdot \Delta cos(\theta_\eta^*) \cdot \Delta\phi_\eta^*$.

The integrated luminosity $\mathcal{L}$ is

$$\mathcal{L} = n_b \mu_t \tag{1.14}$$

where n_b is the number of beam particles that passed through the target during the measurement, which is given by the total integrated charge Q and the charge per electron q_e as $n_b = \frac{Q}{q_e}$, and μ_t is the number of target particles per unit surface that the beam encountered. μ_t is given by the physical properties of the target:

$$\mu_t = \frac{\rho t A}{\omega} \tag{1.15}$$

where ρ is the density of the target in mass per unit area, t is the thickness of the target along the direction of the beam, ω is the molar weight of the target material and A is Avagadro's number.

The target material for the measurement reported in this thesis was hydrogen, the integrated charge was $Q = 186.1\mu C$, and the target thickness was $3.8cm$, which was determined from the reconstructed vertex position in data. This experiment typically ran at an instantaneous luminosity $\frac{d\mathcal{L}}{dt}$ of $4 \cdot 10^{33} cm^{-2} s^{-1}$.

The observed cross section is the sum of contributions from all baryon resonances as well as non-resonant contributions. In order to identify individual baryon resonance, the cross section is decomposed into partial waves. That is, it is expressed in terms of amplitudes that have good angular momentum and parity quantum numbers. There will then be a connection between a particular partial wave and the baryon resonances that are allowed by the selection rules due to angular momentum and parity to decay into that partial wave. These partial waves are commonly labelled by either the "electromagnetic

multipole notation", which emphasizes the initial $\gamma_v N$ state, or the "πN notation", which emphasizes the decay into the πN final state.

The electromagnetic multipole notation emphasizes the partial waves of the initial state $\gamma_v N$ system and is $E_{l\pm}$, $M_{l\pm}$, or $S_{l\pm}$ and can be understood from the coupling of angular momentum of the γN state. Since there are three possible spin orientations for the spin 1 virtual photon (two for photoproduction) and two possible spin orientations for the spin $\frac{1}{2}$ nucleon, there are a total of $3 \times 2 = 6$ amplitudes (4 for photoproduction). The total angular momentum is given by

$$\vec{j} = \vec{l} + \vec{s}_\gamma + \vec{s}_N \tag{1.16}$$

where $\vec{s}_\gamma$ is the spin of the photon, $\vec{s}_N$ is the spin of the initial state nucleon and $\vec{l}$ is the relative orbital angular momentum between the photon and nucleon. The photon spin and orbital angular momentum are coupled to give

$$\vec{L} = \vec{l} + \vec{s}_\gamma. \tag{1.17}$$

Since $s_\gamma = 1$, $L = l-1$, l, or $l+1$. The $L = l \pm 1$ couplings are denoted by E (electric) and S (scalar) amplitudes and the $L = l$ couplings by M (magnetic) amplitudes. What is left is the coupling of $\vec{L}$ to $\vec{s}_N$ via $J = L \pm \frac{1}{2}$. This coupling results in $J = l \pm \frac{1}{2}$, which is denoted in the electromagnetic transition notation by $l\pm$. Table 1.1 is a summary of the electromagnetic transition notation. The minimum l allowed given in the last column is because the total spin J must be at least $\frac{1}{2}$. There are no $M0\pm$ amplitudes since this would require a coupling $\vec{L} = \vec{l} + \vec{s}_\gamma$ of $\vec{0} = \vec{0} + \vec{1}$.

E_{l+}	$L = l+1$	$J = l + \frac{1}{2}$	$l \geq 0$
E_{l-}	$L = l-1$	$J = l - \frac{1}{2}$	$l \geq 1$
M_{l+}	$L = l$	$J = l + \frac{1}{2}$	$l \geq 1$
M_{l-}	$L = l$	$J = l - \frac{1}{2}$	$l \geq 1$
S_{l+}	$L = l+1$	$J = l + \frac{1}{2}$	$l \geq 0$
S_{l-}	$L = l-1$	$J = l - \frac{1}{2}$	$l \geq 1$

Table 1.1: The electromagnetic multipole transition notation. The first column is the multipole amplitude symbol, the second column shows the coupling of the photon spin and orbital angular momentum, the third column shows the total angular momentum of the γ_v system, and the fourth column gives the limit on the photon orbital angular momentum.

The quantum numbers of the baryon resonances that could be excited by a particular multipole amplitudes can be determined by considerations of angular momentum and parity. Since the intrinsic parity of the photon is -1, the parity of the state reached

via a transition multipole is $(-)^{l+1}$. For instance, the E_{0+} amplitude leads to transitions from the $J^P\ \frac{1}{2}^+$ ground state nucleon to the $\frac{1}{2}^-$ baryon resonances.

Baryon resonances are labelled by their isospin I, spin J and parity P as IJ^P. Another common notation is to label them by their decay into the πN channel. The πN notation is $L_{(2I)(2J)}$ where L is the orbital angular momentum in the πN channel, I is the isospin and J is the total angular momentum. It is a traditional notation since baryon resonances were first observed in the πN channel. The πN amplitude notation is determined by considerations of angular momentum and parity. Since the intrinsic parity of the pion is -1, the parity in the πN final state is $(-)^{L+1}$. For instance, an $IJ^P\ \frac{1}{2}\frac{1}{2}^-$ baryon resonance must decay to an even L partial wave in the πN channel and hence corresponds to the S_{11} πN channel. Table 1.2 lists the multipole amplitudes that excite baryon resonances up to spin $\frac{3}{2}$, the corresponding πN notation and the masses of the observed states. The resonance that is the primary subject of this investigation is the $IJ^P\ \frac{1}{2}\frac{1}{2}^-$ with a mass of 1535 MeV. In is represented by E_{0+} and S_{0+} electromagnetic transition multipoles and the S11 πN partial wave.

electromagnetic transition	baryon resonance	πN partial wave	observed states (MeV)
$M_{1-}\ S_{1-}$	$\frac{1}{2}\frac{1}{2}^+$	P_{11}	1440 1710
$E_{0+}\ S_{0+}$	$\frac{1}{2}\frac{1}{2}^-$	S_{11}	1535 1650
$E_{1+}\ M_{1+}\ S_{1+}$	$\frac{1}{2}\frac{3}{2}^+$	P_{13}	1720 1900
$E_{2-}\ M_{2-}\ S_{2-}$	$\frac{1}{2}\frac{3}{2}^-$	D_{13}	1520 1700

Table 1.2: The isospin $\frac{1}{2}$baryon resonances under 2 GeV. Only the PDG 4-star resonances are shown.

The cross section is decomposed into partial wave multipoles via standard procedures [22]. In the region of the $\frac{1}{2}\frac{1}{2}^-(1535)$, the dominant η electroproduction multipoles are E_{0+} and S_{0+} (as will be seen later in this chapter), so it is appropriate to perform a multipole expansion up to $l = 2$ and retain only those terms that are proportional to E_{0+} or S_{0+}. When this done, like terms in meson decay angles may be grouped to give

$$\frac{d^2\sigma}{d\Omega_\eta^*} = \frac{|p_\eta^*|W}{KM_p}\Big[A + B\cdot cos(\theta_\eta^*) + C\cdot cos^2(\theta_\eta^*) + \tag{1.18}$$
$$D\cdot sin(\theta_\eta^*)\cdot cos(\phi_\eta^*) + E\cdot sin(\theta_\eta^*)\cdot cos(\theta_\eta^*)\ cos(\phi_\eta^*) + F\cdot sin^2(\theta_\eta^*)\cdot cos(2\phi_\eta^*)\Big]$$

The multipole parameters A-F are given by

$$A = |E_{0+}|^2 + \epsilon\frac{Q^2}{|p_\gamma^*|^2}|S_{0+}|^2 -$$

$$
\begin{aligned}
& Re\left[E_{0+}^{*}\left(E_{2-}-3M_{2-}\right)\right]-4\epsilon\frac{Q^2}{|p_\gamma^*|^2}\cdot Re\left[S_{0+}^{*}S_{2-}\right] \\
B &= -2Re\left[E_{0+}^{*}\left(M_{1-}-3E_{1+}-M_{1+}\right)\right]+2\epsilon\frac{Q^2}{|p_\gamma^*|^2}\cdot Re\left[S_{0+}^{*}\left(4S_{1+}+S_{1-}\right)\right] \\
C &= 3Re\left[E_{0+}^{*}\left(E_{2-}-3M_{2-}\right)\right]+12\epsilon\frac{Q^2}{|p_\gamma^*|^2}\cdot Re\left[S_{0+}^{*}S_{2-}\right] \qquad (1.19) \\
D &= -\sqrt{2\epsilon(\epsilon+1)\frac{Q^2}{|p_\gamma^*|^2}}\cdot Re\left[E_{0+}^{*}\left(S_{1-}-2S_{1+}\right)+S_{0+}^{*}\left(3E_{1+}+M_{1-}-M_{1+}\right)\right] \\
E &= -3\sqrt{2\epsilon(\epsilon+1)\frac{Q^2}{|p_\gamma^*|^2}}\cdot Re\left[2E_{0+}^{*}S_{2-}+S_{0+}^{*}\left(M_{2-}-E_{2-}\right)\right] \\
F &= -3\epsilon\cdot Re\left[E_{0+}^{*}\left(E_{2-}+M_{2-}\right)\right]
\end{aligned}
$$

1.3 Review of Data

Before this experiment, the majority of the η electroproduction differential cross section data was taken at the DESY facility in Germany between 1973 and 1983 [2],[6],[7]. Recently, high quality near threshold photoproduction measurements have been reported from the TAPS detector at MAMI in Mainz [24], and high Q^2 electroproduction measurements in Hall C of JLab [3]. The η electroproduction data to date span a region in Q^2 from 0 to $3GeV^2$ and in W from threshold to $1.775GeV$. This information is summarized in Fig. 1.5. The measurement presented in this thesis does not expand the W or Q^2 coverage, but rather represents a significant improvement on the center of mass meson decay angle coverage, which is important for extracting multipole parameters.

Fig. 1.5 gives no indication of the quality of the data that existed before this work, or of the angular coverage. When performing fits to multipole parameters as in eqn. 1.2.2, the ability to distinguish the D, E, and F parameters comes partly from the separation between the $cos(\phi_\eta^*)$ and $cos(2\phi_\eta^*)$ terms. It is thus important to have good coverage in ϕ_η^*, particularly at $\phi_\eta^* = 0°$ and $\phi_\eta^* = 90°$ where $cos(\phi_\eta^*)$ and $cos(2\phi_\eta^*)$ are most different. Fig. 1.6 shows the overlap in angular coverage between the data of [2] and [6] and the current study. The data represented in this study has significantly better ϕ_η^* coverage, as the previous DESY data had only a few data points above $\phi_\eta^* = 90°$. It is for this reason that the parameterized multipole fits done by [2] and [6] were restricted to the A and B parameters of eqn. 1.2.2. The improved angular coverage is an inherent feature of data from the large acceptance CLAS detector. The new data from CLAS represents a significant improvement in the ability to extract multipoles from η electroproduction data. The data presented in this thesis is from the first electroproduction run period at CLAS.

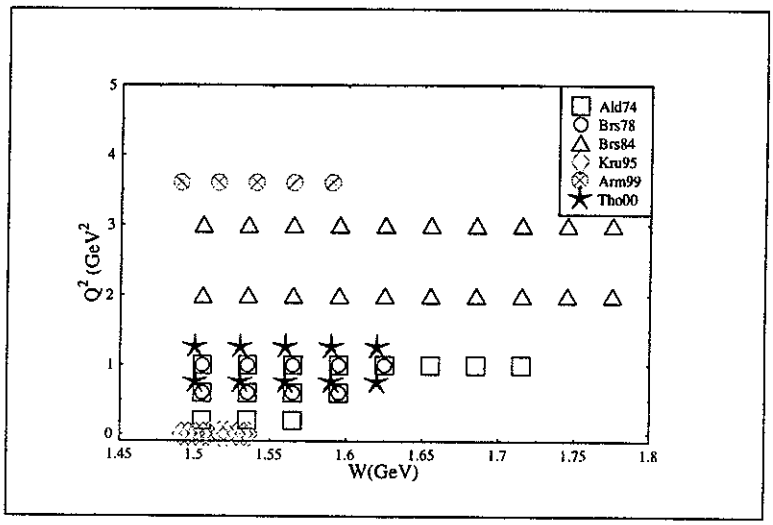

Figure 1.5: Kinematic coverage of η photo- and electroproduction. A marker is placed wherever there is angular distribution data. References for the data are as follows: Ald74[2], Brs78[6], Brs84[7], Kru95[24], Arm99[3], Tho00[this thesis].

At the time this thesis was written there was approximately 5 times more data that was in the process of being analyzed. The kinematic coverage shown in Figs. 1.5 and 1.6 will be significantly expanded.

To summarize the existing η electroproduction angular distribution data, the multipole parameters fit by [2], [6], [7] and [24] are plotted in Figs. 1.7, 1.8, and 1.9. All of these represent fits to the multipole parameters A and B only, except for the $Q^2 = 0$ data of [24], which also included C. In [2], [6], [7] there was not adequate coverage in ϕ_η^* to fit D, E, or F.

Note that at Q^2 less than $2GeV^2$, the form of A is as that discussed in Section 1.1. If one assumes that A is dominated by E_{0+}, this behavior can be attributed to an $IJ^P\ \frac{1}{2}\frac{1}{2}^-$ resonance close to threshold whose strong energy dependent width gives rise to a monotonically decreasing amplitude. Note also that A appears to fall off much slower at $Q^2 = 0GeV^2$. This is indicative that the width of the $\frac{1}{2}\frac{1}{2}^-(1535)$ observed by [24] is significantly broader. Their determination of the width was $200 \pm 40MeV$, which is indeed large compared to typical values of $150 \pm 30MeV$.

Further discussion of these data is delayed until the results and discussion of this study are presented in Chapter 6.

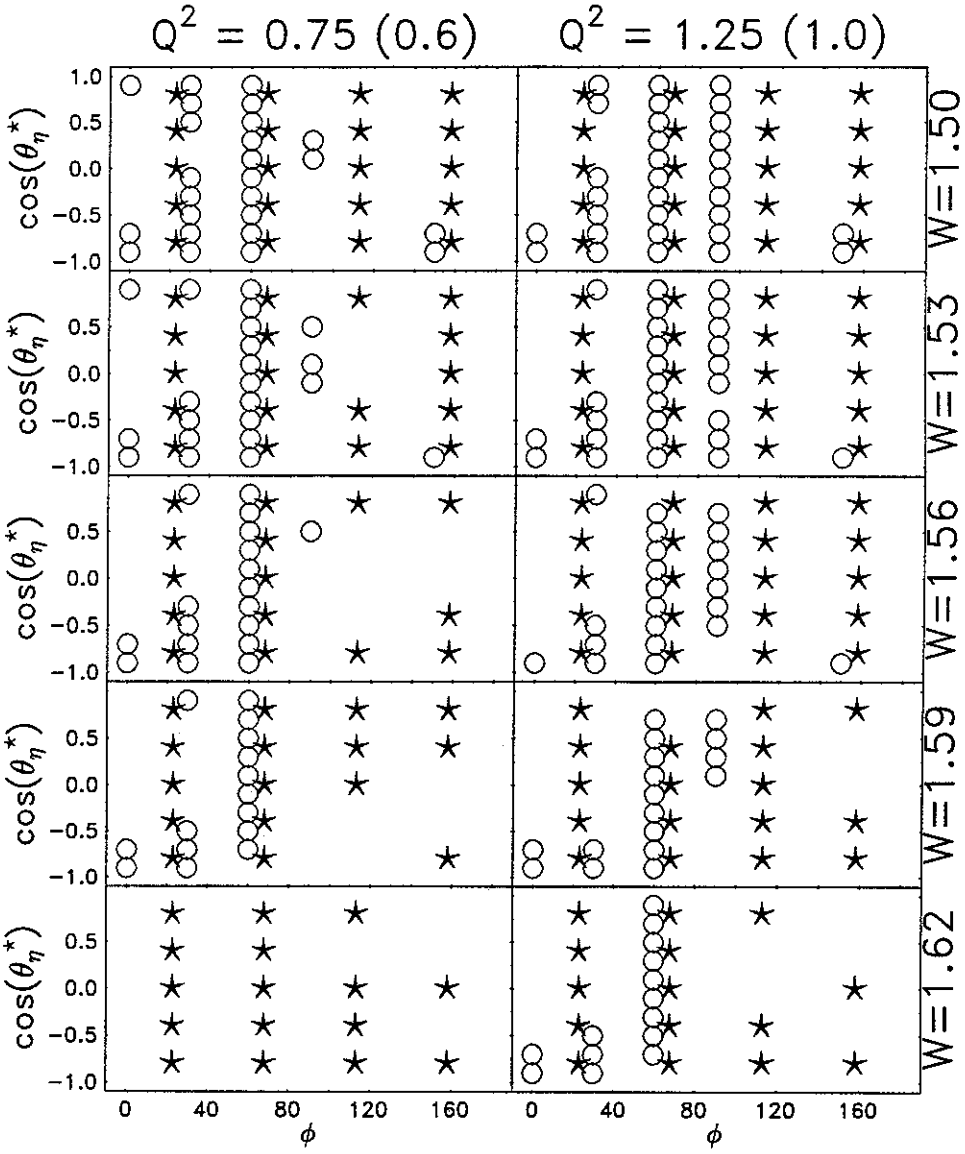

Figure 1.6: The angular coverage of electroproduction at the kinematics of this study. A marker is placed where there is an angular distribution point. The circles represent e data of [2] and [6] and the squares represent the data in this thesis. The two columns of plots are for two Q^2 bins and the columns of plots are the 5 W bins. The W bins of [2] and [6] were very similar to the current study (centered only $5MeV$ higher, and the Q^2 bins were centered at 0.6 and $1.0GeV^2$, which is noted in parenthesis in the label on the top of each column.

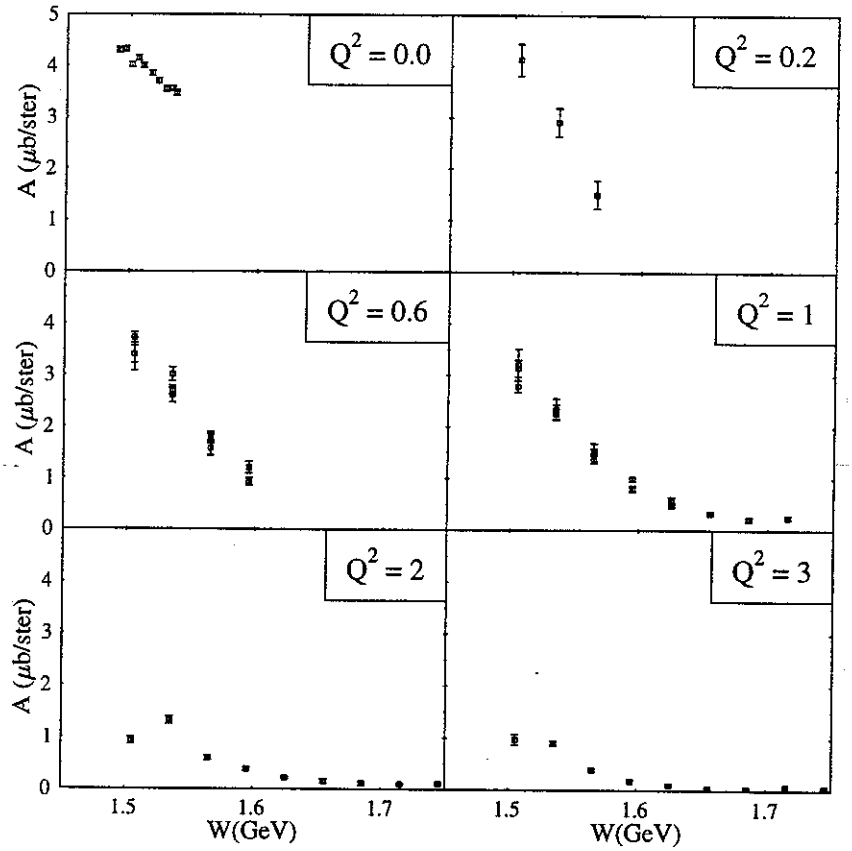

Figure 1.7: The multipole parameter A from previous experiments. The data at $Q^2 = 0GeV^2$ are from [24], the data at $Q^2 = 0.2GeV^2$ are from [2], the data at $Q^2 = .6$ and $1GeV^2$ are from [2] and [6] and the data at $Q^2 = 2$ and $Q^2 = 3GeV^2$ is from [7]. The fits were done with only A and B terms except for the $Q^2 = 0GeV^2$ case, which also included a C term.

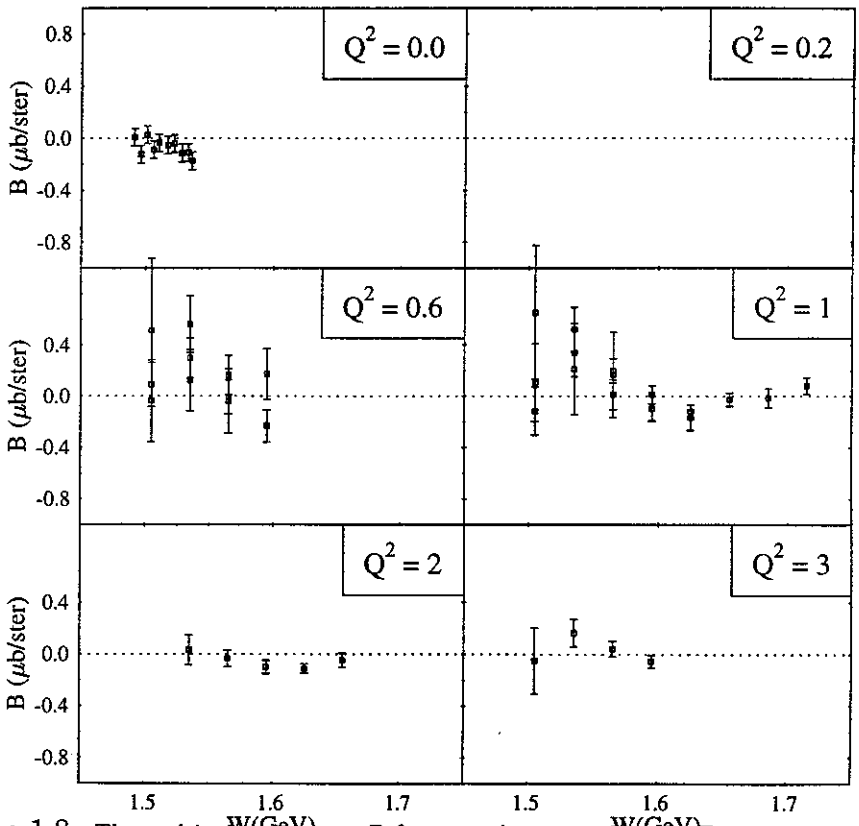

Figure 1.8: The multipole parameter B from previous experiments. Data sources are as in Fig. 1.8

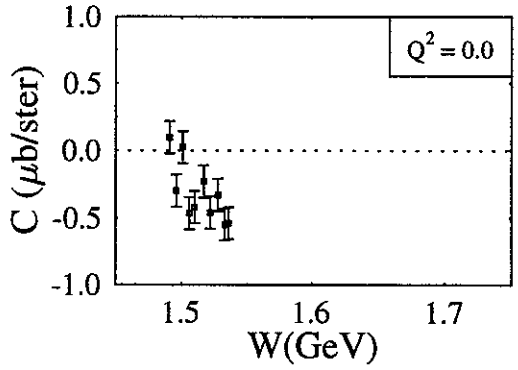

Figure 1.9: The multipole parameter C from previous experiments. Data is from [24].

Chapter 2

Apparatus

This chapter presents the experimental apparatus used in the measurement of electroproduction of the η meson reported in this thesis:

$$e^- p \rightarrow e^- p \eta \tag{2.1}$$

This measurement is via the missing mass technique; the η mesons are not directly observed, but rather are reconstructed from the kinematics of the other particles in the reaction. In order to do this, it is necessary to have: 1) identification of the final state particles, and 2) measurements of their momenta. Layers of drift chambers (DC) measure the momenta of charged particles by tracing their trajectory in a magnetic field, threshold Cerenkov counters (CC) and electromagnetic calorimeters (EC) provide electron identification, and time of flight scintillator detectors (TOF) provide proton identification.

The CLAS detector is based on a superconducting toroidal magnet with a maximum field intensity of about 2 Tesla. The toroidal field is oriented primarily in the azimuthal direction about the beam line and is generated by six sets of superconducting coils. The detector array is built up in layers around the target as shown in Figure 2.1. Each detector layer is made up of six separate sections (called sectors) as shown in Figure 2.2.

There are three layers of drift chambers named, in order from the target outwards, Region 1, 2 and 3, that provide coverage from 8° to 140° (measured as the polar angle relative the the beamline). Region 2 is in the region of the magnetic field. The Cerenkov counter and electromagnetic calorimeter coverage is from 8° to 45° , thus electron detection is only possible at forward angles. In two sectors, there are additional electromagnetic calorimeters that extend the coverage out to 80°, but those detectors are not used in this experiment. The time of flight detectors have a very large coverage from 9° to 140°, which allows for the detection of protons over a broad kinematic range. All of the detectors have virtually complete coverage in the azimuthal dimension, having only

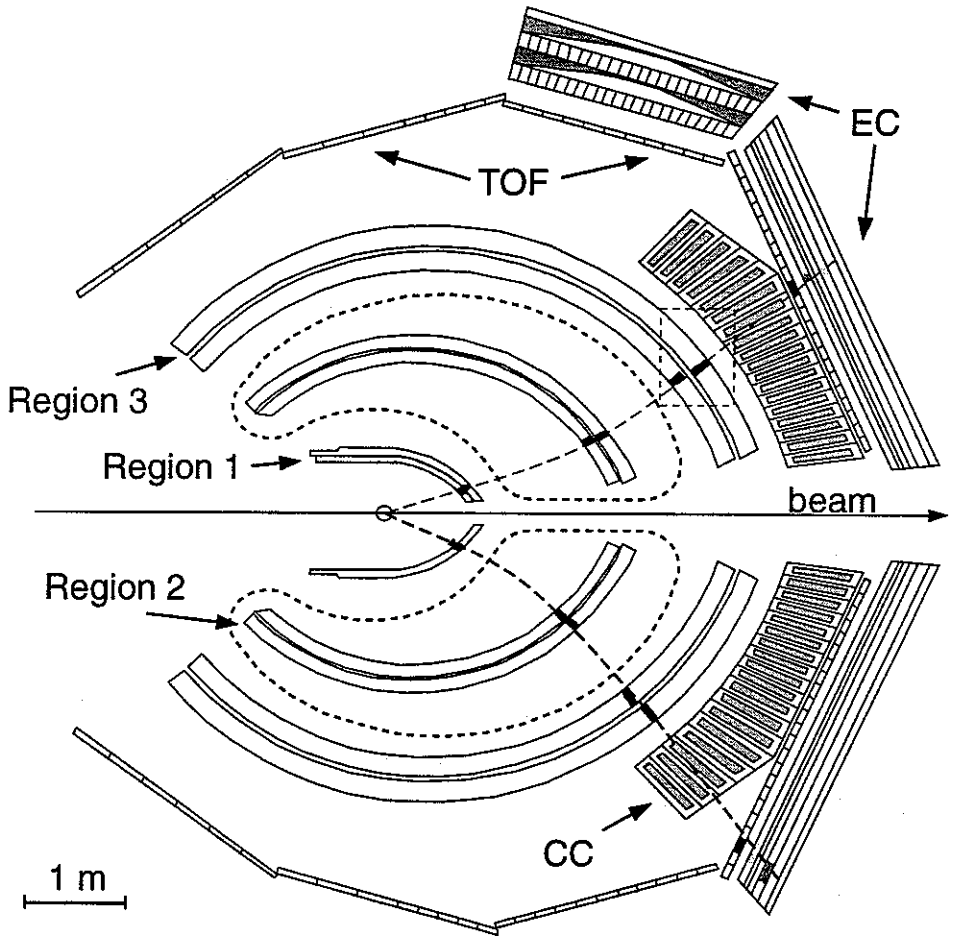

Figure 2.1: A cross section view of the CLAS detector viewed perpendicular to the beamline. The trajectory of two charged particles is shown with the corresponding hits in the detectors highlighted. The magnet coils, and the region of the magnetic field, are outlined with a dashed line. Not shown in this figure is a small toroidal magnet (called the mini-torus) that sits inside of Region1. The role of this magnet is to sweep low energy Møller electrons towards the beamline so that they do not swamp the drift chambers. The rectangular area that is highlighted is detailed later in Figure 2.5 This figure was taken from [11].

10° gaps for the magnet coils and the regions obscured by them. Photomultiplier tubes and readout electronics occupy this magnet coil "shadow" region.

The target used in this experiment was liquid Hydrogen enclosed in a crygonically cooled capsule approximately $4cm$ in length and $1cm$ in diameter. The entrance and exit windows of the target capsule are $15\mu m$ Aluminum. To prevent vaporization of the liquid Hydrogen due to heating by the electron beam, the beam was continually moved throughout the target by a "miniraster" magnet.

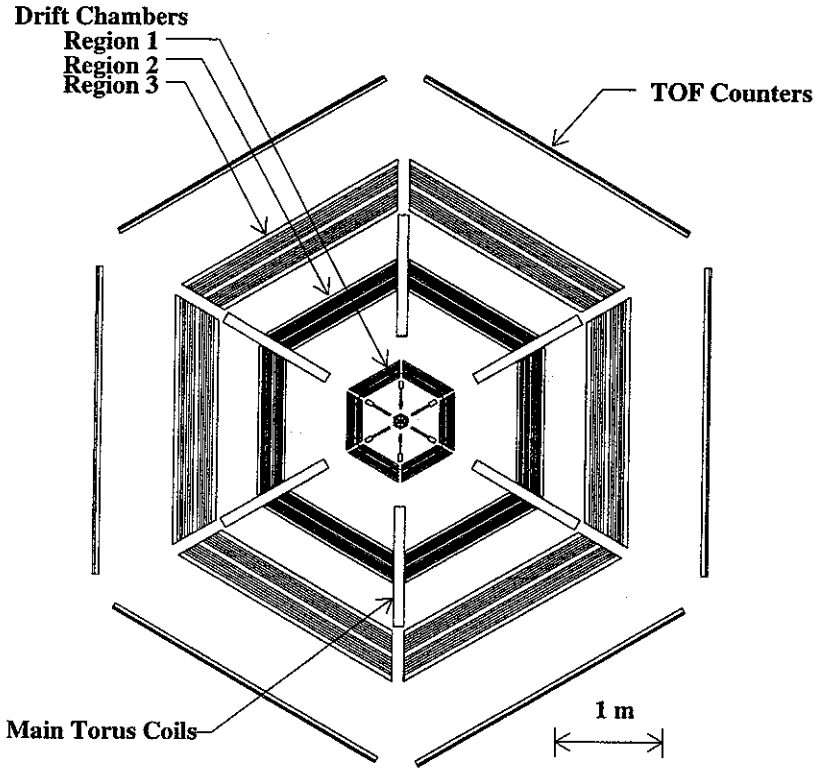

Figure 2.2: A cross section view of the CLAS detector viewed down the beamline. Wings of the mini-torus magnet are shown inside of Region 1. In the drift chamber regions, the orientation of the wires of the drift chambers are represented by lines. This figure was taken from [11].

In the following sections, after a brief description of the accelerator, the roles that each of the detectors takes in momenta determination and particle identification are explained.

2.1 Accelerator and Beam Line

The accelerator at TJLab utilizes a recirculating linear accelerator design as shown in 2.3. After electrons from the source are injected into the accelerator, they undergo to up to 5 passes, gaining up to 800MeV for each pass. At the switchyard, the beam is directed into the three experimental end-stations, where spectrometers are located.

Electrons are generated continuously at the injector with a thermionic gun. The electron beam is hence continuous (as opposed to pulsed), aside from a microbunch beam structure. The acceleration occurs along the linear accelerator sections in radio frequency, cryogenically cooled superconducting cavities. At any given moment, there may be up to 5 electron beams, with 5 different energies, being accelerated by the same cavities.

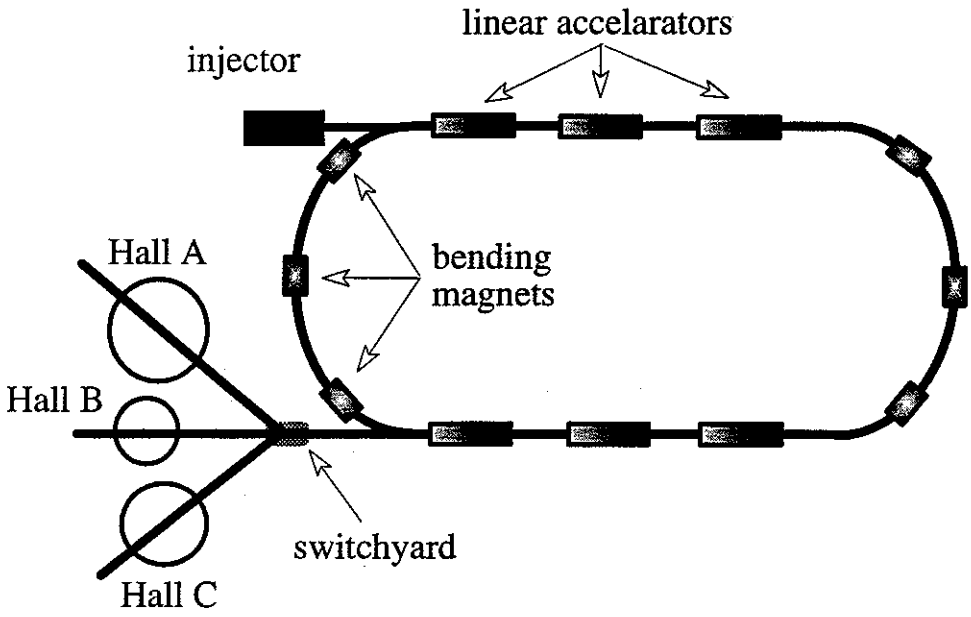

Figure 2.3: Schematic of the accelerator.

When the electron beams are turned around to be recirculated, the beam is split into the 5 different energies to be bent by magnets. The switchyard has three magnets which direct the beams to the experimental halls. The beams are structured in microbunches separated by approximately $2ns$; that allows beams of the same or different energies to be delivered to the three experimental end stations at different currents. The beam energy spread was typically $\frac{\Delta E}{E} < 10^{-4}$.

2.2 Drift Chambers

The determination of the momenta of charged tracks is done by drift chambers, which track the trajectory of charged particles. The principal of operation of a drift chamber is the collection of the electrons from the ionization of a gas as charged particles traverse it. The gas is in an electric field of typically $2.4kV/cm$, and when a charge particle ionizes the gas, the electrons and ions drift in opposite directions. As the electrons drift toward the sense wires, they collide with other atoms in the gas, resulting in additional ionization and amplification. The gas used was a $90\% - 10\%$ mixture of Argon and CO_2. The Argon provides the majority of the ionization and the gain of $\approx 10^4$, while the CO_2 absorbs x-rays that would otherwise result in a cataclysmic ionization avalanche (as in the case of a Geiger tube). The time that it takes the electrons to drift to the sense wires is measured to provide an accurate determination of the location of the track. The

intrinsic resolution of a drift chamber with $90\% - 10\%$ Argon - CO_2 is approximately $100\mu m$. The resolution achieved in this experiment was around $500\mu m$, most likely limited by knowledge of geometry and time dependence in calibration parameters. The final momentum resolution of the drift chambers was about 0.5% for low momentum tracks, and 1.5% for high momentum tracks. Further details of the construction and calibration of the CLAS drift chambers can be found in [11].

The CLAS drift chambers are arranged in three roughly spherical shells as shown in Figure 2.1. Each shell is made up of six identical drift chambers delimited by the coils of the toroidal magnet. One such drift chamber is shown schematically in Fig. 2.4. Circuit boards that provide pulse shaping and discrimination are mounted on the endplates, while the electronics that perform timing and readout to the data acquisition are in common electronics crates.

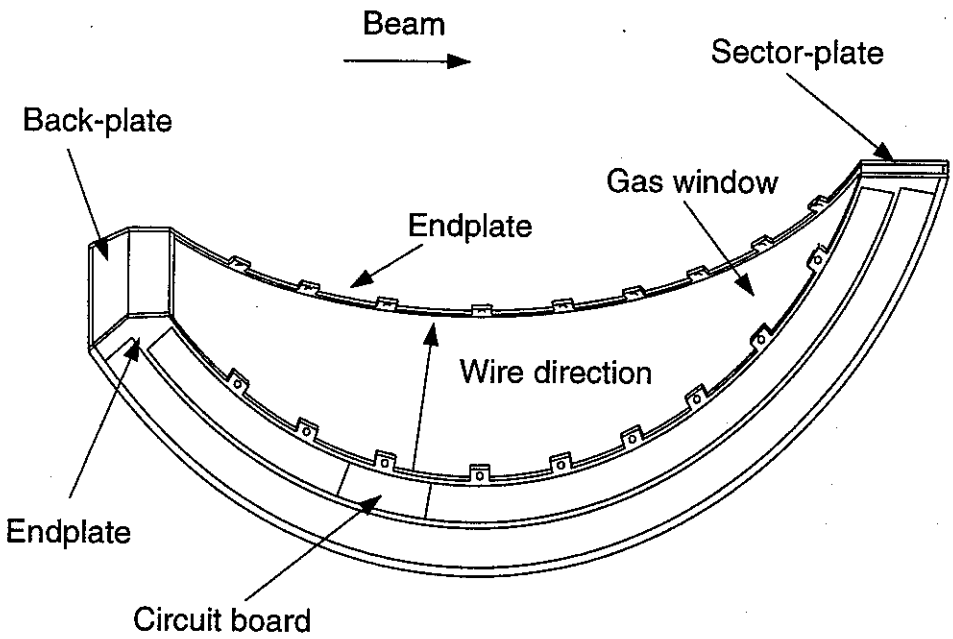

Figure 2.4: A single sector of a CLAS drift chamber. The back-plate, sector-plate and end-plates are made up of stiff structural materials, and the gas window is a thin membrane. This figure was taken from [11].

The wires are strung between the endplates of each chamber such that they are approximately in the azimuthal direction about the beamline. There are two groups of wires in each drift chamber, with a relative tilt of $6.5°$ to provide azimuthal information. The cell pattern is hexagonal with each drift cell formed by six field wires with a sense wire at the center. This is illustrated in Fig. 2.5.

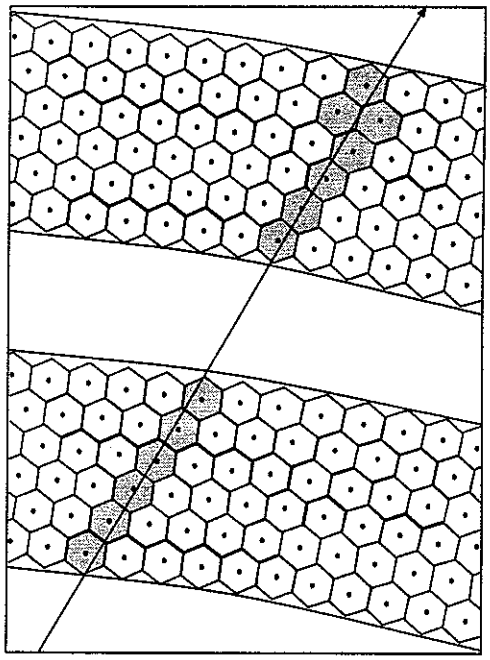

Figure 2.5: The cell pattern for the CLAS drift chambers. Shown are the two groups of wires of each drift chamber. One group is tilted by 6.5° relative to the other. The locations of the field shaping wires are connected with lines, making a hexagon with a sense wire at the center of each. The trajectory of a charged track is shown along with the cells that it fired. This figure was taken from [11].

2.3 Cerenkov Detectors

Electron identification is achieved primarily by the threshold Cerenkov detectors. These devices provide a signal when an electron passes through them, but not for other particles. Cerenkov radiation is the emission of electromagnetic radiation by a charged particle when it transitions to a medium where its velocity exceeds the local phase velocity of light. The threshold for Cerenkov light is $\beta \geq \frac{1}{n}$ where n is the index of refraction. The gas used in the CLAS Cerenkov detectors is perfluorbutate C_4F_{10}, which has an index of refraction of 1.00153, leading to a particle energy threshold for Cerenkov light of $E \geq \gamma_t m$, where $\gamma_t = 18.09$ and m is the mass of the particle. For electrons, this is only $9MeV$, which is considerably less than the trigger threshold, while for pions the threshold is $2.5GeV$, which is kinematically impossible with the $2.4GeV$ beam energy of this experiment.

The CLAS Cerenkov detectors are large volumes (6 cubic meters each) filled with gas and mirrors to reflect the Cerenkov light to photomultiplier tubes (PMTs) for conversion and readout. The mirrors reflect the light away from the active area of the detectors to the PMTs, which are situated in regions obscured by the coils of the main

torus magnet. Fig. 2.6 shows a schematic of a Cerenkov detector and an example of the path taken by Cerenkov light as it is reflected into the PMTs. The geometric shape of the mirrors is such that the light collection efficiency is optimized. A study of elastic scattering events showed that, within the fiducial volume cut described in section 4.3.3, the efficiency of the Cerenkov detector is $> 99\%$. Additional detail on the Cerenkov detectors can be found in [1].

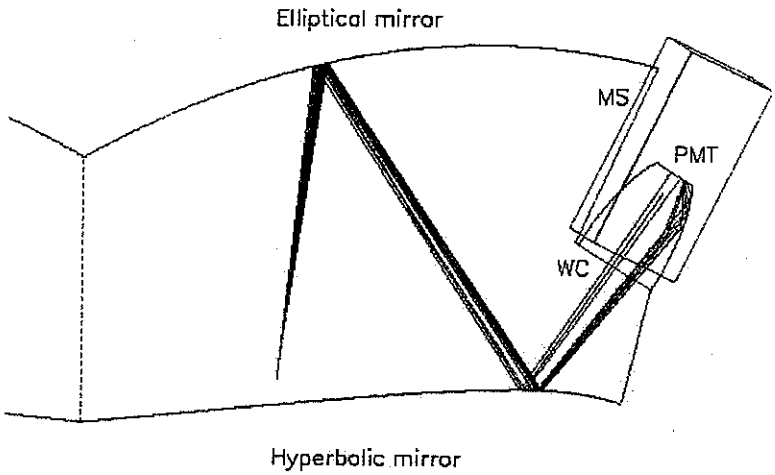

Figure 2.6: A schematic drawing of a Cerenkov light detector. The mirrors and a photomultiplier tube are shown along with an example of the trajectory of Cerenkov light rays. Structural material is not shown. Since the Cerenkov detector is in the fringe of the magnetic field, the PMT is protected by a magnetic shield (MS). Light is collected at the PMT by a Winston light collection cone (WC). The shape of the mirrors is chosen to optimize light collection efficiency.

2.4 Electromagnetic Calorimeters

Electron identification is aided by information from the electromagnetic calorimeters (ECs). The ECs measure the total energy of charged particles by stopping them and measuring the energy deposited in scintillating plastic (BC412). For the particle energies in this experiment, the energy of electrons is equal to their momenta to one part in 10^7: $E \approx p$, where E is measured by the calorimeters and p is measured by the drift chambers. Then combined with the momentum measurement from the drift chamber, the EC provides additional particle identification cuts. Electron identification is explained in detail in section 4.3.2.

The ECs, which have a forward angular coverage as shown in Fig. 2.1, consist of 39 alternating layers of lead ($0.23\ cm$) and scintillating plastic ($1\ cm$). The lead serves to slow particles by the conversion of Bremsstrahlung radiation via ($\gamma \rightarrow e^+e^-$), while

the scintillator serves to convert the energy of the resultant charged particles to light which is detected by photomultiplier tubes. Since some of the energy is absorbed in the lead, there is a conversion factor (known as the sampling fraction) which for electrons was 0.310. This represents the fraction of the energy that is deposited that is detected in the scintillating layers. The layers are divided into two "stacks" of 24 and 15 layers each. Within each stack, the scintillator paddle strips are grouped into three superlayers which are oriented 180° relative to each other. The intersection of activated paddles provides information on the position of the hit on the face of the EC. Light from the paddles is directed to the PMTs, which reside in the region obscured by the coils of the main torus magnet, by fiber optic guides. For more detail on the design and calibration of the ECs, see [30].

2.5 Time of Flight Scintillators

Proton identification is performed by the time of flight scintillators (TOFs). The TOFs measure the flight time of particles which, along with the flight path information from the drift chambers, allows a determination of a particles' relative velocity β. The mass of particles is then determined from $m = p/(\beta\gamma)$. Proton identification is presented in more detail in section 4.3.1.

The time of flight detectors are composed of bars of scintillator (BC-408) $5.08cm$ thick, $15cm$ (at forward angles) or $22cm$ (at backward angles) wide and from $32cm$ (at the forward angles) to 450cm (at backward angles) in length, covering $206m^2$. The bars are oriented in the azimuthal direction relative to the beam axis and provide only polar angle hit position information. The final time resolution of the TOFs was $120ps$ which provided more than adequate separation between protons and pions. Considerable detail on the TOFs is given in [31].

2.6 Trigger and Data Acquisition

The trigger initiator for the detector data to be read out and written to tape is a minimum bias electron trigger which only requires an EC and a CC hit above the trigger threshold in the same sector . The trigger thresholds were $0.30GeV$ for the EC and the equivalent of less than one photoelectron for the CC. This trigger yielded an approximately $\frac{1}{3}$ electron efficiency. The other two thirds of the events written to tape had no electron in them (according the the particle identification algorithms presented later) and were discarded.

For the differential cross section data presented in this thesis, the electron acceptance was limited by geometric acceptance and was not affected by the threshold. The hardware trigger threshold was set at $0.30GeV$, but due to resolution, this is not a perfect threshold in electron energy. By studying the elastic cross section from CLAS data, K. Egiyan [16] determined that the trigger was fully efficient by an electron energy of $500\ MeV$. For the kinematics of this study, there are virtually no electrons below $500MeV$.

The beam current was measured by a Faraday cup at the beam dump. The signal from the Faraday cup electronics was read out by a scalar that was gated on the DAQ live signal. The DAQ live time was $70 - 80\%$.

After the electronics readout is triggered, the raw data is compiled into data structures by a program running on the data acquisition computer. These raw data structures are written to a data buffer memory area (called the DD Ring) which can be accessed by a variety of applications or copied in memory to other computers. The DD Ring is used by programs which run monitoring software to analyze and assess the performance of the detectors and provide feedback to the personnel running the experiment in the control room. Another program which accesses the DD Ring is the Event Recorder which writes the data to RAIDs (Redundant Arrays of Inexpensive Disks). Several times per day the data is copied from the RAIDs to a tape silo in the computer center. The event rates for this experiment were typically $450\ Hz$, resulting in data rates of $1\ Mb/s$.

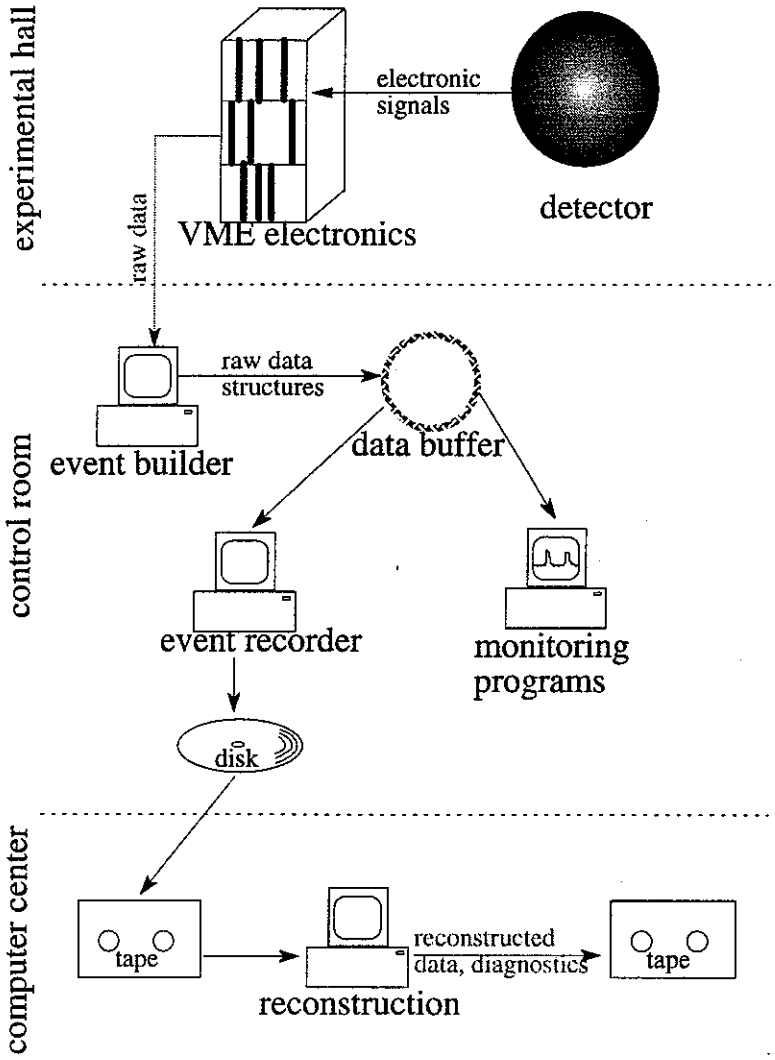

Figure 2.7: A conceptual schematic of the data acquisition.

Chapter 3

Stringing the Region 1 Drift Chamber

Region 1 is the inner drift chamber of CLAS. It is composed of six separate drift chambers (called sectors) as shown in Fig. 3.1. As with any large drift chamber, the construction of Region 1 has presented many unique problems. Some of these challenges have come about because the long endplates of the sectors are not stiff to the scale of wire tensions. This lack of stiffness of the sectors lead to two important effects that required compensation.

First, the forces applied to the endplates by the detector wires causes the endplates to warp to such a degree that the tensions of wires are dramatically effected. The deflection of the endplates was compensated for by pretensioning the sectors prior to stringing. That is, relatively few heavy steel wires were installed in order to deform the endplates prior to stringing. The placement and loads of these pretension wires is not arbitrary. In order to understand how to pretension Region 1, a mathematical model for the deformation of the endplates was constructed.

Second, because the endplates are thin, the sectors sag due to gravity. This is an important factor in the tensions of the stereo angle wires. The sag of the sectors was addressed by measuring its effect on the tensions of the stereo angle wires and simply compensating for it in stringing weights.

Region 1 uses $140\mu m$ gold coated aluminum field shaping wires and $20\mu m$ gold coated tungsten sense wires. In compensating for the effects mentioned above, it was desired to keep the tensions on the field wires within 20g of the nominal 100g and the tensions on the sense wires to within 6g of the nominal 30g. These criteria determined the number of pretension wires, the number of pretension transfer steps, and the number of different sag compensation stringing weights used. Since 90% of the entire load on the endplates is due to the field wires, the pretension load was transferred to the field wires first, then the sense wires were strung. The effective spring constant of the sense wires is a factor of 9.2 less than that of field wires (eqns. 3.3), so for sense wires, the gravitational

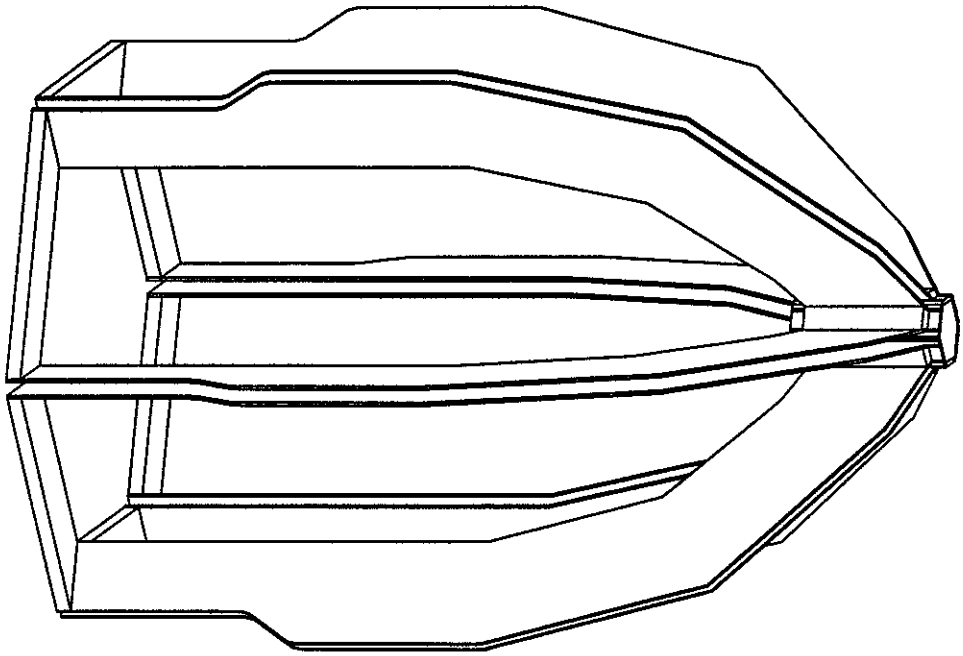

Figure 3.1: The CLAS Region 1 drift chamber A drawing of Region 1 showing the endplates, backplates, noseplates, and the hexagonal pipe that attaches the noseplates together. The posts that provide structural support before the sectors are integrated are not show. Each sector is assembled and strung separately; it is only at the last stage that the six sectors are integrated.

sag of sectors is not an important factor either. The warping and gravitational sag of the endplates are effects that are only relevant to the tensions on the field wires.

3.1 Pretensioning

The pretensioning of Region 1 is presented. First, evidence is presented showing that it was necessary to compensate for the warping of the endplates. Next is an outline of the model used to understand the deformation of the surfaces of the endplates as a result of forces applied to them by wires. This model was used to choose the placement and load of the pretension wires. This model was also used as a guide in constructing a scheme to transfer tension from the pretension wires to the detector wires.

3.1.1 The Need for Pretensioning

This section describes the need for pretensioning the CLAS Region 1 drift chamber. The loss of wire tension due to the warping of the endplates is described and observations in a Region 1 full scale prototype are presented.

The endplates of Region 1 are constructed from plate aluminum 7.9mm in thickness. Each of the six sectors has 3435 field and guard wires strung at a nominal tension of 100g and 1296 sense wires strung at a nominal tension of 30 g for a total of 3.75 kN (843 lbs) of force on each endplate. The endplates will deform as a result of this heavy load and the surface of the endplates will no longer be flat. As the sector is strung, the wires that were strung earlier will lose tension because the wires that were strung later will pull the endplates together. Fig. 3.2 shows this effect after stringing about 12% of a full-scale prototype sector.

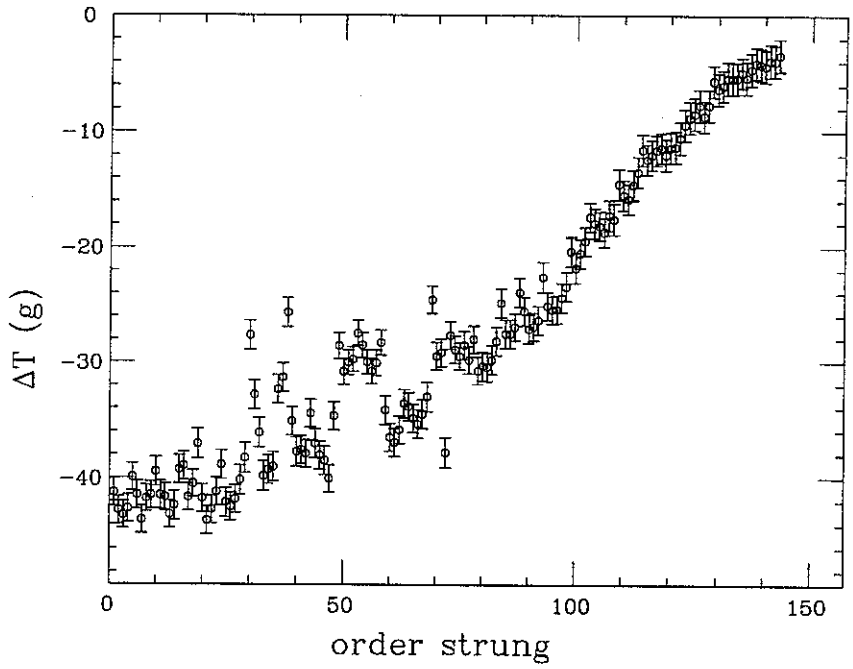

Figure 3.2: Wire tension loss due to stringing. The tension change on tension monitoring wires strung in the full scale Region 1 prototype plotted versus the order that those wires were strung. The tension monitoring wires that were strung first lost tension as a result of the wires that were strung later. Since only a small section of the prototype was strung, this effect would be much worse in the real detector if there were no pretensioning.

Based on measurements of this endplate deformation in the prototype and a model that will be presented later in this paper, it was anticipated that if we did not

compensate for this phenomenon in a sector where 100% of the detector wires are strung, some wires would go completely slack. For a wire with some tension applied to it such that Hooke's law is applicable, a change in length ΔL of a wire of length L will lead to a change in effective mass Δm (the effective mass is just $m = T/g$, where g is the acceleration due to gravity) according to

$$\Delta m = k \cdot \frac{\Delta L}{L} \tag{3.1}$$

The constant k is given by

$$k = \frac{Y \cdot A}{g} \tag{3.2}$$

where Y is Young's modulus and A is the cross sectional are of the wire. Young's modulus was measured for the $140\mu m$ gold coated aluminum field wire, and for the $20\mu m$ gold coated sense wire and obtained

$$\begin{aligned} k_{field} &= 1.10 \cdot 10^5 \, grams \\ k_{sense} &= 1.19 \cdot 10^4 \, grams \end{aligned} \tag{3.3}$$

It was predicted that due to the deformation of the endplate, the length of some wires in the sectors would change by as much as 0.064cm, which corresponds to 105g by eqn. 3.1. This length change is certainly outside of the range where the wire will obey Hooke's law, but the conclusion that these wires will go slack is still valid.

The observation of wire tension loss due to endplate deformation in the Region 1 full scale prototype and our predictions of the scale of the effect in the actual detector indicated a real need for pretensioning. The objectives of pretensioning are twofold. First, the pretensioning should mock the deflection of the endplates with relatively few pretensioning wires that are installed prior to stringing. And second, the tension in the pretension wires should be transfered to the detector wire in such a way that the final tensions on the detector wires are within an acceptable range of nominal. Both of these objectives necessitate some quantitative understanding of how the surface of the endplate is deflected as a result of the forces applied to it by wires. It was felt that a model describing the surface of the endplate would be a more efficient approach than an exact solution derived from the complicated boundary conditions and the material properties of the endplate.

3.1.2 A Model for Endplate Deflection

Fig. 3.3 shows the geometry of the problem. All points are referenced to a coordinate system that is on the flat surface of one endplate. An arbitrary origin is

chosen. The deflection of the endplate from flatness, $D(\vec{x})$, at the point $\vec{x}$ due to the force T exerted on the endplate by the wire located at $\vec{p}$ is determined. Posts are located at the points described by $\vec{h}_i$. The point $\vec{x}$ is located along a ray originating from the wire. The direction of this ray is described by the unit vector $\hat{r}$ as shown.

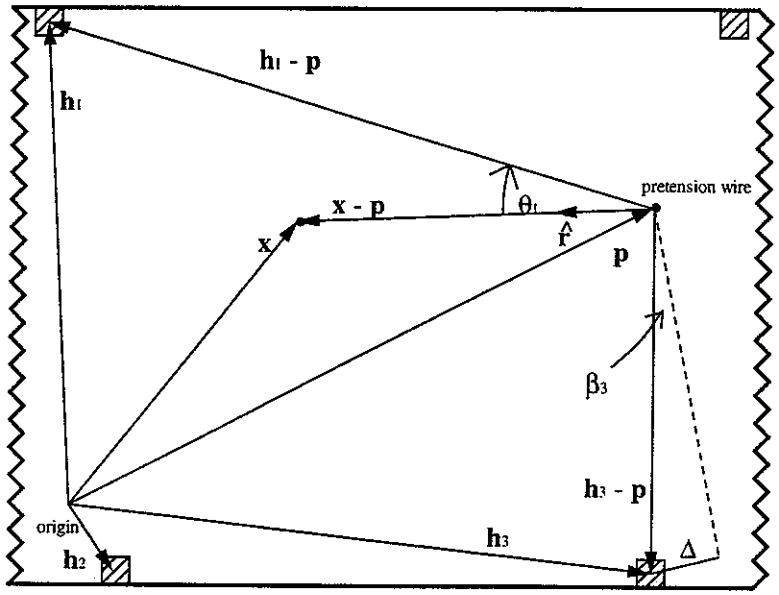

Figure 3.3: A schematic drawing defining the geometry on the surface of an endplate. The border of the endplate, which continues to the left and right, is shown as a bold line. Posts are indicated by hatched squares and are located at the points given by $\vec{h}_i$. A wire (detector wire or pretension wire) is located at the point $\vec{p}$ and the point at which the endplate deflection is being considered is given by the point $\vec{x}$.

Our approach was to use intuitive physical principles to construct a model which describes the deflection of the endplate due to the forces applied to it by wires. The model contains some parameters which could then be fit by taking measurements of endplate deflections. There are two general assumptions used to choose a form for $D(\vec{x})$: 1) The magnitude of the deflection of the endplate at the location of the wire is proportional to the tension in that wire. 2) The shape of the endplate along polar rays centered at the wire is a straight line. With these assumptions, the deflection of the endplate is written

$$D(\vec{x}) = T \cdot [m(\theta) \cdot |\vec{p} - \vec{x}| + K(\vec{p})] \tag{3.4}$$

Here $m(\theta)$ is the slope of the endplate along a ray centered at the wire, θ is the polar angle of the ray, and $T \cdot K(\vec{p})$ is the deflection of the endplate at the location of the pretension wire. It is $m(\theta)$ that describes the wrinkles forced in the endplate by posts.

As can be seen from eqn. 3.4, the ideas of the model presented here are very simple. The geometry of the problem, though, makes the implementation of the model

more complicated. Specifically, the model must be able to accommodate boundary conditions of zero deflection at various locations. The endplates are fastened at the upstream and downstream ends to rigid plates, and during construction, the endplates are fastened to each other by 22 rigid posts. At these points, the deflection of the endplates is constrained to be zero. As Fig. 3.4 shows, the location of these boundary conditions (and also the shape of the endplates) is in no way simple.

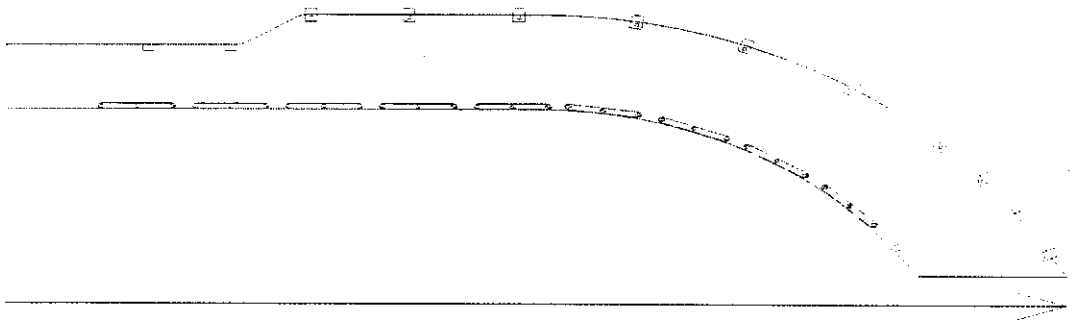

Figure 3.4: The surface of an endplate. The beam axis and direction are indicated by the arrow. The length of the endplate along the beam axis is 2.28m. The shaded region is where the detector wires are strung in two superlayers: one with wires perpendicular to the beam axis and one with wires tilted at a 6° angle relative to the beam axis. The posts along the top edge are located where the rectangular mounting brackets are shown. The posts along the bottom edge are located at the center of the long mounting brackets. The deflection of the endplate is constrained to be zero at the location of posts and where the endplate attaches to rigid plates at the upstream (left) vertical edge and the downstream horizontal edge. The geometry of these constraints makes for a complex set of boundary conditions that a model of endplate deflection must obey.

The model can conceptually be broken down into two aspects: 1) $K(\vec{p})$, the magnitude of the deflection of the endplate at the location of the wire and the dependence of this deflection on the proximity to posts and rigid edges, 2) $m(\theta)$, the shape of the endplate along polar rays originating at the wire and the dependence of the shape of these rays on the polar angle.

3.1.2.1 Deflection at the Wire: Flexibility

Let $S(\vec{p})$ be the deflection of the endplate from flatness at the location of a wire. $S(\vec{p})$ should depend on two things: the tension in that wire and the distance of that wire from the rigid constraints of plates and posts. As already mentioned, it was assumed that the deflection of the endplate at a wire is proportional to the tension in that wire: $S(\vec{p}) = T \cdot K(\vec{p})$. Fig. 3.5 shows that for tensions less that 133N (30lbs), this is indeed the case.

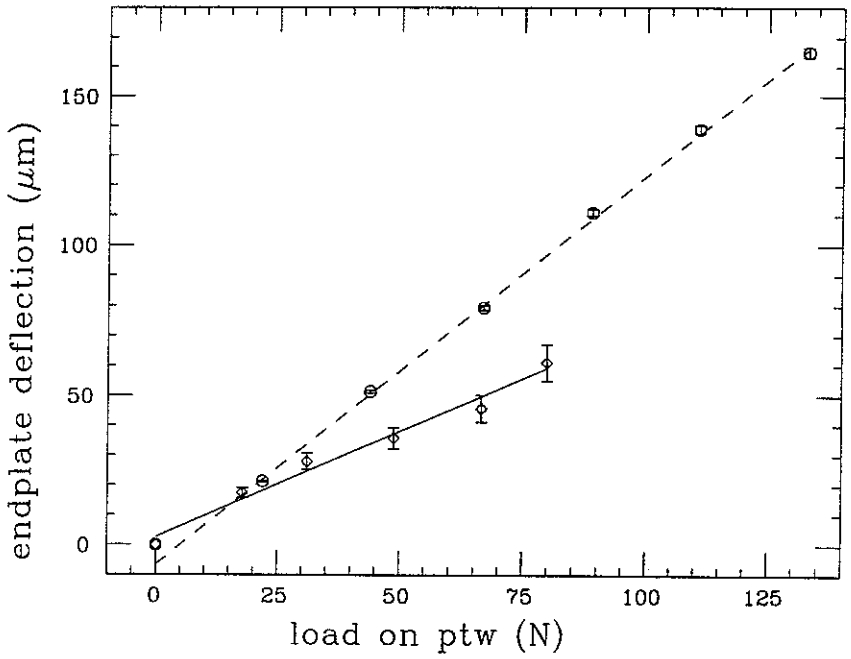

Figure 3.5: The deflection of the endplate at the positions of two wires plotted as a function of the loads on the wires. Since these two wires are at different locations on the endplate, the slopes of the two lines should not necessarily be the same. The slope of the line is $K(\vec{p})$. The wire represented by the diamond symbols and the solid line was located at a more rigid place in the sector than was the wire represented by the circular symbols and dashed line.

$K(\vec{p})$ is a measure of the flexibility of the endplate and should depend on the location of the wire relative to posts and rigid edges. $K(\vec{p})$ is subjected to two limits: 1) The endplates are rigid at posts, $K(\vec{h_i}) = 0$. 2) The flexibility of the endplates approaches some asymptotic value far from posts or rigid edges. A Gaussian was chosen as the mathematical form for the transition between these two limits. For a single post, the flexibility of the endplate is written as

$$K_i(\vec{p}) = K_0 \cdot \left(1 - e^{-\frac{1}{2\alpha^2}\left|\vec{p}-\vec{h_i}\right|^2}\right). \tag{3.5}$$

K_0 is the asymptotic value of the flexibility; its value for an infinite sheet of material. α is a parameter which describes the dependence of the flexibility on the proximity to posts and rigid edges. Multiple posts and rigid edges are accommodated by including a factor of $(1 - e^{-\frac{1}{2\alpha^2}\left|\vec{p}-\vec{h_i}\right|^2})$ for each post:

$$K(\vec{p}) = A \cdot \prod_i \left(1 - e^{-\frac{1}{2\alpha^2}\left|\vec{p}-\vec{h_i}\right|^2}\right). \tag{3.6}$$

Fig. 3.6 shows the flexibility for a simple hypothetical endplate. A and α are parameters that are fit to measurements of endplate deflection.

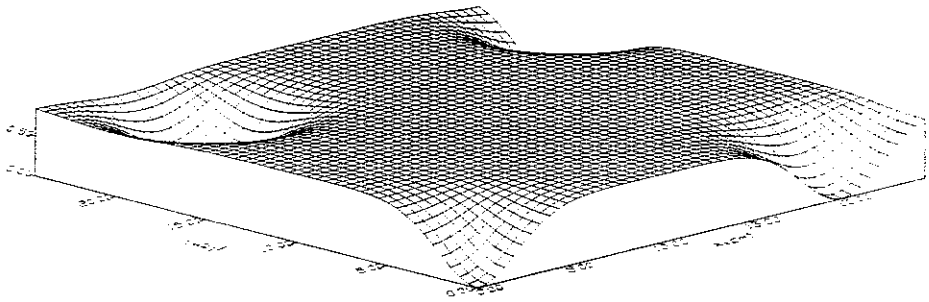

Figure 3.6: The flexibility of the endplate (in units of $\mu m/N$) plotted over the surface of a hypothetical endplate. Posts are located where the flexibility goes to zero.

3.1.2.2 Shape Along Polar Rays

It is assumed that the surface of the endplate along polar rays centered at the wire under consideration is straight. By taking endplate deflection measurements, it is demonstrated that this is the case for wire tensions less than 133N (30lbs), as shown in Fig. 3.7. The slope of the endplate along these rays is $m(\theta)$ from eqn. 3.4.

Consider the simple case where there is only one post. Let $m_i(\theta)$ be the contribution to the slope of the endplate along the ray $\hat{r}$ due to that post. $m_i(\theta)$ has two limits, similar to $K(\vec{p})$. 1) When the ray from the wire points to a post $\left(\hat{r} = \frac{\vec{p}-\vec{h_i}}{|\vec{p}-\vec{h_i}|}\right)$, $m_i(\theta)$ is determined from $S(\vec{p})$ and the distance from the wire to the post $\left|\vec{p}-\vec{h_i}\right|$. Let θ_i be the polar angle from the wire to the i_{th} post. Then

$$m_i(\theta_i) = -\frac{S(\vec{p})}{\left|\vec{p}-\vec{h_i}\right|} \tag{3.7}$$

2) When $\hat{r}$ points in a direction far from any posts, $m_i(\theta)$ should approach some asymptotic value. It is assumed that the form of the transition between these two limits is Gaussian:

$$m_i(\theta) = p_0 + p_i \cdot e^{-\frac{1}{2\beta_i^2}(\theta-\theta_i)^2} \tag{3.8}$$

Here p_0 is the asymptotic value that $m(\theta)$ takes when $\hat{r}$ points away from any posts. For an infinite sheet of material, p_0 is the slope of the surface of the material along a ray

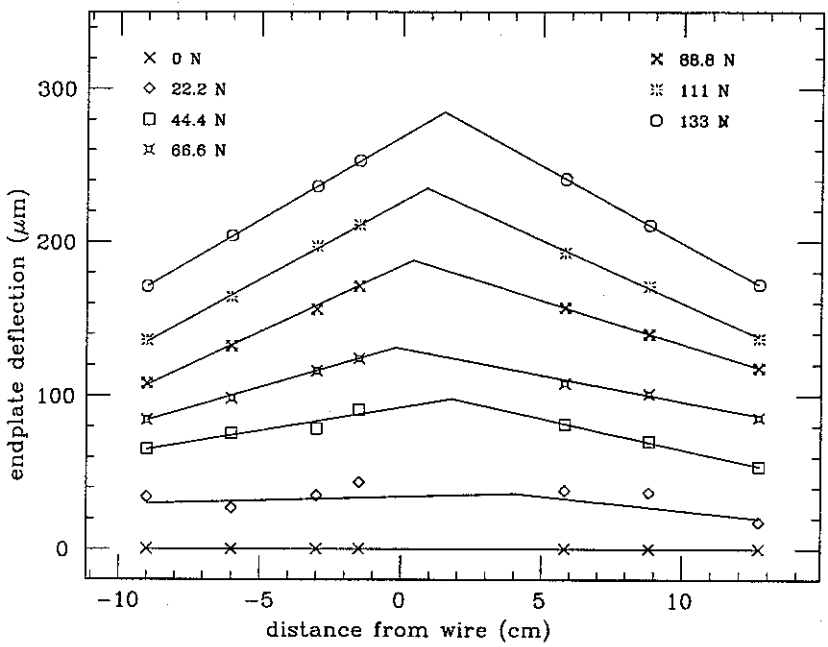

Figure 3.7: Deflection of the endplate The deflection of the endplate is plotted as a function of distance from the wire for various loads. This essentially shows cross sections of the surface of the endplate with different loads applied to a wire. The distance from the wire is along a particular polar ray from the wire. The solid line is the shape of the deflected endplate that is inferred by assuming a linear shape along polar rays.

centered at a wire that has one unit of tension applied to it. β_i is the angular width of the Gaussian wrinkle formed by a post. β_i depends on the distance between the wire and the post, but can be related, as shown in Fig. 3.3, to a parameter Δ which represents in some sense the stiffness of the material (similar to α).

$$\beta_i = cos^{-1}\left(\frac{2\left|\vec{p}-\vec{h}_i\right|^2 - \Delta^2}{2\left|\vec{p}-\vec{h}_i\right|^2}\right) \tag{3.9}$$

Of course, in reality there are many posts. Multiple posts are accommodated by including a term of Eqn. 3.8 for each post:

$$m(\theta) = p_0 + \sum_i p_i \cdot e^{-\frac{1}{2\beta_i^2}(\theta-\theta_i)^2} \tag{3.10}$$

In this equation, the p_i are treated as n unknowns (n is the number of posts being considered), but there are also n equations from which to determine the value of the p_i:

when θ is such that the polar ray from the wire points at one of the posts, the value of $m(\theta)$ is known from eqn. 3.7.

With the flexibility $K(\vec{p})$ given by eqn. 3.6, and the wrinkle shape $m(\theta)$ given by eqn. 3.10, the endplate deflection is completely determined by eqn. 3.4. Fig. 3.8 shows the endplate deflection for a hypothetical endplate.

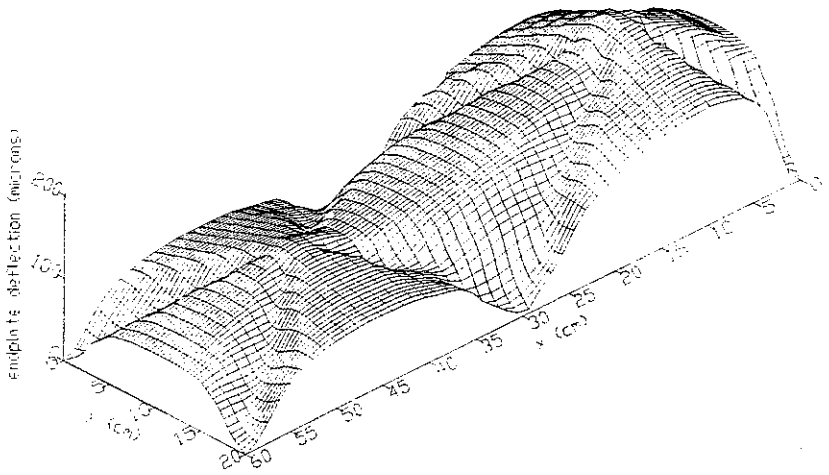

Figure 3.8: Deflection of an endplate with posts. The surface of an endplate with six posts located at (0,0), (30,0), (60,0), (60,20), (30,20), and (0,20), and two wires located at (10.5, 10.5) and (45.5,10.5) with loads of 111N and 66.6N respectively.

Four parameters were during the construction of the model. These parameters were fit to measurements of endplate deflection. The values determined for them are:

$$\begin{aligned} K_0 &= 2.16\ \mu m\ N^{-1} \\ \alpha &= 2.21\ cm \\ \Delta &= 2.19\ cm \\ p_0 &= 0.111\ \mu m\ cm^{-1} \end{aligned} \tag{3.11}$$

3.1.3 Pretensioning Scheme

With a model for endplate deflection in place, a scheme for pretensioning Region 1 could be considered. The model was used to determine the correct number, location, and load for the pretension wires. The transfer of tension from the pretension wires to the field wires was also modeled.

In choosing the pretension wires, the goal was to keep the tension change on wires to less than 10 grams, while using as few as possible pretension wires. The deflection of the endplate with all of the detector wires was first determined. This represents the "strung" shape of the surface of the endplate if all wires were installed at nominal tensions.

Next, an analogous calculation, was carried out for endplate deflection with pretension wires and varied the number, location, and load of pretension wires until the difference between the "pretensioned" and "strung" endplate surfaces was such that the corresponding change in wire tensions was less that 10g. Our final pretensioning consisted of 67 wires with effective mass loads ranging from 2 to 14 kg.

When the load in a pretension wire is reduced, the detector wires that have been installed to that point will become tighter. The detector wire installed immediately before a pretension transfer is then tighter than the detector wire installed immediately after a pretension transfer. A second objective in working out a pretension transfer procedure was to keep this tension difference between certain adjacent wires to less than 10g. The issue then is the number of pretension transfers performed on each pretension wire, and the point in stringing that each pretension transfer is performed. For the sake of expediency in stringing the sectors, it was desirable to have no more than three tension transfers performed on each pretension wire.

A scenario for pretension transfer was determined by calculating endplate deflections for each pretension wire individually. It was determined that three or fewer pretension transfers could be performed, each of equal tension change and with an equal number of detector wires strung between each, and stay within the specification mentioned above.

3.2 Gravitational Sag

The Region 1 sectors were strung on their sides (beam axis horizontal) so that the wire could be lowered through the feedthroughs in both endplates. During construction, each sector was mounted on a stringing frame and attached to it at the nose and back plates. The frames allow the sector to be oriented at any azimuthal angle. The sector azimuthal angle is here defined as the angle of the midplane between the two endplates as one would see it looking from upstream. 9 o'clock is then the orientation of the sector where the midplane between the endplates is parallel to the floor and to the left as seen from upstream. The sectors were strung in the 9 o'clock orientation.

Stringing the sectors at the 9 o'clock orientation facilitated installation of the wires, but allowed the sector to sag, as they were mounted to the stringing frame only at the nose and back. When a sector is oriented such that the surfaces of the endplates are nearly parallel with the ground (the surfaces of the endplates are mounted 30° to each other), they bow down due to their own weight. But when a sector is oriented such that the surfaces of the endplates are nearly perpendicular to the ground, the sectors are stiff in the direction that the force of gravity is acting, and there is no sag. It was verified

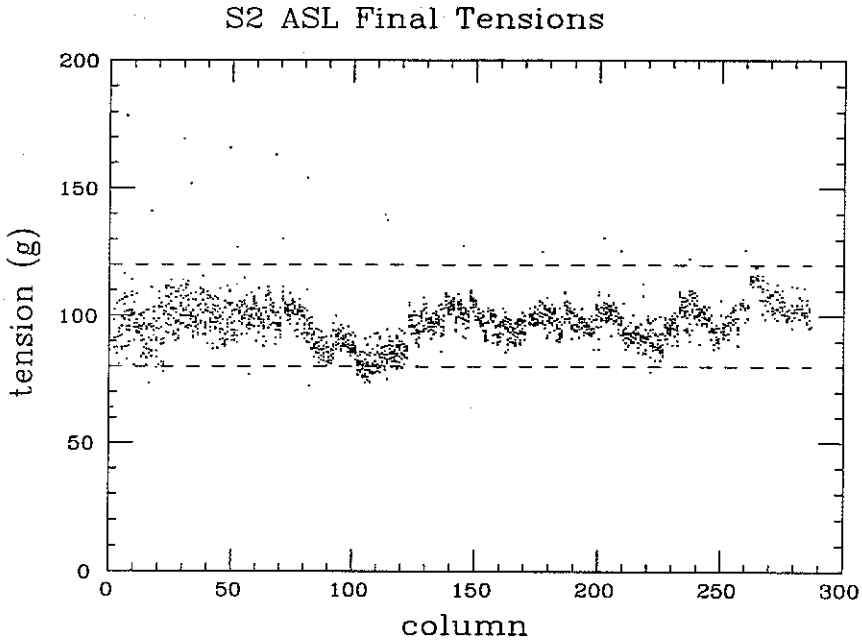

Figure 3.9: The final tensions of the field and guard wires in the sector 2 axial superlayer. The pretensioning for sector 2 was determined using a model that solved the endplate deflection for an entire sector simultaneously.

that wire tensions in the 6 or 12 o'clock orientations best matched those of a sector that was not mounted to a stringing frame and not subjected to gravitational sag. In the 3 o'clock or 9 o'clock orientations, each of the sectors sagged by about 6mm at the middle. As illustrated in Fig. 3.10, this will cause the stereo superlayer wires at the nose to be shorter, and the wires at the back to be longer, relative to the 12 o'clock or 6 o'clock orientations, where the sectors do not sag. The tensions in the axial superlayer wires will be unaffected by the gravitational sag of the sector.

It was determined the effect of the gravitational sag of the sectors by measuring wire tensions at 9 o'clock (where the sectors are strung) and at 12 o'clock. This allowed us to compensate for the sagging of the sector by adjusting nominal stringing tensions along the length of the sector. As Fig. 3.11 shows, the sector sag effect is dramatic. The sense wires are about nine times less sensitive in tension to length changes (see eqns. 3.3). Because of this, gravitational sag while stringing the stereo angle sense wire was not compensated for.

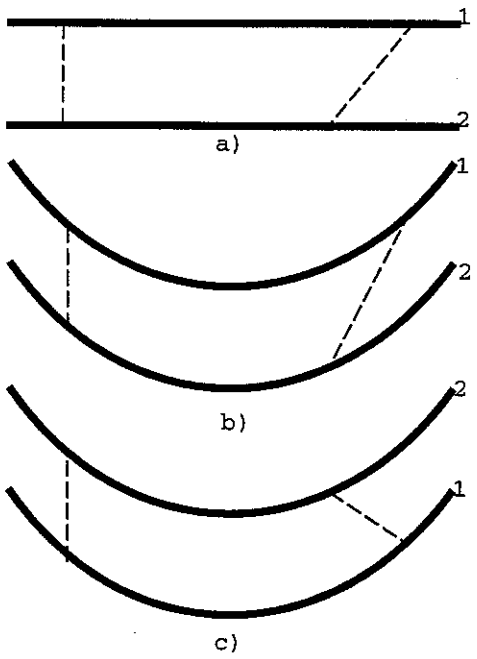

Figure 3.10: Illustration of gravitaional sag. An illustration of two plates supported at the ends and the effect of gravitational sag on wires strung between the plates. The drawings show cross sections of two plates (bold lines) with two wires (dashed lines) strung between them. The wire that is perpendicular to the plates is analogous to an axial wire and the wire that is not normal to the plates is analogous to a stereo angle wire. The plates are numbered 1 and 2 in order to reference the stereo angle. The configuration of the plates and wires without gravitational sag is shown in Fig. (a). An exaggerated gravitational sag is shown in Fig.(b), where the lengthening of the stereo angle wire is evident. Fig. (c) shows the situation where the plates have been flipped over (plate 2 is on top) and the stereo angle wire is shortened. To first order, the length of the axial wire is unaffected by gravitational sag.

As previously mentioned, the gravitational sag of the sectors were addressed during stringing by compensating for it in the nominal stringing tensions. The objective here was to string the stereo superlayer field wires at whatever tension was necessary such that when the sector was oriented at 12 o'clock or 6 o'clock the field wire tensions were $110 \pm 20g$. The stereo superlayer field wires were strung at tensions T_{string} which was adjusted from the nominal tension T_{nom} $(110g)$ by an amount ΔT, which is the amount by which the tension is expected to change when the sector is oriented at 12 o'clock. T_{string} varies along the length of the endplate.

$$T_{string} = T_{nom} + \Delta T \tag{3.12}$$

ΔT was measured by measuring the tension in a set of wires when the sector was oriented at 9 o'clock and when it was oriented at 12 o'clock. Then $\Delta T = T_9 - T_{12}$.

Fig. 3.11 shows ΔT as measured in a fully pretensioned sector. As shown in that figure, 15 different stringing steps were used to string the stereo superlayer of sector 2 ranging from 50g to 190g. Since the endplates are rigidly fastened to a plate at the nose of the sectors, the gravitational sag of the sector must be zero there. Then the solid line in Fig. 3.11 must return to 0g at column 0. Table 3.1 lists the stringing weights used to compensate for the sag effect, and the final tensions stereo superlayer wires are show in Fig. 3.12.

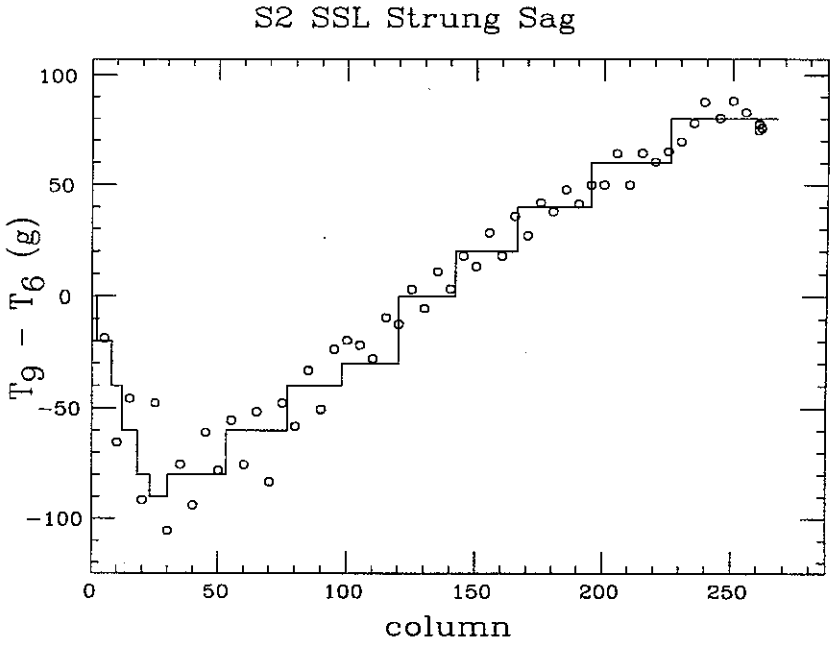

Figure 3.11: The sag effect after all of the detector wires had been installed. The circles show the measurements and the solid line shows the compensation curve that was used. That $T_9 - T_{12}$ goes to 0g at column 0 is necessitated by the fact that the endplates are rigidly fastened to a plate there. The same effect is not observed in the rear of the sectors because the wires there are far from the rear rigid fastening plate as can be seen from 3.4.

Columns	Nominal Stringing Tension (g)
1 - 2	100
3 - 8	80
9 - 12	60
13 - 18	40
19 - 23	20
24 - 30	10
31 - 53	20
54 - 77	40
78 - 98	60
99 -120	80
121 -142	100
143 -166	120
167 -195	140
196 -226	160
227 -267	180

Table 3.1: The nominal field and guard wire tensions for the stereo superlayer of sector 3. This gravitational sag compensation was arrived at by taking measurements of the sector 2 gravitational sag after it was completely strung (see Fig. 3.11)

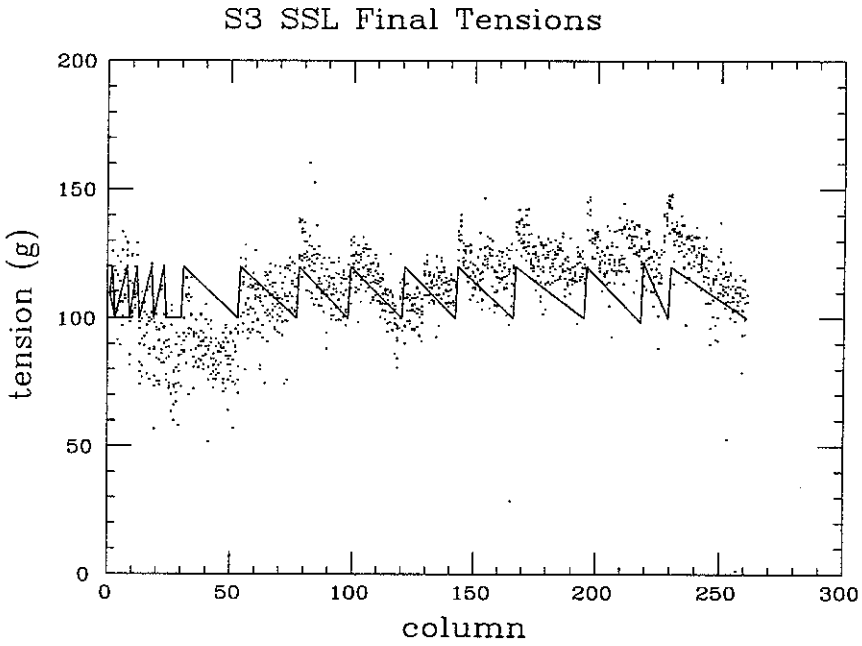

Figure 3.12: The final tensions on the field and guard wires of the sector 3 stereo superlayer wires. The solid line shows the tensions that would be expected if the sag compensation scheme were correct. The sag compensation scheme used was based on measurements taken on sector 2 (Fig. 3.11), and that the final tensions do not lie near the solid line in the nose is indicative that the gravitational sag of sectors 2 and three is different.

Chapter 4

Reconstruction

This chapter presents the reconstruction of four momenta and identified particles from the CLAS detector data. Information from the drift chambers are used to determine the trajectories of charged particles through CLAS. These trajectories are used to project tracks to the outer detectors in order to identify corresponding hits. The information from all detectors is combined to give particle identification to the tracks.

4.1 Tracking and Start Time Reconstruction

One of the unique features of the CLAS detector is that during electron beam operation, there is no start time counter. This means that there is no direct measure of the time in the event at which the particles were at the target. The event start time is determined by identifying an electron in the event and reconstructing the event start time from that particle's time of flight. The first stage of track reconstruction, hit-based tracking (HBT), which uses only the wire positions and not the drift times of hits, is used to identify an electron from which to obtain the event start time. Once this start time is known, the drift time information is used in the second stage of track reconstruction, time-based tracking (TBT).

Hit-based tracking is based on a series of pattern finding algorithms. First, in a procedure known as segment finding, cells within a superlayer that may be associated with a track are identified. Then, in a procedure known as linking, the track segments that link together to form a complete track are identified. Fig. 4.1 illustrates this procedure.

The segment finding procedure utilizes a dictionary of known segments that are generated from simulation. The known segments are coded in terms of the offset of the hits in each layer from the hit in layer two. So a track segment that is perpendicular to a layer would be coded as {0,0,0,0,0,0}. The bottom track segment in Fig. 4.1 would be coded as {0,0,1,1,2,2}. Since the upper track segment in Fig. 4.1 has two hits in layer 5, there are two track segments, which would be coded as {0,0,1,1,1,1} and {0,0,1,1,2,1}.

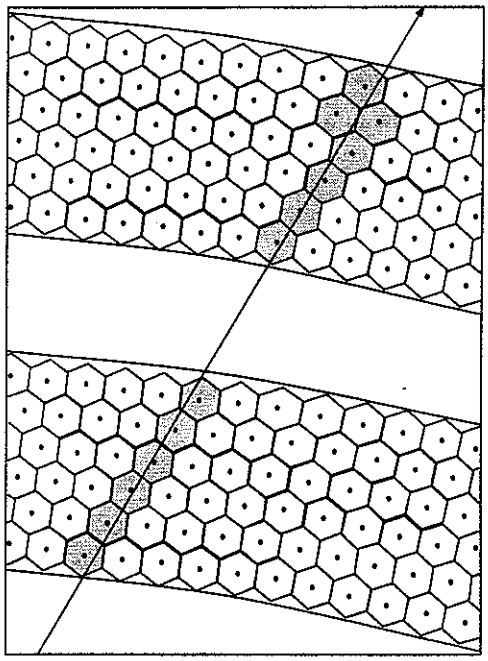

Figure 4.1: Two superlayers of the drift chamber with a track passing through them. Cells that had hits on them are shaded. Segment finding is the procedure of identifying the cells within a superlayer that may be associated with a track. In this illustration, the shaded cells would be identified as one track segment in the botttom superlayer and two in the top. Linking is the procedure of associating segments from the superlayers together to identify a track. One segment from each superlayer can be linked to form a track. There are four other superlayers that are not shown in this illustration. This figure was taken from [11].

The procedure used for linking is similar to segment finding. There is a pattern dictionary of tracks that are coded in terms of the cell number in the second layer of each superlayer. A linking code of {29,30,27,25,15,14} represents a track that intersects, in the third layer, cell 29 of the first superlayer, cell 30 of the second superlayer, etc. All combinations of track segments are made and, if the linking code matches one in the pattern dictionary for at least four superlayers, that combination is considered a track candidate. These hit-based track candidates are then fit for their momenta using the center of the cell as the hit position.

The hit-based tracks are used to identify the start time of the event. In order to reconstruct the start time, the path length and flight time must be known. The path length is given by the hit-based tracking, and the flight time is determined from the time of flight scintillators. The flight time of a particle is given by

$$t = \frac{L}{\beta \cdot c} \tag{4.1}$$

where L is the path length of the particle's trajectory (determined from tracking) and c is the speed of light. The start time can then only be reconstructed if there is a particle

in the event for which β is known. Since the lowest momentum electrons encountered in this experiment are $0.300 GeV/c$, for which $1 - \beta = 1.5 \cdot 10^{-6}$, electrons can be used to determine the start time of each event. This is appropriate since the data acquisition is designed to trigger on electrons (see section 2.6).

The reconstruction of the start time is then reduced to the identification of an electron in the event. This preliminary electron identification algorithm, which is used only to obtain a start time for the event, is a simple sort with sort order

$$\begin{array}{ll} momentum & (d) \\ charge & (a) \\ ECmatch & (d) \\ CCmatch & (d) \\ TOFmatch & (d) \end{array} \tag{4.2}$$

Here (d) indicates a descending sort and (a) indicates an ascending sort. That is, the tracks are first sorted in descending order of their momenta, then in ascending order of charge, etc. All of the sort items are integers (± 1 for charge or an integer flag for matching) except for momentum. The match flag is zero if the track did not point to a hit in the corresponding detector and greater than zero if it did. The matching of tracks to the outer detectors is presented in section 4.2. For matching to the calorimeter, there is an intermediate "non-fiducial" value of the matching flag if the hit was within 10cm of the detector. The particle that will end up at the top of the sort list, and be used to determine the start time, is the highest momentum, lowest charge track with the best match to the outer detectors, priority being given first to the time of flight, then to the Cerenkov counter, and last to the calorimeter. Since a match to the TOF counter is required to obtain a start time, this is the last item sorted on.

This algorithm preferentially sorts electrons to the top of the list and will always give a start time particle (as long as there was at least one particle in the event with a TOF match). For the data set used for this analysis, only 0.38% of the time did this algorithm fail to find the electron as determined by the subsequent final electron identification algorithm of section 4.3.2. Table 4.1 give the number of times that each particle was used to determine the start time for a representative run.

The start time is determined from

$$t_{start} = t_{TOF} - \frac{L}{c} \tag{4.3}$$

where t_{TOF} is the time in the time of flight detector, and L is the path-length of the trajectory as determined from the drift chambers.

e^-	e^+	π^+	π^-
149433	67	103	404

Table 4.1: The number of times that each particle was used used for the start time for the skimmed data of run 8774. 99.62% of the time the track from which the start time was taken is later identified as an electron.

The determination of the start as presented above was used to calculate time of flight for proton identification. The start time used for drift chamber drift times was obtained with a similar "preliminary" electron identification scheme. The absolute drift time for the hits in the drift chamber is used to obtain a refined measure of the momenta. This drift time yields (via a calibration function) a distance from the wire. Carman et. al. [11] present the details of the drift time calibration for the drift chambers. These hit positions are then used to fit the track to yield a three momentum at the vertex[1], as well as a trajectory that can be used to project the track to the outer detectors (Cerenkov detector, time of flight detector, and electromagnetic calorimeter).

4.2 Matching to Outer Detectors

Based on their momenta as measured by the drift chambers, time based tracks are traced from the vertex to the outer detectors. A hit in that outer detector within some matching cut is associated with the track. The matching cut is different for each outer detector.

Similar to the paddles of the time of flight detector, the mirrors of the CC are oriented such that there is no azimuthal hit position information (other than which sector the hit is in), so track matching to the CC is done based upon the difference in polar angle between the projection of the track onto the face of the CC and a hit in the CC. Due to the manner in which light is reflected by the mirrors, there is a small 1.5 deg offset in the polar hit position. The CC matching cut is 12° in polar angle, or about 3 segments. This is a very loose cut, but leads only to a 5% accidental matching for π^-. These accidental matches are addressed by the particle identification cuts of section 4.3.2.

For the TOF, the matching cut is on the projection of the hit onto the z-axis and is 30 cm. Since scintillators of the TOF are approximately oriented along the azimuthal direction within a sector, the hit position along the lab z-axis is dependent only upon geometry (given entirely by which scintillator is hit). The hit position in the lab x and y coordinates is determined by the timing difference between the phototubes on each end

[1]The magnitude of the momentum is determined from the bending of the track in the main torus magnetic field

of the paddle, and is hence very sensitive to the calibration. It is for this reason that only the z-component of the hit is used for matching.

The EC has three layers of scintillator paddles in each stack (inner or outer) oriented 60° relative to each other. The hit position reconstructed from the EC thus has x, y, and z position information which depends only upon knowledge of geometry. The EC matching is done according to the distance on the face of the detector from the projected track location to the nearest EC hit. This matching radius is 30cm.

Table 4.2 summarizes the matching to the outer detectors. The values of the cuts selected are intentionally very loose and have only a very small effect on the final analysis. Since the matching algorithm associates the *closest* detector hit with the track, these cuts could in fact be made arbitrarily larger.

detector	criterion	cut
CC	polar angle	12°
TOF	position along beam line	$30cm$
EC	separation on face of EC	$30cm$

Table 4.2: Matching cuts to the outer detectors.

Figs. 4.2, 4.3, and 4.4 show spectra of the matching residue for electrons, pions, and protons in the CC, TOF, and EC. The particle identification criteria are presented later in section 4.3. The matching residue is for the closest hit to the track: $\Delta = R_{track} - R_{hit}$, where R is the corresponding hit position quantity (polar angle for the CC, position along the beam axis for the TOF, and position on the face of the detector for the EC).

For electrons, there are no events outside of the CC matching cuts in Fig. 4.2 because the electron identification algorithm requires a match to the the CC. The electron events that are outside of the TOF matching cuts are events where the start time came from another particle. The EC matching residue has an enhancement starting at $\approx 20cm$ due to the particles for which a hit in the inner stack of the EC was missing. In these cases, the matching is between the hit in the outer stack and the projection of the track onto the face of the inner stack and there is an offset because the tracks are not in general perpendicular to the face of the calorimeter. For later versions of the reconstruction code the matching was refined to project tracks to the outer stack when a hit in the inner stack was missing. The electrons that are outside of the EC matching cuts were outside of the fiducial volume of the EC (see the electron identification logic of eqn. 4.7).

In Fig. 4.3, there is no peak in the CC matching residues for pions and the broad feature indicates that there were only coincidental matches to the CC for pions. This illustrates the effectiveness of the CC in identifying electrons. The structure in the

TOF matching residue is due to the fact that there are paddles of two different widths: $15cm$ at forward angles and $22cm$ at backward angles. This structure is not present in the electron TOF matching because all of the TOF paddles in the forward carriage, where the CC located, are $15cm$ wide. There are events outside TOF matching cuts because in cases where there was no match to the TOF, which occured because there were a few dead scintillator tubes, the particle identification was based on timing information in the EC. However the EC was not calibrated and these particles were always identified as pions (which is why there no events outside the TOF matching cuts for protons in Fig. 4.4). Over all events, this effect was a fraction of a percent, but since it can have strong kinematic correlations, dead scintillator paddles are accounted for in the simulation.

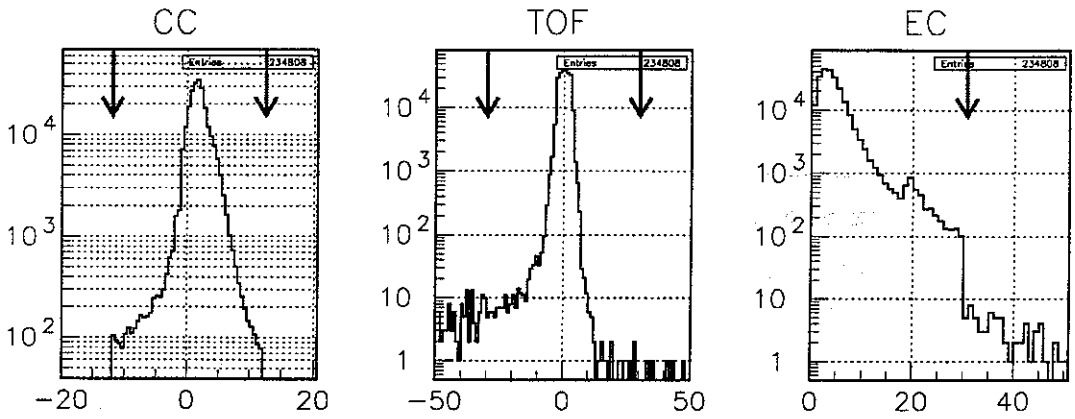

Figure 4.2: The electron matching residues in the CC TOF and EC. The matching cuts employed are marked by the arrows. Since a match to the CC is required for electrons, there are no events outside of the matching cuts.

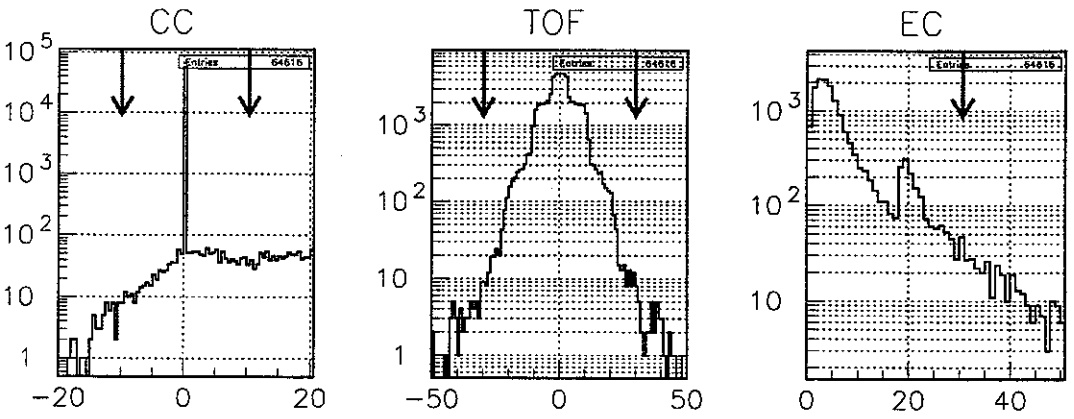

Figure 4.3: The pion matching residues in the CC TOF and EC. The spike at 0 for matching to the CC are all of the particles that did not have a TOF hit in the same sector as the track.

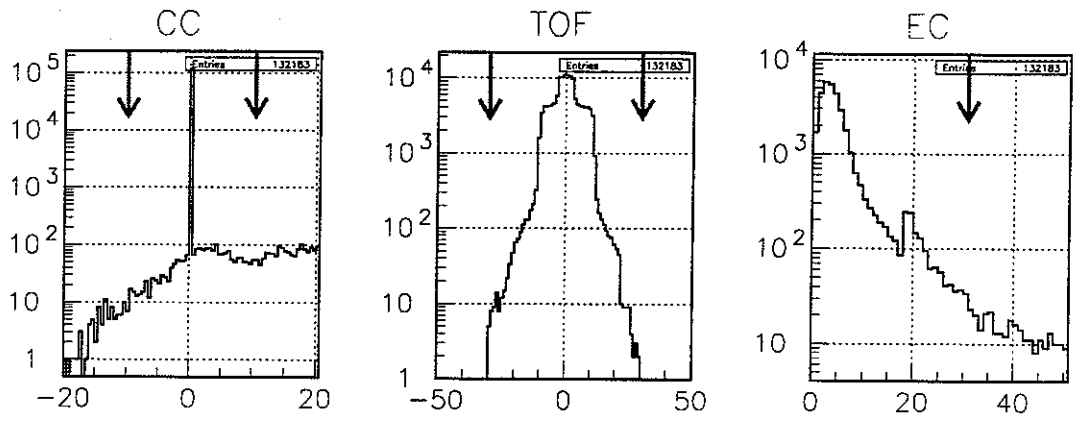

Figure 4.4: The proton matching residues in the CC TOF and EC.

4.3 Particle Identification

Once tracks are matched to hits in the outer detectors as described in the previous section, the information in those detectors is used to perform particle identification. Protons are identified by reconstructing the mass of particles from their momentum and time of flight. Electrons are identified primarily by requiring a match to the Cerenkov counter. Additional cuts on energy deposited in the electromagnetic calorimeter are used to reduce misidentification of pions as electrons that comes about from pions that match to noise or coincidental hits in the Cerenkov detector.

4.3.1 Proton Identification

The identification of protons is based on the tracking information from the DCs and the time of flight information from the TOFs. For each track that matches to the TOF, the speed of the particle, in units of c, is calculated from the path length and the time of flight.

$$\beta = \frac{L}{t \cdot c} \tag{4.4}$$

where L is the path-length from the vertex to the face of the TOF and t is the time of flight as determined from the TOF. This flight time is relative to the start time discussed in section 4.1 as $t = t_{TOF} - t_{start}$. The mass of the particle is then determined from

$$m = \frac{|\vec{p}|}{\beta\gamma} \tag{4.5}$$

where $\vec{p}$ is the momentum of the particle and $\gamma = \frac{1}{\sqrt{1-\beta^2}}$. A histogram of the mass for particles other than electrons is shown in Fig. 4.5 along with the cuts used for particle identification. The systematic effects due this cut are addressed in section 6.1.2.

The proton identification algorithm is done according to the logic

$$(Q = +1) \cdot (0.8 < m < 1.2) \tag{4.6}$$

where a match to the TOF is implicit since this is required to determine m.

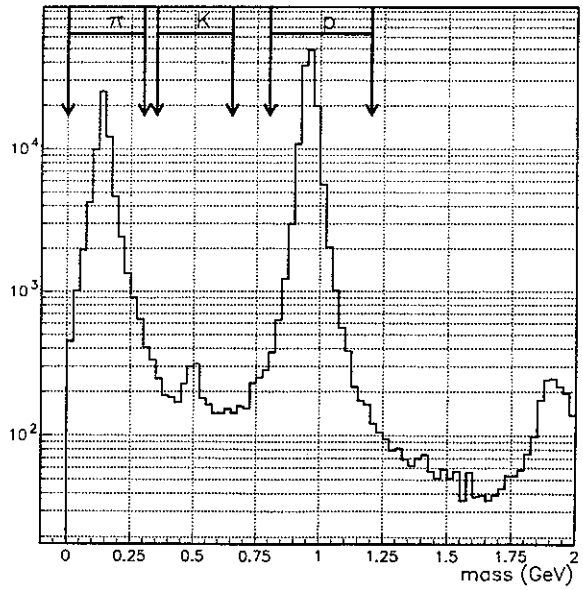

Figure 4.5: The hadronic mass spectrum. The cuts used for hadronic particle identification are shown by the arrows. The unlabelled peak at high mass is deuterons that are produced from the target window foils.

As the momenta of particles increase, their time of flight converges as their speed approaches c, and greater time of flight resolution is needed to separate protons from pions. The ability to separate protons from pions is measured by this convergence at high momentum. Fig. 4.6 illustrates that for the kinematics of this experiment, there was good separation in hadronic particle identification.

4.3.2 Electron Identification

For this analysis, it is most important that the electron identification algorithm be as efficient as reasonably possible. That is, that when there is an electron in the event, it is identified with a high efficiency. Since the trigger for this experiment resulted in a 33% electron yield, the majority of the events had no electron in them at all. These tended to be events where the electron scattered at a small angle and missed the drift chambers, but caused hits in the Cerenkov detector and electromagnetic calorimeter (due to showers from the electron striking the beamline or support material). Non-electron events where another

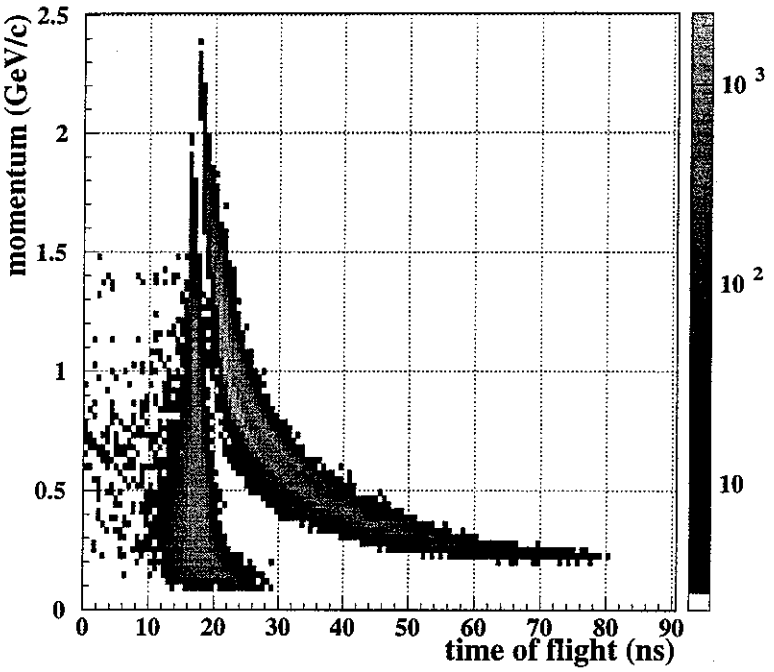

Figure 4.6: Separation in hadronic particle identification. Pions, becoming relativistic ($\beta = 0.95$), by a momentum of $0.42 GeV/c$, show up as the band on the left with a hook at low momentum where they are becoming non-relativistic. Protons, being much heavier, do not become relativistic until a momentum of $2.9 GeV/c$, and show up as the band on the right. There is a clear separation between pions and protons for the kinematics of this experiment.

negative particle (a π^- for example) is identified as an electron just go into the background of $ep \rightarrow epX$ spectra. Since this background is subtracted in a phenomenological way, such events serve to degrade the signal to noise ratio, but do not lead to a contamination in the η peak. The Cerenkov detector is the main means of electron identification. Other cuts are applied to reduce the contamination by pions, but these cuts are intentionally kept loose in order to avoid losing real electrons. These additional cuts make use of the different ways in which electrons and pions deposit energy in the calorimeter. The CLAS electron identification presented here is around 98% efficient, and the pion contamination is approximately 5%.

Once tracks are matched to hits in the outer detectors, the information in those detectors is used to identify electrons. The electron identification algorithm is based on the logic

$$(Q = -1) \cdot CC \cdot EC \cdot \left[\left(EC_{Fid} \cdot E_{inner} \cdot \left[\frac{E}{p} \right] \right) + \overline{EC_{Fid}} \right] \tag{4.7}$$

where Q is the charge of the track, CC and EC are true if there are matched hits in those detectors, EC_{Fid} is true if the EC hit is more than $10cm$ from the edge of the EC[2], EC_{inner} is a cut on the energy deposited in the inner stack of the EC, and $\left[\frac{E}{p}\right]$ is a cut put on the relationship between energy measured in the calorimeter (E) and the tracks momentum (p) as measured by the drift chambers. An electron is thus defined as a negative track that matches to the CC and EC and satisfies $\frac{E}{p}$ and E_{inner} cuts if the EC hit is in the fiducial volume. When an electron is within $10cm$ of the edge of the calorimeter, part of the shower can "leak" out the side; all of the energy will not be detected and the energy measurement will be inaccurate. This is evident by the horizontal "non-fiducial drip" band at high momenta in Fig. 4.7. There are in fact non-fiducial electrons at all momenta, but the elastic scattering (which occurs predominately at high momenta and low angle) results in an enhancement there. The calorimeter fiducial cut is not an issue in the final analysis since, as discussed in Section 4.3.3, there is a Cerenkov detector fiducial cut which turns out to be inside of the calorimeter fiducial cut.

The $\frac{E}{p}$ cut employed is based the relationship between the momentum of the tracks as measured by the drift chambers and the total energy deposited in the calorimeter.

$$E_1 < p - E < E_2 \tag{4.8}$$

where p is the momentum of the track, E is the sampling fraction corrected energy of the particle as measured by the calorimeter and the values for the cuts used were $E_1 = -260MeV$ and $E_2 = 560MeV$. The $\frac{E}{p}$ cut for electron identification is illustrated in Fig. 4.7.

Some attention was given to avoiding misidentifying pions as electrons. The Cerenkov detector was most effective in distinguishing electrons from pions (see Fig. 4.3). The CC matching requirement alone is enough to distinguish electrons from pions to 95%. The remaining 5% were pions that matched to random or coincidental hits in the CC. The E_{inner} cut alone distinguishes electrons from pions to 66%, and the $\frac{E}{p}$ cut is only effective to 7%. The electron identification cuts are then about 98.5% efficient at rejecting pions. The remaining 1.5% will only contribute a smooth background to the ep missing mass spectra and the resultant error in extracting η yields is negligible.

The E_{inner} cut is intended to reduce the pion contamination. For the energies in this experiment, the primary mode of interaction of pions in the calorimeter is ionization, whereas the electrons interact via pair production and showering. The relationship between E_{inner} and E_{outer} for pions is one of minimum ionization, where the energy deposited is nearly independent of the pion energy. The ratio E_{outer} to E_{inner} for pions is in fact just

[2]This *calorimeter* fiducial cut is not the same as the *Cerenkov detector* fiducial discussed in section 4.3.3.

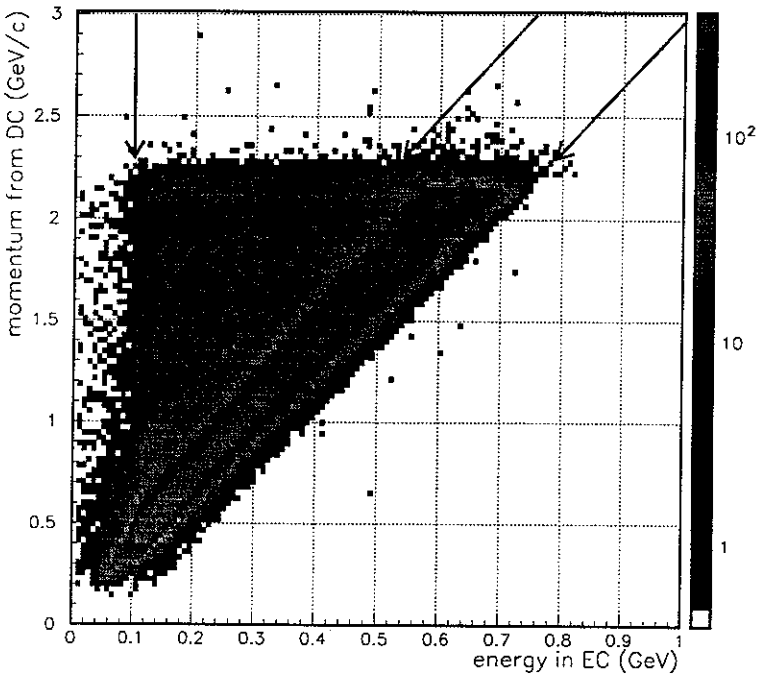

Figure 4.7: Electron identification in E-p. The momentum measured by the drift chambers versus the energy measured by the calorimeter for particles identified as electrons. The $\frac{E}{p}$ cut is marked by the tilted arrows and the hardware trigger threshold in marked by the vertical arrow. The events which lie outside the $\frac{E}{p}$ cut were non-fiducial. These events lie to the left of the electron band due to the fact that the energy for these tracks is measured too low because the shower was not contained within the calorimeter.

the ratio of the thicknesses of the outer stack to the inner stack of the EC (8:5). Pions typically deposit only $29MeV$ in the inner stack of the EC. Electrons, on the other hand, begin showering in the inner stack and deposit typically more than $80MeV$ of energy there. Fig. 4.8 shows the E_{inner} spectra for pions and electrons along with the E_{inner} cut used.

There are sources of particle identification inefficiencies that are very difficult to overcome at the level of reconstruction algorithms. For instance, two particles may overlap in a detector, causing a loss of information from that detector. η mesons decay to charge modes (primarily $\pi^+\pi^-\ \pi^0$) 29% of the time, so there are on the average 2.7 charged particles in the final state. Moreover, the photons from the η neutral decay modes, or Bremsstrahlung radiation from the scattered electron, may interact in the electromagnetic calorimeter and corrupt the energy measurement used for electron identification. These effects are taken into account by having all of them fully implemented in the Monte Carlo simulation that is used to calculate acceptance correction factors.

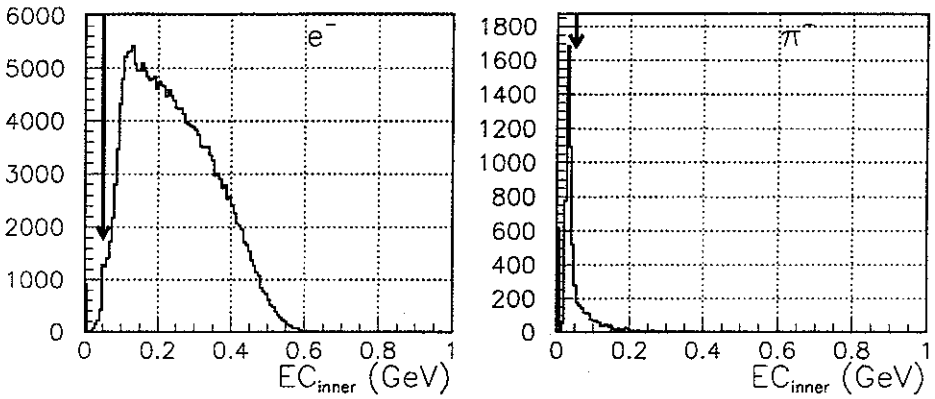

Figure 4.8: The energy deposited by electrons and pions in the inner stack of the calorimeter. The cut used for electron identification is marked by the arrow.

A comprehensive set of particle identification diagnostic plots and more discussions are given in Appendix A.

4.3.3 Cerenkov Detector Fiducial Cut

The accurate determination of absolute cross section hinges on having a good simulation of the experiment from which to derive acceptance corrections. The simulation for this experiment (as presented later in section 5.2), was a good representation of the detector except at the edges of the Cerenkov detector. This is because the complicated geometry of the Cerenkov detector mirrors was not implemented in the simulation. Away from the edges, the Cerenkov detector efficiency was high and the simulation was accurate. A Cerenkov detector fiducial cut was applied to avoid the edges where the efficiency is rapidly (and uncertainly) varying[3]. Fig. 4.9 shows the efficiency of the Cerenkov detector as determined from elastic scattering events. Inside the fiducial cut, the average efficiency is greater than 99%. Near the edges of the detector, the electron detection efficiency becomes erratic due to the geometry of the mirrors. There is a band of high efficiency outside of the gas volume of the detector that corresponds to electrons striking the photomultiplier tubes directly. The inclusive differential elastic scattering cross section was measured using these cuts and agreed to within a few percent with the known cross section [29].

[3]These cuts have become a standard part of analysis of CLAS electroproduction data. [9]

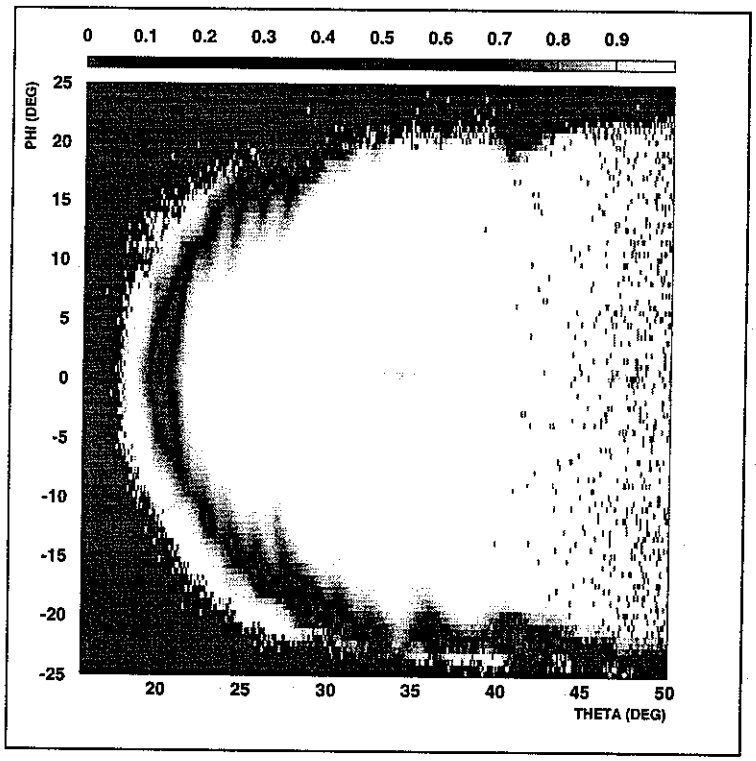

Figure 4.9: The Cerenkov detector efficiency. The efficiency is plotted versus the scattering angles of the electron in the laboratory frame. For the elastic scattering data shown here, those angles map uniquely onto the face of the Cerenkov detector. The narrow fingers of low efficiency that extend in ϕ from the edges are gaps between the mirrors. This figure was taken from [1].

Chapter 5

Analysis

The analysis techniques used to extract η rates from four vectors and identified particles are presented in this chapter. η mesons are measured from the missing mass in $ep \rightarrow epX$. Acceptance and radiative correction factors are determined from a simulation model of the detector and a peaking approximation radiative effect model. Rates are extracted from the ep missing mass by fitting the spectra to a function that has a representation of the η peak with a radiative tail, and a polynomial background.

5.1 Binning

The table below shows the binning on W, Q^2, $cos(\theta^*_\eta)$, and ϕ^*_η used in this study. This choice was driven by statistics and physics considerations. The number of bins in $cos(\theta^*_\eta)$ and ϕ^*_η is such that there is adequate ability to distinguish the multipole terms $A - F$ of equation 1.2.2. Since there was no beam or target polarization in the experiment, the observed η rates must be symmetric about $\phi^*_\eta = 180°$. Symmetric bins in ϕ^*_η could, in principle, have been summed, but it was desirable to use this symmetry as a check throughout the stages of the analysis. When the cross section are fit to the multipole parameters of equation 1.2.2, they are fit from $\phi^*_\eta = 0$ to 360°, so there is no loss of information.

	min	max	width
W(MeV)	1485	1635	30
$Q^2(GeV^2)$	0.5	1.5	0.5
$cos(\theta^*_\eta)$	-1	1	0.4
ϕ^*_η	0	360°	45°

5.2 Acceptance and Radiative Corrections

The quantities that are directly observed in the experiment are N_i, the number of $e^- p \rightarrow e^- p \eta$ events in the kinematic bins labelled by i. There are two factors that are needed to relate N_i to an absolute cross section: 1) the integrated luminosity and 2) a correction factor that takes into account radiative effects and the acceptance of the detector. This correction factor consists of a radiative correction $\mathcal{R}$ and an acceptance correction $\mathcal{A}$:

$$\frac{d\sigma^4}{dW dQ^2 d\Omega_\eta^*}(W, Q^2, cos(\theta_\eta^*), \phi_\eta^*) = \frac{N_i}{\Delta} \cdot \frac{1}{\mathcal{L}} \cdot \frac{\mathcal{R}}{\mathcal{A}} \tag{5.1}$$

where N_i is the measured rate, $\mathcal{L}$ is the integrated luminosity, and Δ is the product of the bin widths in W, Q^2, $cos(\theta_\eta^*)$, and ϕ_η^*.

The acceptance correction factor $\mathcal{A}$ accounts for the fact that a given cross section as measured by the detector is deformed by experimental factors such as detector geometry. By far the largest component of acceptance is geometry, but other effects like multiple scattering, resolution, and reconstruction software efficiency are also accounted for. The acceptance is the probability that an event will be detected and reconstructed in the experiment and is a function of kinematics and final state. After the acceptance correction is applied, distributions are transformed from what was observed in the experiment to what would be observed with a perfect detector and perfect reconstruction software. Correcting for the acceptance requires an analytic model of the detector and its digital response to particles passing through it.

The radiative correction factor $\mathcal{R}$ accounts for the fact that the cross section measured in the experiment includes processes where real or virtual photons are emitted from the charged particles in the reaction. Since these photons are not measured, the true kinematics of the interaction are experimentally hidden. Fig. 5.1 illustrates this. But a fundamental understanding of the processes that underlie the radiative effects (Quantum Electrodynamics) allows the construction of an analytic model and the calculation of radiative correction factors. After these corrections, the distributions incident upon the detector are transformed to those at the "bare" vertex. Standard procedures have been developed in the particle physics community for the determination of radiative corrections, most based on the seminal 1969 work of Mo and Tsai [28]. The formalism adopted for this work is an extension of that by Makins et. al. [27].

Bremsstrahlung radiation, labelled γ_{brem} in Fig. 5.1 occurs as a result of a charged particle being accelerated by the electromagnetic fields of either the material it passes through before or after the interaction (called *external* radiation), or as a result of the acceleration that results from scattering from the target nucleon (called *internal*

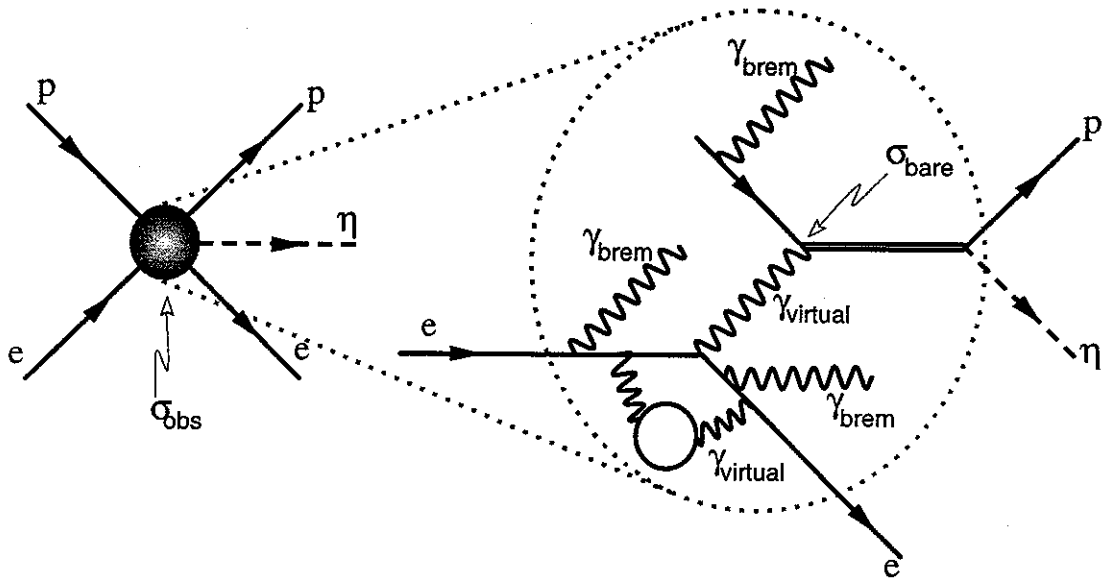

Figure 5.1: Radiative effects. The cross section observed in the experiment, here represented by σ_{obs}, is an amalgam of processes that are not measured, like Bremsstrahlung radiation and loop effects. The radiative correction is the process of transforming this observed cross section to the desired cross section, here labelled σ_{bare}. Radiated Bremsstrahlung photons are not measured and are hence inside of the dotted line. In this figure, many processes are shown simultaneously for illustrative purposes.

radiation). The radiative effects shown in Fig. 5.1 are all internal. Internal radiation and external radiation prior to the interaction are modeled at the event generator level while external radiation as the charged particles leave the target and traverse the material of the detector is handled by the detector simulation program.

5.2.1 Formulation

The determination of acceptance and radiative correction factors involves the generation of known non-radiative data that is compared to data that has been subjected to radiative effects and simulation of the detector response and reconstruction software. In practice, the radiative and acceptance correction factors are combined into one. This is because there may be correlated effects (for example Bremsstrahlung photons may disrupt the measurement of other particles in the detector) that can only be taken into account when the two effects are determined simultaneously.

The concept behind the calculation of these correction factors is very simple. Suppose that $e^-p \rightarrow e^-p\eta$ events are generated without radiative effects and there are 1000 events observed in a particular kinematic bin. $e^-p \rightarrow e^-p\eta$ data is then generated with radiative effects and this data is used to simulate the digital response of the detector (the response of the ADCs and TDCs). This simulated data is then reconstructed with

the same software used on the real data. Suppose that after this process, there where 500 $e^-p \rightarrow e^-p\eta$ events observed in the same kinematic bin referred to before. Then the correction factor for that bin would be $\frac{1000}{500} = 2$. Correction factors calculated in this way take into account detector as well as software inefficiencies. The rest of this section presents the details of the practical realization of this simple concept, as well as the details of the model used for radiative effects.

Acceptance and radiative corrections are applied to the measured yield in each bin, Y_i^m, to obtain a corrected yield Y_i^c.

$$Y_i^c = \frac{R_i}{A_i} \cdot Y_i^m \tag{5.2}$$

where R_i is the radiative correction factor and A_i is the acceptance for the bin labeled by i.

The radiative correction factor R_i accounts for two effects. Vertex corrections lead to a modification of the cross section, and Bremsstrahlung radiation leads to modifications in the kinematics, which cause events to be shuffled amongst bins. Vertex effects are processes that involve virtual photons and do not change the external kinematics of the reaction. They do, however, change the kinematics at the $ep\gamma_v$ and $e'p\gamma_v$ vertices, causing a change in the cross section. For Bremsstrahlung radiation processes, where there is one or more real photon that carries away momentum, the external kinematics of the reaction are changed, which can cause events to migrate between bins. These two effects are combined into a single factor:

$$R_i = \frac{d\sigma_i}{d\sigma_i^r} \cdot \frac{1}{b_i} \tag{5.3}$$

Here $d\sigma_i$ is the vertex differential cross section ($d\sigma$ is shorthand for $\frac{d\sigma^4}{\Delta W \Delta Q^2 \Delta\Omega_\eta^*}$) and $d\sigma_i^r$ is the vertex corrected differential cross section. b_i represents the fraction by which the yield changes in a bin due to the shuffling between bins.

The correction factor is obtained bin by bin from the non-radiative yield and the radiative, fully simulated yield.

$$\begin{aligned} S_i &= \frac{d\sigma_i}{d\sigma_{max}} \cdot t_i \\ S_i' &= \frac{d\sigma_i^r}{d\sigma_{max}^r} \cdot t_i^r \cdot b_i^s \cdot A_i \end{aligned} \tag{5.4}$$

Where S_i is the generated yield in the kinematic bin labelled by i, S_i' is the yield with radiative effects and acceptance, $d\sigma_{max}$ is the maximum cross section that was used for normalization in an acceptance/rejection manner, and t_i is the number of events

thrown into that bin. Radiative effects are again denoted with an r superscript. In the determination of the yield S_i', the same analysis is applied as is used on real data, including the fiducial cut and the ep missing mass fitting techniques.

The correction factor of equation 5.2 can then be expressed via the simulation yields of equation 5.4.

$$\frac{R_i}{A_i} = \frac{S_i}{S_i'} \frac{d\sigma_{max}}{d\sigma^r_{max}} \frac{t^r_i}{t_i} \tag{5.5}$$

The maximum cross section used in the Monte Carlo, $d\sigma_{max}$ and $d\sigma^r_{max}$ can in principle be set equal to each other (that is, equal to the greater to the two), but at the cost of some Monte Carlo efficiency.

The number of throws in each bin, t_i and t^r_i cannot trivially be set equal to each other. For the event generator simulation without radiative effects, events are thrown uniformly across the binned variables (W, Q^2, $cos(\theta^*_\eta)$, and ϕ^*_η), but, due to Bremsstrahlung radiation from the beam, events are not thrown uniformly in W and Q^2 when radiative effects are used. The reason for this is as follows.

For a given beam energy, there is a kinematically allowed region in $W^2 - Q^2$ space. This space is bordered by three constraints, one at $Q^2 \geq 0$, another at $W^2 \geq (M_p + M_\eta)^2$, and another which results from $Q^2 \leq 4EE'$ (all in the limit $M_e = 0$). The last constraint depends upon the incident electron energy E. Because of Bremsstrahlung radiation from the beam, the incident electron energy (and hence the allowed region in $W^2 - Q^2$ space) is different for each generated event. Events are not thrown uniformly in W and Q^2 bins when radiative effects are used. Hence one cannot assume that $\frac{t^r_i}{t_i} = \frac{t^r_{total}}{t_{total}}$, and is necessary to keep track of the number of throws, t_i and t^r_i in eqn. 5.5, in each bin.

5.2.2 Event Generator

The event generator is a program that is used to produce the events for the Monte Carlo simulation. It has a model for the production process (decay of an $\frac{1}{2}\frac{1}{2}^-$ Breit-Wigner resonance), and an implementation of radiative effects (peaking approximation). There is no representation of multipion background in the event generator.

5.2.2.1 Radiative Effects

In an electroproduction experiment, photons, being massless, can be produced copiously. This includes both real, or Bremsstrahlung , and virtual photons. Bremsstrahlung photons are emitted as charged particles (in this case most importantly the beam and scattered electrons), interact with the fields of the matter through which they are passing,

including the target nucleon. Virtual photon processes are those where a photon is emitted from a charged particle before the interaction with the target, and is reabsorbed after the interaction. These radiative effects lead to a discrepancy between actual momenta at the vertex and the measured external momenta of the beam and final state particles. The kinematic bin for kinematic quantities like W, Q^2, $cos(\theta_\eta^*)$, and ϕ_η^* can be misassigned. Moreover, the virtual photon flux from equation 1.9 is evaluated at the wrong point, and the magnitude of the cross section is changed.

The magnitude of the cross section is also changed due to the quantum mechanical interference of bare vertex and radiative processes that come in at the same order in α. Fig. 5.2 shows Feynman diagrams for the three lowest order processes. If only these processes were included, the cross section would be $\sigma \sim |M_2 + M_4|^2 + |M_3|^2$. Amplitudes M_2 and M_4 are added coherently because they have indistinguishable final states. Then to the lowest two orders, the cross section goes as $\sigma \sim |M_2|^2 + 2Re(M_2 M_4^\dagger) + |M_3|^2$. The first term is of order α^2 and the next two terms are of order α^3. In this way the bare vertex amplitude, M_2 interferes with radiative amplitudes.

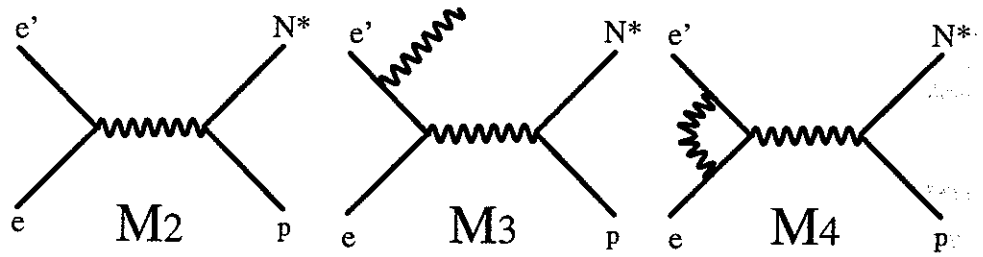

Figure 5.2: Electroproduction feynman diagrams showing the bare vertex and the next two order radiative diagrams. The matrix elements corresponding to the processes are subscripted by the number of electromagnetic vertices in the process. There are additional diagrams at the same order to those shown here which correspond to permutations of the radiative photon on different lepton legs.

A detailed explanation of the model for radiative effects used in this analysis can be found in [27]. Only the final results, and a brief discussion of the basic assumptions are presented here.

In the formulation of Makins et. al. [27], Bremsstrahlung photons are assumed to be radiated in the direction of the particle that they emanate from. This is what is known as the peaking approximation. This is a well understood approximation in electron scattering and is good to within 1% for the kinematics of this measurement [27] [28].

In the limit that the photon energy ω is much less than the momenta of the initial and final state fermions (known as the soft photon approximation), the cross section

for emitting a single Bremsstrahlung photon can be written

$$\frac{d^5\sigma}{d\Omega_e d\Omega_\gamma d\omega} = \left.\frac{d^2\sigma}{d\Omega}\right|_{bare} \frac{A\left(\Omega_\gamma\right)}{\omega} \tag{5.6}$$

where $\left.\frac{d^2\sigma}{d\Omega}\right|_{bare}$ is the bare vertex electroproduction cross section and the photon cross section is separated in to an angular part, $A\left(\Omega_\gamma\right)$, and an energy part, $\frac{1}{\omega}$. In the peaking approximation, the Bremsstrahlung angular amplitude is written

$$A_{peak}\left(\Omega_\gamma\right) = \lambda_e \delta\left(\hat{\omega} - \hat{p}_e\right) + \lambda_{e'} \delta\left(\hat{\omega} - \hat{p}_{e'}\right) \lambda_{p'} \delta\left(\hat{\omega} - \hat{p}_{p'}\right) \tag{5.7}$$

with

$$\begin{aligned} \lambda_e &= \frac{\alpha}{\pi}\left[\ln\left(\frac{4p_e^2}{m_e^2}\right) - 1\right] \\ \lambda_{e'} &= \frac{\alpha}{\pi}\left[\ln\left(\frac{4p_{e'}^2}{m_e^2}\right) - 1\right] \\ \lambda_{p'} &= \frac{\alpha}{\pi}\left[\ln\left(\frac{E_{p'} + p'}{E_{p'} - p'}\right) - 2\right] \end{aligned} \tag{5.8}$$

Equation 5.6 describes the emission of real photons, processes like those labelled M_3 in Fig. 5.2. When virtual effects like that labelled M_4 in Fig. 5.2 are included, the final result of [27] is:

$$\frac{d^5\sigma}{d\Omega_e d\omega_e d\omega_{e'} d\omega_{p'}} = \left.\frac{d^2\sigma}{d\Omega}\right|_{bare} \frac{d^3\sigma}{d\omega_e d\omega_{e'} d\omega_{p'}} \left(1 - \delta_{hard}\right) e^{-\delta_{soft}} \tag{5.9}$$

The three terms on the right hand side of equation 5.9 are the bare vertex cross section, $\left.\frac{d^2\sigma}{d\Omega}\right|_{bare}$, the Bremsstrahlung photon cross section $\frac{d^3\sigma}{d\omega_e d\omega_{e'} d\omega_{p'}}$, the virtual photon correction $\left(1 - \delta_{hard}\right)$, and the soft Bremsstrahlung correction $e^{-\delta_{soft}}$. The radiative terms are

$$\frac{d^3\sigma}{d\omega_e d\omega_{e'} d\omega_{p'}} = \frac{\lambda_e \lambda_{e'} \lambda_{p'}}{\omega_e^{1+\lambda_e} \omega_{e'}^{1+\lambda_{e'}} \omega_{p'}^{1+\lambda_{p'}}} \tag{5.10}$$

$$1 - \delta_{hard} = 1 - 2\alpha\left[\frac{1}{\pi} - \frac{3}{4\pi}\ln\left(\frac{Q^2}{m_e^2}\right) - \sum_i \delta_i^{vp}\left(Q^2\right)\right] \tag{5.11}$$

$$e^{-\delta_{soft}} = \frac{1}{\left(\sqrt{E_e E_{e'}}\right)^{\lambda_e} \left(\sqrt{E_e E_{e'}}\right)^{\lambda_{e'}} \left(\sqrt{m_p E_{p'}}\right)^{\lambda_{p'}}} \tag{5.12}$$

The vacuum polarization term in equation 5.11 is summed over the different lepton flavors:

$$\delta_i^{vp} = \frac{1}{3\pi}\left[\ln\frac{Q^2}{m_i^2} - \frac{5}{3}\right] \tag{5.13}$$

5.2.2.2 Model for η Electroproduction

In the framework presented in section 1.2.2, the virtual photon η production cross section is

$$\frac{d\sigma_v}{d\Omega} = \frac{|q_\eta| W}{K M_p} \left(|E_{0+}|^2 + \epsilon \frac{Q^2}{|q_\eta|^2} |S_{0+}|^2 \right) \tag{5.14}$$

where $|q_\eta|$ is the center of mass momentum of the η, k is the center of mass momentum of the virtual photon, and ϵ is the virtual photon longitudinal polarization. Brasse et. al. [6] have made a separation of $|E_{0+}|^2$ and $|L_{0+}|^2$ and find that the ratio of $|L_{0+}|^2$ to $|E_{0+}|^2$ from $W = 1.505 - 1.565\ GeV$ and $Q^2 = 0.60 - 1.0\ GeV^2$ is small and poorly determined ($20\% \pm 20\%$). For this reason we take $|S_{0+}|^2 = 0$.

The model employed for the amplitude E_{0+} is a relativistic Breit-Wigner with an energy dependent width.

$$E_{0+} = \frac{\Gamma^* W^*}{W^{*2} - W^2 - i W^* \Gamma(W)} \tag{5.15}$$

where W^* is the resonance centroid mass and Γ^* is the partial width of the resonance. $\Gamma(W)$ gives the energy dependence of the partial width and accounts for the penetration of the angular momentum barrier. It is expressed in terms of Blatt-Weisskopf function and for $l = 0$ is simply

$$\Gamma(W) = \Gamma^* \left(b_\eta \frac{q_\eta}{q_\eta^*} + b_\pi \frac{q_\pi}{q_\pi^*} + b_{\pi\pi} \right) \tag{5.16}$$

where b is the branching ratio into the subscripted final state, q is the momentum of the meson at the center of mass energy W, and q^* is the momentum of the meson at the center of mass energy W^*. The values of the branching ratio are taken from [12] and are

$$\begin{aligned} b_\eta &= 0.5 \\ b_\pi &= 0.4 \\ b_{\pi\pi} &= 0.1 \end{aligned}$$

5.2.2.3 Procedure

Procedurally, the event generator can be broken down into the following steps:

1. Bremsstrahlung radiation of the beam electron.
2. Determine $\sigma(W, Q^2, cos(\theta_\eta^*), \phi_\eta^*)$.
3. Apply vertex and soft photon corrections to $\sigma(W, Q^2, cos(\theta_\eta^*), \phi_\eta^*)$.
4. Bremsstrahlung radiation of final state particles.
5. Determine probability to keep event.

Bremsstrahlung radiation, steps 1. and 3. above, are done in the same manner according to equation 5.10. Bremsstrahlung photon energies that are distributed according

to eqn. 5.10 could be obtained via Monte Carlo acceptance-rejection techniques, but since the equation is analytically integrable, it is much more efficient to use the inverse transform method. See [12] for a concise explanation. With this technique, events distributed according to a normalized probability distribution function $p(x)$ can be obtained from a random number generator via $x = P^{-1}(r)$ where $P(x) = \int_{-\infty}^{x} p(x')dx'$ and r is a random number between 0 and 1.

In this case, the limits of the normalization integral are from 0 to ω_{max}, the energy of the particle undergoing the Bremsstrahlung radiation. The normalized Bremsstrahlung probability distributions are then

$$p(\omega) = \frac{\lambda}{\omega_{max}} \left(\frac{\omega_{max}}{\omega}\right)^{1-\lambda} \tag{5.17}$$

and Bremsstrahlung photon energies are obtained from

$$\omega = \omega_{max} r^{\frac{1}{\lambda}} \tag{5.18}$$

Once the beam electron has been radiated in this manner, the vertex cross section at the $\gamma_v p, e'p$ vertex is determined. W, Q^2, $cos(\theta_\eta^*)$, and ϕ_η^* are randomly sampled over their available space. $cos(\theta_\eta^*)$ and ϕ_η^* range from -1.0 to 1.0 and 0.0 to 2π respectively. The limits on W and Q^2 depend upon the incident electron energy at the vertex, and since that is effected by Bremsstrahlung radiation, change from event to event. The vertex cross section is determined by the electroproduction model described in section 5.2.2.2. The generation of the event continues if $\frac{d\sigma}{d\sigma_{max}} > r$, where $d\sigma_{max}$ is the maximum value of the cross section within the kinemtatic region being sampled, and r is a random number between 0 and 1, that is, the final event sample is generated via an acceptance-rejection (Von Neumann) technique. If the event is to be kept, the laboratory momenta for the final state electron, proton, η meson, and any Bremsstrahlung photons are calculated and this is used as the input to the detector simulation/digitization stage.

5.2.3 Detector Simulation / Digitization

The detector simulation and digitization was performed with a GEANT [35] Monte Carlo program. The material included in the simulation is:

- Target cell and support structure
- Beam line
- Minitorus magnet and shielding
- Torus magnet and support structure
- Drift chambers
- Cerenkov counters
- Time of flight scintillators
- Electromagnetic calorimeters
- Structural material for all detectors

The drift chamber and cerenkov detector volumes are occupied with the appropriate gases, however, the wires of the drift chamber are not represented. The detector geometry used is taken from measurements during the run period and is the same as that used in the analysis of real data. The photons from Bremsstrahlung radiation are also simulated as is the decay of the η meson.

Simulation event files are written out in BOS format and dead channels in the drift chambers and time of flight scintillators are knocked out before analysis. The simulation data is analyzed by the same reconstruction code as real data. For simulation, the calibrations used are an ideal set and are just inverses of the functions used to digitize the data. The magnetic field used for simulation is the same as that used to reconstruct real data.

Fig. 5.3 shows a comparison of the η peak (integrated over W, Q^2, $cos(\theta^*_\eta)$, and ϕ^*_η) between data and simulation. The widths of the peak from simulation is about 36% narrower than the data peak, but this is to be expected to some degree. Firstly, the simulation has "ideal" calibrations. That is, the calibrations (drift chamber drift time function, time of flight scintillator calibration, etc.) used to reconstruct the simulation data are perfect inverses of the functions used to generate the data. In a similar manner, the magnetic field and geometry for the simulation are "ideal".

The simulation yields, the S'_i from equation 5.5 are extracted from the reconstructed simulation data with the same fitting program used to extract the yields from the data. The fits are the same as for the real data except that the ep missing mass peaks are allowed to be free parameters. Because the statistics in the simulation is a factor of 2.5 times more than the data, and, more importantly, because there is no background in the simulation, there is no need to constrain the peak width. Fig. 5.4 shows representative fits the simulation data for a particular W and Q^2 bin. The entire set of plots are presented in appendix C.

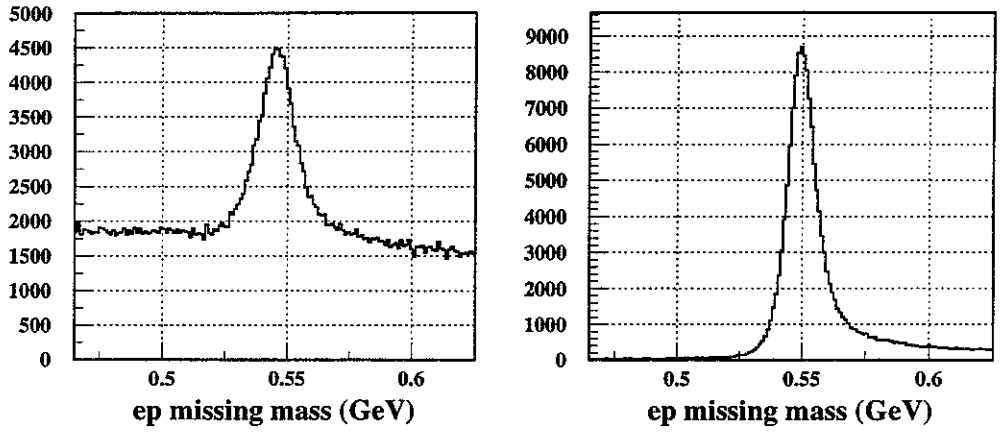

Figure 5.3: Comparison between data and simulation ep missing mass peaks. Data is on the left and the simulation is on the right. In the simulation peak, the radiative tail is evident, whereas for real data, it is washed out by the multipion background.

5.2.4 Proton Ineffeciciency Correction

It is possible that not all of the inefficiencies that are present in the data acquisition, particle detection, or reconstruction are well modeled by the simulation program. Such situations are inevitable to some degree and are a result of inadequacies in the simulation program. A study of the exclusive final state $ep \rightarrow ep\pi^-\pi^+$ exposed such an unsimulated tracking inefficiency [14]. The inefficiency was then parameterized and implemented in simulation.

In this study, proton tracks were identified via a missing mass cut on $ep \rightarrow e\pi^-\pi^+X$ events. Additional cuts were applied to ensure that the proton track pointed to the fiducial volume of the detector, that there were drift chamber hits within 5 wires of the projection of the track into the drift chambers, and that the proton did not project to a dead scintillator paddle. Hence the protons selected with these cuts should have been reconstructed. The proton tracking inefficiency was then defined as the fraction of these protons that did not get reconstructed. The measurement was then performed on simulated data and it was found that this proton track reconstruction was not reproduced in simulated data.

This inefficiency was implemented in the simulation by parameterizing it as a function of the proton momentum and scattering angle, and subjecting each proton track

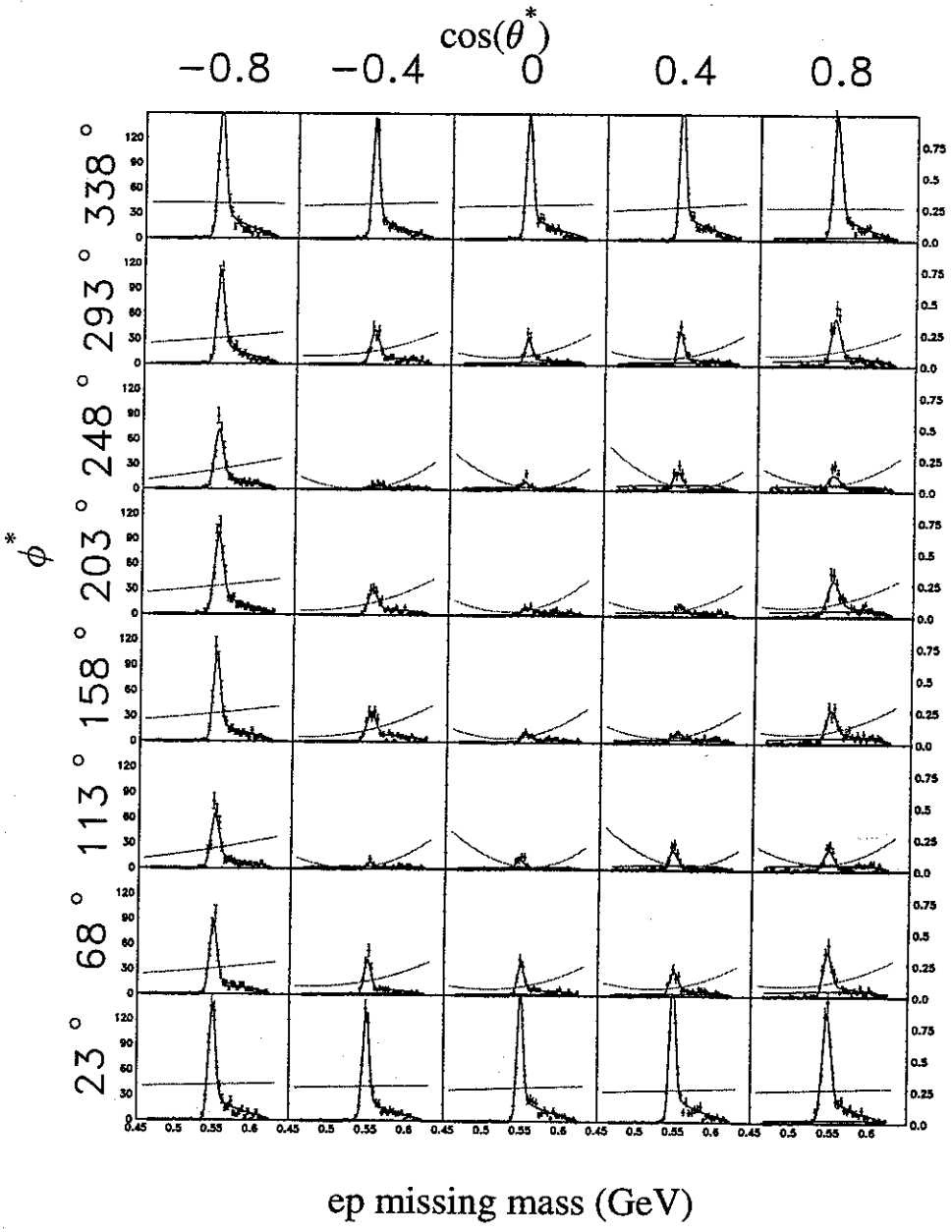

Figure 5.4: Representative ep missing mass fits for simulation data. Shown is $W = 1.545 - 1.575\ GeV$ and $Q^2 = 0.5 - 1.0\ GeV^2$. The green curve is the acceptance function that is used to scale the fit function (see section 5.3). There are four free parameters in the fit: the signal amplitude, the peak centroid and width, and the amplitude of the background. The radiative tail and the shape of the background are constrained in the manner described in section 5.3. The background determined from the fit is, appropriately, very small.

in the simulation to it. The function used in the parameterization is

$$I(p, \theta_\eta^*) = Ae^{\bar{Bp\theta}} \qquad (5.19)$$

where p is the laboratory frame momentum of the proton, and θ is the laboratory frame scattering angle of the proton. A and B are fit parameters and were determined to be $A = 0.605 \pm 0.065$ and $B = 0.1403 \pm 0.066 GeV^{-1}$.

This inefficiency function was applied to protons during the reconstruction of simulated data. The effect is negligible for the majority of points, but there are some kinematics where the change is as large as the typical 15% statistical uncertainty. This occurs at high W for ϕ_η^* near 180°, which is also where the acceptance is low and is the source of a small fraction of the data.

5.2.5 Characterization of CLAS Acceptance

Fig. 5.5 shows the acceptance of the electron plotted as a function of the center of mass energy W and the virtual photon momentum transfer Q^2. The low acceptance at low W and Q^2 is due to the beampipe and the convergence of the toroidal coils at small θ_e^{lab}.

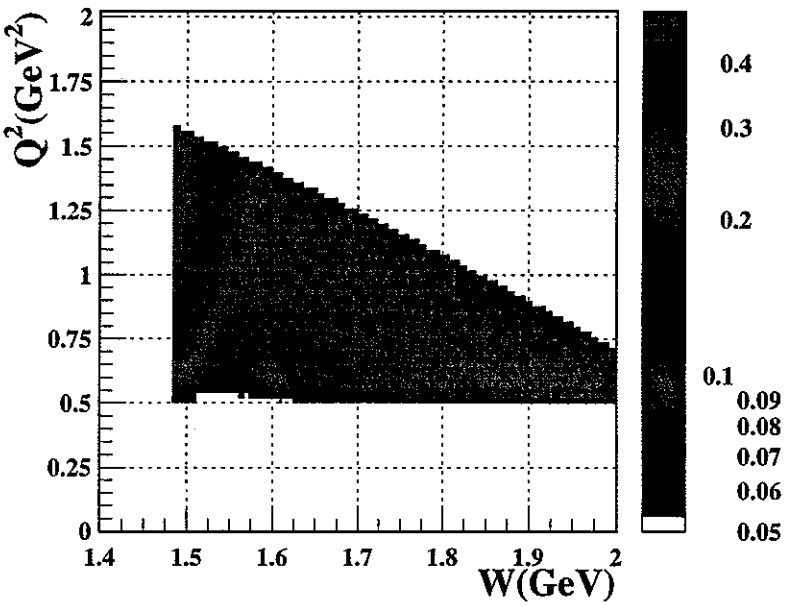

Figure 5.5: η acceptance plotted as a function of W and Q^2. This is the acceptance of the electron only and does not represent acceptance effects due the correlations between the electron and proton.

The acceptance effects introduced by the correlation between the electron and proton can be seen in Fig. 5.6. The ep acceptance should in general be the highest when

ϕ_η^* is 0 or 180 degrees. In these situations, the electron and proton will be coplanar in the laboratory frame. Since the the detector is symmetric about reflection in ϕ_η^*, these events will have a higher acceptance. That is, for ϕ_η^* near 0 or 180 degrees, the angle between the electron and the proton in the laboratory frame is 180°, so if the electron is detected, the proton will be in the opposite sector and will also be detected. In this case, the acceptance of the electron and proton are completely correlated. But as ϕ_η^* changes from 0 or 180 degrees, the electron and proton are no longer coplanar in the laboratory frame and the acceptance of the electron and proton is no longer completely correlated as one or the other may be directed at a coil of the torus magnet. As ϕ_η^* change further from 0 or 180 degrees, the ep acceptance will continue to drop until the correlation between the electron and proton is such that they are only two sectors apart, instead of three, the acceptance will then rebound somewhat. These features of the acceptance are evident from Fig. 5.7.

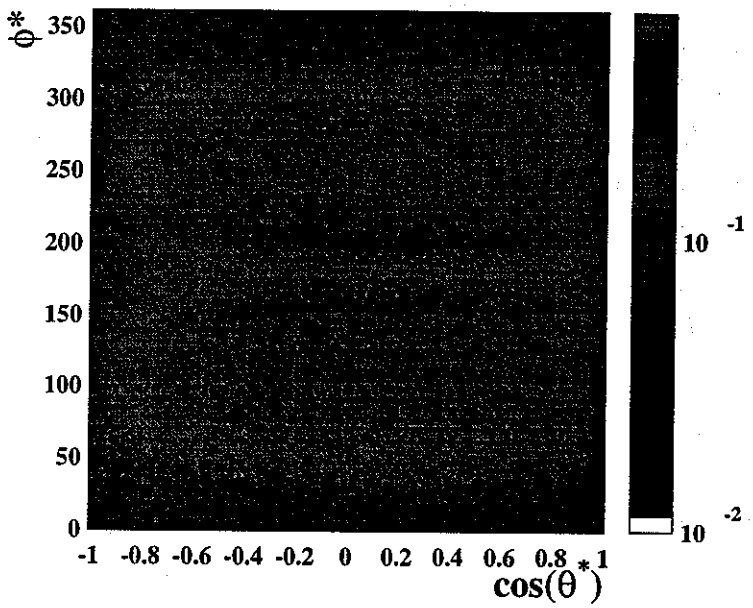

Figure 5.6: The ep acceptance plotted as a function of the η meson center of mass decay angles.

The unique nature of the CLAS acceptance is illustrated by using the correlation between the electron and proton, as shown in Figs. 5.8 and 5.9, to understand two of the acceptance curves shown in Fig. 5.4. Consider first the upper most right plot in that figure that corresponds to $cos(\theta_\eta^*) = 0.6 - 1.0$ and $\phi_\eta^* = 315 - 360°$. The laboratory

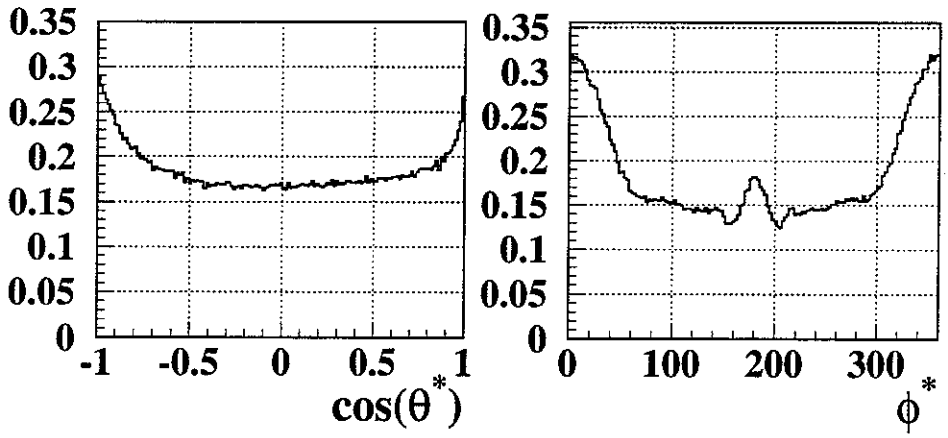

Figure 5.7: Projections of the ep acceptance onto the η meson center of mass decay angle axes. The dips in acceptance near ϕ_η^* of 60° and 160° are due to situations where when the electron is detected, the proton tends to point to a coil (or visa-versa).

frame correlation (in terms of the x and y direction cosines) between the electron and proton for the kinematics at the center of that bin is shown in Fig. 5.8. In this plot, the electron is fixed in ϕ_e^{lab} to 0°, and is marked by a star. That position is completely determined by W and Q^2. The regions obscured by the coils of the torus magnet are shaded. As the momentum of the proton changes such that the value of missing mass spans $0.465 - 0.625\,GeV$, the proton stays entirely within the geometric acceptance and never points to a magnet coil. In reality, the electron is randomly spun around in ϕ_e^{lab} and the (constant) acceptance in that bin represents that averaging.

Fig. 5.9 represents the situation for the plot in Fig. 5.4 that corresponds to $cos(\theta_\eta^*) = -0.2 - +0.2$ and $\phi_\eta^* = 145 - 180°$ (third from the left, fourth from the bottom). For ϕ_e^{lab} equal to 0°, the proton is entirely in the magnet coil and the acceptance is zero. The nonzero and curved nature of the acceptance curve in the corresponding plot in Fig. 5.4] is again a result of the averaging as the electron spins around in ϕ_e^{lab}.

5.3 Fitting e^-p Missing Mass Peaks

Fig. 5.10 shows an example of ep missing mass spectra from which a yield must be extracted. There are a total of 400 such spectra that must be fit accurately and reliably. Such ep missing mass spectra are composed of an η peak and radiative tail, and a multipion background. That is,

$$N(M_X) = N_\eta(M_X) + N_{bkg}(M_X) \tag{5.20}$$

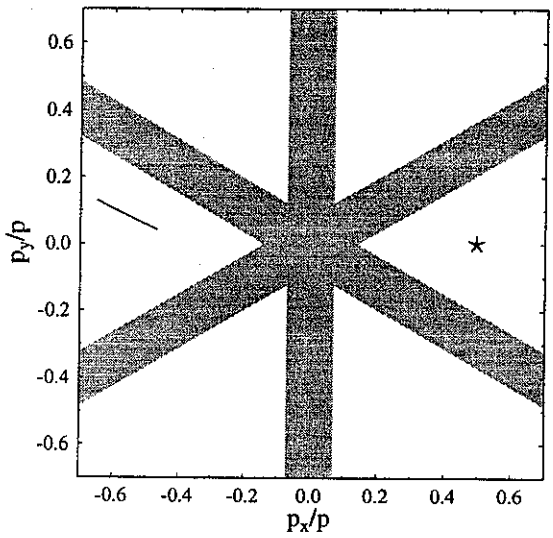

Figure 5.8: The correlation between the electron and the proton in the laboratory frame for $W = 1.560\ GeV$, $Q^2 = 0.75\ GeV^2$, $cos(\theta^*_\eta) = 0.8$ and $\phi^*_\eta = 23.5°$ plotted as the x and y direction cosines of the particle vectors. The region obscured by the coils of the torus magnet are shaded. As the ep missing mass varies from 465 MeV to 625 MeV (with the electron fixed at the locus marked by the star, the proton traces out the path represented by the line.

where $N_\eta(M_X)$ is the η peak with radiative tail, and $N_{bkg}(M_X)$ is the background. Radiative effects are those where the beam or scattered electron emits a real photon as a result of the interaction with the target nucleon, and are discussed in detail in section 5.2. The background to the $ep \rightarrow epM_X$ spectra consist mainly of multipion $ep \rightarrow ep\pi\pi$ events[1]. This channel has been measured to be a significant branching fraction of a number of baryon resonances, specifically, $40 - 50\%$ of the $IJ^P\ \frac{1}{2}\frac{3}{2}^-(1520)$, $75 - 90\%$ of the $\frac{3}{2}\frac{3}{2}^+(1600)$, and $70 - 80\%$ of the $\frac{3}{2}\frac{1}{2}^-(1620)$. At this time, there is not a complete enough experimental determination of $ep \rightarrow ep\pi\pi$ to subtract it off explicitly (in fact, measurements of $ep \rightarrow ep\pi\pi$ are a major part of the program at CLAS). If it were possible to construct a physics model for $ep \rightarrow ep\pi\pi$ which was based on experimental data, this model could be incorporated into the event generator for the simulation, and the multipion background could be derived from it (much in the same manner as is done for radiative effects.) Instead, it is necessary to take a purely phenomenological approach and fit the background to a smooth function.

[1]There are are also small contributions to the background due to multiple scattering events and misidentified particles.

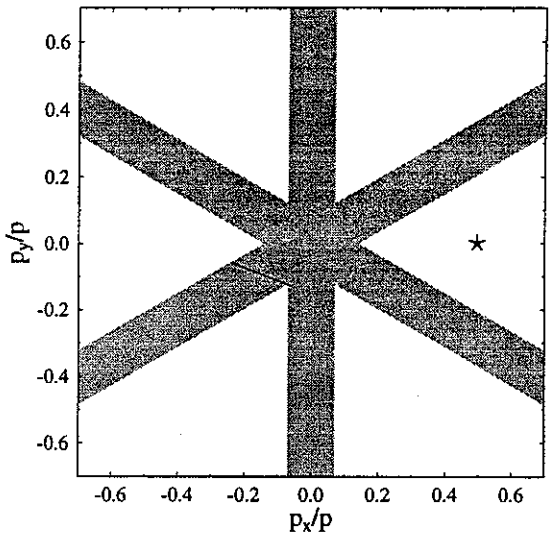

Figure 5.9: The correlation between the electron and the proton in the laboratory frame for $W = 1.560\ GeV$, $Q^2 = 0.75\ GeV^2$, $cos(\theta^*_\eta) = 0.0$ and $\phi^*_\eta = 157.5°$

The η yield in each spectra is determined by representing the signal and background as a parameterized function and fitting the parameters to the data of each spectra. The yield can then be determined by integrating $N_\eta(M_X)$. The assumptions and models used to represent $N_\eta(M_X)$ and $N_{bkg}(M_X)$ are presented in the next sections. In short, the η peak is represented by a Gaussian with an exponential radiative tail, and the multipion background by a polynomial background. The total fit function is corrected by an acceptance function so that it will have the proper form.

Given unlimited statistics, and a fit function that is a good representation of the data, all of the parameters of the fit would be well determined. However, due to statistical limitations, some of the parameters are poorly determined. The presence of a relatively large background signal, as seen in Fig. 5.10, makes it particularly difficult to distinguish the radiative tail from the background when the statistics are small. For these reasons, it is necessary to constrain some of the fit parameters. A good simulation is key in providing guidance as to how to constrain the fit.

The parameters for the radiative tail are determined entirely from simulation. The Gaussian peak width is parameterized as a function of W, Q^2 and ϕ^*_η, and is not allowed to be a free parameter. The form of this parameterization is inspired by simulation, but the actual coefficients are determined from data. The shape of the multipion

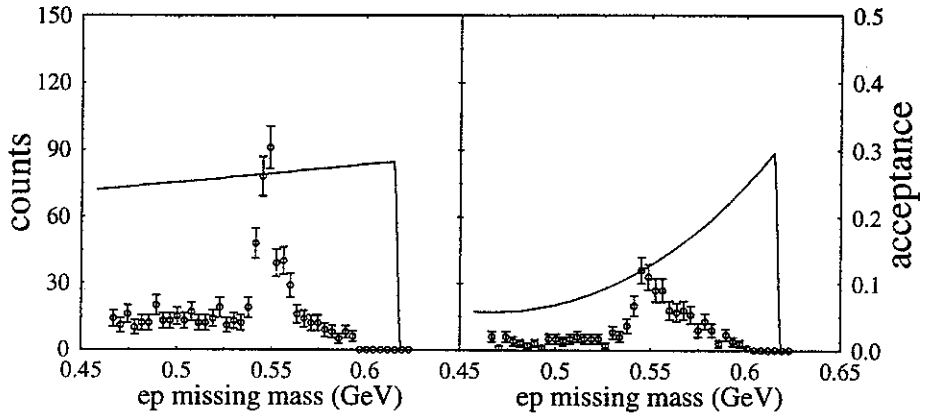

Figure 5.10: Example ep missing mass plot. The plot on the left is for $W = 1.515 - 1.545 GeV$, $Q^2 = 0.5 - 0.75 GeV^2$, $\phi_\eta^* = 0 - 45°$, and $cos(\theta_\eta^*) = -0.2 - +0.2$. The plot on the right is for the same ranges of W, Q^2, and $cos(\theta_\eta^*)$, but $\phi_\eta^* = 45 - 90°$. The data points are number of counts and refer to the left abscissa and the curve is the acceptance and refers to the abscissa on the right. The kinematic limit in missing mass for this W bin is $0.607 GeV$, above which there is no data.

background is parameterized as a function of W and Q^2 and this parameterization is determined from the data.

There are two free parameters in each fit, the amplitude of η signal, and the amplitude of the non-η background. In the next sections, the formulations and assumptions used in fitting the ep missing mass peaks and multipion background are presented.

5.3.1 Geometric Acceptance

The two ep missing mass spectra shown in Fig. 5.10 are for the same W, Q^2, and $cos(\theta_\eta^*)$ bins, but different ϕ_η^* bins. The character of these spectra is quite different even though they only differ in ϕ_η^*; the background and η peak changes dramatically between the two plots. The reason for this effect can be understood by noting the acceptance curve that is overlaid on the plots. The spectra shown in Fig. 5.10 are in fact some true physical distributions that are modulated by the resolution and acceptance of the detector. That is, for the yield in a particular W, Q^2, $cos(\theta_\eta^*)$, and ϕ_η^* bin,

$$N(M_X) = A(M_X)\,[D_\eta(M_X) + D_{bkg}(M_X)] \tag{5.21}$$

where $A(M_X)$ is the detector acceptance and $D_\eta(M_X)$ and $D_{bkg}(M_X)$ are the underlying distributions for the η signal and background, respectively. This acceptance represents the probability that the scattered electron and proton will both be detected.

The correlations between the final state electron and proton are mapped onto a dependence of the acceptance on missing mass. There are five variables which uniquely determine the final state: three momenta each for the electron and proton with one constraint due to the rotational symmetry about the beam axis. These could equivalently also be chosen as W and Q^2 (which uniquely determine the scattered electron up to an azimuthal angle ϕ_e), and $cos(\theta_\eta^*)$, ϕ_η^*, and ep missing mass M_X (which uniquely determine the scattered proton). Then at each value of W, Q^2, ϕ_η^*, $cos(\theta_\eta^*)$, and M_X there is an acceptance probability that is related to the laboratory frame momenta of the electron and proton. When fitting to the ep missing mass spectra, the fit function should be corrected by this acceptance as in eqn. 5.21. In this way, the fit function will have the proper functional form in ep missing mass.

The ep missing mass acceptance functions $A(M_X)$ are determined from an $ep \rightarrow epX$ event generator[2] where the momenta of the final state electron and proton are distributed such that the ep missing mass spans the region of the η. For the accepted events, the electron and proton are subjected to the fiducial cut described in section 4.3.3. This acceptance is not based on a full GEANT simulation of the detector because it was impractical to perform full simulation on the number of events needed. Then, independently in each bin of W, Q^2, ϕ_η^*, and $cos(\theta_\eta^*)$, the acceptance is fit to a third order polynomial in M_X. Fig 5.11 shows these acceptance functions for a particular W and Q^2 bin. The acceptance functions for all bins are shown in appendix B. These curves are only used to modulate the fit function by the detector acceptance, and are not used to obtain the acceptance for $e^-p \rightarrow e^-p\eta$. The $e^-p \rightarrow e^-p\eta$ acceptance is based on a full GEANT simulation as described in section 5.2.3.

5.3.2 η Peak and Radiative Tail

The η peak fit function, $D_\eta(M_X)$ in eqn. 5.20 was parameterized as an η peak and an exponential radiative tail, both convoluted by a Gaussian resolution function. This section describes how the radiative tail parameters of $D_\eta(M_X)$ are determined from simulation.

$D_\eta(M_X)$ represents some underlying distribution, $F_\eta(M_X)$ that is smeared by the resolution of the detector:

$$D_\eta(M_X) = \int_{-\infty}^{\infty} S\left(M_X - M_X'\right) F_\eta(M_X') dM_X' \tag{5.22}$$

[2]The event generator is a program named *EtaGen*.

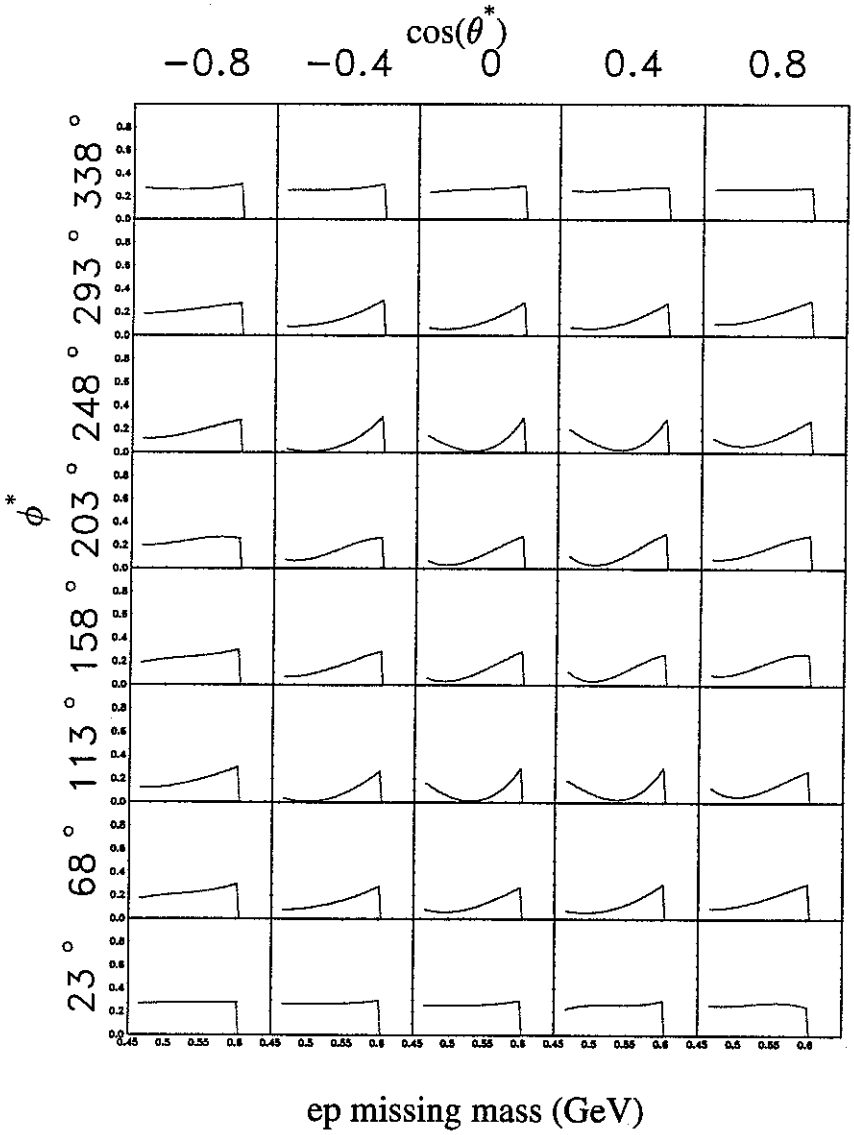

Figure 5.11: The acceptance probability plotted as a function of ep missing mass for $W = 1.545 - 1.575 GeV, Q^2 = 0.5 - 1.0 GeV^2$. The drop-off at at the high missing mass side is the kinematic maximum ep missing mass for this W bin.

where $S\left(M_X - M_X'\right)$ is the resolution function. For example, if the resolution function is a Gaussian and the underlying distribution is a delta function, then the fit function would be a Gaussian.

Due to radiative effects, which skew the measured kinematics, $D(M_X)$ is not a delta function. Fig. 5.12 shows a Monte Carlo generated ep missing mass spectrum with radiative effects, but before the acceptance and resolution simulation of section 5.2.

This is the underlying distribution, a delta function peak with an exponential radiative tail, that is subjected to acceptance and resolution effects.

$$F_\eta(M_X) = n_\eta \left[\alpha\delta\left(M_\eta - M_X\right) + (1-\alpha)\Theta(M_\eta - M_X)\tau e^{-\tau(M_X - M_\eta)}\right] \tag{5.23}$$

There are three parameters here: n_η (the η yield), α (the fraction of the distribution that is unaffected by radiative effects), and τ (which describes the curvature of the radiative tail).

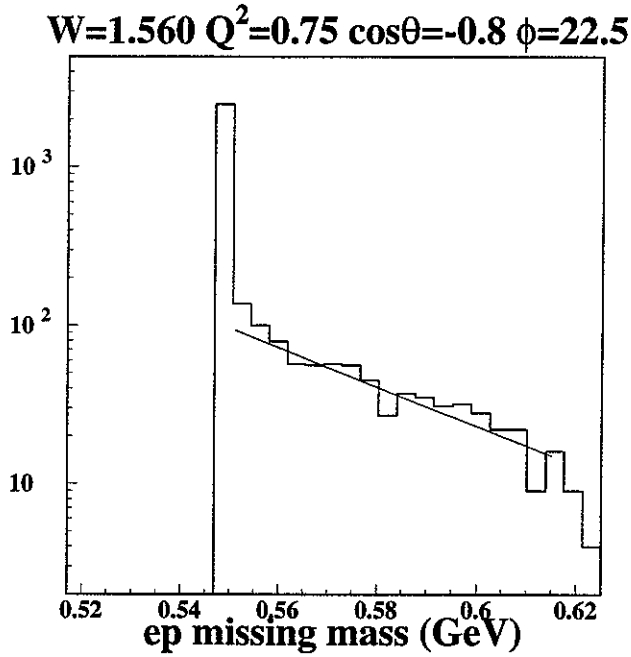

Figure 5.12: A sample generated η distribution. The distribution consists of a peak which is unaffected by radiative effects, and an exponential radiative tail. The line is a fit to the exponential tail. The falloff at high M_X is a binning effect.

We take a Gaussian as the detector resolution function, so after convolution with a Gaussian smearing function (see eqn. 5.22), the η peak fit function is

$$D(M_X) = n_\eta \left[\alpha D_p(M_X) + (1-\alpha)\, D_t(M_X)\right] \tag{5.24}$$

where $D_p(M_X)$ is the peak fit function

$$D_p(M_X) = \frac{1}{\sqrt{2\pi}\sigma} e^{-\frac{(M_X - M_\eta)^2}{2\sigma^2}}, \tag{5.25}$$

$D_t(M_X)$ is the radiative tail fit function

$$D_t(M_X) = \frac{\tau}{2} e^{-\tau\left(M_X - M_\eta + \frac{\tau\sigma^2}{2}\right)} \left[1 - \xi\left(\tau\sigma - \frac{M_X - M_\eta}{\sigma}\right)\right], \tag{5.26}$$

and $\xi(x)$ is the error function.

The parameters which describe the radiative tail α in eqn. 5.24, and τ in eqn. 5.26 were determined from fits to simulation like those shown in Fig. 5.13. It was found that they were both correlated only with W as shown in Fig. 5.14. Since equations 5.24 - 5.26 are normalized, $1-\alpha$ is the fraction of events in the radiative tail and is typically $40-50\%$. The behavior of α and τ as the threshold of $W = 1.487GeV$ is approached is a necessary consequence of the shrinking phase space. Specifically, α must approach 1 at threshold. This simply means that very near threshold there is no phase space available for radiated events and all events should be attributed to the non-radiative peak. The situation is similar for τ, which describes the flatness of the radiative tail. Near threshold, the radiative tail must fall off faster (larger τ) due to shrinking phase space. In this way the qualitative features of the radiative tail parameters shown in Fig. 5.14 can be understood. The details are left to the parameterization. The parameterization used for both α and τ involves a turning point below which the decreasing phase space is manifested.

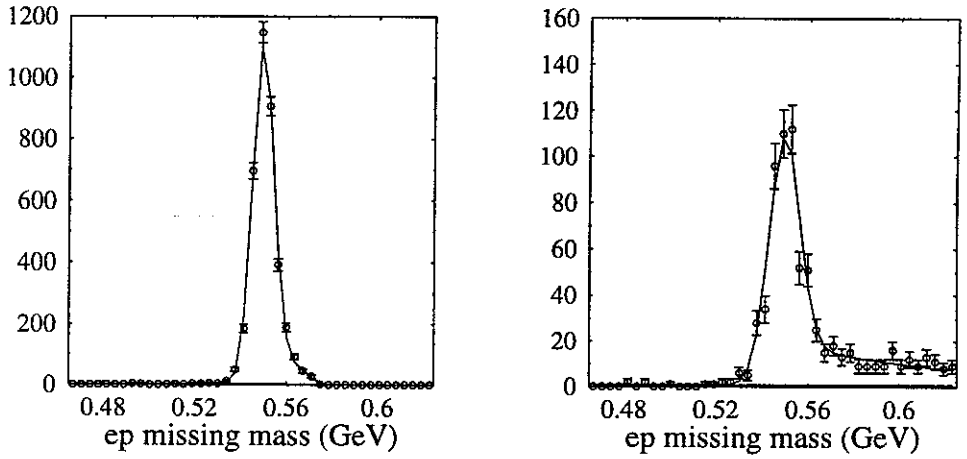

Figure 5.13: Representative fits to simulation data ep missing mass. The plot on the left is for $W = 1.505 - 1.515GeV$ and $Q^2 = 0.5 - 0.75GeV^2$. The plot on the right is for $W = 1.705 - 1.715GeV$ and the same Q^2. The rapid falloff of the tail in the left plot is due to the loss of phase space near the kinematic limit of $0.577GeV$.

The parameterization used for α is

$$\begin{aligned} W < W'_\alpha: \quad \alpha &= 1 + b_{\alpha 1}\left(1 - e^{-m_{\alpha 1}\Delta W}\right) \\ W \geq W'_\alpha: \quad \alpha &= m_{\alpha 2}\Delta W + b_{\alpha 2} \end{aligned} \tag{5.27}$$

W'_α is the turning point below which the phase space effect dominates. Note that the parameterization for α in eqn. 5.27 has the proper threshold dependence of $\alpha \to 1$ as

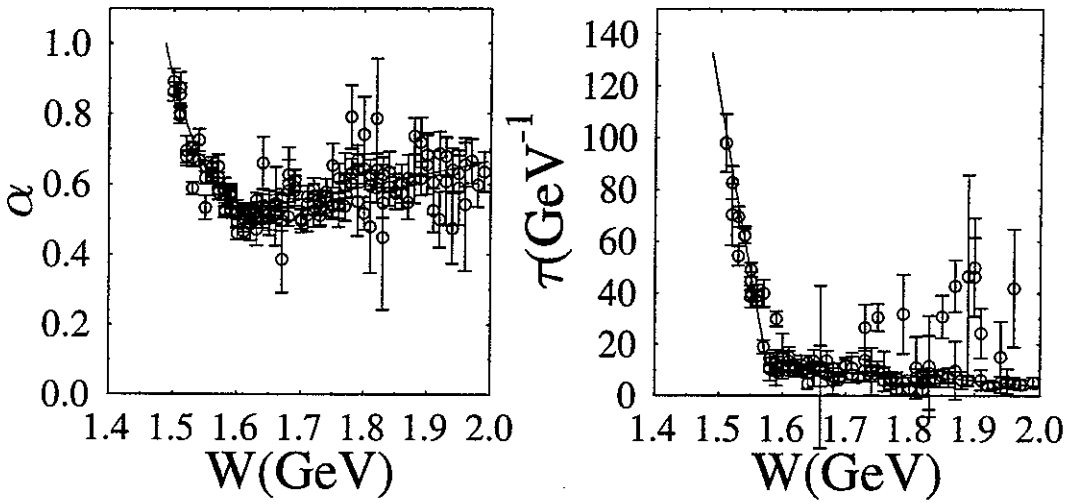

Figure 5.14: The radiative tail parameters as determined from simulation. No dependence in Q^2 or meson decay angles was found. The data shown here are integrated over meson decay angles and is binned finer in W ($10MeV$) and Q^2 ($0.25GeV^2$) than the real data. At each W there are 4 Q^2 points ranging from $0.5GeV^2$ to $1.5GeV^2$. The plot on the left is of the fraction of events that is unaffected by radiative effects, and the plot on the right is of the flatness of the radiative tail. The curve, which begins at threshold, is the parameterization used for the final fits. There is no data near threshold because, as seen in the plot on the left of Fig. 5.13, phase space is shrinking and the radiative tail is disappearing. α is extrapolated to a threshold value of 1 and τ is extrapolated linearly to threshold. The points at high W in the τ plot that yielded high values τ were anomalous fits and had no bearing in the parameterization of τ.

$\Delta W \to 0$. The coefficients of the parameterization determined from the data shown in Fig. 5.14 are:

$$\begin{array}{rcll} W'_\alpha & = & 1.600 & GeV \\ m_{\alpha 1} & = & 14.26 & GeV^{-1} \\ b_{\alpha 1} & = & -0.600 & GeV \\ m_{\alpha 2} & = & 0.366 & GeV^{-1} \\ b_{\alpha 2} & = & 0.479 & GeV \end{array}$$

The parameterization used for τ is

$$\begin{aligned} W < W'_\tau : \ \tau &= m_{\tau 1}\Delta W + b_{\tau 1} \\ W \leq W'_\tau : \ \tau &= m_{\tau 2}\Delta W + b_{\tau 2} \end{aligned} \tag{5.28}$$

with the coefficients of the parameterization again fit to the simulation data shown in Fig. 5.14:

$$\begin{array}{rcll} W'_\tau & = & 1.575 & GeV \\ m_{\tau 1} & = & -1365. & GeV^{-2} \\ b_{\tau 1} & = & 133.2 & GeV^{-1} \\ m_{\tau 2} & = & -21.95 & GeV^{-2} \\ b_{\tau 2} & = & 15.01 & GeV^{-1} \end{array}$$

The widths of the Gaussian peaks, σ in eqn. 5.25 were determined from a parameterization derived from simulation data. The coefficients of the parameterization were determined from fits to real data. Fig. 5.15 shows the widths from simulation, data, and the parameterization used for the final fits. The simulation reproduced the main features of the ep missing mass peaks well.

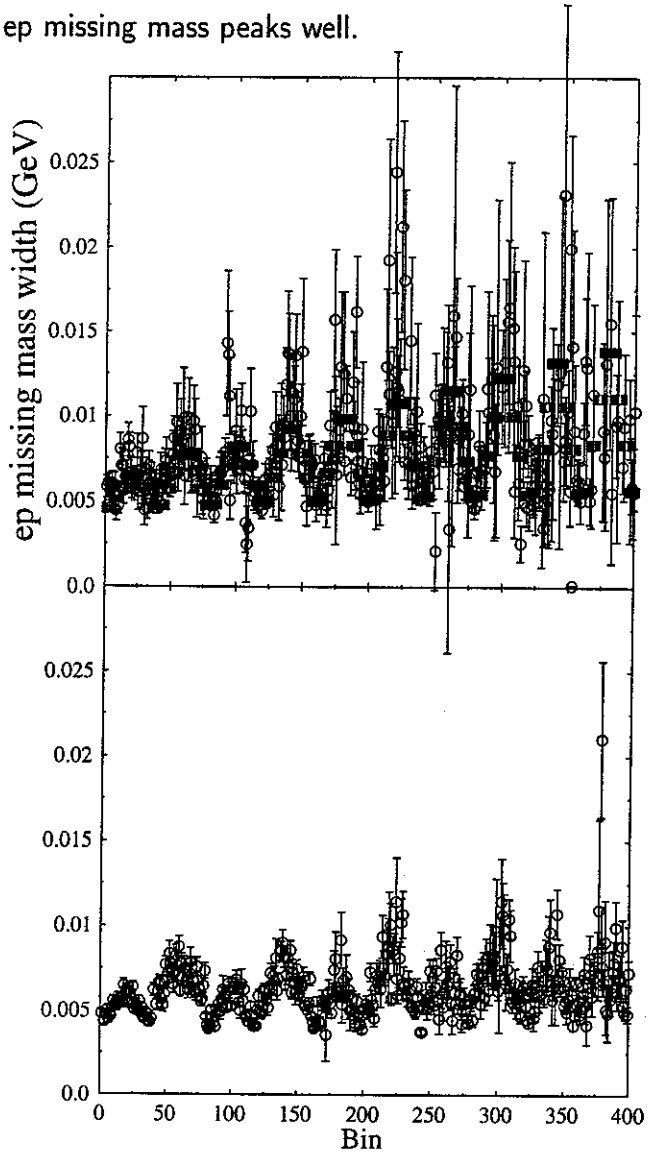

Figure 5.15: ep missing mass peak widths from data and simulation. The widths are plotted versus a bin number which is such that the 40 angular bins at a given W and Q^2 bin are grouped together. The first 40 bins are $W = 1.485-1.515$ GeV and $Q^2 = 0.5-1.0$ GeV^2, the second 40 bins are $W = 1.485 - 1.515$ GeV and $Q^2 = 1.0 - 1.5$ GeV^2, the third set of 40 bins are $W = 1.515 - 1.545$ GeV and $Q^2 = 0.5 - 1.0$ GeV^2, etc. The top plot is the widths determined from experimental data with the parameterization used for the width in the final fit overlaid. The bottom plot is the widths determined from the simulation data. The kinematic dependence on the η peak width is seen as a resolution effect inherent in the CLAS detector.

The measure of quality of the fit function given by eqn. 5.24 is in its ability to represent the data (in this case simulation data). All of the final fits to the simulation data can be found in appendices B and C. Fig. 5.16 shows the reduced χ^2 distribution for the fits to the simulation data (which has no background). That the χ^2 distribution is peaked at 1.0 is a good indication that the fit function is an appropriate representation of the data, although the width of the χ^2 distribution is somewhat broader than would be expected due to purely statistical fluctuations.

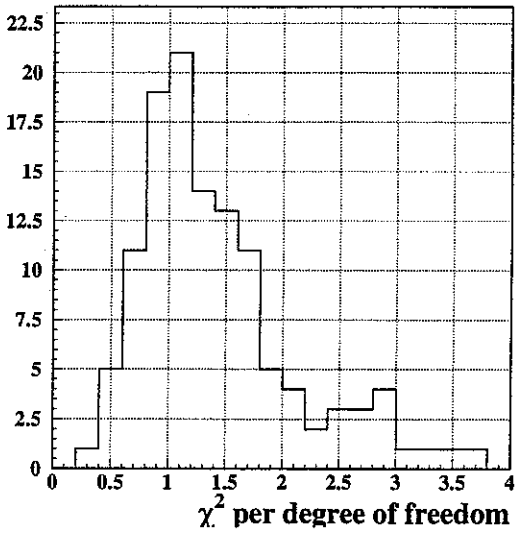

Figure 5.16: The reduced χ^2 distribution for the fits to simulation data.

5.3.3 Multipion Background

The fit function used for the multipion background $D_{bkg}(M_X)$ in eqn. 5.21 is

$$D_{bkg}(M_X) = b_0 \left(2\sqrt{\Delta m' \Delta m} - \Delta m\right) \tag{5.29}$$

where Δm is the difference between the kinematically maximum value of missing mass and M_X, $\Delta m = m_{max} - M_X$. The parameters of the fit are b_0, the strength of the background, and $\Delta m'$. This form was inspired by phase space considerations. Near threshold, the phase space for the two body decay of a resonance is proportional to $x = \sqrt{\Delta m}$. The chosen parameterization of the background is then a polynomial in Δm that has the correct phase space dependence. Systematic errors associated with this choice are addressed in section 6.1.3.

Statistical limitations did not allow the parameter $\Delta m'$ to be free in the final fits, so it was parameterized from fits to data. Fig. 5.17 shows the variation of $\Delta m'$ with

W for the four total distribution Q^2bins. The parameterization chosen for $\Delta m'$ is

$$\Delta m' = C + C_W W + C_{WQ} W Q^2 \tag{5.30}$$

with

$$\begin{aligned} C &= -0.491 \pm 0.0185 \quad GeV \\ C_W &= 0.38 \pm 0.106 \\ C_{WQ} &= -.015 \pm 0.0085 \quad GeV^{-2} \end{aligned}$$

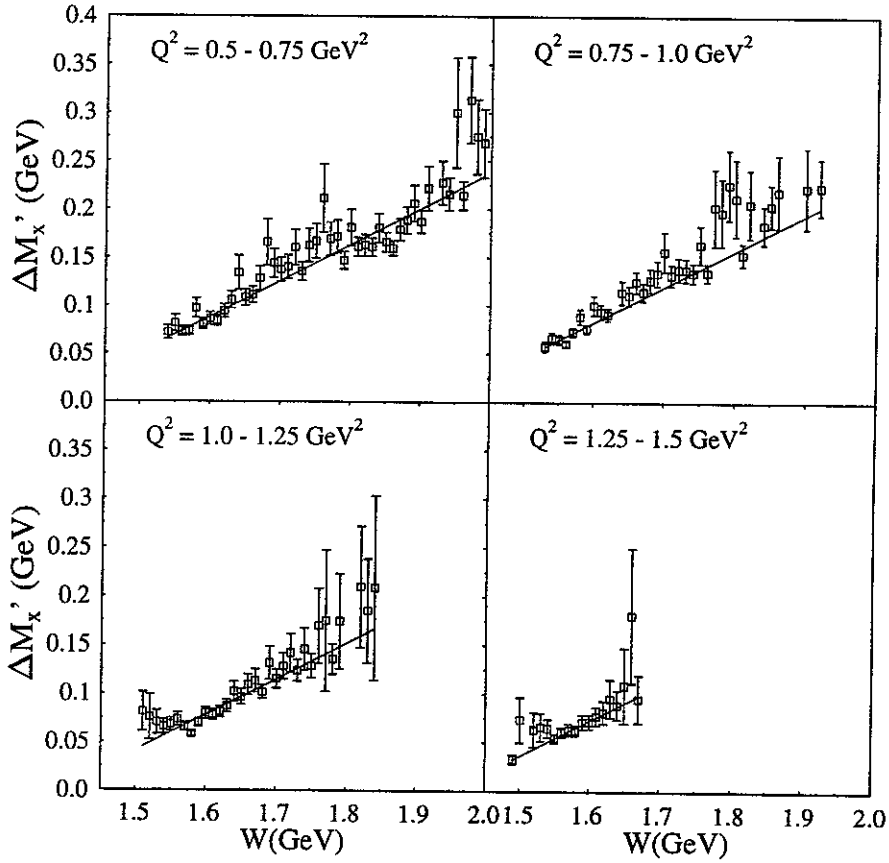

Figure 5.17: The variation of $\Delta m'$ with W in the four total distribution bins.

5.3.4 Final Fits

The final fit function is reproduced here for reference.

$$N(M_X) = A(M_X)\left\{n_\eta\left[\alpha D_p(M_X) + (1-\alpha)\, D_t(M_X)\right] + D_{bkg}(M_X)\right\} \tag{5.31}$$

with

$$D_p(M_X) \;=\; \frac{1}{\sqrt{2\pi}\sigma} e^{-\frac{(M_X - M_\eta)^2}{2\sigma^2}}$$

$$D_t(M_X) = \frac{\tau}{2} e^{-\tau\left(M_X - M_\eta + \frac{\tau\sigma^2}{2}\right)} \left[1 - \xi\left(\tau\sigma - \frac{M_X - M_\eta}{\sigma}\right)\right] \quad (5.32)$$
$$D_{bkg}(M_X) = b_0\left(2\sqrt{\Delta m' \Delta m} - \Delta m\right)$$

$A(M_X)$ is determined in the manner presented in section 5.3.1 and α, σ, τ, and $\Delta m'$ are parameterized in the ways presented in the previous sections. Table 5.1 summarizes the parameters of the ep missing mass fits. There were two free parameters in each fit: the η signal amplitude and the strength of the background.

η signal	n_η	amplitude	free parameter
	M_η	Gaussian centroid	fixed by data
	σ	Gaussian width	determined from data; form of parameterization inspired by simulation
	$1-\alpha$	fraction in radiative tail	determined from simulation
	τ	curvature of radiative tail	determined from simulation
background	b_0	amplitude	free parameter
	$\Delta m'$	"roll-over" point	parameterized in W

Table 5.1: Parameters of the ep missing mass fit function.

The fits are performed via the maximum likelihood technique for Poisson distributed data [5]. Independently in each bin, the free parameters of the fit function are varied until the maximum of the likelihood function is found. In practice, this is accomplished by minimizing the negative log of the likelihood function.

$$-ln\mathcal{L} = \sum_i \left[N(M_{X_i}; n_\eta, M_\eta, \sigma_\eta) - N_i + ln\left(\frac{N_i}{N(M_{X_i}; n_\eta, M_\eta, \sigma_\eta)}\right)\right] \quad (5.33)$$

where F is the fit function, and N_i is the number of counts observed in the data. The fits were performed with the standard MINUIT [19] minimization package. The uncertainties in the fit parameters are determined from the MINOS routines of MINUIT and include correlations.

Fig. 5.18 shows a representative missing mass plot and illustrates the components of the fit function discussed above. The falloff in the spectra beginning at $M_X = 0.577 GeV$ is due to the finite binning in W, which begins at $M_X = 1.515 - M_p = 0.577\ GeV$ and ends at $M_X = 1.545 - M_p = 0.607\ GeV$.

The distribution of the centroids of the η peak is shown in Fig. 5.19. The peak centroids are typically $2MeV$ low, which is indicative of a small miscalibration of the detector.

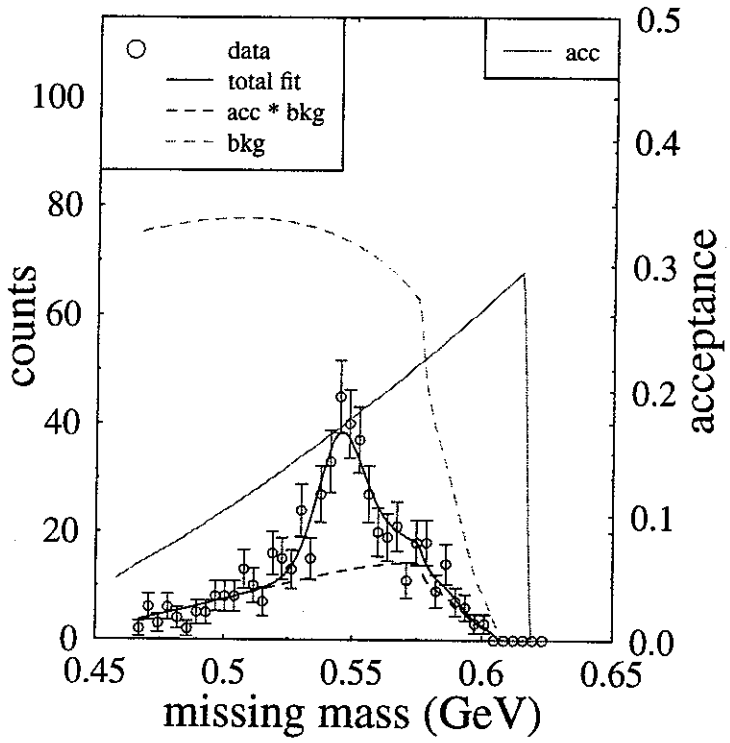

Figure 5.18: A representative ep missing mass fit. Shown is one of the angular distribution ep missing mass data and fit for $W = 1.515 - 1.545/GeV$, $Q^2 = 0.5 - 1.0GeV^2$. "bkg" labels the background function (B(M_X) in eqn. 5.29) and "acc" labels the acceptance function (A(M_X) in eqn. 5.21). The radiative tail is evident on the high $M_X$side of the η peak. The acceptance function is plotted above the kinematic limit in M_X, but that information is of course not used.

The amplitude of the background, b_0 in eqn. 5.29 is shown in Fig. 5.20. As can be seen by the small scatter from point to point, the background is in general very well determined.

Fig. 5.21 shows the χ^2 per degree of freedom distributions. That these distributions peak at 1.0 is indicative that the fit function is a good representation of the data. The spread is somewhat broader than would be expected from purely statistical variations.

5.4 Target Window Corrections

This section describes the technique used to correct for the fact some events result from scattering from the material in the target windows as opposed to the liquid Hydrogen. The tracks reconstruction resolution was not adequate to use a simple vertex cut to reject the events coming from the target windows, so a subtraction technique based upon the η yield seen from the windows in empty target runs was used.

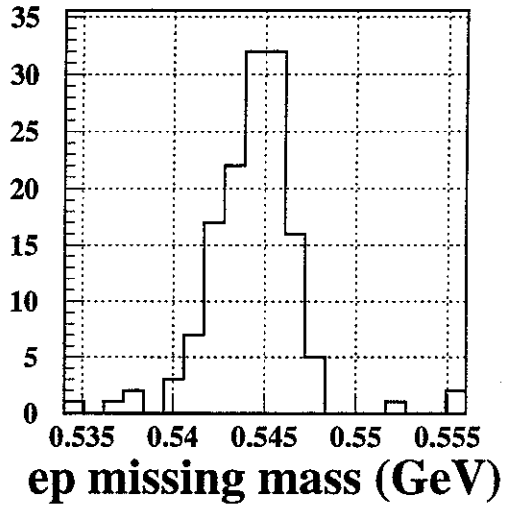

Figure 5.19: The distribution of the η peak centroid, M_η for the total distribution fits.

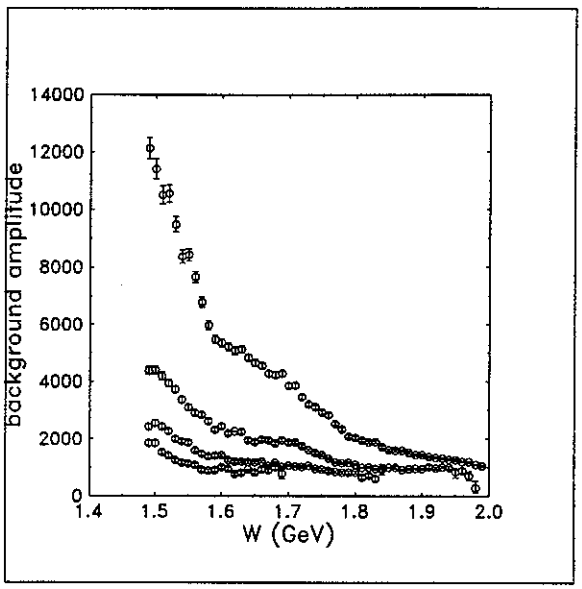

Figure 5.20: The amplitude of the background plotted versus W. There are four distinct sets of points corresponding to the four different Q^2 bins. The lowest set of points corresponds to the lowest Q^2 points.

The vertex reconstruction for a typical run is shown in Fig. 5.22. There is an enhancement in the vertex z position at the downstream end of the target that is understood to come from a layer of ice that condensed on the target window. Fig. 5.25

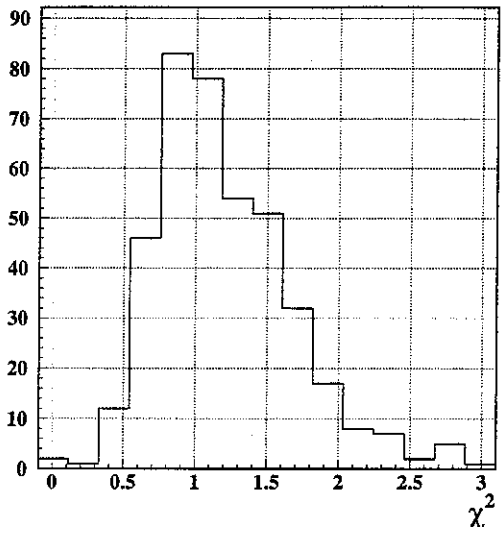

Figure 5.21: Reduced χ^2 distributions for angular distribution ep missing mass fits.

shows that events with an $ep\eta$ final state come from the thick downstream window, as well as from throughout the target. Figs. 5.23 and 5.24 show the vertex reconstruction for two empty target runs that were taken 4 days apart. In Fig. 5.23, the upstream and downstream target windows are clearly visible. The accumulation of ice on the downstream window makes it about twice as thick as the upstream window. In Fig. 5.24 it can be seen that this layer of ice has grown dramatically in the 4 days between runs 8708 and 8786.

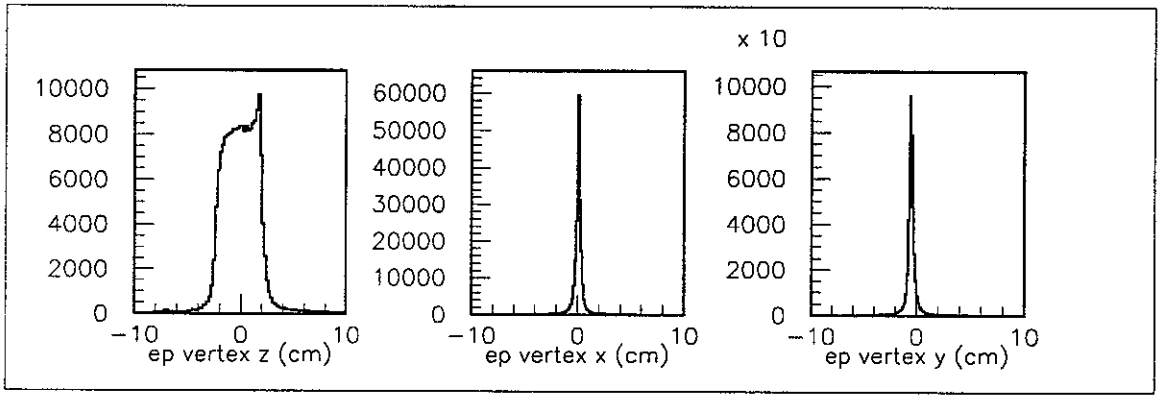

Figure 5.22: Vertex reconstruction for the typical full target run 8737. The target cell extends from -2cm to 2cm in z. The enhancement at the downstream target wall (z=2cm) is due to a buildup of condensation. The beam was sub-millimeter in diameter, so the x and y vertex positions are essentially a measure of tracking resolution.

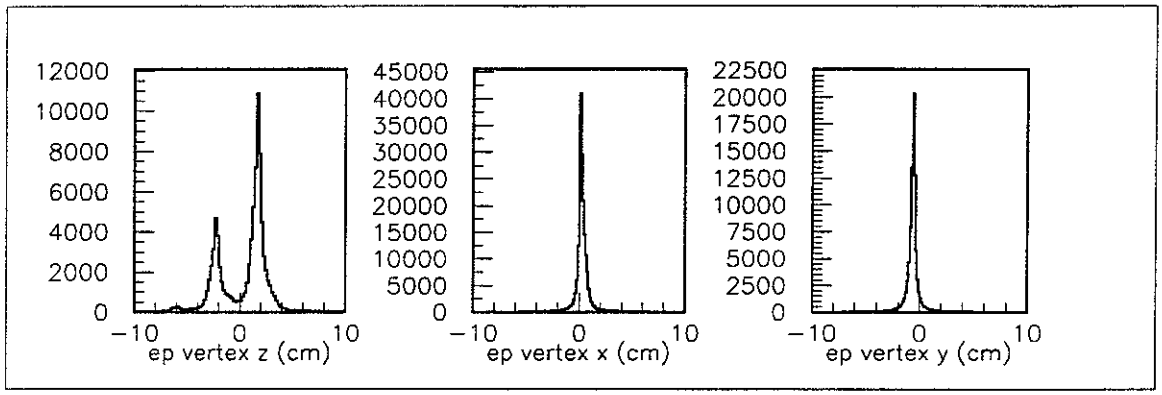

Figure 5.23: Vertex reconstruction for the empty target run 8708. The target cell windows are clearly visible in the z position. This data was taken early in the run before the condensation had built up very much. A vacuum foil in the beam pipe is also visible at z=-7cm.

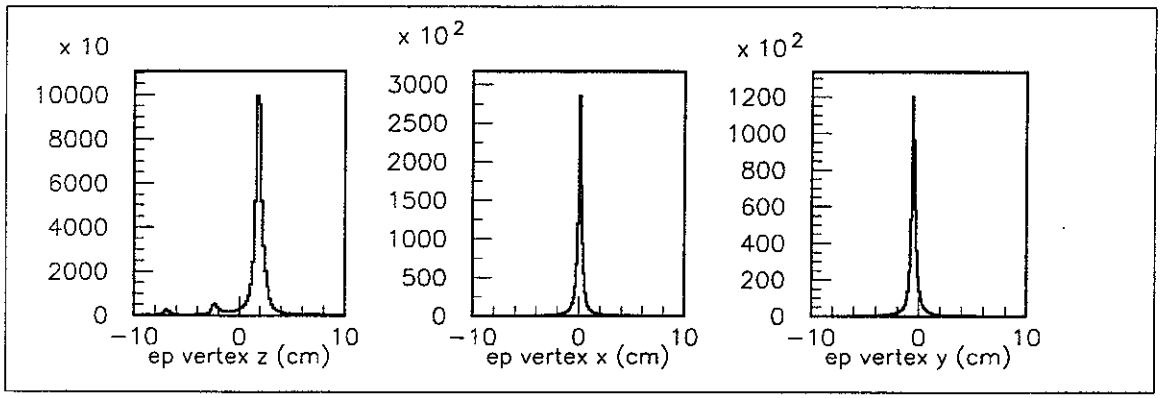

Figure 5.24: Vertex reconstruction for the empty target run 8786. The downstream window is dramatically enhanced. This data was taken late in the experiment, when the condensation was substantial.

Since the track reconstruction resolution was not adequate to eliminate the contribution from the target windows with a simple vertex cut, a subtraction technique had to be employed. The rate of η production from the hydrogen target in a particular bin is given by:

$$r_\eta = r'_\eta - r^w_\eta \tag{5.34}$$

where

$r'_\eta \equiv \eta$ production rate including contribution from windows
$r^w_\eta \equiv \eta$ production rate from the target windows

Here lower case r refers to a rate in a bin and in what follows upper case R refers to a rate summed over all bins.

The rate from target windows, r^w_η can be estimated from empty target runs. Figs. 5.26 and 5.27 show that there are deuterons that come primarily from the target

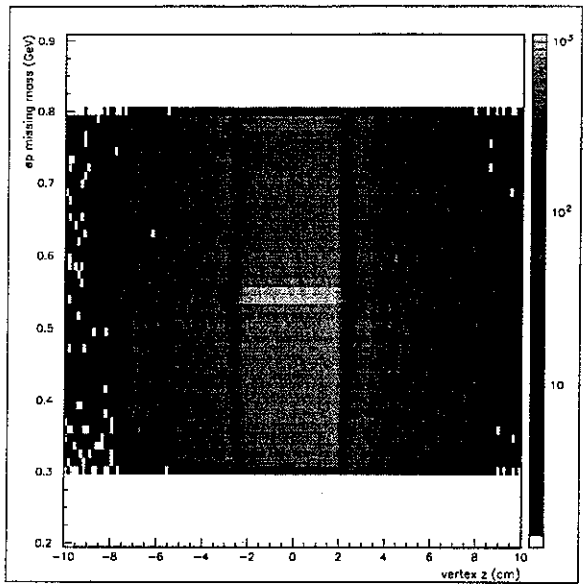

Figure 5.25: The ep missing mass plotted versus the vertex z position. η production can be seen to originate from throughout the target cell and extent into the downstream target wall.

windows. Then by monitoring the number of deuterons, the target windows are monitored.

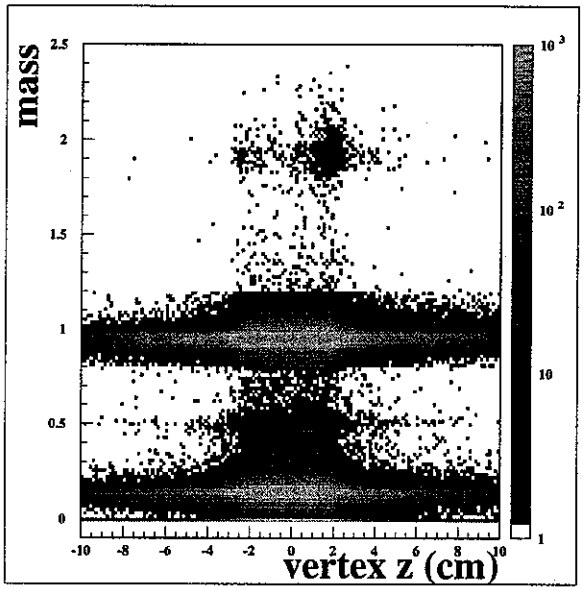

Figure 5.26: The charged particle reconstructed mass plotted versus the ep z vertex position for full target data. There are four bands evident. Pions, kaons, protons and deuterons. The pions, kaons, and protons can be seen to be uniformly distributed through the target whereas the deuterons come predominantly from the target windows. In this plot, the z-scale has been suppressed by an order of magnitude to emphasize the small deuteron peak.

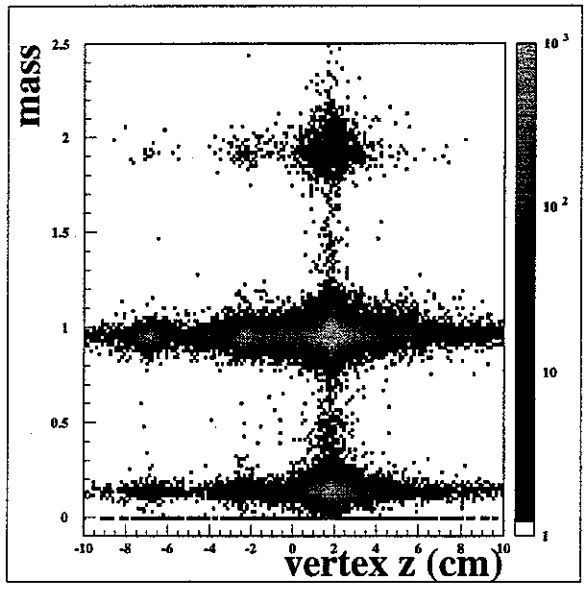

Figure 5.27: The charged particle reconstructed mass plotted versus the ep z vertex position for empty target data.

$$r_\eta^w = r_\eta^{et} \cdot \frac{R_d}{R_d^{et}} \tag{5.35}$$

where

r_η^{et} $\equiv$ η production rate from empty target run
R_d $\equiv$ deuteron rate from run being analyzed
R_d^{et} $\equiv$ deuteron rate from empty target run

The factor $\frac{R_d}{R_d^{et}}$ is included to take into account variation of the window thickness from run to run due to potential buildup of ice.

Because of limited statistics in the empty target runs, the binned η rate, r_η^{et} cannot be determined. It is estimated in the following way:

$$r_\eta^{et} = R_\eta^{et} \cdot \frac{r'_\eta}{R'_\eta} \tag{5.36}$$

This assumes that the distribution of the η production from the windows is the same as that from the hydrogen target.

Then we have

$$r_\eta = \alpha_{window} \cdot r'_\eta \tag{5.37}$$

Where α_{window} is the target window correction factor:

$$\alpha_{window} = 1 - \frac{R_\eta^{et}}{R'_\eta} \cdot \frac{R_d}{R_d^{et}} \tag{5.38}$$

In this way, the deuteron rate is used to monitor the thickness of the target windows.

The η production rate from the empty target run R_η^{et}, shown in Fig. 5.28, was determined from run 8786 to be 465 $\pm$ 22 over 25.85 μC of integrated charge.

$$R_\eta^{et} = 18.0 \pm 0.9 \mu C^{-1} \tag{5.39}$$

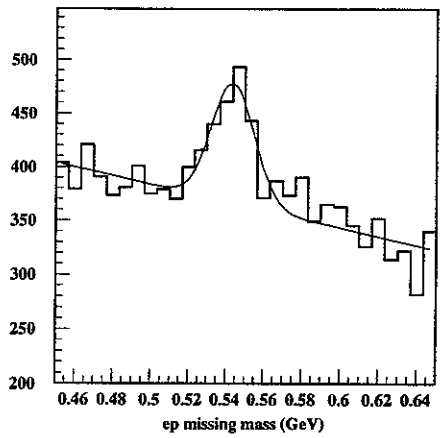

Figure 5.28: The ep missing mass spectrum from which the number of etas in the empty target run is obtained.

The deuteron rate, R_d was measured for each run to monitor the thickness of condensation on the target windows. Fig. 5.29 shows the evolution of the deuteron rate.

The target window correction factor determined in this way is

$$\alpha_{window} = 0.933 \tag{5.40}$$

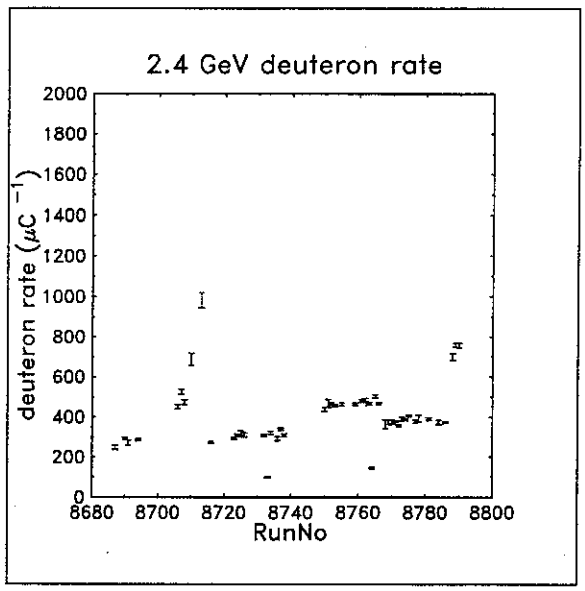
2.4 GeV deuteron rate
deuteron rate (μC^{-1})
2000
1800
1600
1400
1200
1000
800
600
400
200
0
8680
8700
8720
8740
8760
8780
8800
RunNo

Figure 5.29:

Chapter 6

Results and Discussion

The potential sources of systematic errors are investigated. The systematic errors are found to be dependent on kinematics, and the uncertainties are thereby applied bin-by-bin to the differential cross section. The differential cross sections of this and previous experiments are used to extract multipole-decomposed parameters in a self-consistent way. Under certain assumptions, resonance properties of the $\frac{1}{2}\frac{1}{2}^{-}(1535)$ are determined from these parameters. The excitation amplitude $A^{p}_{1/2}(Q^2)$ is determined (again from this and previous data, in a self-consistent manner) from these resonance properties.

6.1 Systematic Studies

In an analysis such as the one presented in this thesis, there are assumptions and models that are used that may introduce systematic errors in determining the cross section. This section reports the results of the studies that were carried out to estimate these systematic errors. It is convenient to categorize these systematic errors as being due to reconstruction, η peak fitting, or acceptance corrections. Reconstruction systematic errors come about from the procedures, algorithms and calibrations that are used to reconstruct the raw data from the detector into identified particles and momenta. η peak fitting systematic errors arise from the models and assumptions used to fit ep missing mass peaks and extract the η yield in each bin. And finally, systematic errors may be introduced due the models and assumptions used in making the radiative and acceptance corrections of section 5.2.

Systematic errors can manifest themselves as either overall scale errors, which effect the extracted cross section the same at all kinematics, or as kinematically dependent errors. A systematic error in the determination of the luminosity is an example of a scale error. However, most systematic errors are, at least potentially, kinematic dependent, and the studies presented in this section take that fully into account. Except where otherwise noted, systematic errors are determined bin by bin.

The nature of and methods used to measure systematic effects are presented in sections 6.1.1 through 6.1.4. Section 6.1.5 presents the results of the systematic studies. Plots of the systematic effects are presented in Appendix D.

6.1.1 Systematic Errors of Luminosity

There are possible sources of systematic error in the determination of the luminosity. These include the measurement of the beam current and the target properties. The inclusive elastic scattering cross section was calculated by L. C. Smith [29], and was consistent with previous precise measurements to within 3%. For this reason, all systematic errors associated with luminosity are taken to be 3%.

6.1.2 Systematic Errors of Event Reconstruction

The systematic errors associated with the electron identification algorithms were estimated by scanning events with a graphical single event display program. Electrons are easily identified as negative particles with matching hits in the Cerenkov detector and electromagnetic calorimeter. It was found that the most common source of missing an electron was due to the E/p cut. In a small fraction of events, there failed to be a hit reconstructed in both the inner and outer layers of the calorimeter. This caused the particle's energy to be determined incorrectly and the E/p cut to fail. The hand scan indicated that the electron identification inefficiency was less than 2%. This is most certainly an upper limit since pions can look like electrons to the eye if there was an associated errant hit in the Cerenkov detector. This sometimes happened due to a backsplash from the electromagnetic calorimeter in to the Cerenkov counter.

The cuts associated with electron identification were made very loosely and systematic errors introduced from them are very small. The systematic error associated with the electron identification cuts were studies by changing them incrementally in steps of $+10\%$ and monitoring the η yield. The systematic error associated with electron identification cuts was found to be $< 1\%$ [21].

Proton identification is based on a cut on hadronic mass determined from time of flight (see section 4.3.1). Systematic errors may be introduced if there are significant tails on the proton hadronic mass peak. These potential systematic errors were studied by changing the hadronic mass cut for protons and noting the change in η yield. A change in the proton cuts from $.8 \leq m < 1.2GeV$ (the values used in the final analysis) to $.6 \leq m < 1.5GeV$ resulted in only a $1.1 \pm 0.3\%$ change in the η yield.

6.1.3 Systematic Errors of η Peak Fitting

The procedure used to fit ep missing mass peaks and extract η yields was presented in section 5.3. The fit function is reproduced here for reference.

$$
\begin{aligned}
D(M_X) &= D_\eta(M_X) + D_{bkg}(M_X) \qquad (6.1)\\
D_\eta(M_X) &= n_\eta \left\{ \alpha \frac{1}{\sqrt{2\pi}\sigma_\eta} e^{-\frac{(M_X - M_\eta)^2}{2\sigma_\eta^2}} \right.\\
&\quad \left. + (1-\alpha)\frac{\tau}{2} e^{-\tau\left(M_X - M_\eta + \frac{\tau\sigma_\eta^2}{2}\right)} \left[1 - \xi\left(\tau\sigma_\eta - \frac{M_X - M_\eta}{\sigma_\eta}\right)\right] \right\}\\
D_{bkg}(M_X) &= b_0 \left\{ 2\sqrt{\Delta m' \Delta m} - \Delta m \right\}
\end{aligned}
$$

Where Δm is the difference between M_X and the kinematic limit of missing mass:

$$\Delta m = W - M_p - M_X. \qquad (6.2)$$

In each fit, the *free* parameters are n_η, the number of η events, and b_0, the strength of the background. There are also parameters α, τ, M_η, σ_η, and $\Delta m'$ which have been determined from simulation or data and are parameterized in terms of the kinematics variables. There are potential systematic errors introduced in the treatment of these.

η Gaussian peak centroid M_η and width σ_η: M_η was varied by 3 MeV from the value of 544.5 MeV used in the final fits. This was approximately a one-sigma change. In the final fits, the η peak width σ_η was parameterized as a function of W, Q^2, and ϕ_η^*. To study the potential systematic errors of this parameterization, the width was changed by 10%. The results of this study are presented in the appendix in Figs. D.7 and D.8.

Radiative tail parameters α and τ: Both parameterized as a function of W in the final fits, the radiative tail parameters were varied by 10% to study potential systematic errors. This value was chosen because it was judged that these parameters were well represented by the chosen parameterization to within 10% (see Figure 5.14.). The results of this study are presented in the appendix in Figs. D.11 , D.12, D.13, and D.14

Background function $D_{bkg}(M_X)$: The background to the $ep \to epM_X$ spectra consist mainly of multipion $ep \to ep\pi\pi$ events. There is not a complete enough experimental determination of $ep \to ep\pi\pi$ to allow the explicit subtraction of this background, so a fit function is used. The background fit function of equation 6.1 was chosen because it allowed a smooth polynomial representation and because it goes to zero as phase space at the kinematic limit of $M_X = W - M_p$. With such little knowledge of $ep \to ep\pi\pi$, this is a choice of convenience, so to study the systematic effects of the $D_{bkg}(M_X)$, fits

to ep missing mass spectra were performed with $D_{bkg}(M_X) = b_0$, that is, a function that is flat in M_X. The average χ^2 for the fits with a flat background was 1.349 while for the polynomial background it was 1.252, indicating that the polynomial background was a better representation of the data. Moreover, the fits with a flat background were more sensitive to the starting values of the free parameters than the polynomial background fits, also indicating that the polynomial background is a better representation. Thus the polynomial background was used in the final fits, but the flat background was used to study the systematic effects. The plots of this systematic study can be found in the appendix in Figs. D.5 and D.6.

6.1.4 Systematic Errors of Acceptance

One source of systematic errors is inherent in applying correction factors to binned data. The correction factor calculated for a particular bin represents a weighted average correction factor for that bin. That is, the correction factor within a bin is weighted by the thrown distribution. If the thrown distribution matches the experimental distribution exactly, then the weighting is appropriate, but in cases where there is a significant mismatch between the experimentally extracted distribution and the distributions used for simulation, systematic errors may be introduced. In an ideal situation, the physics models used for determining acceptance and radiative corrections would match the physics extracted from the experiment exactly. Of course it is usually the case that this physics is unknown and in practice it is necessary to implement some assumptions. These assumptions are valid in so much as they are consistent with the data and the results do not depend on them as they are varied over a reasonable range.

Two sources of this type of systematic error were investigated: the distribution used for the determination of the fit function acceptance, and the distribution used for the determination of the η acceptance.

The ep missing mass fit function is corrected by an acceptance that is calculated from $ep \rightarrow epX$ events where the momenta of the final state electron and proton are such that the invariant mass M_X spans the region of the η. This acceptance function is used to give the fit function the correct form, but is not used for the final η acceptance since it is not derived from a full simulation with radiative effects, η decay, etc. The event generator distribution used to determine the fit function acceptance was flat in the kinematic variables W, Q^2, $cos(\theta^*_\eta)$, and ϕ^*_η. To study the systematics of this, the event generator distribution was changed to one that represents the electroproduction of η via a $\frac{1}{2}\frac{1}{2}^-$ baryon resonance with a Breit Wigner amplitude centroid of $1.53\ GeV$ and width of $.120\ GeV$. The plot of this study can be found in the appendix in Figs. D.1 and D.2.

The second source of acceptance systematic errors investigated was the distribution used to determine the acceptance of η events. As described in section 5.2.2, the event generator used for making radiative and acceptance corrections has several physics assumptions, The most dramatic of which is that η electroproduction is dominated a $\frac{1}{2}\frac{1}{2}^-$ Breit-Wigner amplitude with no Q^2 dependence. This is a three-fold assumption: 1) that the center of mass η angular distribution is isotropic, and 2) that the energy (W) dependence is of a Breit-Wigner resonance, and 3) that there is no dependence of the amplitude on the virtual photon momentum transfer Q^2.

To study the sensitivity of the extracted angular cross sections to the angular distribution in the event generator, correction factors were calculated with two different models: 1) a flat angular distribution as used in the final analysis and 2) a angular distribution with very strong P and D wave components. For this systematic study, the acceptances calculated with the two above models was based on the fiducial acceptance cut of section 4.3.3. The plots of this study can be found in the appendix in Figs. D.3 and D.4

For this study, the physics model in the event generator was as that presented in section 1.1.

$$\frac{d\sigma}{d\Omega_\eta^*} = \frac{|p_\eta^*|W}{m_p K}\left(A + Bcos\theta_\eta^* + Ccos^2\theta_\eta^* + Dsin\theta_\eta^* + Esin\theta_\eta^* cos\theta_\eta^* cos\phi_\eta^* + Fsin^2\theta_\eta^* cos2\phi_\eta^*\right). \quad (6.3)$$

The isotropic angular distribution is generated with $B = C = D = E = F = 0.0$ and the non-isotropic distribution with $A = 1.6, B = -0.5, C = -1.0, D = 0.0, E = 0.0, F = -0.5\ \mu b/ster$. These values were chosen as they were the extremes of what was could be fit to the data. Fig. 6.1 shows the angular distribution of the event generator run with strong P and D wave components.

6.1.5 Summary of Systematic Errors

A summary of the systematic errors arrived at in the studies presented in the previous sections is presented in Table 6.1. The systematics of luminosity and reconstruction are assumed to be scale errors. The systematic errors of η peak fitting and acceptance are kinematically dependent and the number summarized in Table 6.1 represents a weighted average over all bins, where the weighting factor is the statistical uncertainty in the data.

In each kinematic bin, the results of the systematic error studies are added in quadrature. These resulting total systematic errors are presented in Figures 6.2 and 6.3.

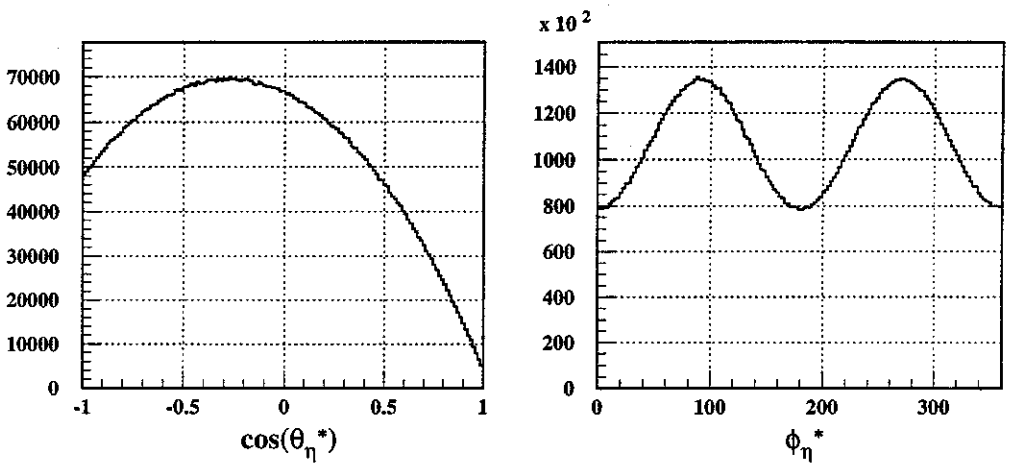

Figure 6.1: The η angular distribution used to study the systematic effects of the event generator.

In these plots, the error bar on each point does not represent the uncertainty in the systematic error, but rather represents the statistical error of the data. The statistical and systematic errors are plotted together in this way to ease comparison. The total systematic error is typically slightly smaller than the statistical error. There are strong kinematic trends in the systematic errors, particularly at the forward scattering angles of $cos(\theta_\eta^*) = 1$. The plots of the systematic errors from each of the effects listed in Table 6.1 are presented in Appendix D and show that this is a general trend. Since the relative weighting of the differential cross section is effected, this can have a significant impact on extracted partial wave parameters. It is important to determine and incorporate the systematic effect on a bin-by-bin basis (as opposed to a single scale systematic error).

6.2 Cross Sections and Multipole Fits

The final cross sections are given in Figures 6.4 and 6.5, tables of the data can be found in Appendix E. The fits are to the parameterized multipole expansion presented in section 1.1, which is reproduced here for reference. This multipole expansion is under the assumption that E_{0+} dominates. The uncertainties used in the fit for each point are the statistical errors added in quadrature with the systematic errors of the previous section. The systematic errors are accounted for point-by-point. The existence of nonzero multipole parameters $B-F$ may be indicative of baryon resonances other than the $\frac{1}{2}\frac{1}{2}^-(1535)$ decaying into ηN. There are a number of known (via the πN channel)

luminosity		$\approx 3\%$
reconstruction	$e^- id$	$\approx 2\%$
	p id	1.4%
	tracking	1.5%
η peak fitting	M_η	3.4%
	σ_η	5.4%
	α	3.4%
	τ	3.3%
	$D_{bkg}(M_X)$	6.8%
acceptance	fit function	2.3%
	η distribution	4.1%
total		11.8%

Table 6.1: Summary of systematic errors. The values in this table represented a weighted average of the systematic error at each point in W, Q^2, $cos(\theta^*_\eta)$, and ϕ^*_η. The weighting factor is the statistical error so that points that are better determined are weighted more. The total represents all of the systematic errors added in quadrature.

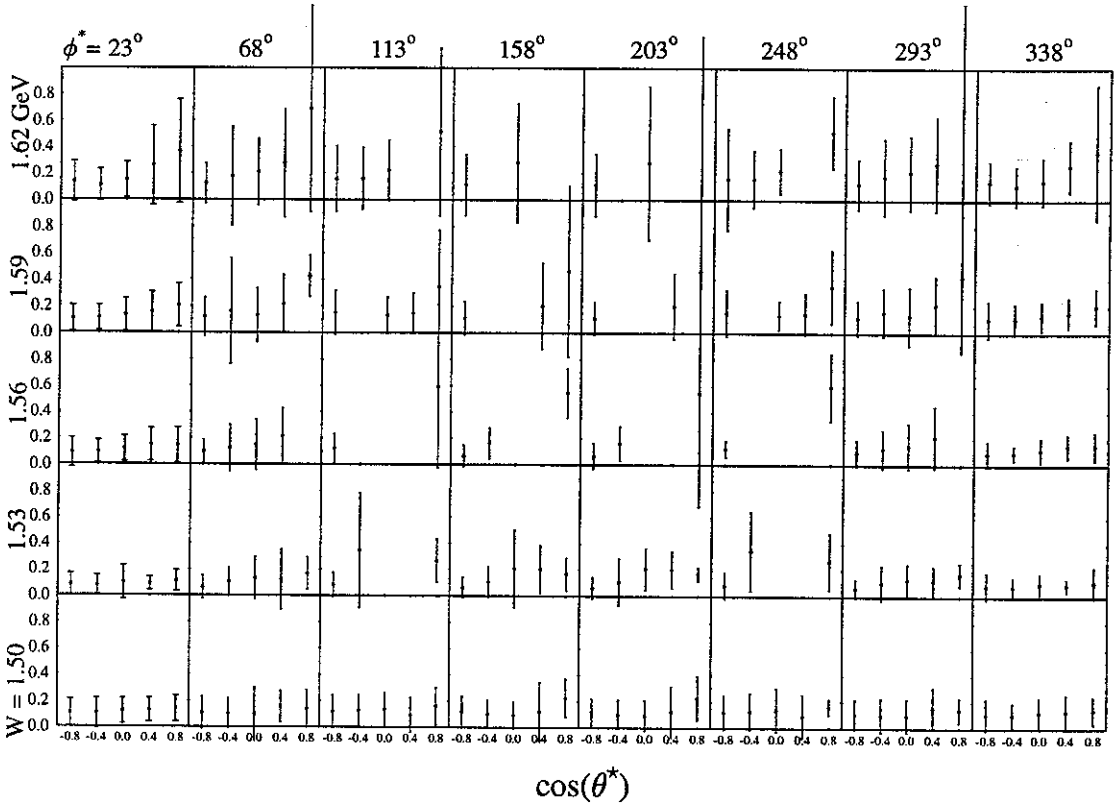

Figure 6.2: The systematic error for $Q^2 = 0.5 - 1.0\ GeV^2$.

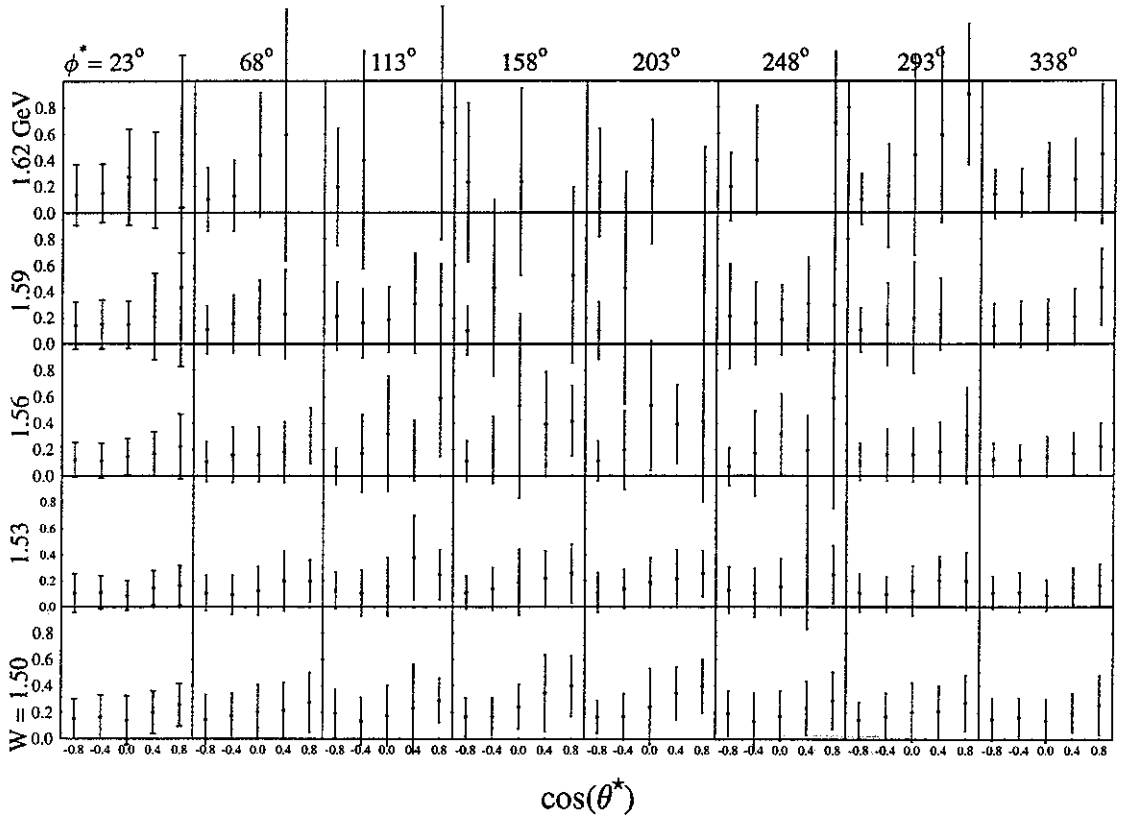

Figure 6.3: The systematic error for $Q^2 = 1.0 - 1.5\ GeV^2$.

baryon resonances in this W region that are relevant. The decay of any of these resonances into the ηN channel would be indicated by an enhancement in the corresponding multipole parameter. The $IJ^P\ \frac{1}{2}\frac{1}{2}^-(1650)$, which would decay in ηN channel via the E_{0+} multipole, has a $3-10\%$ branching fraction into ηN [12]. This and the $\frac{1}{2}\frac{1}{2}^-(1535)$ are the only resonances which have been observed to decay to ηN.

$$\begin{aligned}
\frac{d^2\sigma}{d\Omega_\eta^*} &= \frac{|p_\eta^*|W}{KM_p}\Big[A + B\cdot cos(\theta_\eta^*) + C\cdot cos^2(\theta_\eta^*) \qquad (6.4)\\
&\quad + D\cdot sin(\theta_\eta^*)\cdot cos(\phi_\eta^*) + E\cdot sin(\theta_\eta^*)\cdot cos(\theta_\eta^*)\ cos(\phi_\eta^*) + F\cdot sin^2(\theta_\eta^*)\cdot cos(2\phi_\eta^*)\Big]\\
A &= |E_{0+}|^2 + \epsilon\frac{Q^2}{|q_\eta^*|^2}|S_{0+}|^2 -\\
&\quad Re\left[E_{0+}^*\left(E_{2-} - 3M_{2-}\right)\right] - 4\epsilon\frac{Q^2}{|q_\eta^*|^2}\cdot Re\left[S_{0+}^* S_{2-}\right]\\
B &= -2Re\left[E_{0+}^* M_{1-}\right] + 2\epsilon\frac{Q^2}{|q_\eta^*|^2}\cdot Re\left[S_{0+}^* S_{1-}\right]
\end{aligned}$$

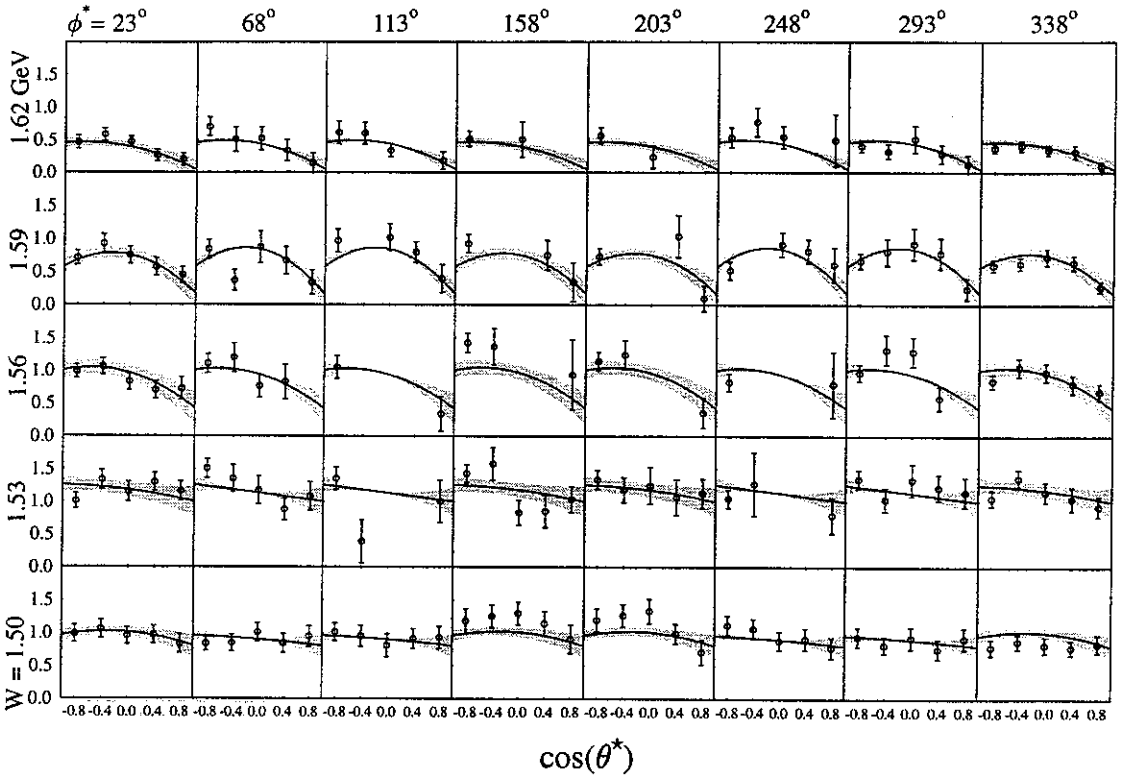

Figure 6.4: Cross section and parameterized multipole fit for $Q^2 = 0.5 - 1.0\ GeV^2$.

$$
\begin{aligned}
C &= 3Re\left[E_{0+}^{*}\left(E_{2-}-3M_{2-}\right)\right]+12\epsilon\frac{Q^2}{|q_\eta^*|^2}\cdot Re\left[S_{0+}^{*}S_{2-}\right] \\
D &= -\sqrt{2\epsilon(\epsilon+1)\frac{Q^2}{|q_\eta^*|^2}}\cdot Re\left[2E_{0+}^{*}S_{1-}+S_{0+}^{*}M_{1-}\right] \\
E &= -3\sqrt{2\epsilon(\epsilon+1)\frac{Q^2}{|q_\eta^*|^2}}\cdot Re\left[2E_{0+}^{*}S_{2-}+S_{0+}^{*}\left(M_{2-}-E_{2-}\right)\right] \\
F &= -3\epsilon\cdot Re\left[E_{0+}^{*}\left(E_{2-}+M_{2-}\right)\right]
\end{aligned}
$$

The parameters B and D represent interference of the strong E_{0+} with the M_{1-}. In the η channel, the M_{1-} multipole would be fed by an $IJ^P\ \frac{1}{2}\frac{1}{2}^+$ baryon resonance. Relevant $\frac{1}{2}\frac{1}{2}^+$ resonances that have been observed in the πN channel are the $\frac{1}{2}\frac{1}{2}^+(1440)$ and the $\frac{1}{2}\frac{1}{2}^+(1710)$. The $\frac{1}{2}\frac{1}{2}^+(1440)$ (named the Roper resonance) has a very broad $350MeV$ width while the $\frac{1}{2}\frac{1}{2}^+(1710)$ has a much narrower $100MeV$ width.

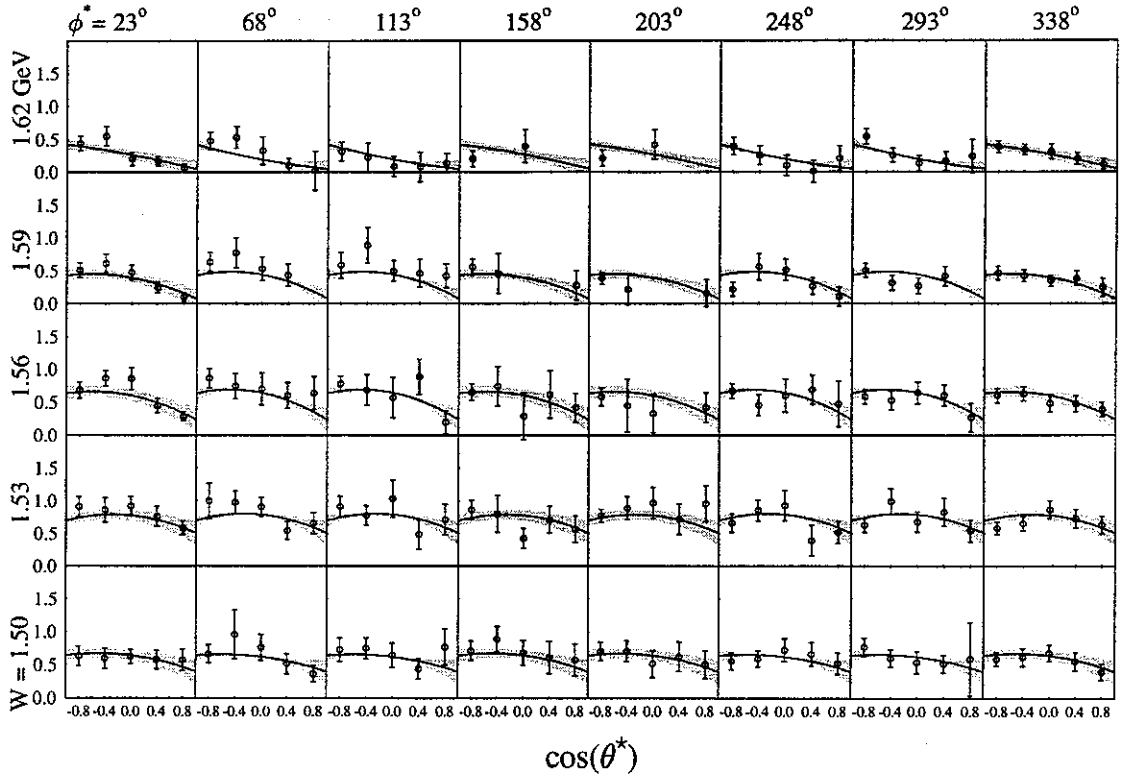

Figure 6.5: Cross section and parameterized multipole fit for $Q^2 = 1.0 - 1.5\ GeV^2$.

The parameters C, E, and F represent interference with E_{0+} and E_{2-} and M_{2-}, which correspond to $\frac{1}{2}\frac{3}{2}^-$ resonances, one of which, the $\frac{1}{2}\frac{3}{2}^-(1520)$ with a $120MeV$ width, is in the W region measured in this experiment.

Even if the $\frac{1}{2}\frac{1}{2}^+$ and $\frac{1}{2}\frac{3}{2}^-$ resonances mentioned above did not have large branching fractions into ηN, they could be observed due to the interference with the $\frac{1}{2}\frac{1}{2}^-(1535)$. As seen in equation 6.2, their (presumably small) multipole amplitudes are multiplied by the large E_{0+}. This "beating" of partial waves is a common technique used in hadron spectroscopy.

Figure 6.6 shows the extracted multipole parameters when all parameters are used in the fit. The first thing to note is that the dependence of A is consistent with a resonance close to threshold whose energy dependent width is so strong that there is no peak (see section 1.1). This is the signature of the $\frac{1}{2}\frac{1}{2}^-(1535)$. Decay of the $\frac{1}{2}\frac{1}{2}^-(1650)$ into ηN would be indicated by a rise in A at high W. However, if the branching fraction of $\frac{1}{2}\frac{1}{2}^-(1650)$ to ηN is not large, this would be masked by the strong decay of the $\frac{1}{2}\frac{1}{2}^-(1535)$.

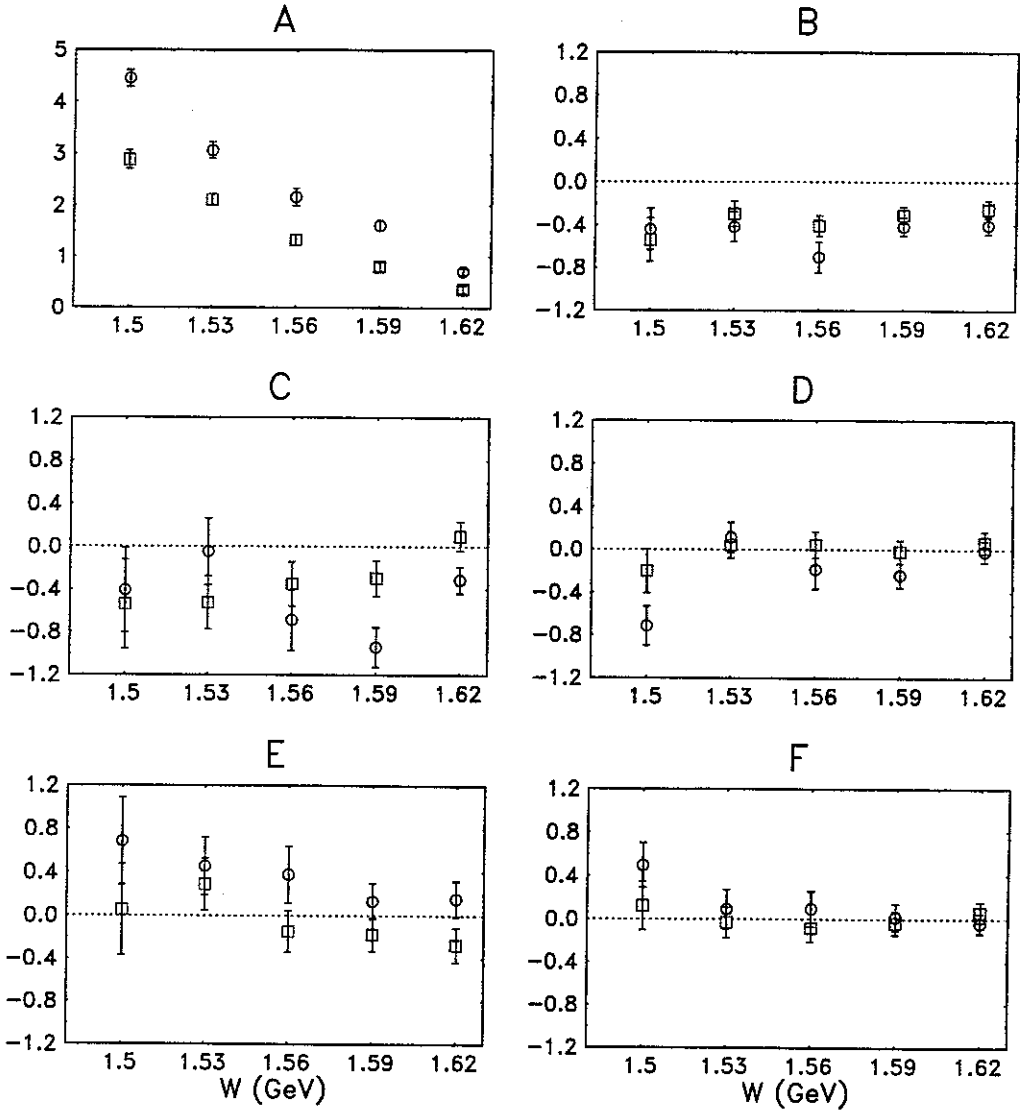

Figure 6.6: Extracted multipole parameters when all are used in the fit. The blue points are low $Q^2 = 0.5 - 1.0\ GeV^2$ and the red points are high $Q^2 = 1.0 - 1.5\ GeV^2$. The units are $\mu b/Ster$ for all parameters.

Due to the angular momentum barrier, one would expect the parameters $B - F$ to go to zero at threshold. At the $W = 1.5\ GeV$, point, there may be some indication that this is not the case, allthough the data is not conclusive. In studying the systematic errors, it was observed that this point was most sensitive, particularly at low Q^2. The multipole parameter B is definitely non-zero above the $p\eta$ threshold and there is an enhancement in both Q^2 around $1.560\ GeV$. C also is nonzero and shows an enhancement around $W = 1.590\ GeV$.

Under the assumption that the longitudinal amplitudes ($S_{l\pm}$) are small, the fit is also performed with $D = E = 0$. Brasse et. al. [6] measured the ratio of the

longitudinal to transverse cross sections and found it was approximately 20% for $Q^2 = 0.6$ and 1.0 GeV^2. However, the error bars on this data were typically $30 - 40\%$, overlapping with zero. The multipole parameters when the cross section data is fit with $D = E = 0$ are shown in Figure 6.7. The change in the remaining parameters is small (within error bars), and the features discussed above remain.

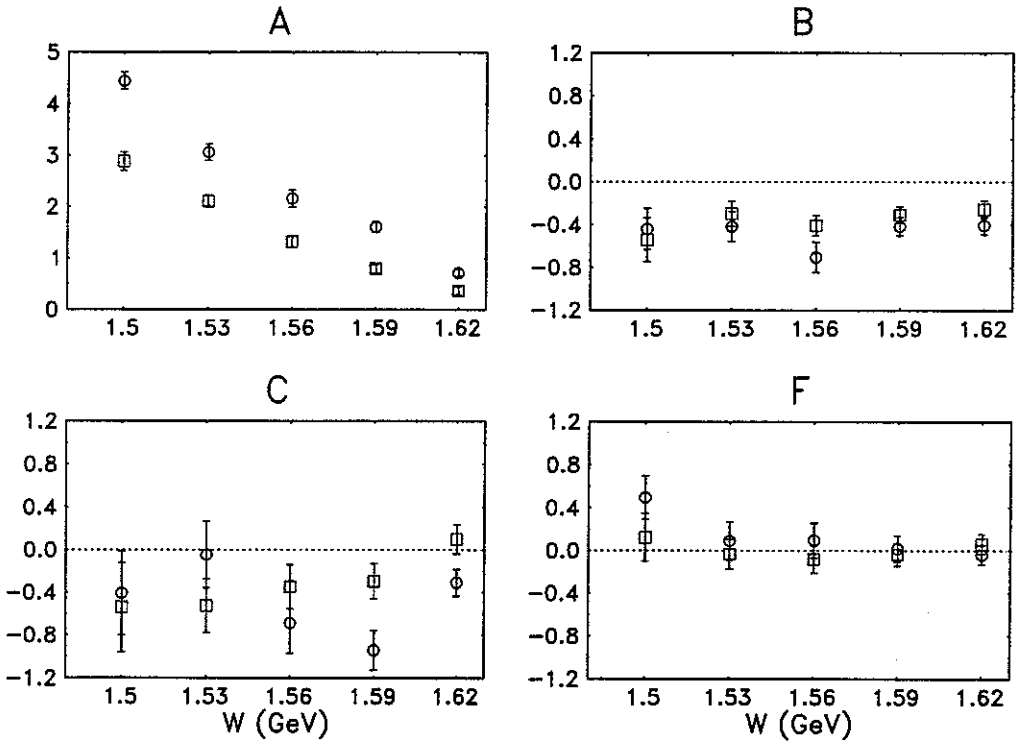

Figure 6.7: Extracted multipole fit parameters when A, B, C, and F are used.

There is strong evidence in the differential cross section presented in this thesis of processes other than decay of $\frac{1}{2}\frac{1}{2}^-(1535)$, particularly around 1.56 GeV. Interference between the $\frac{1}{2}\frac{1}{2}^-(1535)$ and other resonances is a likely source for this effect, even if those other states couple only weakly to ηN. Non-resonant contributions cannot be ruled out. There are several factors that limit further interpretation, by the techinques of this study, of the contribution of non-$\frac{1}{2}\frac{1}{2}^-(1535)$ processes to this data, primarily the lack of use of a coupled channels approach (with some representation of non-resonant contributions) that could be used to extract resonance parameters including the unitarity effects due to other channels.

6.2.1 Comparisons with Previous Results

In the previous η differential cross section measurements ([3] , [6], [7], [24]) parameterized multipole fits like the one presented here were done. Brasse et. al. [6], [7] fit their data to A and B, while Krusche [24] fit to A, B, and C. Figs. 6.8 - 6.10 show comparisons between the A, B, and C multipole parameters determined from those studies and the present work. For parameter A, the agreement is remarkably good. In Fig. 6.8 the data of the present work is overlaid on plots of different Q^2 for comparison purposes.

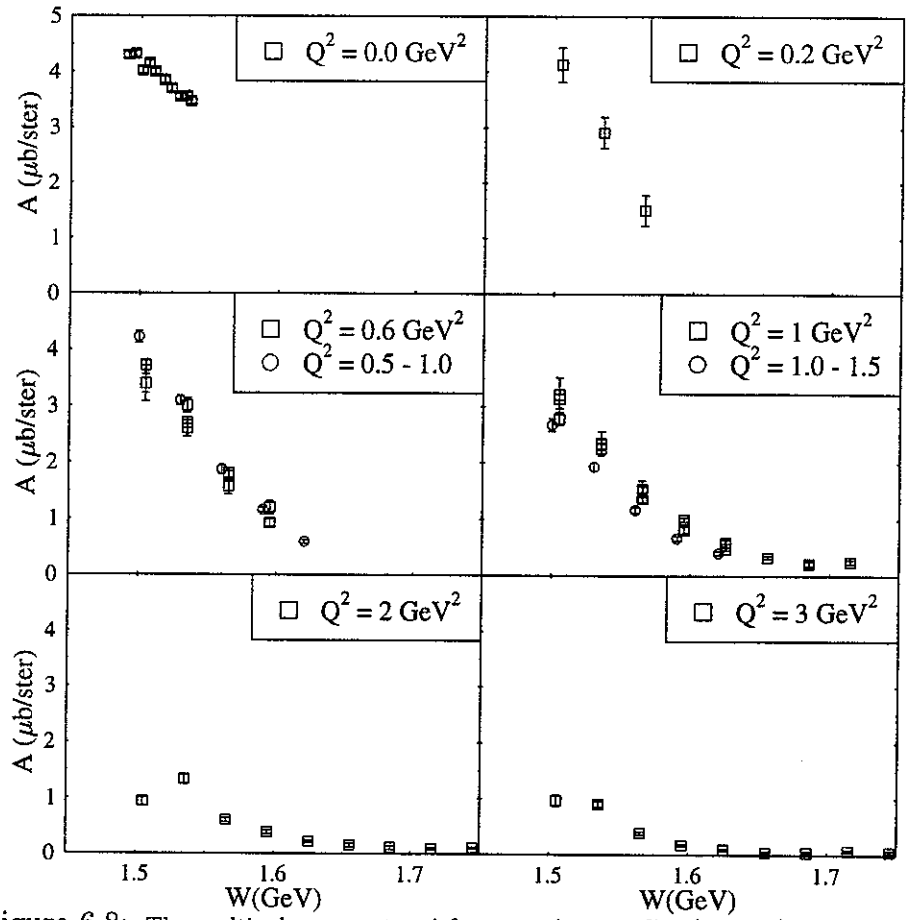

Figure 6.8: The multipole parameter A from previous studies (squares) compared with the results of this work (circles). The photoproduction data is from [24], while the previous electroproduction data is from [6] and [7]. The fit of Krusche et. al. was to multipole parameters A - C, while the fits of Brasse et. al. were to A and B only. In this plot, the fits of the present work were limited to A and B (even while the data allowed more than that) to allow a consistent comparison.

The present work results in a B multipole parameter that is well determined to be small and negative for $W < 1.620\ GeV$, where the previously published results on B were small and positive and that W range. There is no obvious interpretation of the sign of B, except under very special circumstances.

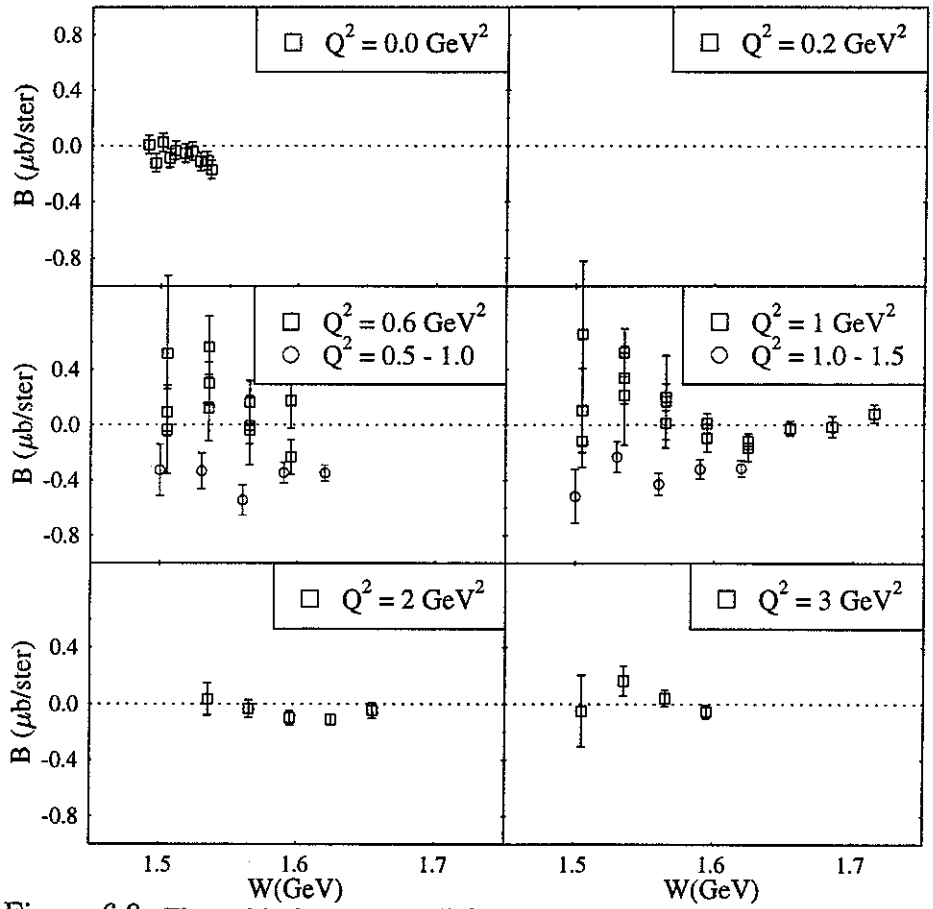

Figure 6.9: The multipole parameter B from previous studies compared with the results of this work.

The only published determination of C is from the analysis of photoproduction data in Krusche et. a. [24]. Their results, along with the results from the present work, are shown in Fig. 6.10.

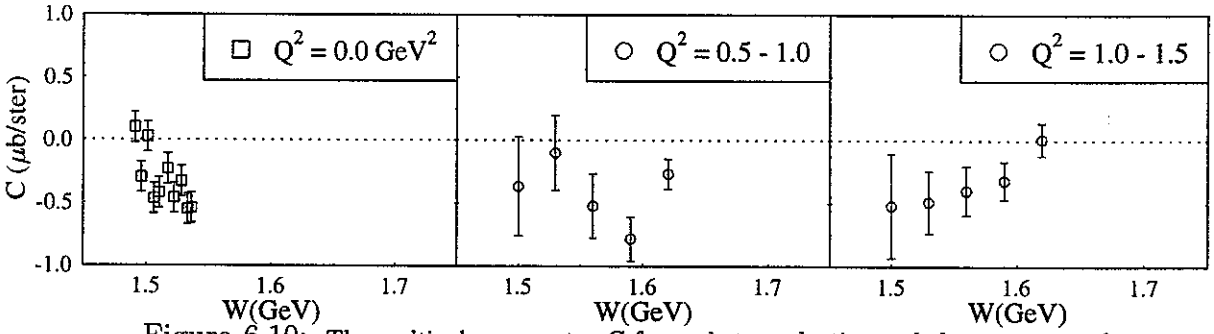

Figure 6.10: The multipole parameter C from photoproduction and the present work. The photoproduction data is from Krusche et. al. [24]. For the fit to the electroproduction data, the multipole parameters A - C were fit in order to be consistent with Krusche et. al.

6.2.2 $\frac{1}{2}\frac{1}{2}^{-}(1535)$ Resonance Parameters

Baryon resonance parameters may be extracted from the multipole parameter A under the assumption that it is dominated by E_{0+}: $A = |E_{0+}|^2$. At each value of Q^2, the A shown in Fig. 6.8 are fit to a relativistic Breit Wigner with an energy dependent width (see section 1.1).

$$E_{0+}(W) = \Phi \frac{W^*\Gamma^*}{W^{*2} - W^2 - iW^*\Gamma(W)}, \tag{6.5}$$

The parameters of the fit are the amplitude Φ, which is equal to $Im[E_{0+}(W^*)]$, the centroid of the resonance W^*, and its width $\Gamma^* = \Gamma(W^*)$. The fits to $|E_{0+}|^2$, and the real and imaginary parts of E_{0+} are shown in Fig. 6.11. The Q^2 dependence of the extracted resonance parameters is tabulated in Table 6.2 and is shown in Fig. 6.12. From these plots, it is apparent that the photoproduction point is in some sense anomalous. It yields a centroid and width that is inconsistent with the electroproduction data. This may in part be due to the fact that the photoproduction data of Krusche et. al. only extended 49 MeV above threshold. In a later study, Krusche, Mukhopadhyay, et. al. [25] included unpublished higher energy (up to 1.600 GeV) photoproduction data [34] and fit the total cross section to extract baryon resonance parameters. Their results were $W^* = 1544 \pm 9\ MeV$ and $\Gamma^* = 203 \pm 10\ MeV$. Since this is a fit to total cross sections, as opposed to partial wave decomposed amplitudes derived from differential cross sections as presented in this work, it implies the assumption that all amplitudes other that E_{0+} are *zero*. The results are then not directly comparable, but, with that in mind, the 203 MeV width is still significantly larger that the results from electroproduction presented in this thesis.

	$Q^2 = 0\ GeV^2$	0.6	$0.5 - 1.0$	
$W^*(MeV)$	$1559.4 \pm .75$	$1530.3 \pm .98$	1529 ± 1.9	
$\Gamma^*(MeV)$	239 ± 1.9	127 ± 5.7	140 ± 10	
$\Phi(GeV^{-1}$	$86.5 \pm .19$	$87.2 \pm .61$	91 ± 1.5	
χ^2	2.1	1.7	3.23	
	Q^2= 1.0	$1.0 - 1.5$	2.0	3.0
$W^*(MeV)$	1533 ± 1.3	1526 ± 2.5	1539 ± 1.6	1527 ± 2.2
$\Gamma^*(MeV)$	124 ± 4.9	118 ± 7.8	110 ± 1.1	72 ± 5.4
$\Phi(GeV^{-1}$	79 ± 1.0	76 ± 1.2	$55.2 \pm .91$	51 ± 1.9
χ^2	2.04	0.84	4.3	1.4

Table 6.2: Extracted baryon resonance parameters. The data from which the numbers were extracted are from: $Q^2 = 0$ Krusche et. al. [24], Q^2= 0.6, 1.0, 2.0, and 3.0 Brasse et. al. [6], [7], $Q^2 = 0.5 - 1.0$ and $Q^2 = 1.0 - 1.5$ this work.

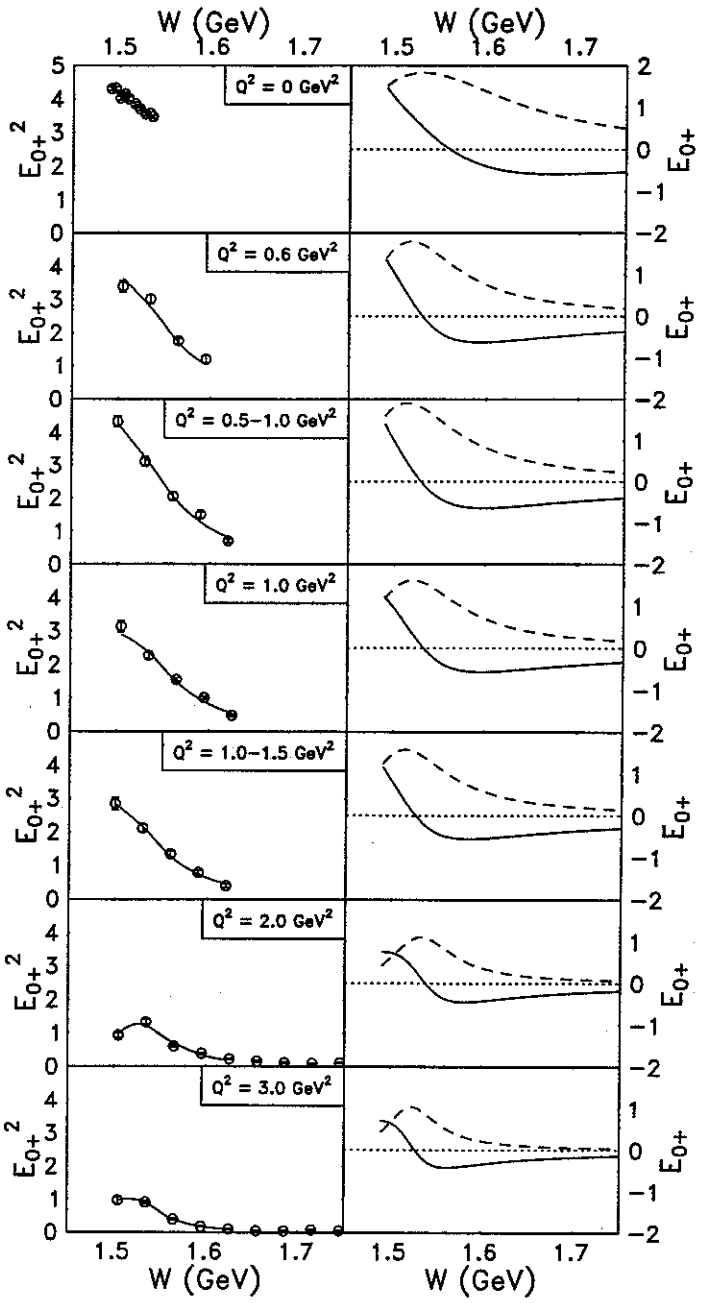

Figure 6.11: Fits to $|E_{0+}|^2$. The right column of plots shows the real (solid line) and imaginary (dashed line) parts of the amplitude as determined by the fit. The units of E_{0+} are $(\mu b/Ster)^{1/2}$. The data presented in this thesis is $Q^2 = 0.5 - 1.0$ and $1.0 - 1.5$.

As Fig. 6.12 illustrates, the electroproduction data yields a well determined and consistent value of the centroid W^*, which is here quoted as $1529 \pm 2\ MeV$. The width, on the other hand, indicates a strong dependence on Q^2. The width of a resonance is associated with the lifetime of the excited state and Q^2 is associated with the scale at which the state is probed. A qqq excited state should have no Q^2 dependence to its width.

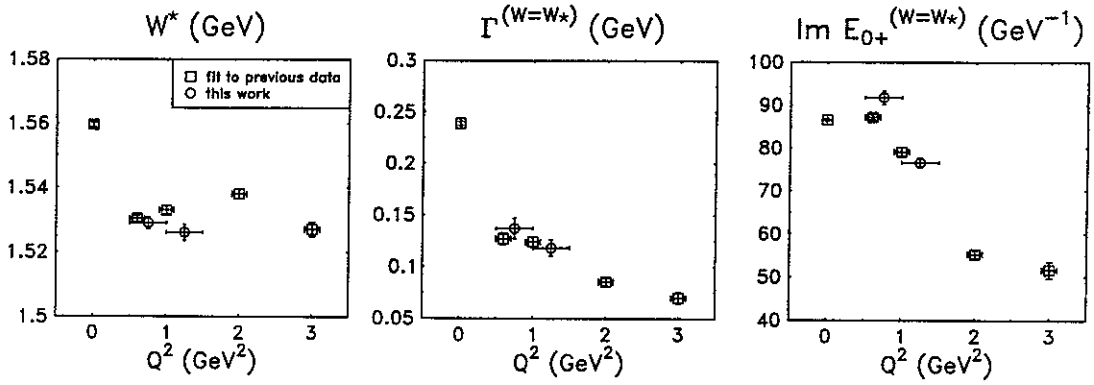

Figure 6.12: $\frac{1}{2}\frac{1}{2}^-(1535)$ baryon resonance parameters.

There may, however, be other contributions to η electroproduction in the region of the $\frac{1}{2}\frac{1}{2}^-(1535)$ other than qqq, like the $\Sigma - K$ hypothesis of Kaiser et. al. [20], or non-resonant processes. Also, coupled channel effects may influence the determination of the width as presented in this thesis. There are a number of states that decay strongly to πN in the region of the $\frac{1}{2}\frac{1}{2}^-(1535)$: $\frac{1}{2}\frac{1}{2}^+(1440)$, $\frac{1}{2}\frac{3}{2}^-(1520)$, and $\frac{1}{2}\frac{1}{2}^-(1650)$. As the cross section in πN channel changes with W due to these other resonances, the cross section in ηN must change also in order to preserve probability (unitarity). If the relative strength of these processes changes with Q^2, a dependence of the $\frac{1}{2}\frac{1}{2}^-(1535)$ width as observed in the ηN channel may be introduced. The recent JLab Hall C measurement by Armstrong et. al. [3] at $Q^2 = 2.4$ and $3.6\ GeV^2$ yielded an $\frac{1}{2}\frac{1}{2}^-(1535)$ width of $154 \pm 20\ MeV$. That analysis, like that of Krusche et. al., was a fit to the η electroproduction total cross section assuming that it was all due to $\frac{1}{2}\frac{1}{2}^-(1535)$. At Q^2 of 2.4 and 3.6 GeV^2 where the Hall C measurements were performed, this may a reasonable assumption. The total cross section goes as $A + \frac{C}{2}$ and the likely source of E_{2-} in this region of W is the $\frac{1}{2}\frac{3}{2}^-(1520)$ resonance. Brasse et. al. [7] inferred the Q^2 dependence of the excitation cross section $\sigma(\gamma_v p \rightarrow N^*)$ for the $\frac{1}{2}\frac{3}{2}^-(1520)$ relative to the $\frac{1}{2}\frac{1}{2}^-(1535)$ from inclusive electroproduction data. Their results indicate that by $Q^2 = 2.4\ GeV^2$, the ratio of $\sigma(\gamma_v p \rightarrow \frac{1}{2}\frac{3}{2}^-(1520))$ to $\sigma(\gamma_v p \rightarrow \frac{1}{2}\frac{1}{2}^-(1535)$ is about 30%. Even if the branching fraction at $W = 1520\ MeV$ of $\frac{1}{2}\frac{3}{2}^-(1520)$ to ηN were as large as 3%, this would be a less than one percent contribution to η electroproduction at $Q^2 = 2.4\ GeV^2$.[1] If, as is argued above, the Hall C determination of the $\frac{1}{2}\frac{1}{2}^-(1535)$ width was not contaminated by higher partial waves, there is significant discrepancy between the data of Brasse et. al. [7] and Armstrong et. al. If that is the case, the Q^2 dependence to the width as shown

[1]Note that the same reasoning leads to a ten percent contribution from $\frac{1}{2}\frac{3}{2}^-(1520)$ to ηp at a Q^2 of $0.5 GeV^2$.

in Fig. 6.12 is no longer present. New high statistics η electroproduction data from Hall B at a beam energy of 4 GeV will have Q^2 coverage out to 3 GeV^2, and will help to resolve this issue.

A resolution of the issue of the $\frac{1}{2}\frac{1}{2}^-(1535)$ width will come with a confirmation of both the photoproduction and high Q^2 measurements. For the sake of continuing this analysis it is assumed that there is no Q^2 dependence to the width. Then it is appropriate to interpret the E_{0+} amplitude in this W region as being due to the excitation of a bound state baryon and the resonance excitation amplitude $A^p_{1/2}(Q^2)$, introduced in section 1.1, may be calculated from

$$A_{1/2}(Q^2) = \sqrt{\frac{2\pi|p^\star_\eta|W^{\star 2}\Gamma^\star}{M_p^2 K b_\eta}} \cdot Im\left[E_{0+}(W = W^*, Q^2)\right] \tag{6.6}$$

where $|p^\star_\eta|$ is the η meson momentum in the laboratory from when $W = W^*$. The branching fraction of the $\frac{1}{2}\frac{1}{2}^-(1535)$ into ηN is taken to be $b_\eta = 0.55$, the $\frac{1}{2}\frac{1}{2}^-(1535)$ mass to be $W^* = 1529 MeV$, and the $\frac{1}{2}\frac{1}{2}^-(1535)$ width at W^* to be $\Gamma^* = 125\ MeV$. $A^p_{1/2}(Q^2)$ determined in this way is plotted in Fig. 6.13.

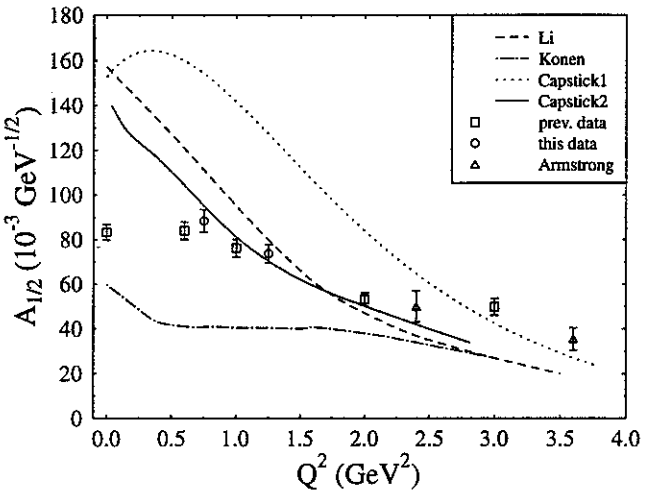

Figure 6.13: The $\frac{1}{2}\frac{1}{2}^-(1535)$ excitation amplitude versus Q^2. The data for the points labelled "prev. data" are from the previous electroproduction differential cross sections of [24], [6], and [7], and is analyzed in a self-consistent way with the data of this work. Error bars on "this data" include systematic uncertainties, while those for "prev. data" are statistical only. The Armstrong [3] results are not part of this self-consistent analysis, but are shown for reference. The theoretical curves are from CQM calculations of [10], [23] and [13], .

6.3 Summary

This thesis has presented the results of an η electroproduction experiment in the region of the $\frac{1}{2}\frac{1}{2}^{-}(1535)$ baryon resonance. Differential cross sections from this and previous experiments were fit in a self-consistent manner to a parameterized multipole expansion. The multipole parameter associated with the $\frac{1}{2}\frac{1}{2}^{-}(1535)$ (under certain assumptions) was fit to a relativistic Breit Wigner resonance form and baryon resonance parameters were extracted. These assumptions are:

- The E_{0+}multipole dominates η electroproduction in this region of W and all term in the multipole expansion that do not contain it can be dropped.
- The longitudinal multipole amplitude S_{0+} is very small or zero.

The mass and width of the $\frac{1}{2}\frac{1}{2}^{-}(1535)$ resonance were extracted. The mass is well determined at $1529 \pm 2\ MeV$, but there is some evidence for a Q^2 dependence to the width, although the high Q^2 measurements of other experiments is inconclusive. However, by further assuming that:

- The E_{0+} amplitude is due entirely to resonant $\frac{1}{2}\frac{1}{2}^{-}(1535)$ excitation.

the excitation amplitude $A^p_{1/2}(Q^2)$ is extracted. Theoretical calculations of this amplitude to not reproduce the relatively flat character.

Appendices

Appendix A

Particle Identification Diagnostics

In this section a set of particle identification diagnostics is presented and discussed. These diagnostics illustrate some of the electron identifications cuts discussed in section 4.3.2, as well as the quality of the calibrations and identification techniques used for charged hadrons. In each set of plots, there is one plot each for all particles, electrons, pions, and protons.

The relationship between the energy deposited in the inner layer and the outer layer of the EC , E_{outer} vs E_{inner} as shown in Fig. A.1, illustrate the good separation between π^- and electrons. Pions and electrons deposit energy in the calorimeter via different mechanisms. As discussed in section 4.3.2, pions of the energies in this experiment interact in the calorimeter primarily via minimum ionization, whereas electrons deposit energy primarily via showering. The good separation between pions and electrons is demonstrated by the lack of mixing between the nature of energy deposition illustrated in Fig. A.1.

The correlation between momentum measured by the drift chambers and total energy measured by the calorimeter (Fig. A.2) illustrate the good separation between electrons and pions as well as between pions and protons. Electrons should of course show up as a line of $E = p$, whereas pions punch through the calorimeter at a low energy due to the fact that they are interacting via ionization instead of showering.

Fig. A.3 shows the relationship between momentum measured by the drift chambers and the time of flight from the TOF detector. Since electrons of the energies in this experiment are relativistic, the time of flight should be constant and independent of momentum. Pions, on the other hand, become relativistic between a momentum of $0.3Gev/c$ where $\beta = 0.91$ and a momentum of $0.5GeV/c$ where $\beta = 0.96$. Pions should then deviate from constant time of flight around $0.4GeV/c$. Protons remain non-relativistic up to a momentum of $2.5Gev/c$, where $\beta = 0.94$. Electrons, pions and protons will then have distinctive signatures in a plot of momentum versus time of flight, as can be seen in Fig. A.3.

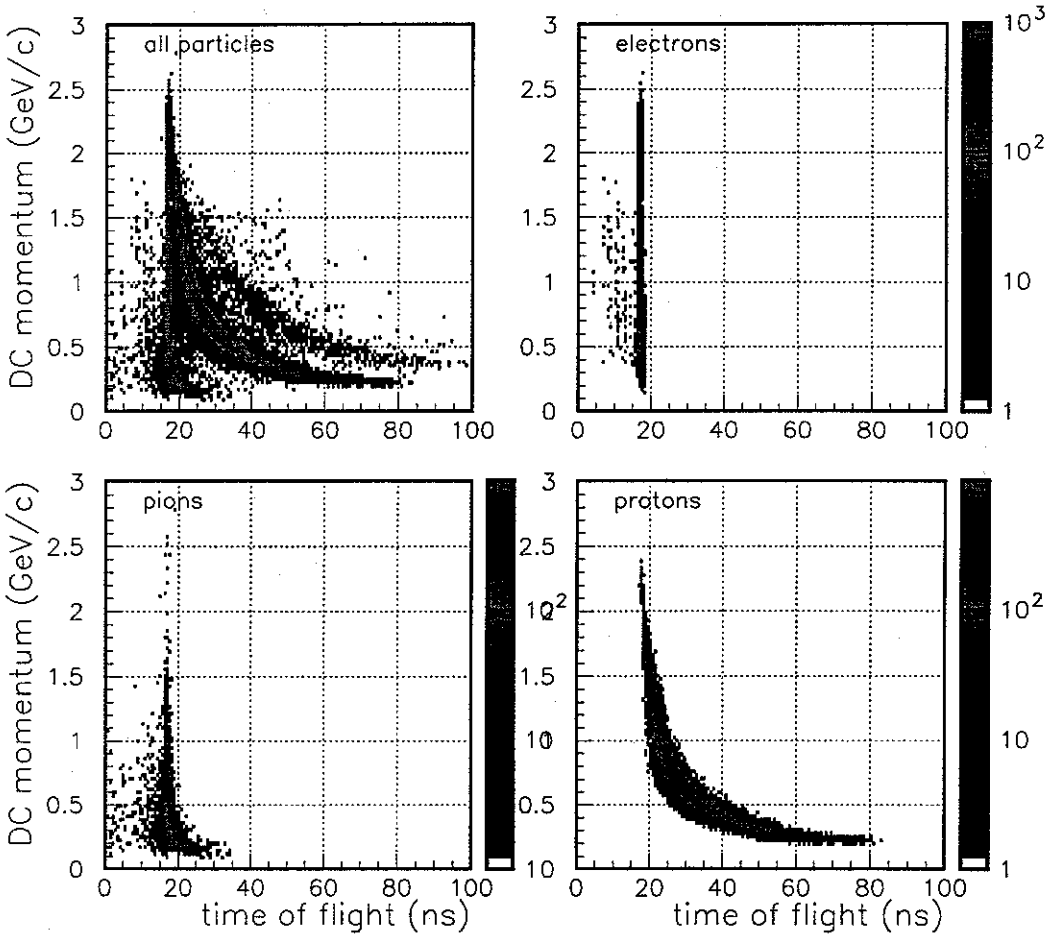

Figure A.3: Momentum versus a time of flight as a particle idendification diagnostic. The distinctive character of this correlation for electrons pions and protons indicates good experimental separation. In the plot for all particles can be seen bands for pions, protons and deuterons.

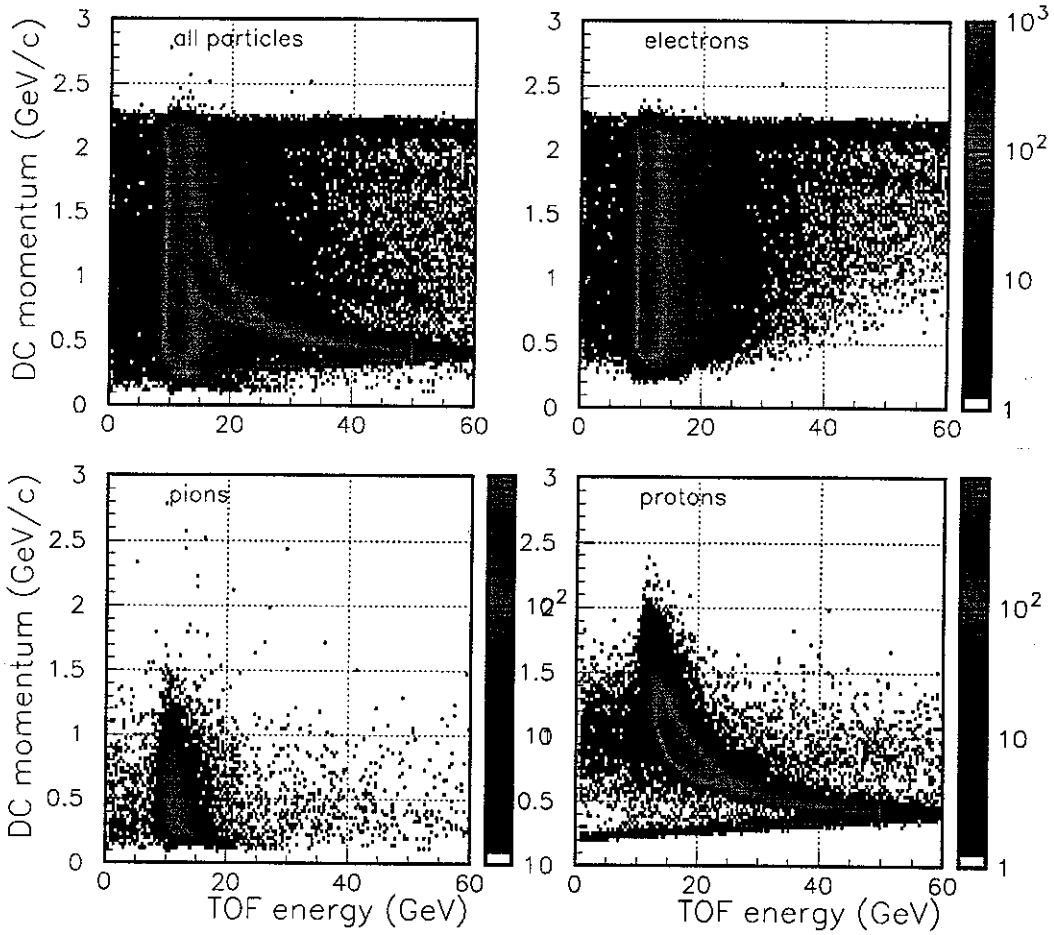
all particles
electrons
pions
protons
DC momentum (GeV/c)
TOF energy (GeV)
0
0.5
1
1.5
2
2.5
3
20
40
60
10
10^2
10^3

Figure A.4:

Appendix B

ep Missing Mass Angular Distribution Fits to Data

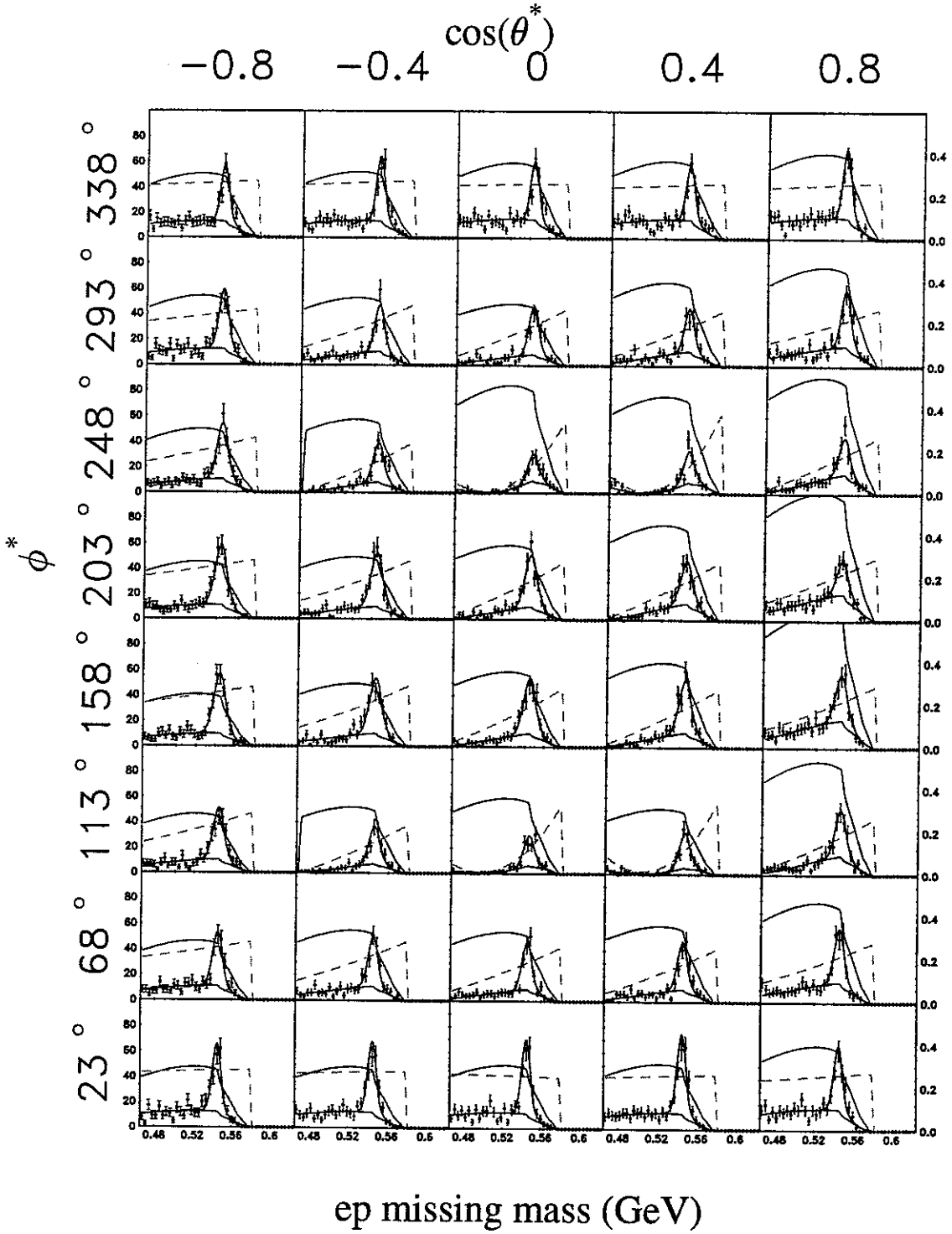

Figure B.1: Angular distrubution ep missing mass data fit for $W = 1.50GeV$ and $Q^2 = 0.75GeV^2$.

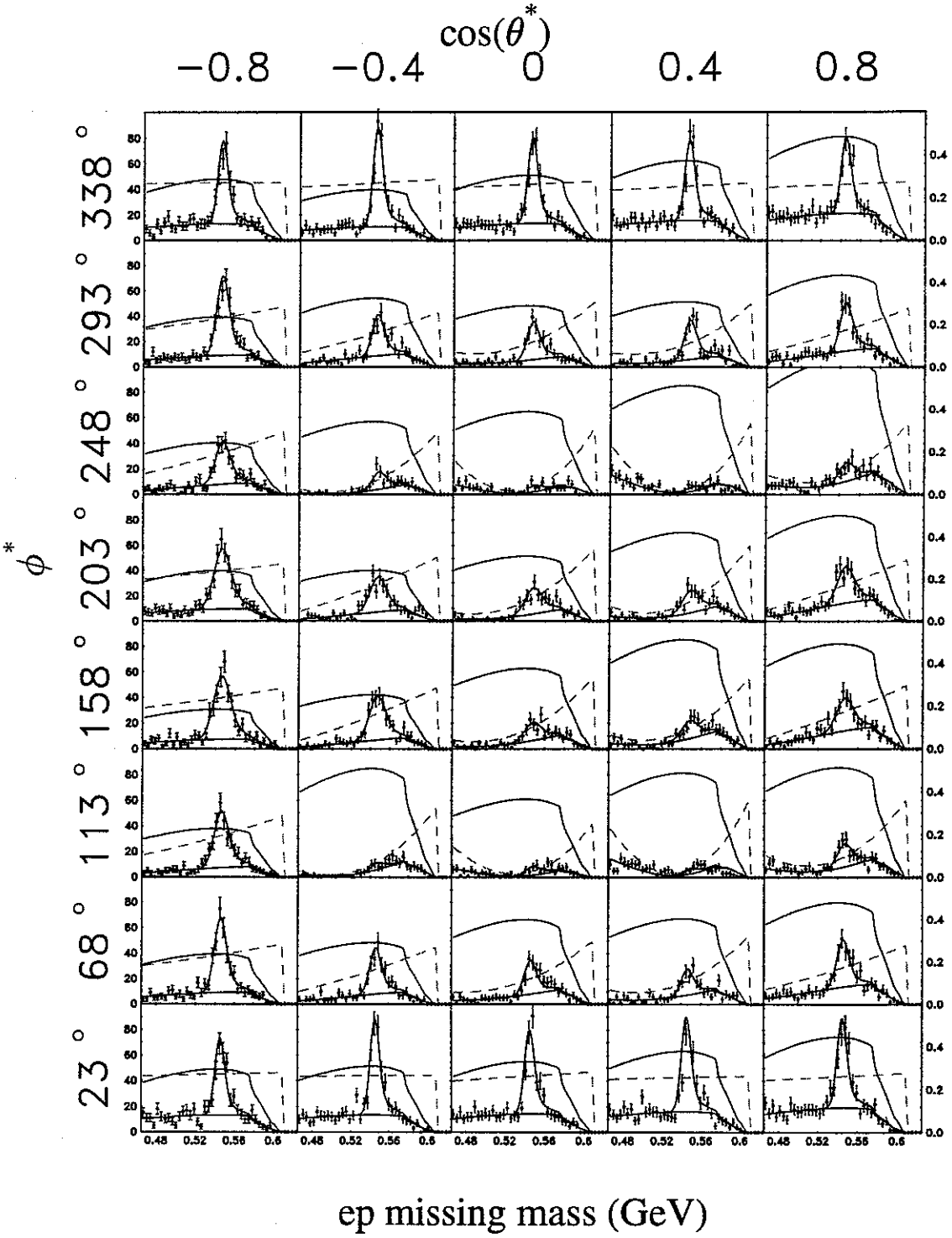

Figure B.2: Angular distrubution ep missing mass data fit for $W = 1.53GeV$ and $Q^2 = 0.75GeV^2$.

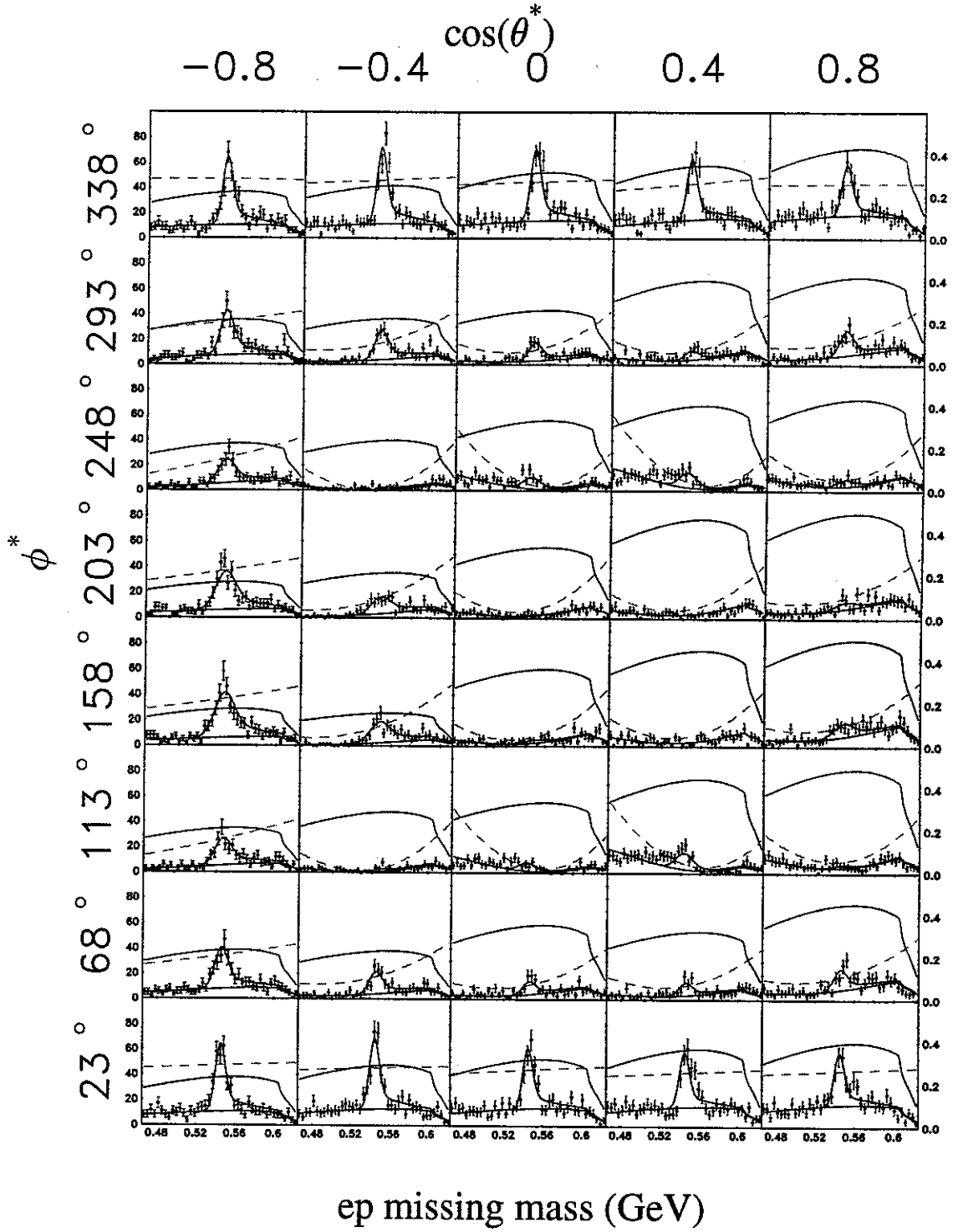

Figure B.3: Angular distrubution ep missing mass data fit for $W = 1.56GeV$ and $Q^2 = 0.75GeV^2$.

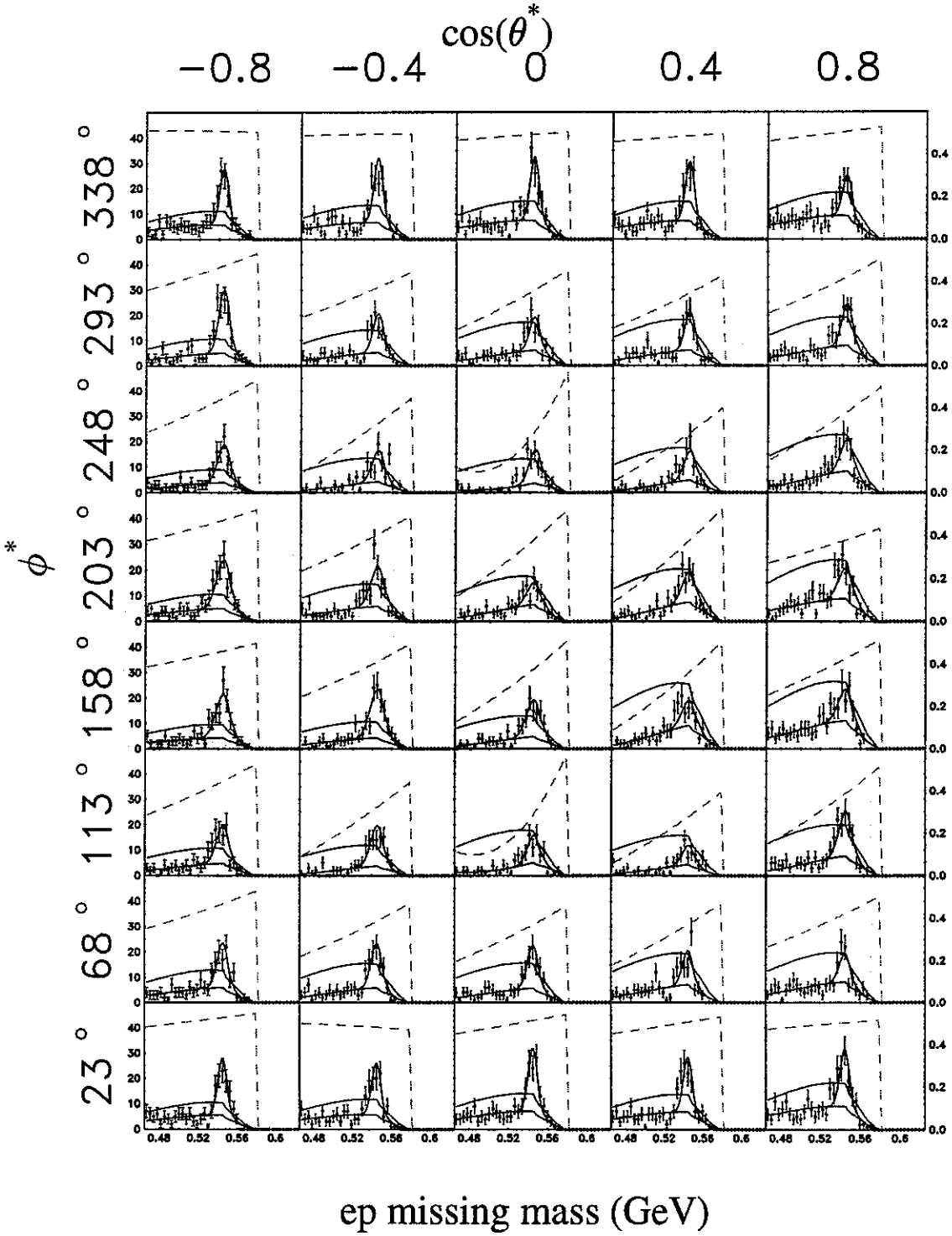

Figure B.6: Angular distrubution ep missing mass data fit for $W = 1.50GeV$ and $Q^2 = 1.25GeV^2$.

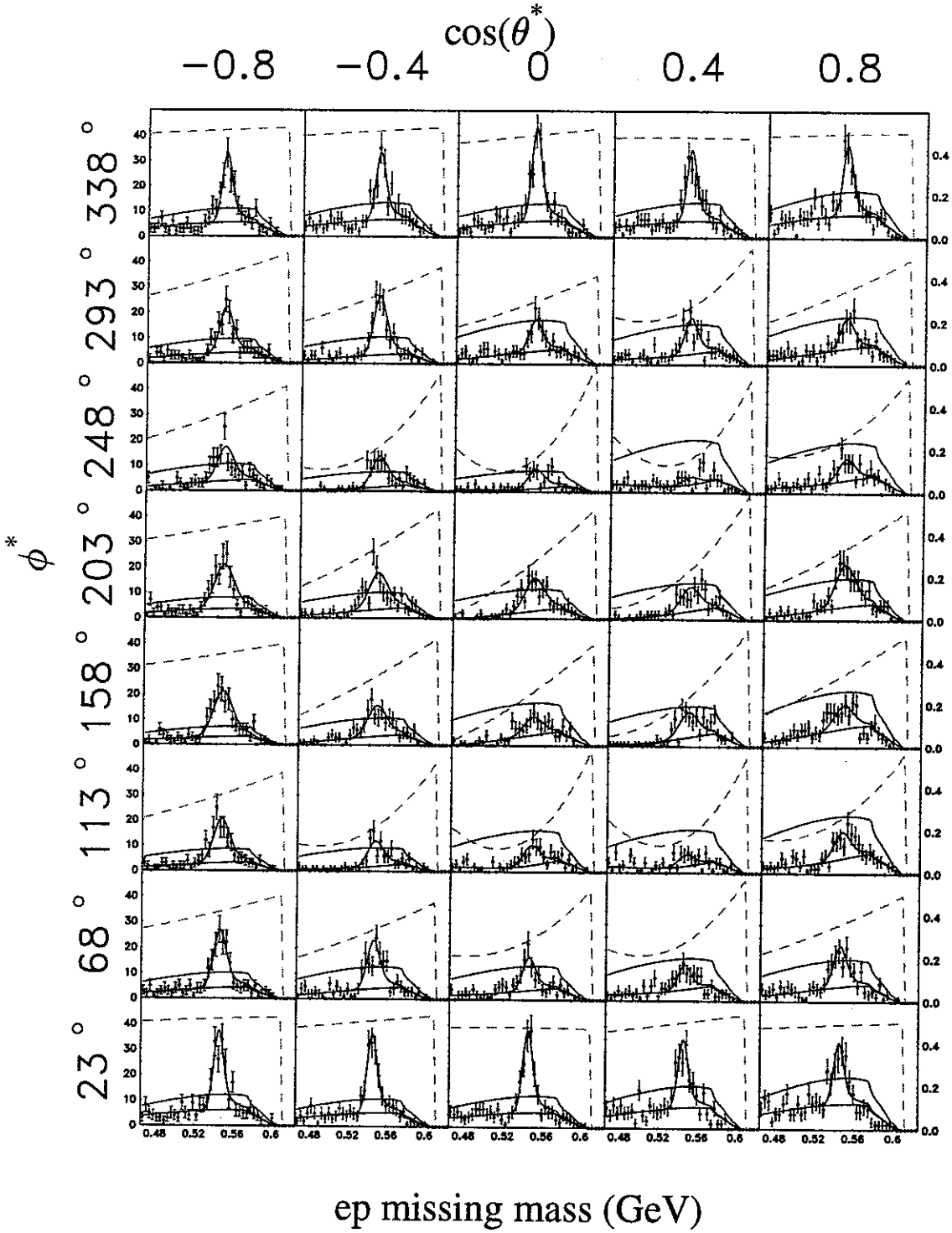

Figure B.7: Angular distrubution ep missing mass data fit for $W = 1.53GeV$ and $Q^2 = 1.25GeV^2$.

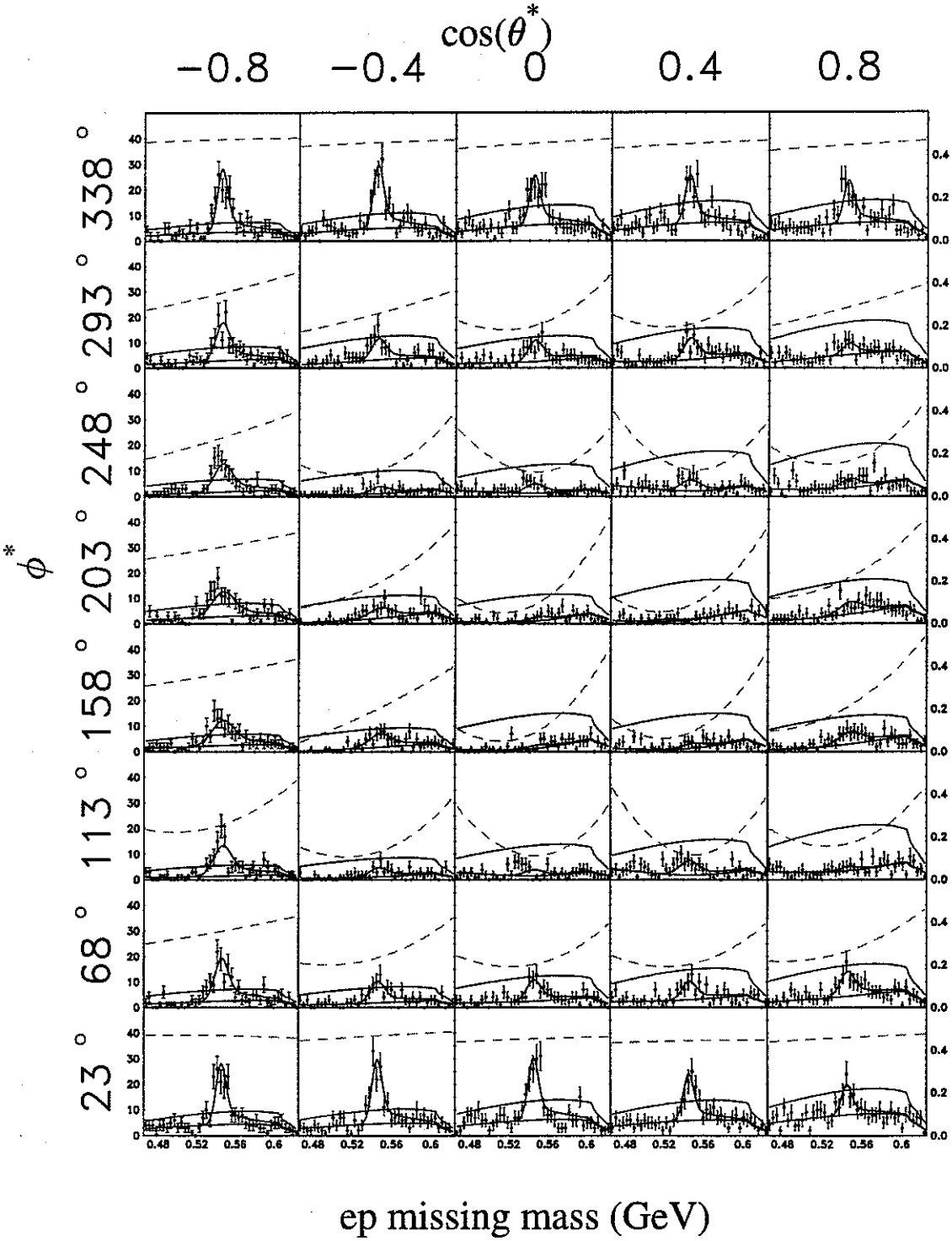

Figure B.8: Angular distrubution ep missing mass data fit for $W = 1.56GeV$ and $Q^2 = 1.25GeV^2$.

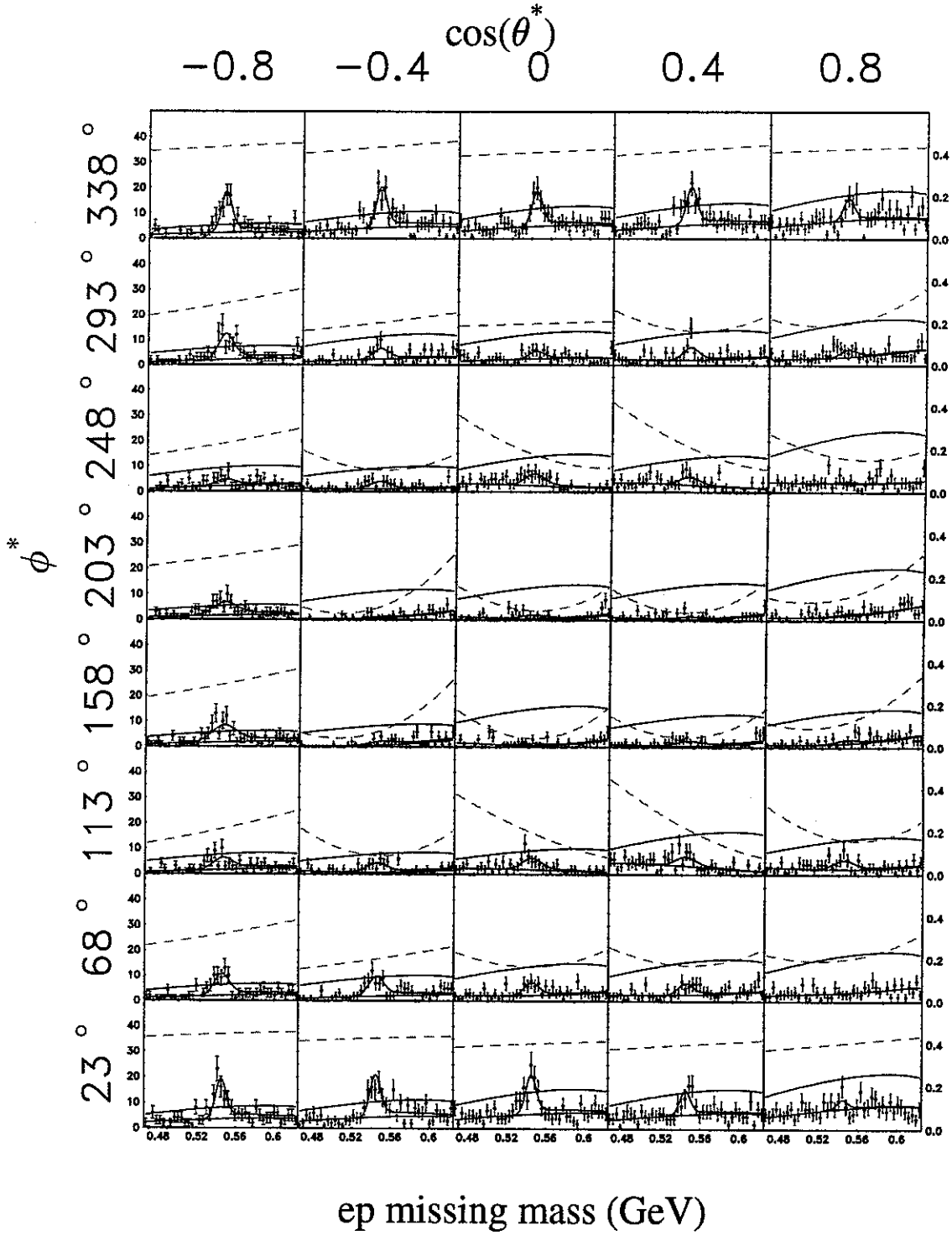

Figure B.9: Angular distrubution ep missing mass data fit for $W = 1.59GeV$ and $Q^2 = 1.25GeV^2$.

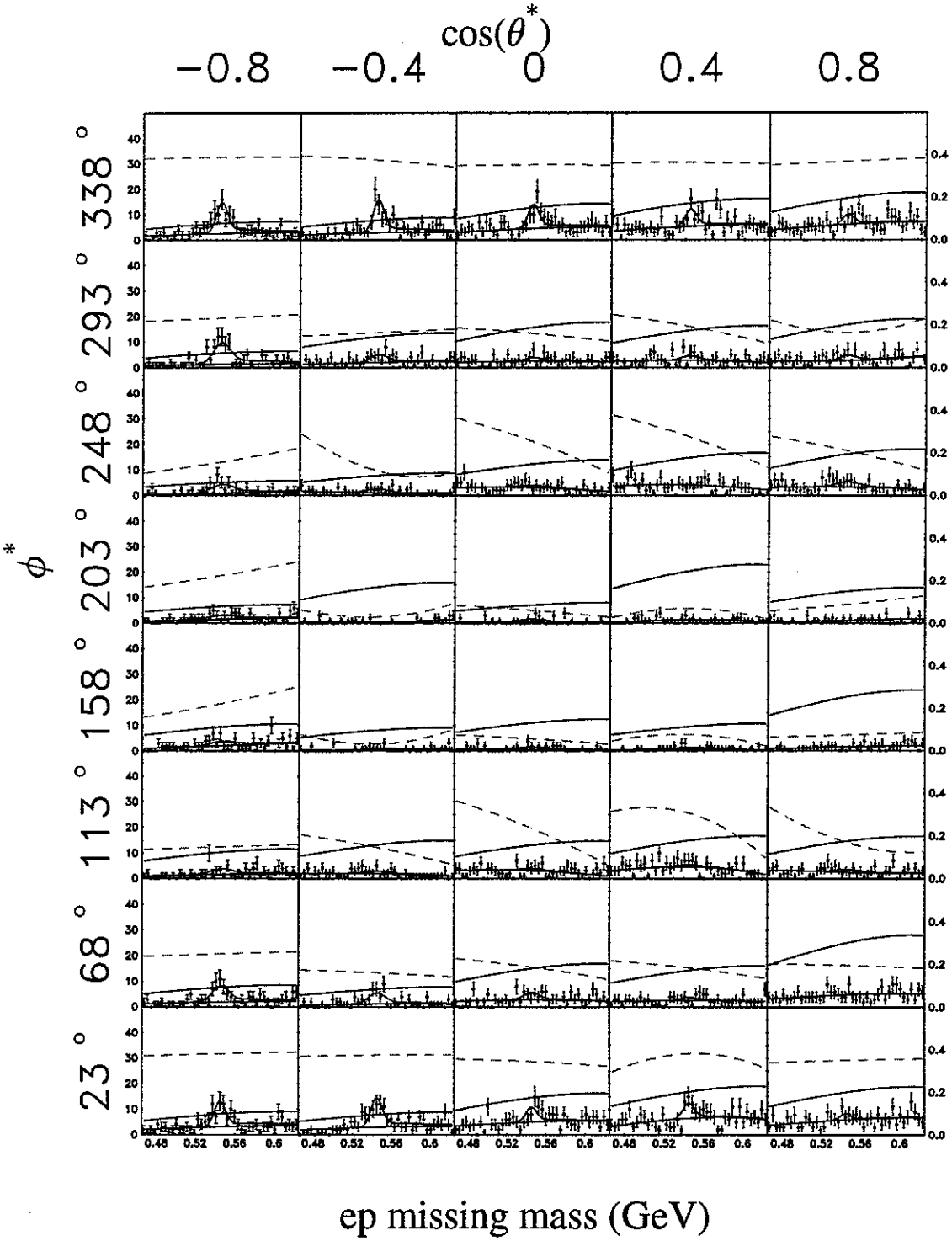

Figure B.10: Angular distrubution ep missing mass data fit for $W = 1.62GeV$ and $Q^2 = 1.25GeV^2$.

Appendix C

ep Missing Mass Angular Distribution Fits to Simulation

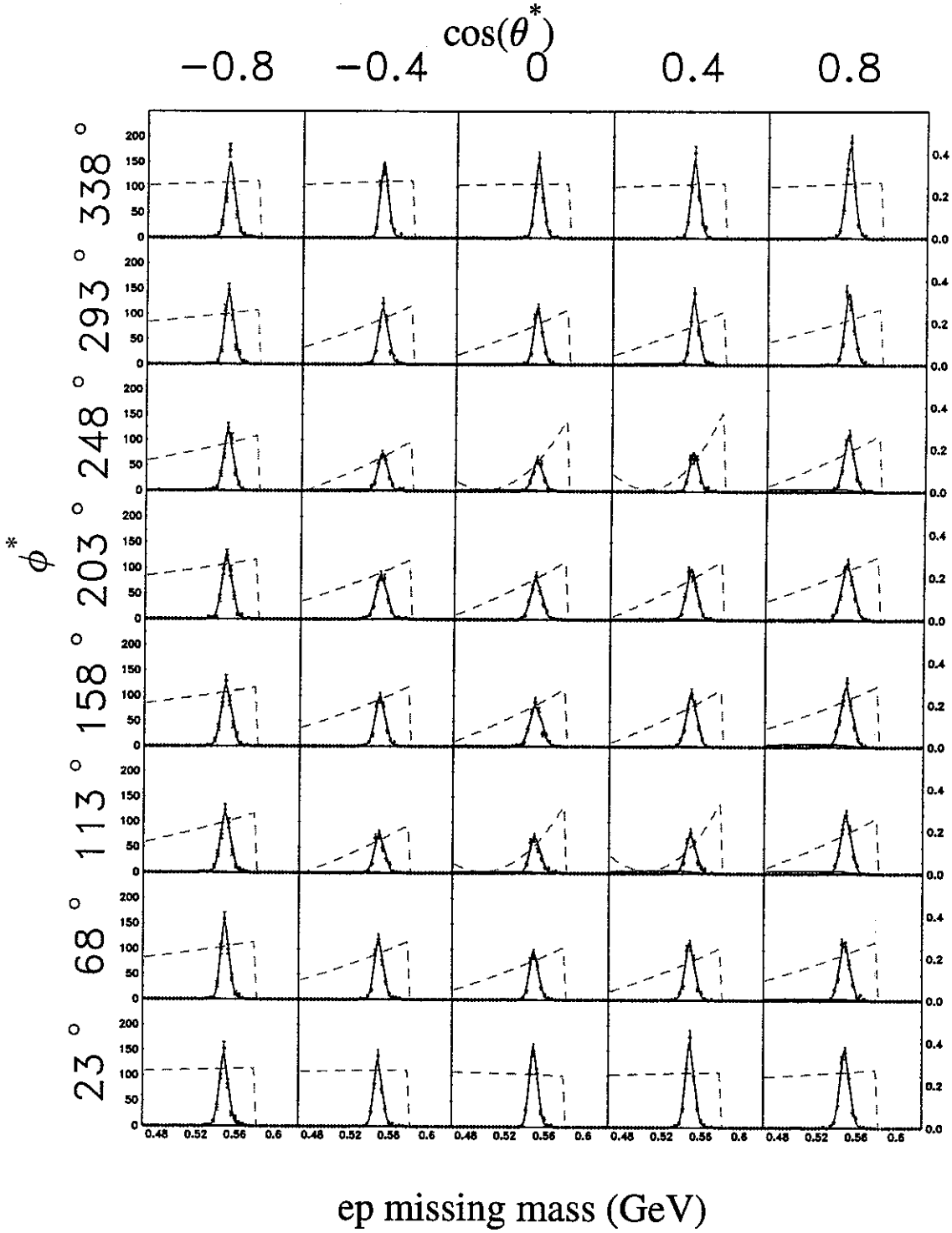

Figure C.1: Angular distrubution ep missing mass simulation fit for $W = 1.50GeV$ and $Q^2 = 0.75GeV^2$.

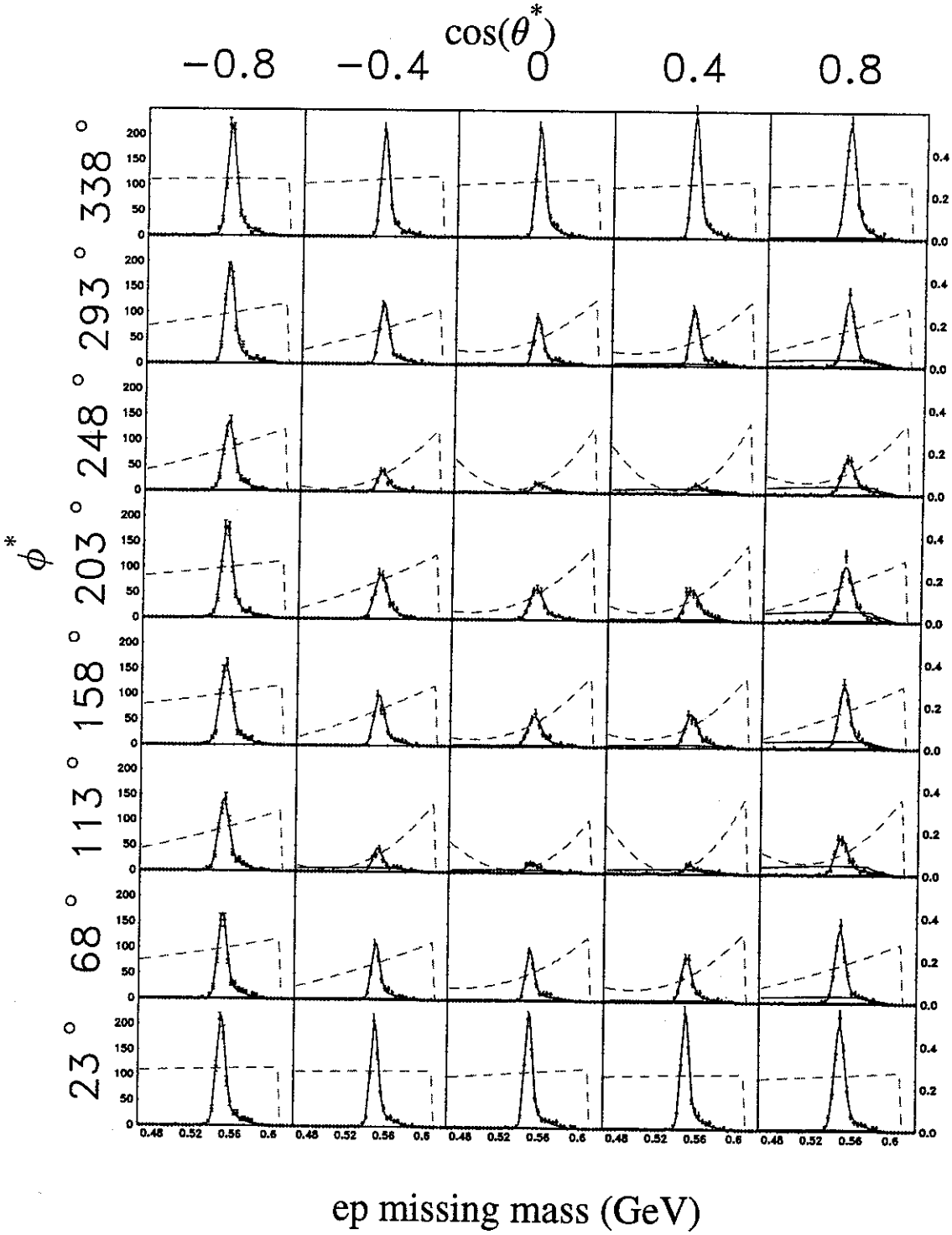

Figure C.2: Angular distrubution ep missing mass simulation fit for $W = 1.53GeV$ and $Q^2 = 0.75GeV^2$.

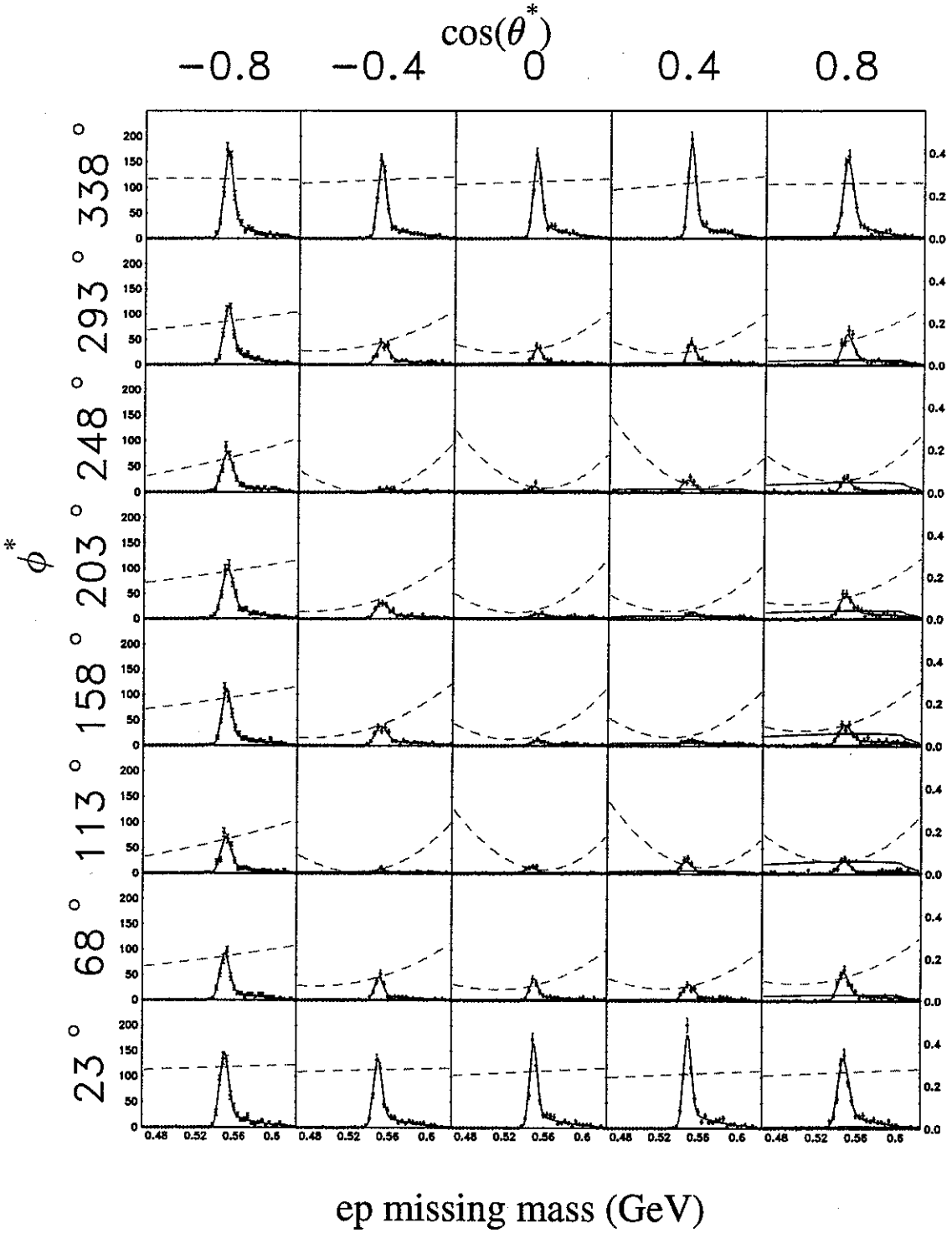

Figure C.3: Angular distrubution ep missing mass simulation fit for $W = 1.56GeV$ and $Q^2 = 0.75GeV^2$.

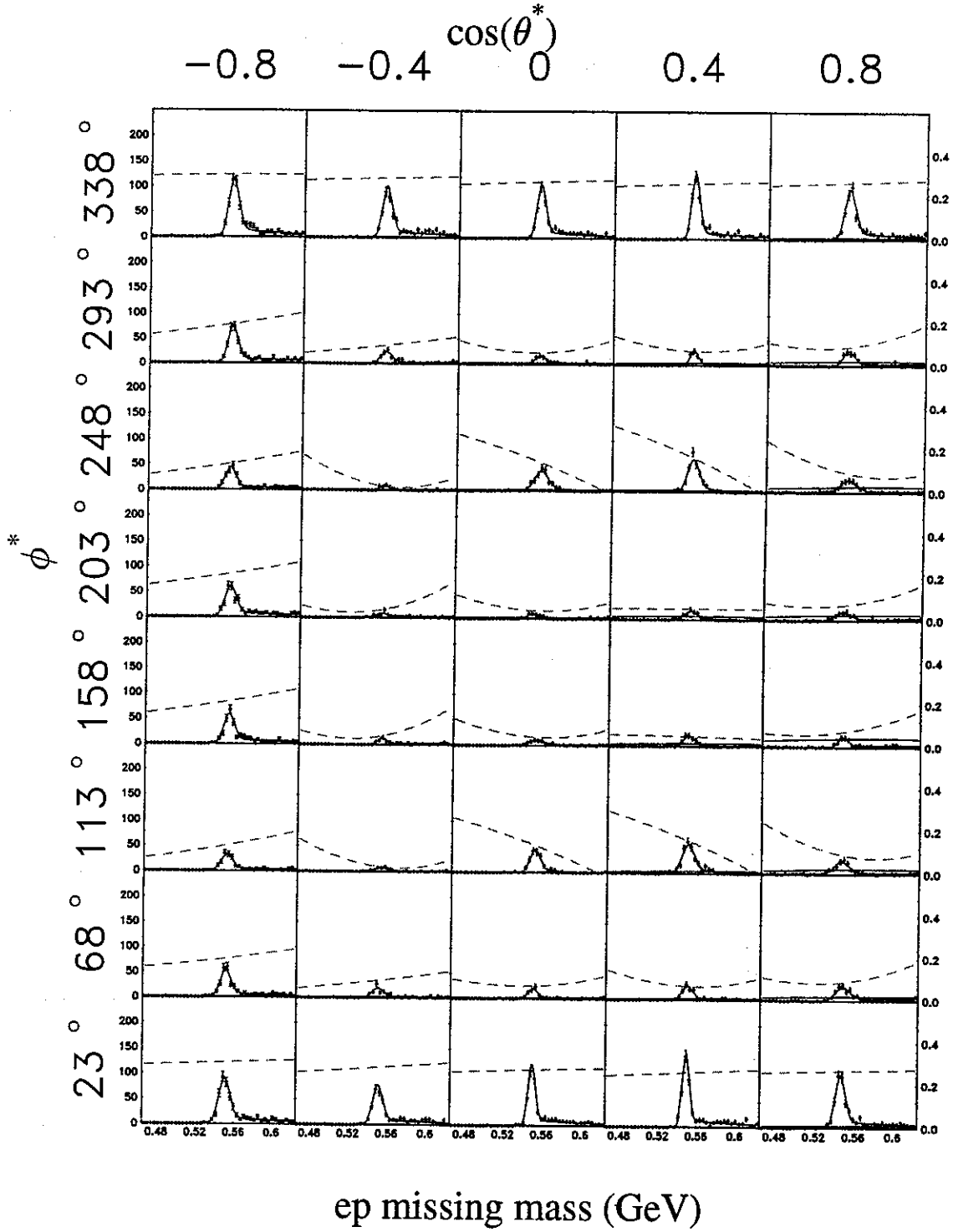

Figure C.4: Angular distrubution ep missing mass simulation fit for $W = 1.59GeV$ and $Q^2 = 0.75GeV^2$.

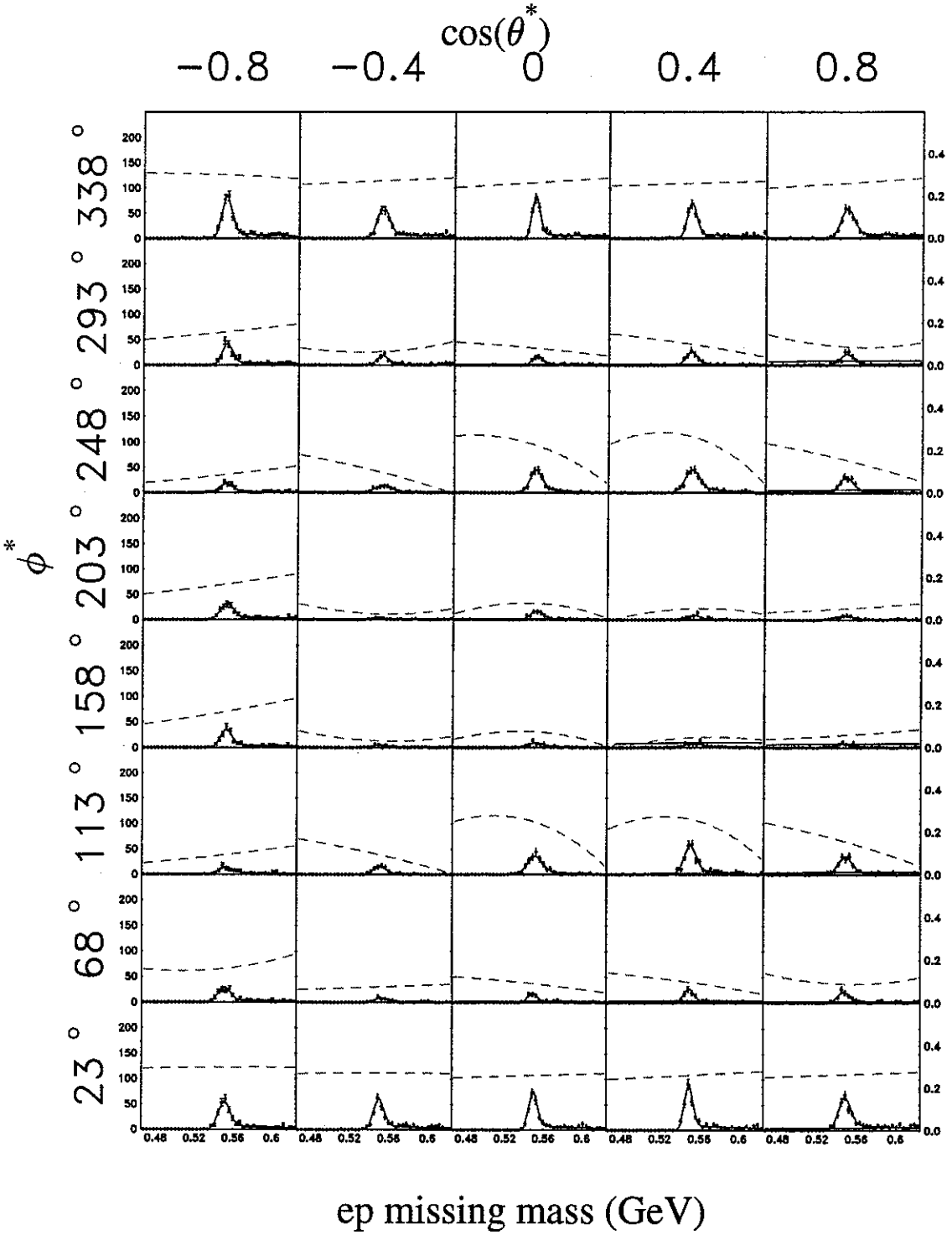

Figure C.5: Angular distrubution ep missing mass simulation fit for $W = 1.62GeV$ and $Q^2 = 0.75GeV^2$.

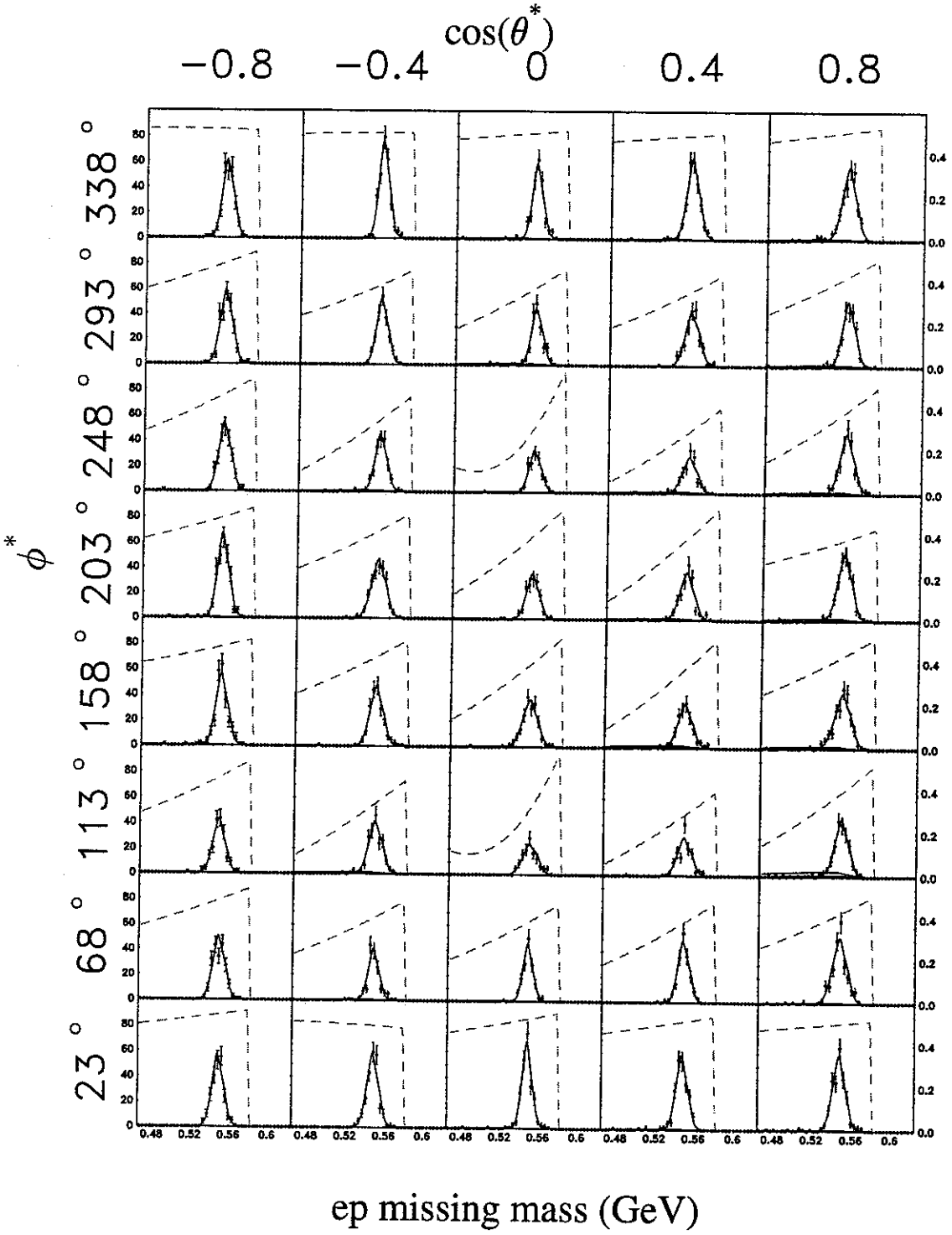

Figure C.6: Angular distrubution ep missing mass simulation fit for $W = 1.50GeV$ and $Q^2 = 1.25GeV^2$.

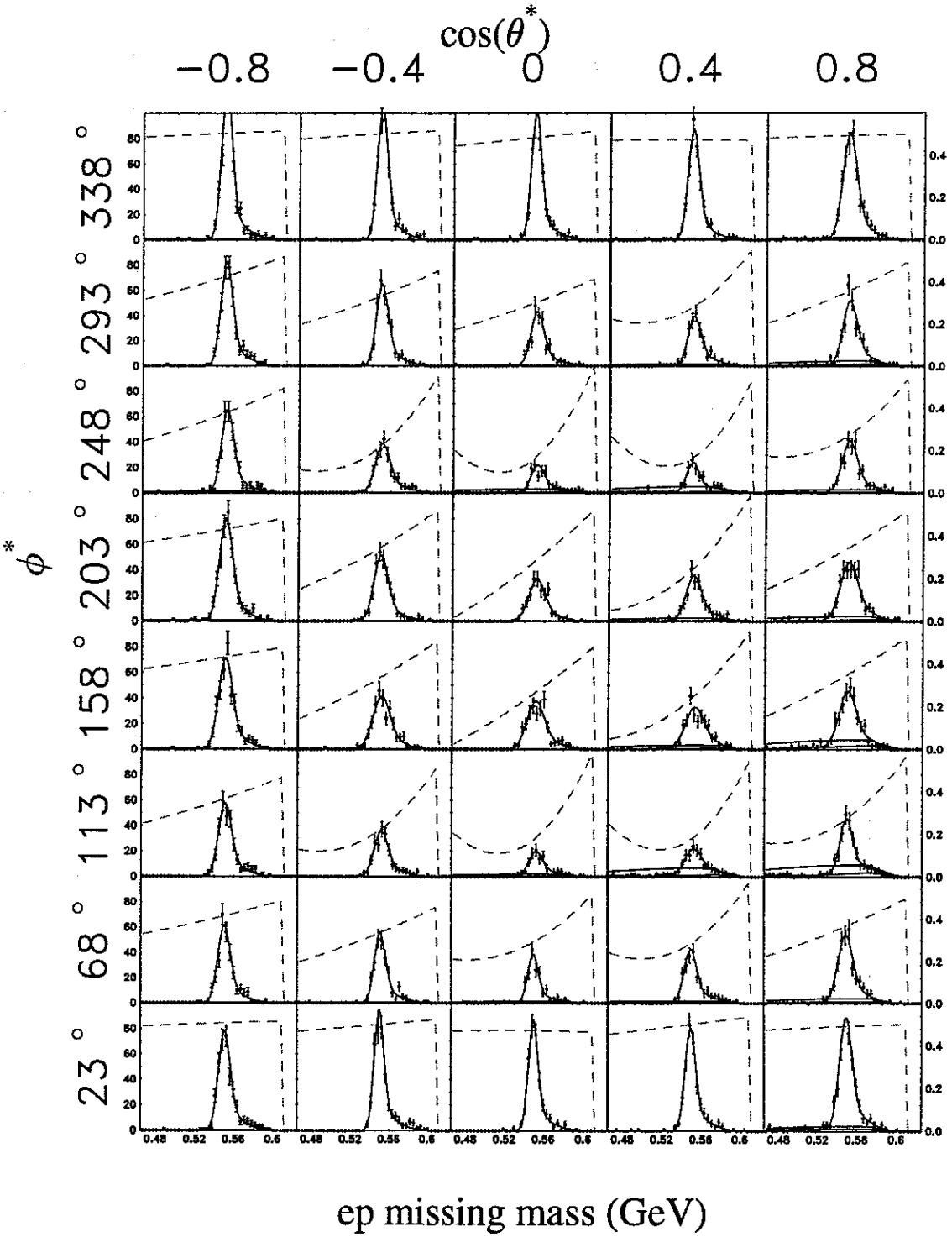

Figure C.7: Angular distrubution ep missing mass simulation fit for $W = 1.53GeV$ and $Q^2 = 1.25GeV^2$.

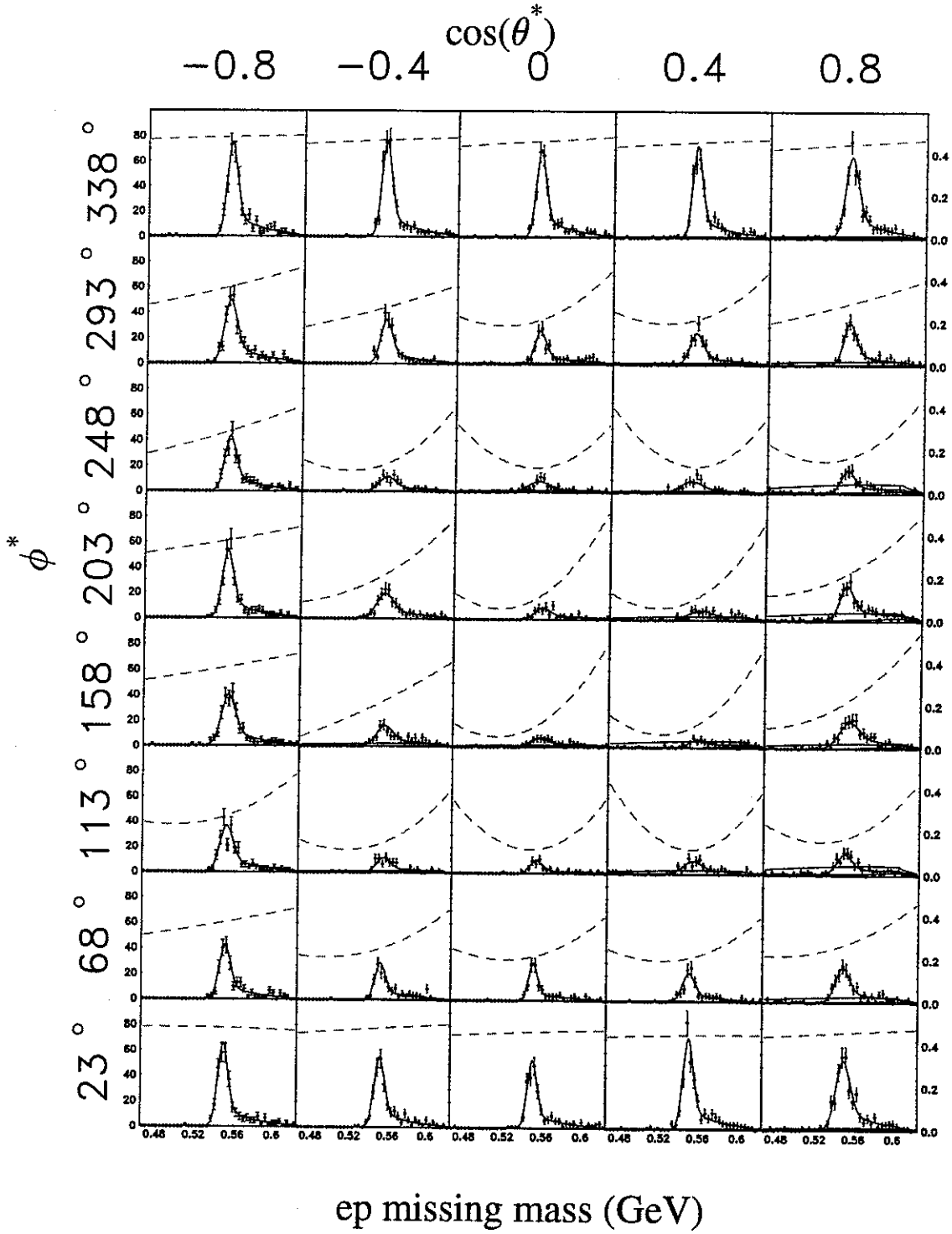

Figure C.8: Angular distrubution ep missing mass simulation fit for $W = 1.56GeV$ and $Q^2 = 1.25GeV^2$.

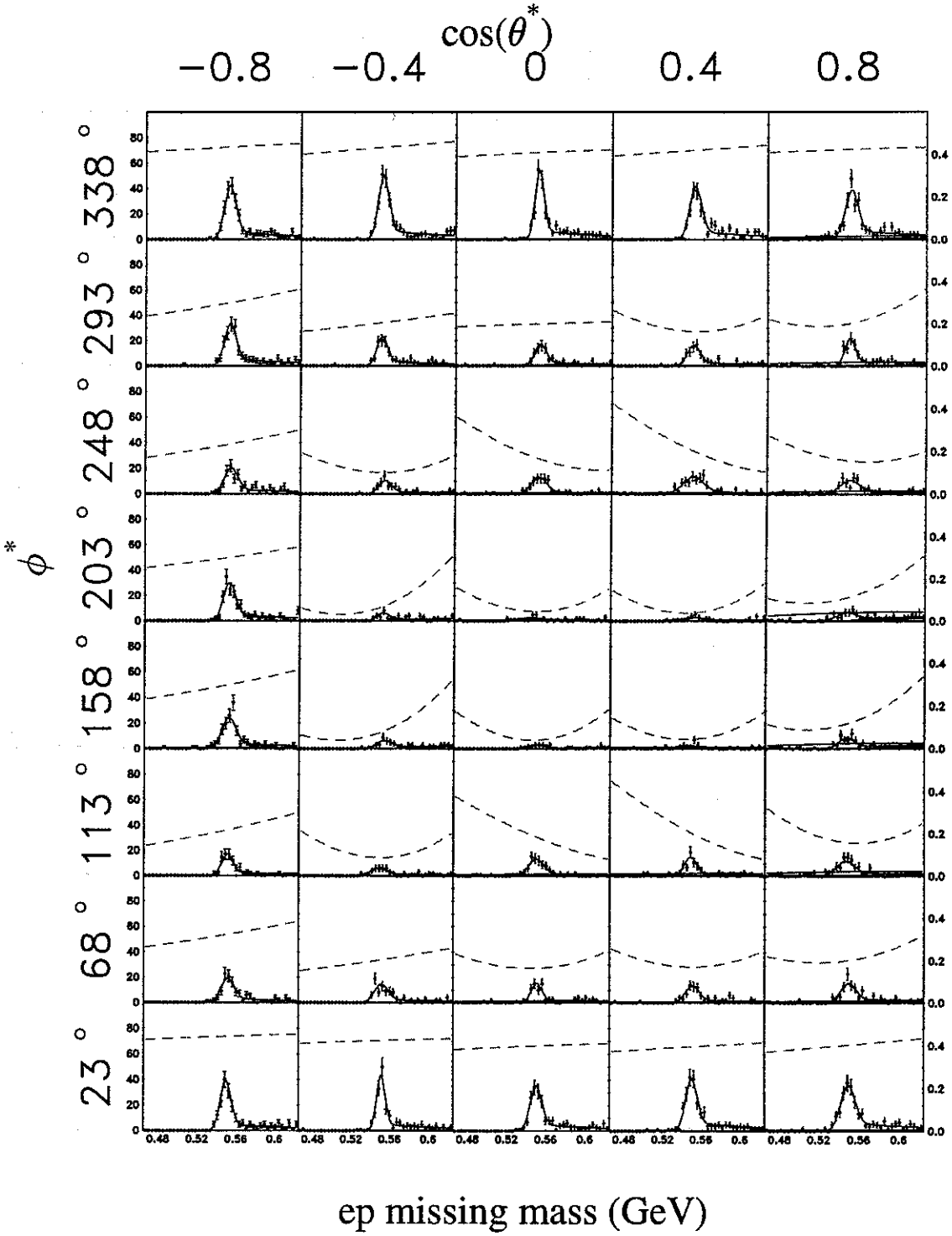

Figure C.9: Angular distrubution ep missing mass simulation fit for $W = 1.59GeV$ and $Q^2 = 1.25GeV^2$.

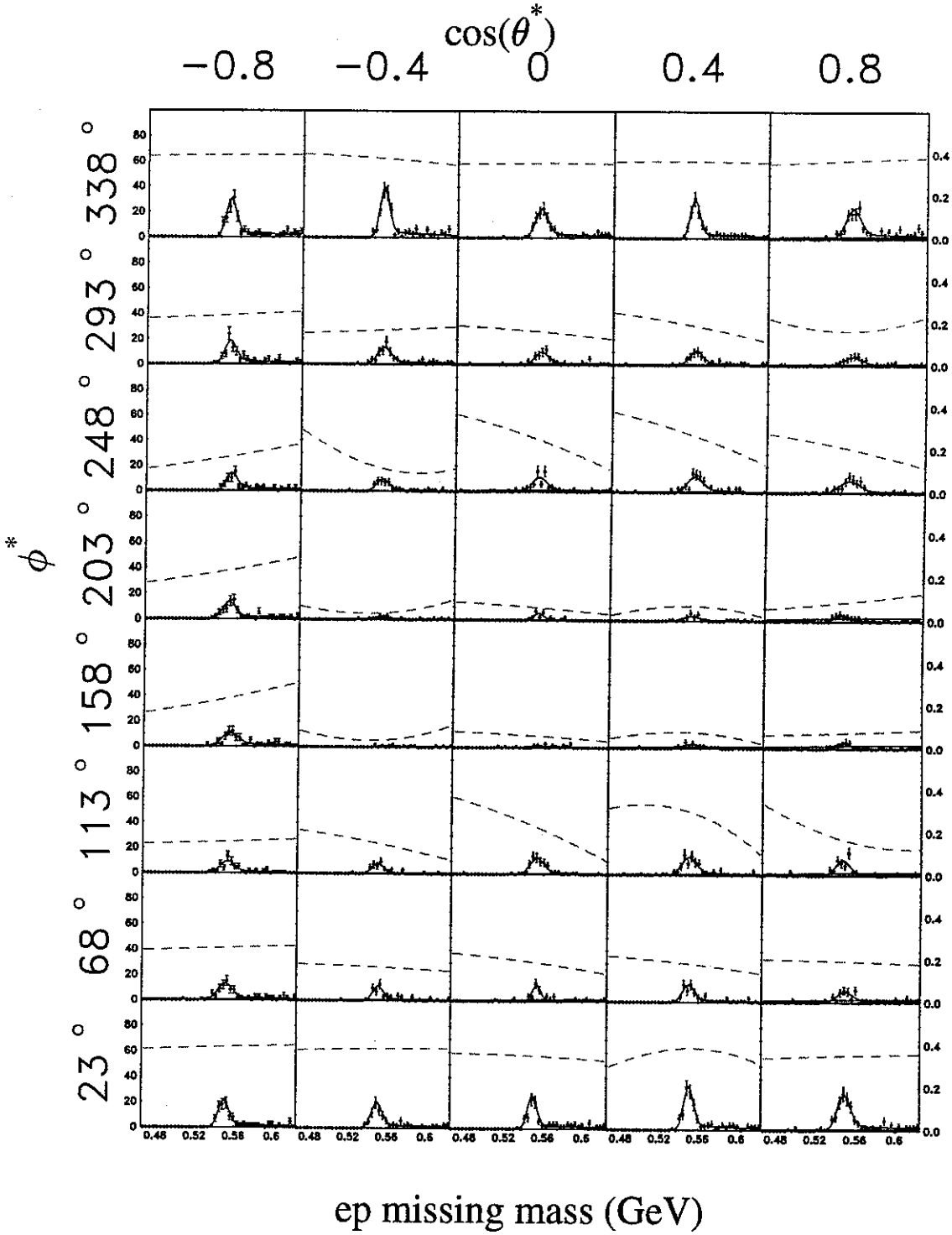

Figure C.10: Angular distrubution ep missing mass simulation fit for $W = 1.62GeV$ and $Q^2 = 1.25GeV^2$.

Appendix D

Systematic Studies Plots

In this appendix are presented the results of the systematic studies discussed in Section 6.1. For each systematic effect studies, there are two pages of plots, one for $Q^2 = 0.5 - 1.0\ GeV^2$ and one for $Q^2 = 1.0 - 1.5\ GeV^2$. In each page of plots are plotted the fractional systematic error with error bars that represent the statistical uncertainty in the data. This allows easy comparison of the scale of systematic and statistical errors.

In Figs. D.1 and D.2 are show the systematic errors associated with the W and Q^2 distributions used to determine the fit function scale factor, $A(M_X)$ of eqn. 5.3.4. This is the systematic effect labelled "acceptance fit function" in table 6.1. For this study, the W and Q^2 thrown distribution was changed from one that was flat (as used for the final analysis) in W and Q^2 to one that had a Breit-Wigner $\frac{1}{2}\frac{1}{2}^-(1535)$ amplitude with a width of $120\ MeV$. The fractional change shown is, in an obvious notation:

$$\frac{flat - \frac{1}{2}\frac{1}{2}^-(1535)}{flat}$$

In Figs. D.3 and D.4 are shown the systematic errors associated with the angular distribution thrown in the event generator used to obtain the final η acceptance. This is the systemetic effect labelled "acceptance η distribution" in Table 6.1. For this study the angular distribution was changed from the one used for the final acceptance calculation, flat in center of mass meson decay angles $cos(\theta^*_\eta)$ and ϕ^*_η to one that had a strong angular dependence. This is explained in more detail in Section 6.1.4. The fractional change shown in the plots is, in an obvious notation,

$$\frac{flat - nonflat}{flat}$$

In Figs. D.5 and D.6 are shown the systematic errors associated with the background fit function, $D_{bkg}(M_X)$ in equation 6.1. This is the systematic error labelled "$D_{bkg}(M_X)$" in Table 6.1. For this study, the background function was changed from that

used in the final analysis, $D_{bkg}(M_X) = b_0 \left\{2\sqrt{\Delta m' \Delta m} - \Delta m\right\}$, to $D_{bkg}(M_X) = b_0$. The fractional change shown in the plots is, in an obvious notation,

$$\frac{flat - nonflat}{flat}$$

In Figs. D.7 and D.8 are shown the systematic errors associated with the centroid of the η used in the fit function shown in equation 6.1. This is the systematic effect labelled "ηpeak fitting M_η" in Table 6.1. For this study, the η peak centroid was changed by 3 MeV from that used in the final fits. The fractional change shown in the plots is, in an obvious notation,

$$\frac{M_\eta^{final} - M_\eta^{+3}}{M_\eta^{final}}$$

In Figs. D.9 and D.10 are shown the systematic errors associated with the choice of the width of the η peak, σ_η in eqn. 6.1. This is the systematic effect labelled "η peak fitting σ_η" in Table 6.1. For this study, the η peak width used for the final analysis, as presented in section 5.3.2, was changed by 10%. The fractional change shown in the plots is, in an obvious notation,

$$\frac{\sigma_\eta^{final} - \sigma_\eta^{+10\%}}{\sigma_\eta^{final}}$$

In Figs. D.11 and D.12 are shown the systematic errors associated with the choice of the radiative tail parameter α of equation 6.1. This is the systematic error labelled "η peak fitting α" in Table 6.1. For this study, α was changed by 10% from that used in the final analysis. The fractional change shown in the plots is, in an obvious notation,

$$\frac{\alpha_\eta^{final} - \alpha_\eta^{+10\%}}{\alpha_\eta^{final}}$$

In Figs. D.13 and D.14 are shown the systematic errors associated with the choice of the radiative tail parameter τ of equation 6.1. This is the systematic error labelled "η peak fitting τ" in Table 6.1. For this study, τ was changed by 10% from that used in the final analysis. The fractional change shown in the plots is, in an obvious notation,

$$\frac{\tau_\eta^{final} - \tau_\eta^{+10\%}}{\tau_\eta^{final}}$$

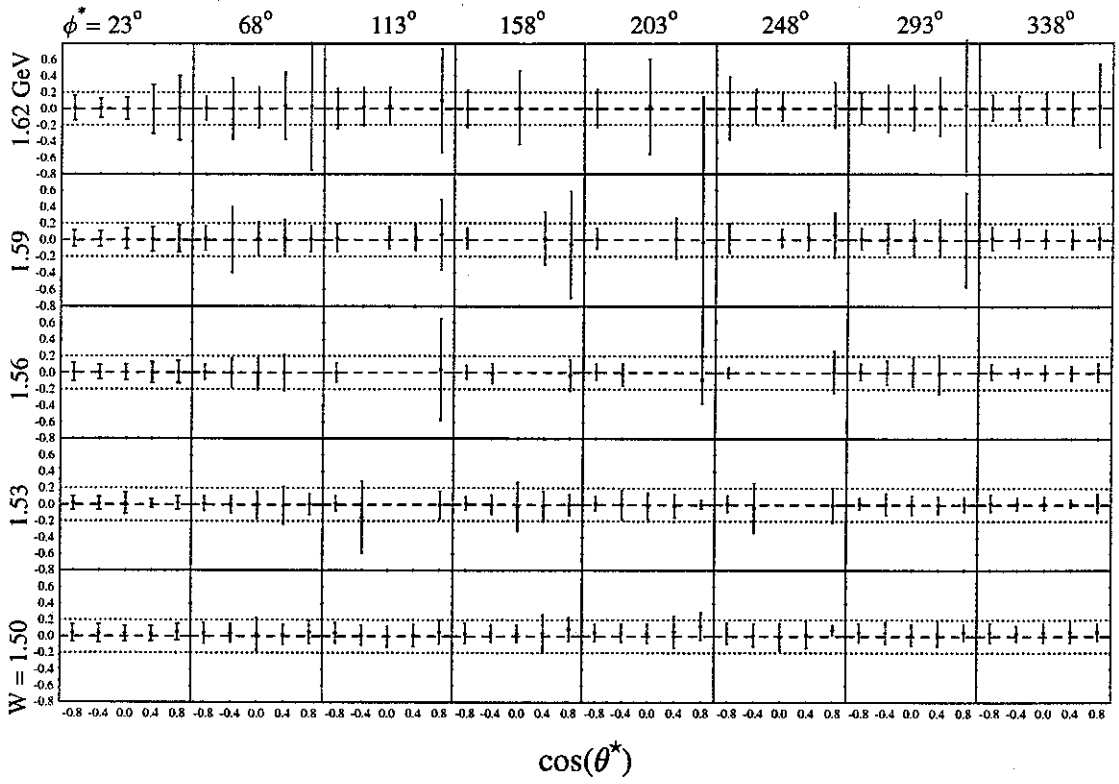

Figure D.1: Fit function acceptance systematic study for $Q^2 = 0.5 - 1.0 GeV^2$.

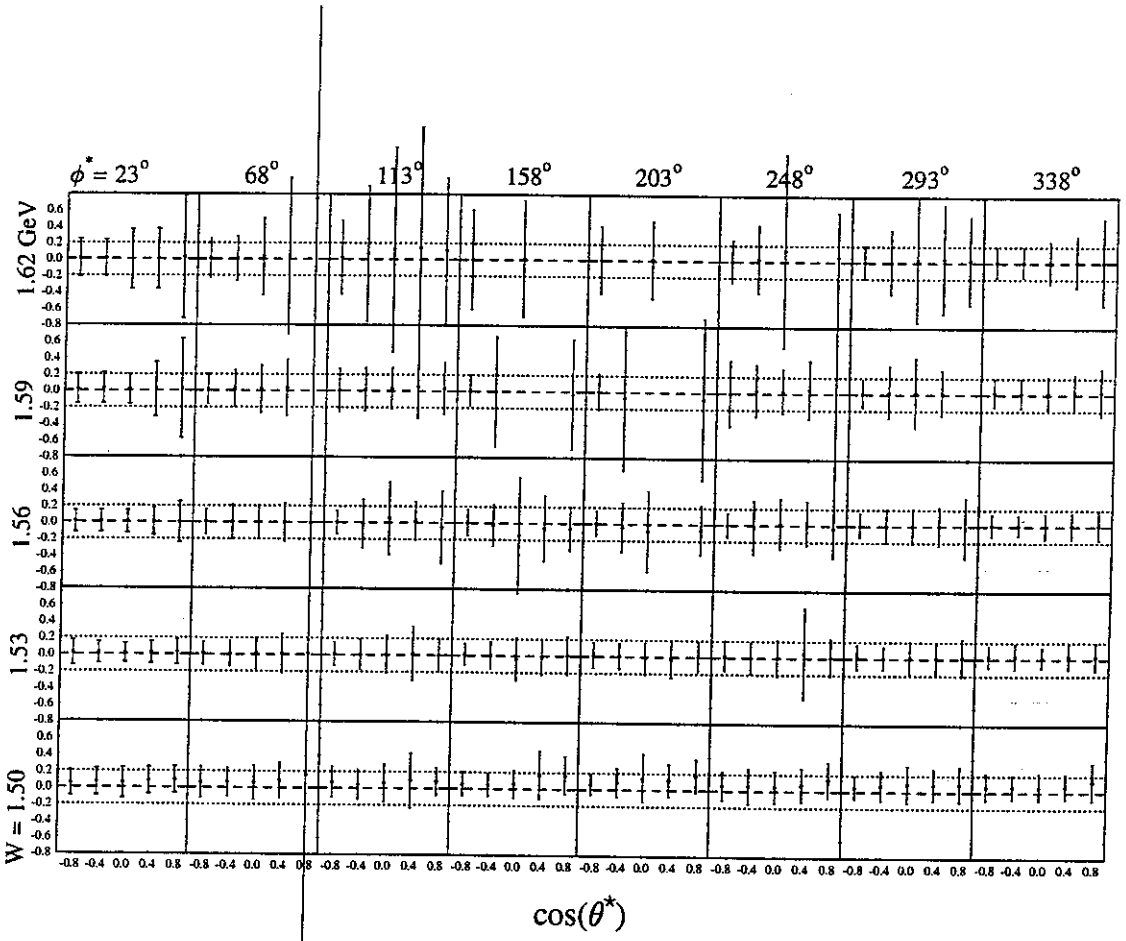

Figure D.2: Fit function acceptance systematic study for $Q^2 = 1.0 - 1.5 GeV^2$.

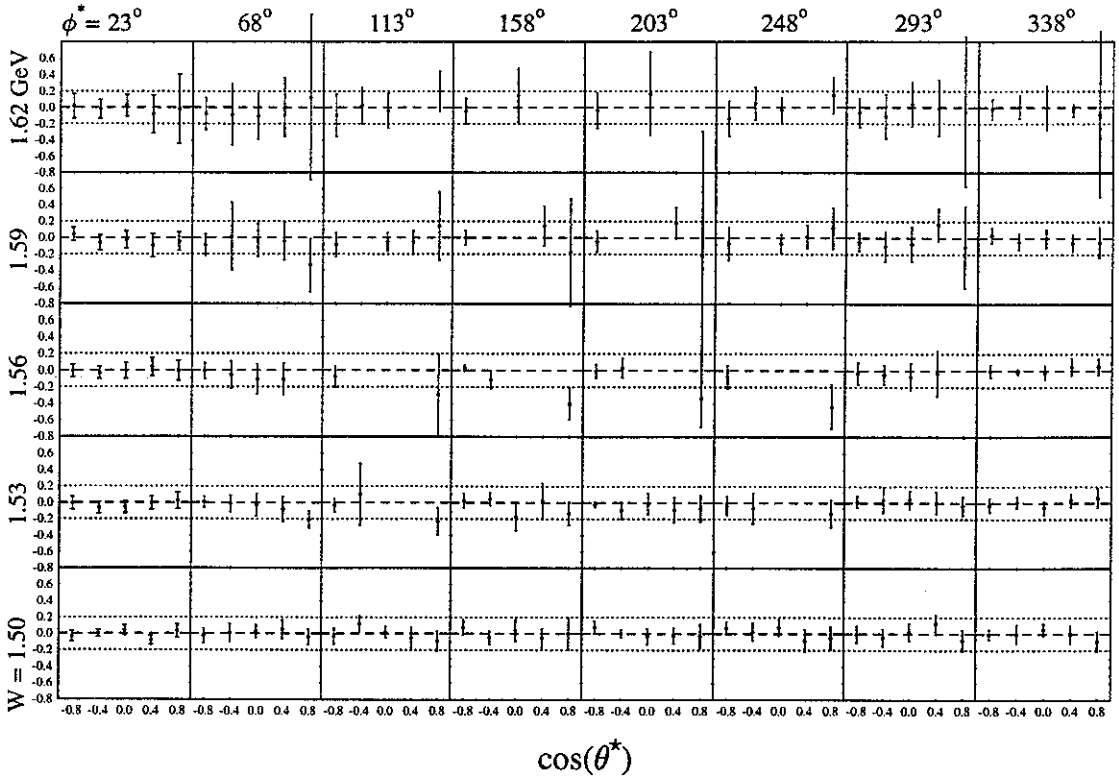

Figure D.3: Eta angular distribution acceptance systematic study for $Q^2 = 0.5-1.0 GeV^2$.

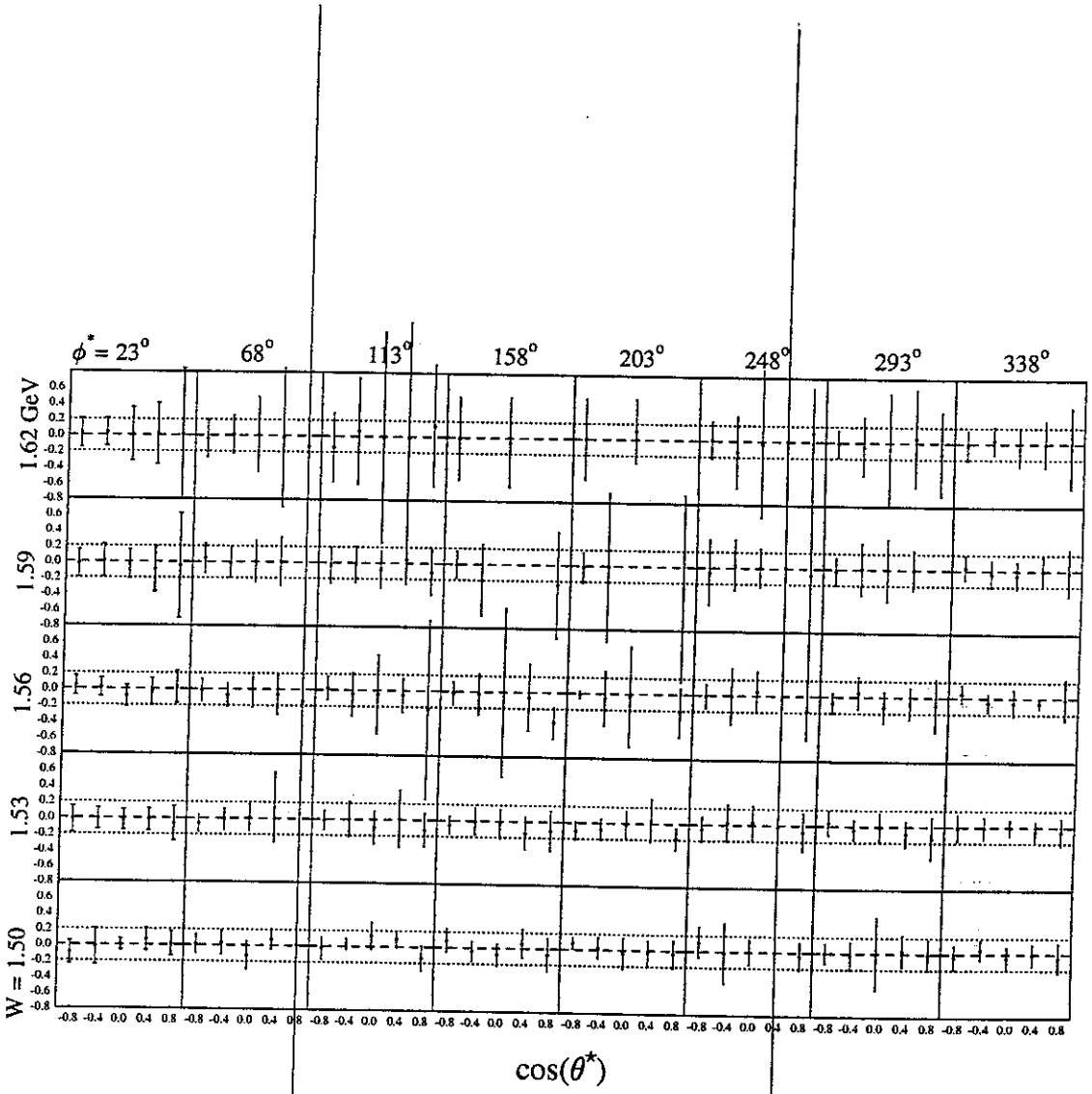

Figure D.4: Eta angular distribution acceptance systematic study for $Q^2 = 1.0-1.5 GeV^2$.

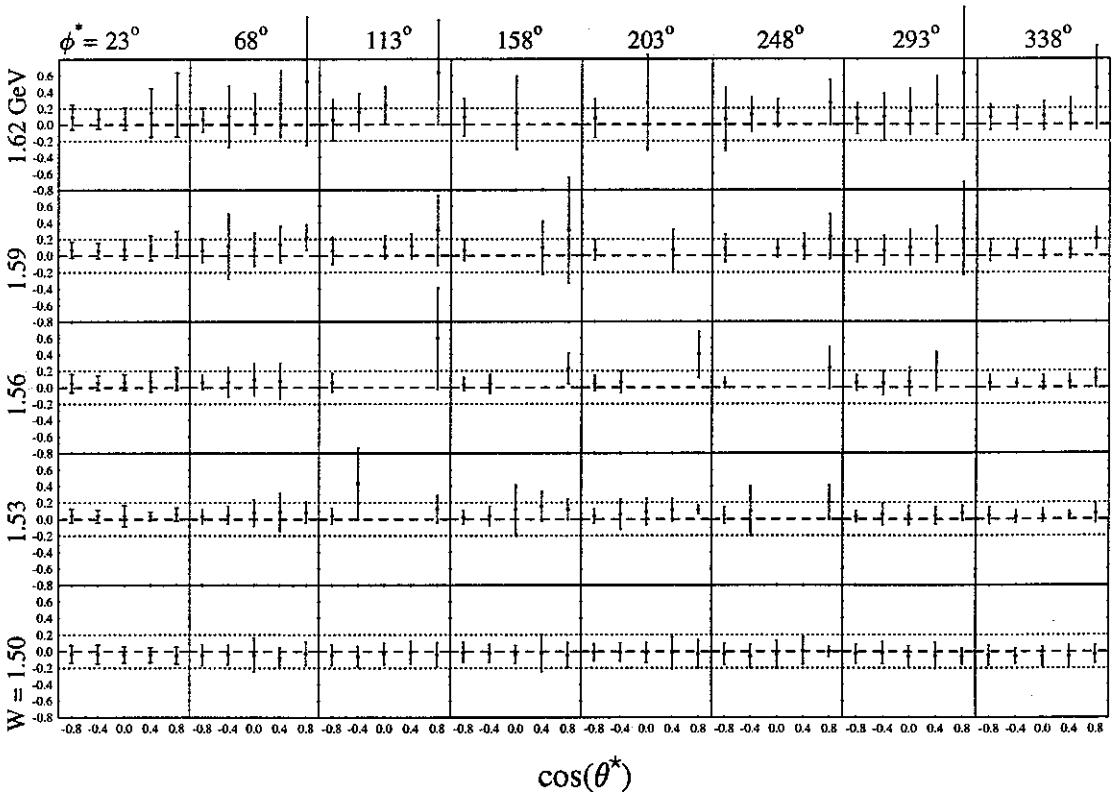

Figure D.5: Background systematic study for $Q^2 = 0.5 - 1.0 GeV^2$.

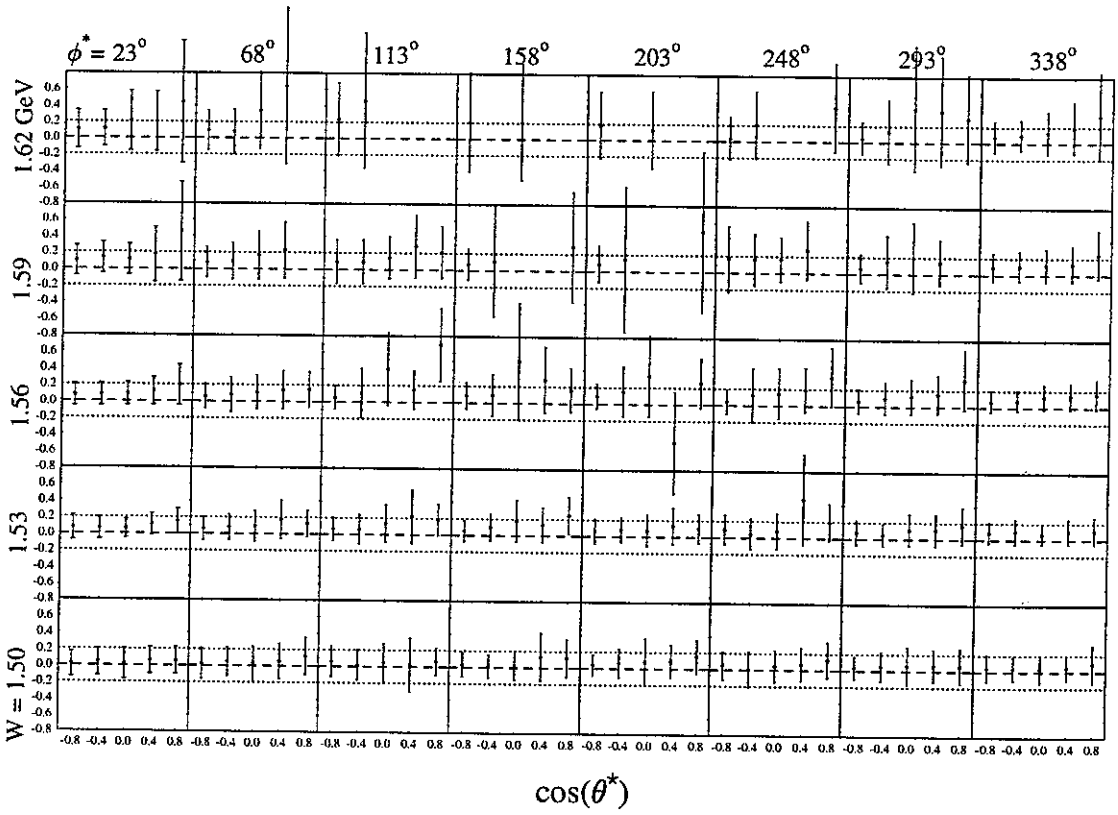

Figure D.6: Background systematic study for $Q^2 = 1.0 - 1.5 GeV^2$.

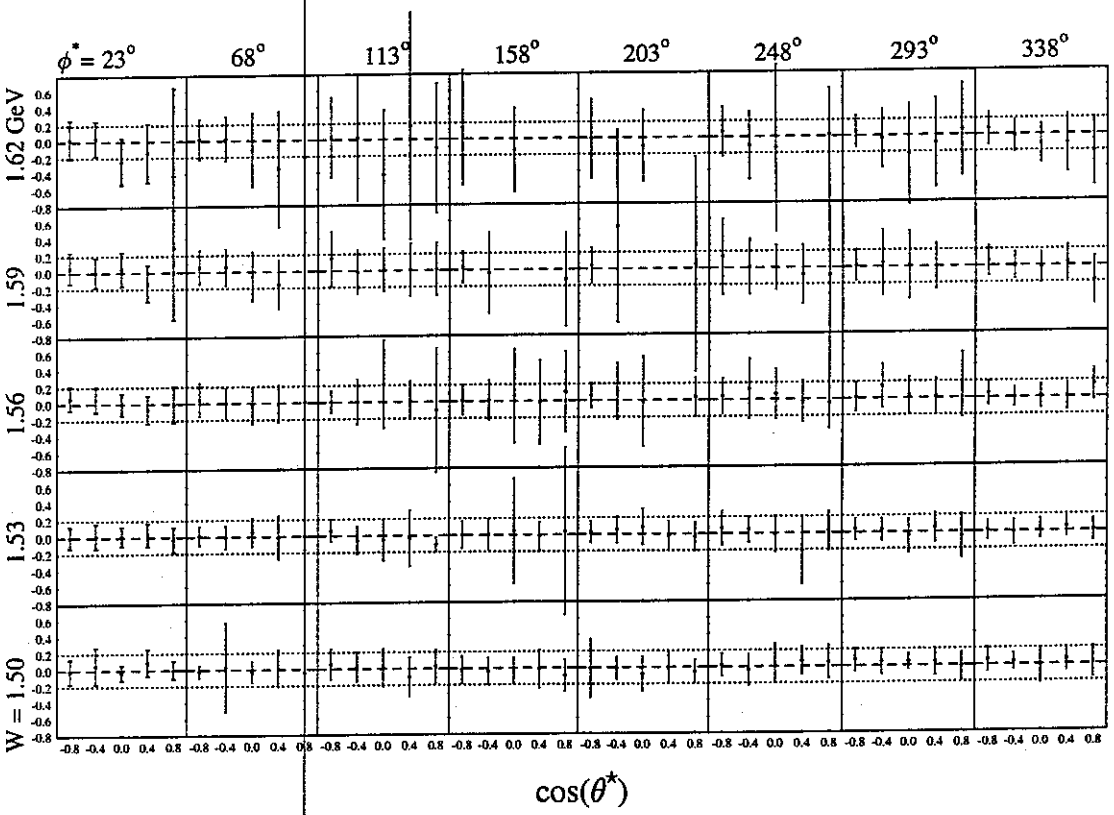

Figure D.8: η peak centroid systematic study for $Q^2 = 1.0 - 1.5 GeV^2$.

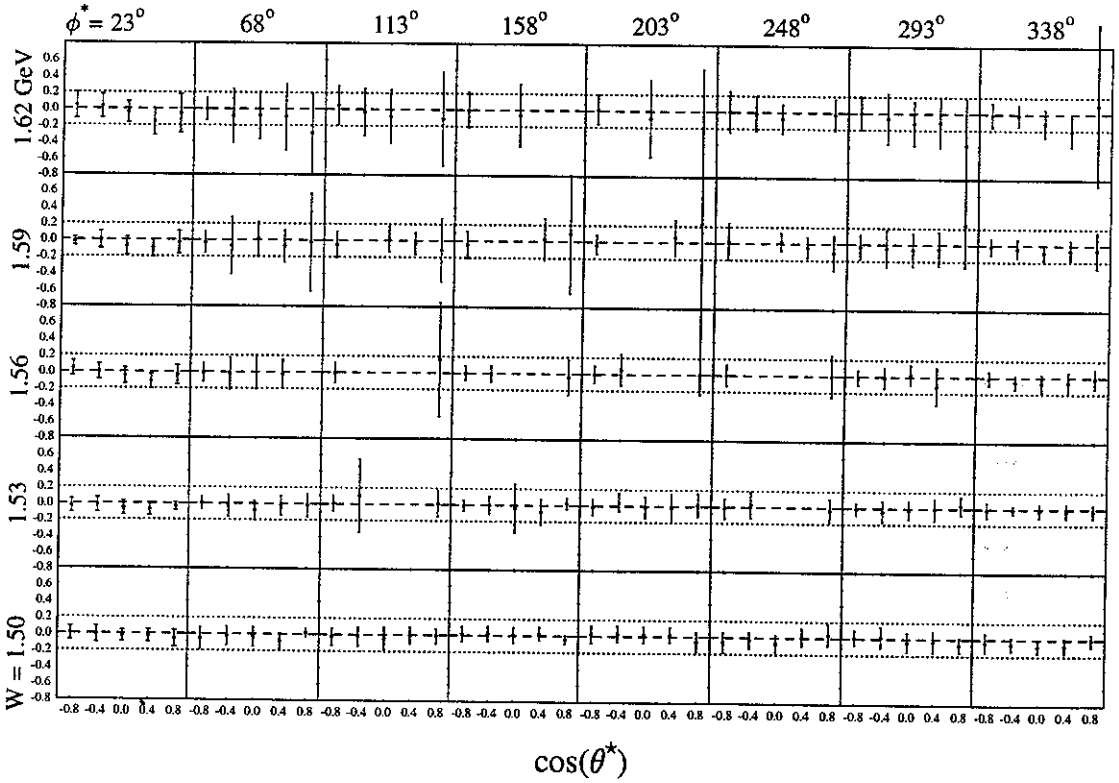

Figure D.7: η peak centroid systematic study for $Q^2 = 0.5 - 1.0 GeV^2$.

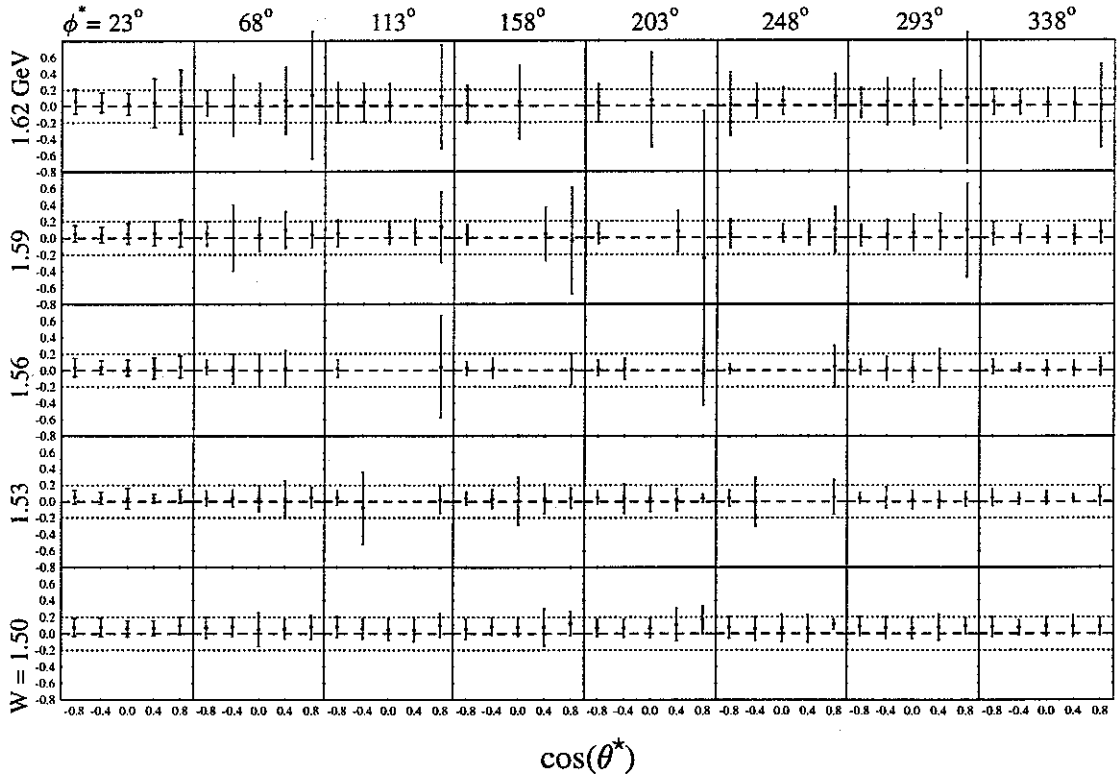

Figure D.9: η peak width systematic study for $Q^2 = 0.5 - 1.0 GeV^2$.

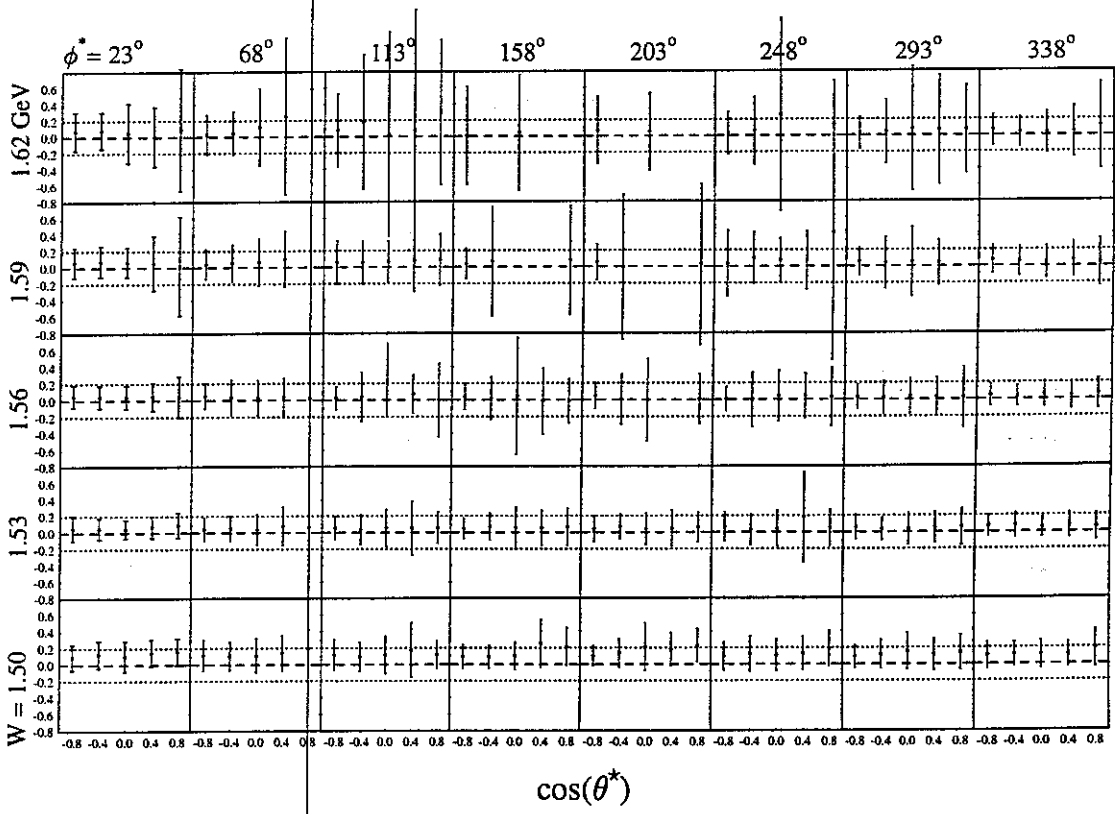

Figure D.10: η peak width systematic study for $Q^2 = 1.0 - 1.5 GeV^2$.

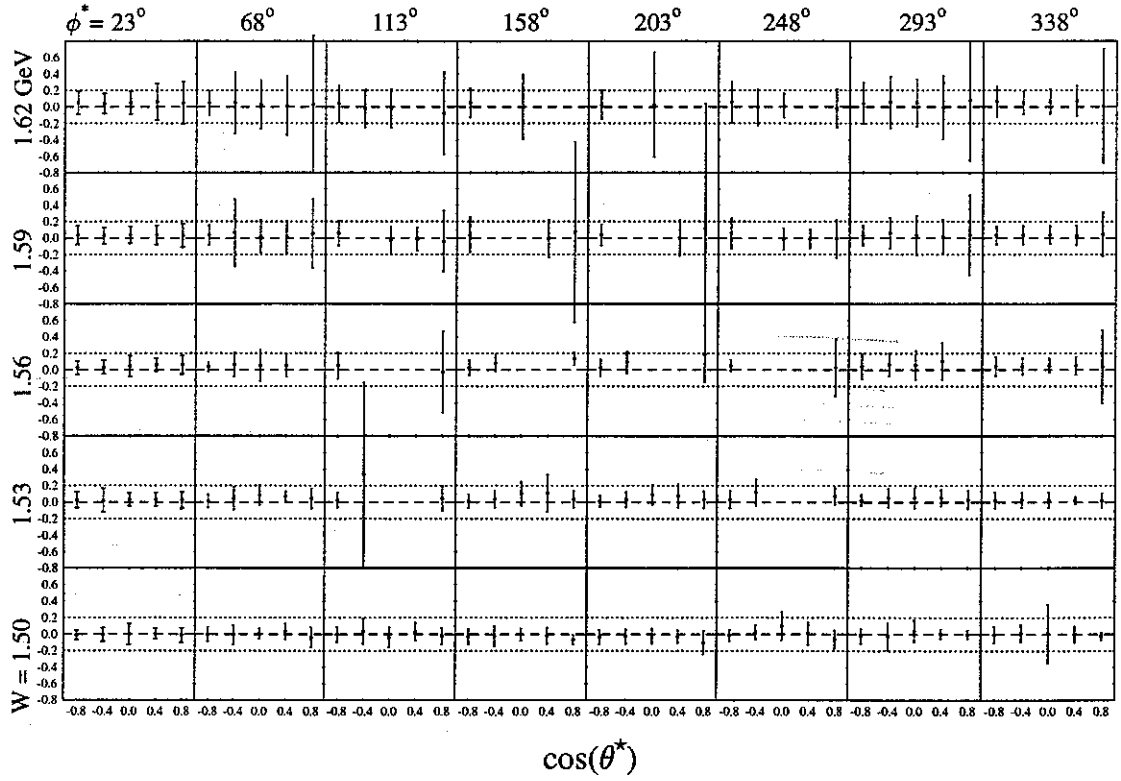

Figure D.11: η peak α systematic study for $Q^2 = 0.5 - 1.0 GeV^2$.

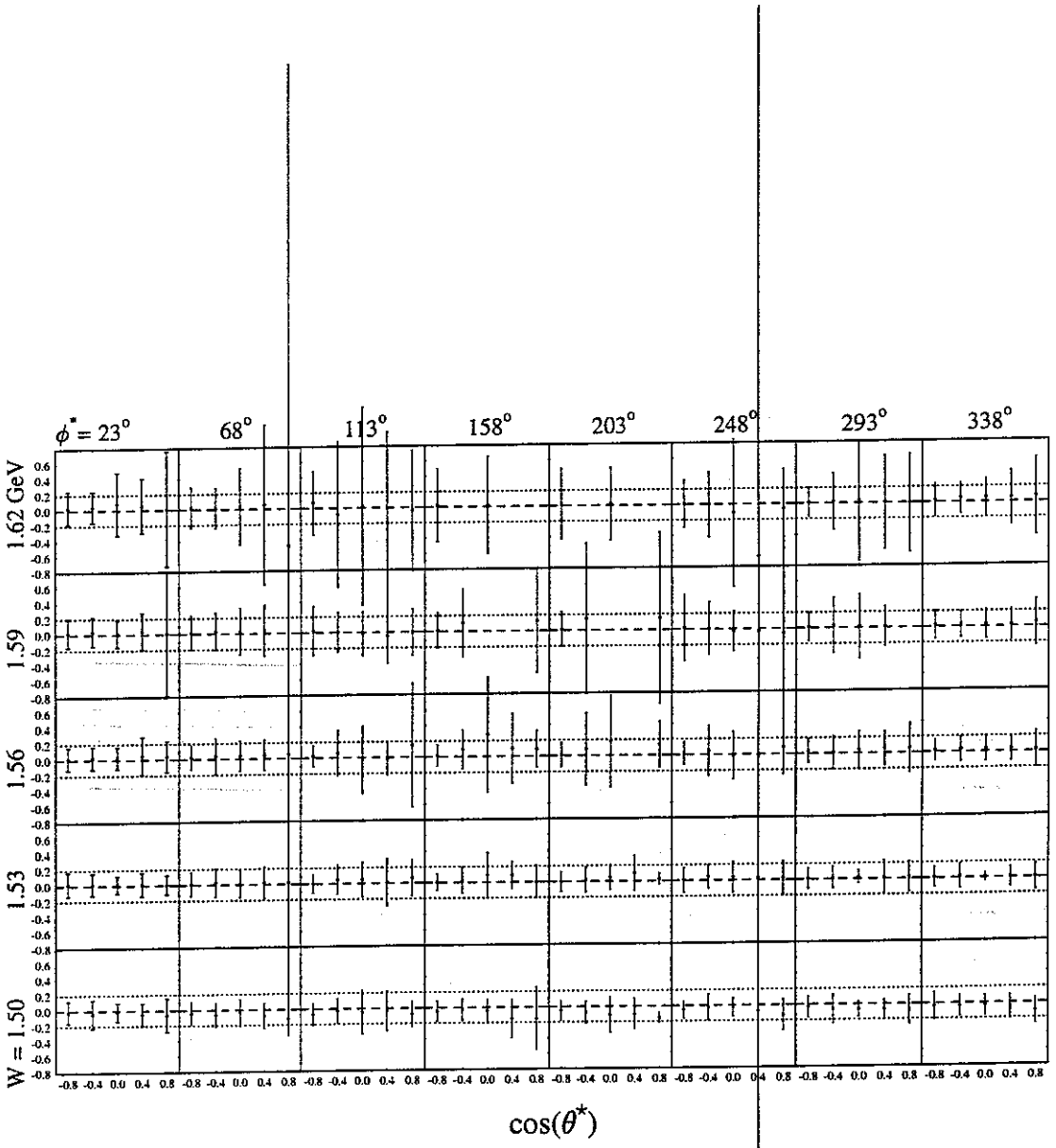

Figure D.12: η peak α systematic study for $Q^2 = 1.0 - 1.5 GeV^2$.

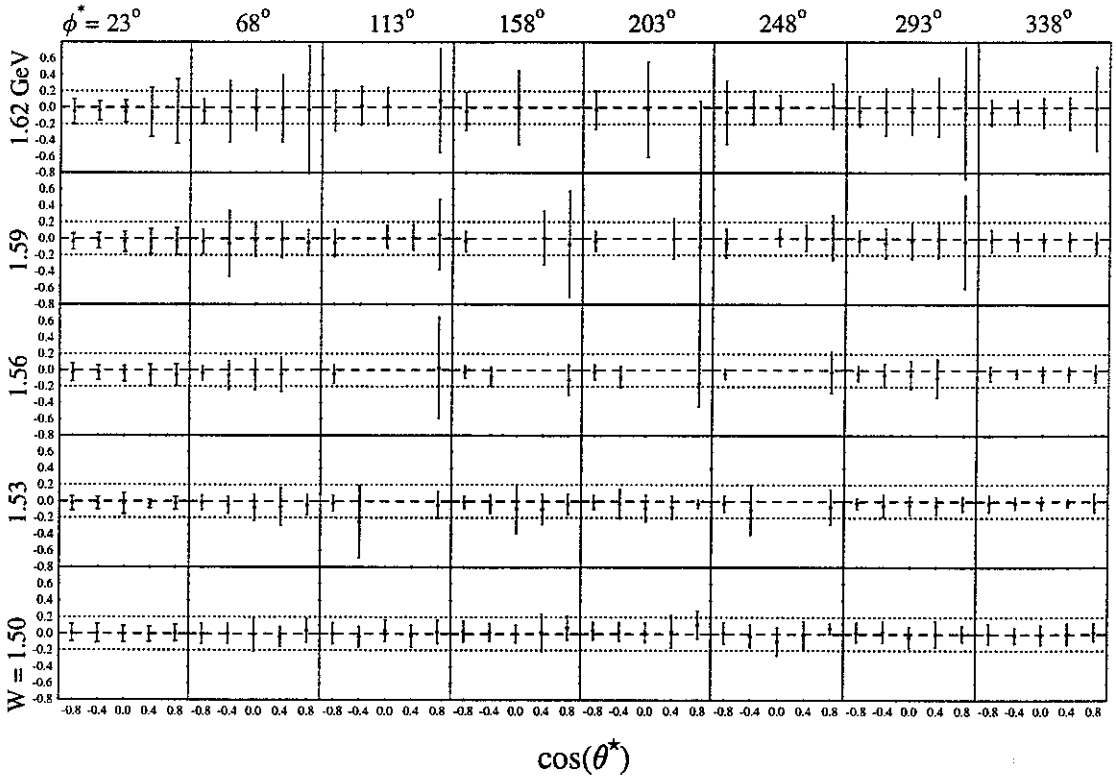

Figure D.13: η peak τ systematic study for $Q^2 = 0.5 - 1.0 GeV^2$.

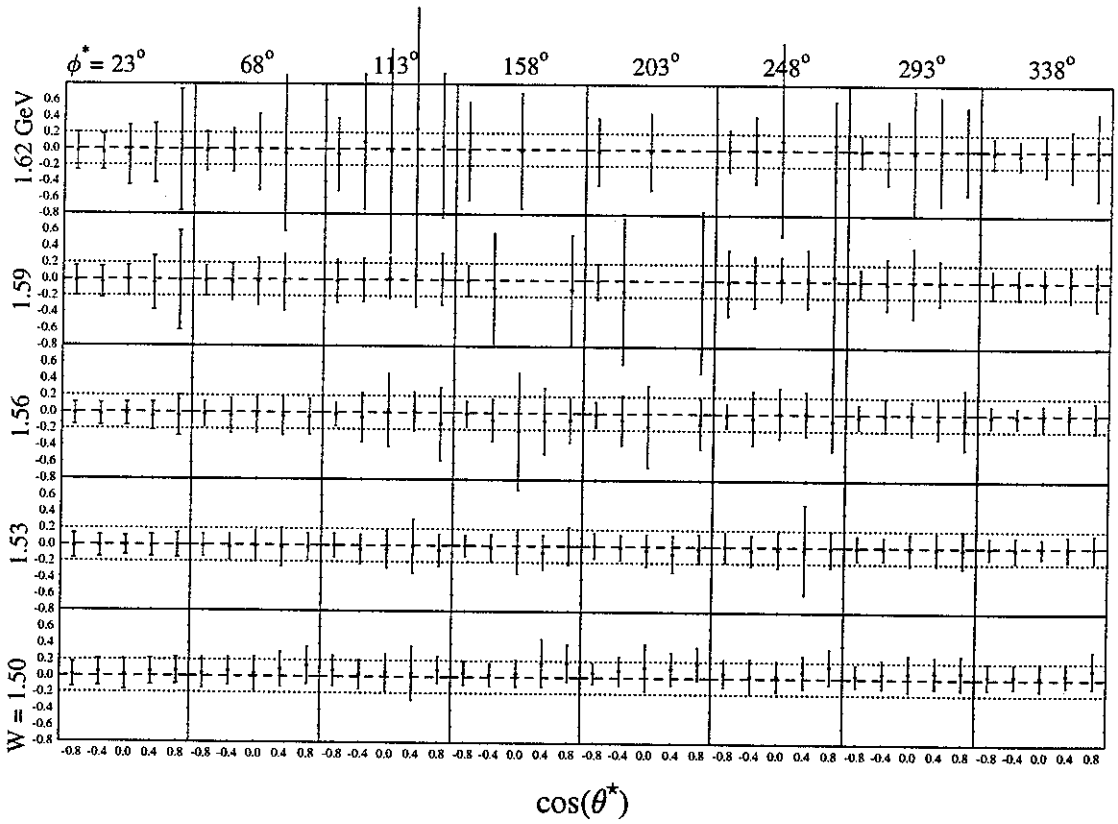

Figure D.14: η peak τ systematic study for $Q^2 = 1.0 - 1.5 GeV^2$.

Appendix E

Tabulated Cross Sections

This appendix contains tables of the differential cross sections. The kinematic values of W, Q^2, $cos(\theta^*_\eta)$, and ϕ^*_η are listed at the bin centers. "Correction" is the acceptance and radiative correction factor. The uncertainty in cross section includes systematic uncertainties.

W(GeV)	$Q^2(GeV^2)$	$cos(\theta^*_\eta)$	ϕ^*_η	Correction	$\frac{d\sigma}{d\Omega^*_\eta}$
1.50	0.75	-0.8	22.5	0.1207 ± 0.0058	0.9886 ± 0.1333
1.50	0.75	-0.4	22.5	0.1166 ± 0.0060	1.0601 ± 0.1401
1.50	0.75	0.0	22.5	0.1337 ± 0.0064	0.9568 ± 0.1281
1.50	0.75	0.4	22.5	0.1416 ± 0.0064	0.9738 ± 0.1347
1.50	0.75	0.8	22.5	0.1339 ± 0.0061	0.8389 ± 0.1414
1.50	0.75	-0.8	67.5	0.1267 ± 0.0060	0.8380 ± 0.1076
1.50	0.75	-0.4	67.5	0.1148 ± 0.0060	0.8482 ± 0.1289
1.50	0.75	0.0	67.5	0.0899 ± 0.0052	1.0118 ± 0.1397
1.50	0.75	0.4	67.5	0.1069 ± 0.0056	0.8422 ± 0.1441
1.50	0.75	0.8	67.5	0.1136 ± 0.0056	0.9494 ± 0.1575
1.50	0.75	-0.8	112.5	0.1118 ± 0.0056	1.0166 ± 0.1341
1.50	0.75	-0.4	112.5	0.0835 ± 0.0051	0.9548 ± 0.1599
1.50	0.75	0.0	112.5	0.0760 ± 0.0048	0.8127 ± 0.1761
1.50	0.75	0.4	112.5	0.0789 ± 0.0048	0.9145 ± 0.1511
1.50	0.75	0.8	112.5	0.1094 ± 0.0055	0.9320 ± 0.1645
1.50	0.75	-0.8	157.5	0.1198 ± 0.0058	1.1830 ± 0.1881
1.50	0.75	-0.4	157.5	0.1055 ± 0.0057	1.2577 ± 0.1702
1.50	0.75	0.0	157.5	0.1018 ± 0.0056	1.2989 ± 0.1702
1.50	0.75	0.4	157.5	0.1098 ± 0.0057	1.1441 ± 0.1831
1.50	0.75	0.8	157.5	0.1257 ± 0.0059	0.9089 ± 0.2171
1.50	0.75	-0.8	157.5	0.1199 ± 0.0058	1.1956 ± 0.1764
1.50	0.75	-0.4	157.5	0.1028 ± 0.0057	1.2676 ± 0.1685
1.50	0.75	0.0	157.5	0.0927 ± 0.0053	1.3354 ± 0.1830
1.50	0.75	0.4	157.5	0.1046 ± 0.0056	0.9906 ± 0.1505
1.50	0.75	0.8	157.5	0.1223 ± 0.0059	0.7111 ± 0.1865
1.50	0.75	-0.8	112.5	0.1089 ± 0.0056	1.1216 ± 0.1463
1.50	0.75	-0.4	112.5	0.0785 ± 0.0050	1.0688 ± 0.1520
1.50	0.75	0.0	112.5	0.0634 ± 0.0044	0.8852 ± 0.1414
1.50	0.75	0.4	112.5	0.0736 ± 0.0046	0.9142 ± 0.1657
1.50	0.75	0.8	112.5	0.1067 ± 0.0054	0.7799 ± 0.1568
1.50	0.75	-0.8	67.5	0.1260 ± 0.0060	0.9444 ± 0.1474
1.50	0.75	-0.4	67.5	0.1118 ± 0.0058	0.8215 ± 0.1257
1.50	0.75	0.0	67.5	0.1001 ± 0.0055	0.9308 ± 0.1653
1.50	0.75	0.4	67.5	0.1105 ± 0.0057	0.7601 ± 0.1502
1.50	0.75	0.8	67.5	0.1216 ± 0.0058	0.9199 ± 0.1650
1.50	0.75	-0.8	22.5	0.1278 ± 0.0060	0.7893 ± 0.1213
1.50	0.75	-0.4	22.5	0.1300 ± 0.0064	0.8779 ± 0.1130
1.50	0.75	0.0	22.5	0.1256 ± 0.0062	0.8258 ± 0.1218
1.50	0.75	0.4	22.5	0.1254 ± 0.0060	0.7861 ± 0.1118
1.50	0.75	0.8	22.5	0.1472 ± 0.0064	0.8448 ± 0.1346

W(GeV)	$Q^2(GeV^2)$	$cos(\theta^*_\eta)$	ϕ^*_η	Correction	$\frac{d\sigma}{d\Omega^*_\eta}$
1.50	1.25	-0.8	22.5	0.2293 ± 0.0158	0.6323 ± 0.1507
1.50	1.25	-0.4	22.5	0.2234 ± 0.0151	0.5949 ± 0.1559
1.50	1.25	0.0	22.5	0.2564 ± 0.0173	0.6235 ± 0.1086
1.50	1.25	0.4	22.5	0.2473 ± 0.0170	0.5765 ± 0.1429
1.50	1.25	0.8	22.5	0.2619 ± 0.0173	0.5736 ± 0.1644
1.50	1.25	-0.8	67.5	0.2074 ± 0.0148	0.6616 ± 0.1388
1.50	1.25	-0.4	67.5	0.1415 ± 0.0119	0.9591 ± 0.3735
1.50	1.25	0.0	67.5	0.1718 ± 0.0141	0.7627 ± 0.1962
1.50	1.25	0.4	67.5	0.2080 ± 0.0156	0.5149 ± 0.1551
1.50	1.25	0.8	67.5	0.2623 ± 0.0173	0.3586 ± 0.1204
1.50	1.25	-0.8	112.5	0.1820 ± 0.0138	0.7294 ± 0.1799
1.50	1.25	-0.4	112.5	0.1841 ± 0.0138	0.7472 ± 0.1592
1.50	1.25	0.0	112.5	0.1466 ± 0.0133	0.6455 ± 0.1827
1.50	1.25	0.4	112.5	0.1565 ± 0.0135	0.4370 ± 0.1514
1.50	1.25	0.8	112.5	0.2054 ± 0.0151	0.7684 ± 0.2755
1.50	1.25	-0.8	157.5	0.2369 ± 0.0161	0.7140 ± 0.1492
1.50	1.25	-0.4	157.5	0.2115 ± 0.0151	0.8903 ± 0.1922
1.50	1.25	0.0	157.5	0.2101 ± 0.0157	0.6813 ± 0.1886
1.50	1.25	0.4	157.5	0.1809 ± 0.0147	0.6082 ± 0.2439
1.50	1.25	0.8	157.5	0.2378 ± 0.0163	0.5715 ± 0.2447
1.50	1.25	-0.8	157.5	0.2680 ± 0.0171	0.7046 ± 0.1431
1.50	1.25	-0.4	157.5	0.2195 ± 0.0151	0.7078 ± 0.1565
1.50	1.25	0.0	157.5	0.1773 ± 0.0145	0.5148 ± 0.2049
1.50	1.25	0.4	157.5	0.2034 ± 0.0158	0.6242 ± 0.2255
1.50	1.25	0.8	157.5	0.2617 ± 0.0173	0.5064 ± 0.2079
1.50	1.25	-0.8	112.5	0.2337 ± 0.0159	0.5551 ± 0.1267
1.50	1.25	-0.4	112.5	0.1798 ± 0.0138	0.5924 ± 0.1244
1.50	1.25	0.0	112.5	0.1563 ± 0.0136	0.7243 ± 0.1726
1.50	1.25	0.4	112.5	0.1554 ± 0.0135	0.6604 ± 0.1806
1.50	1.25	0.8	112.5	0.2276 ± 0.0159	0.5202 ± 0.1635
1.50	1.25	-0.8	67.5	0.2470 ± 0.0162	0.7698 ± 0.1413
1.50	1.25	-0.4	67.5	0.2000 ± 0.0143	0.5996 ± 0.1370
1.50	1.25	0.0	67.5	0.1940 ± 0.0151	0.5375 ± 0.1657
1.50	1.25	0.4	67.5	0.2288 ± 0.0166	0.5119 ± 0.1338
1.50	1.25	0.8	67.5	0.2207 ± 0.0155	0.5922 ± 0.5556
1.50	1.25	-0.8	22.5	0.2443 ± 0.0162	0.5882 ± 0.1037
1.50	1.25	-0.4	22.5	0.2685 ± 0.0168	0.6148 ± 0.1360
1.50	1.25	0.0	22.5	0.2399 ± 0.0169	0.6811 ± 0.1269
1.50	1.25	0.4	22.5	0.2763 ± 0.0178	0.5523 ± 0.1384
1.50	1.25	0.8	22.5	0.2844 ± 0.0183	0.3921 ± 0.1218

W(GeV)	$Q^2(GeV^2)$	$cos(\theta^*_\eta)$	ϕ^*_η	Correction	$\frac{d\sigma}{d\Omega^*_\eta}$
1.53	0.75	-0.8	22.5	0.1565 ± 0.0057	1.0090 ± 0.1136
1.53	0.75	-0.4	22.5	0.1474 ± 0.0058	1.3338 ± 0.1446
1.53	0.75	0.0	22.5	0.1490 ± 0.0057	1.1511 ± 0.1478
1.53	0.75	0.4	22.5	0.1498 ± 0.0056	1.2986 ± 0.1371
1.53	0.75	0.8	22.5	0.1588 ± 0.0056	1.1609 ± 0.1454
1.53	0.75	-0.8	67.5	0.1239 ± 0.0051	1.5073 ± 0.1435
1.53	0.75	-0.4	67.5	0.0857 ± 0.0044	1.3524 ± 0.2067
1.53	0.75	0.0	67.5	0.0729 ± 0.0040	1.1757 ± 0.2151
1.53	0.75	0.4	67.5	0.0756 ± 0.0040	0.8798 ± 0.1682
1.53	0.75	0.8	67.5	0.1091 ± 0.0047	1.0799 ± 0.2171
1.53	0.75	-0.8	112.5	0.1223 ± 0.0050	1.3540 ± 0.1692
1.53	0.75	-0.4	112.5	0.0429 ± 0.0031	0.3880 ± 0.3256
1.53	0.75	0.8	112.5	0.0699 ± 0.0037	1.0044 ± 0.3249
1.53	0.75	-0.8	157.5	0.1469 ± 0.0056	1.4283 ± 0.1392
1.53	0.75	-0.4	157.5	0.0925 ± 0.0046	1.5765 ± 0.2481
1.53	0.75	0.0	157.5	0.0721 ± 0.0041	0.8306 ± 0.1890
1.53	0.75	0.4	157.5	0.0713 ± 0.0039	0.8505 ± 0.2474
1.53	0.75	0.8	157.5	0.1030 ± 0.0046	1.0338 ± 0.1998
1.53	0.75	-0.8	157.5	0.1517 ± 0.0057	1.3384 ± 0.1425
1.53	0.75	-0.4	157.5	0.0989 ± 0.0048	1.1820 ± 0.1920
1.53	0.75	0.0	157.5	0.0707 ± 0.0040	1.2482 ± 0.2777
1.53	0.75	0.4	157.5	0.0729 ± 0.0039	1.0668 ± 0.2739
1.53	0.75	0.8	157.5	0.1081 ± 0.0047	1.1270 ± 0.2220
1.53	0.75	-0.8	112.5	0.1197 ± 0.0050	1.0505 ± 0.1410
1.53	0.75	-0.4	112.5	0.0400 ± 0.0030	1.2722 ± 0.4875
1.53	0.75	0.8	112.5	0.0715 ± 0.0038	0.7935 ± 0.2720
1.53	0.75	-0.8	67.5	0.1477 ± 0.0055	1.3512 ± 0.1394
1.53	0.75	-0.4	67.5	0.1002 ± 0.0047	1.0390 ± 0.1798
1.53	0.75	0.0	67.5	0.0727 ± 0.0040	1.3343 ± 0.2458
1.53	0.75	0.4	67.5	0.0827 ± 0.0041	1.2181 ± 0.1979
1.53	0.75	0.8	67.5	0.1067 ± 0.0046	1.1471 ± 0.2285
1.53	0.75	-0.8	22.5	0.1619 ± 0.0058	1.0569 ± 0.1212
1.53	0.75	-0.4	22.5	0.1496 ± 0.0058	1.3640 ± 0.1323
1.53	0.75	0.0	22.5	0.1536 ± 0.0058	1.1507 ± 0.1554
1.53	0.75	0.4	22.5	0.1588 ± 0.0057	1.0461 ± 0.1822
1.53	0.75	0.8	22.5	0.1706 ± 0.0058	0.9267 ± 0.1538

W(GeV)	$Q^2(GeV^2)$	$cos(\theta^*_\eta)$	ϕ^*_η	Correction	$\frac{d\sigma}{d\Omega^*_\eta}$
1.53	1.25	-0.8	22.5	0.2537 ± 0.0139	0.9154 ± 0.1546
1.53	1.25	-0.4	22.5	0.2674 ± 0.0143	0.8644 ± 0.1866
1.53	1.25	0.0	22.5	0.2555 ± 0.0145	0.9250 ± 0.1445
1.53	1.25	0.4	22.5	0.2600 ± 0.0147	0.7654 ± 0.1531
1.53	1.25	0.8	22.5	0.3056 ± 0.0154	0.5890 ± 0.1061
1.53	1.25	-0.8	67.5	0.2078 ± 0.0124	1.0044 ± 0.2674
1.53	1.25	-0.4	67.5	0.1803 ± 0.0117	0.9786 ± 0.1731
1.53	1.25	0.0	67.5	0.1343 ± 0.0107	0.9118 ± 0.1461
1.53	1.25	0.4	67.5	0.1665 ± 0.0117	0.5466 ± 0.1344
1.53	1.25	0.8	67.5	0.2247 ± 0.0134	0.6589 ± 0.1647
1.53	1.25	-0.8	112.5	0.2120 ± 0.0128	0.9156 ± 0.1589
1.53	1.25	-0.4	112.5	0.1450 ± 0.0104	0.7820 ± 0.1494
1.53	1.25	0.0	112.5	0.0882 ± 0.0085	1.0358 ± 0.2825
1.53	1.25	0.4	112.5	0.1072 ± 0.0093	0.4886 ± 0.2307
1.53	1.25	0.8	112.5	0.1652 ± 0.0115	0.7147 ± 0.2355
1.53	1.25	-0.8	157.5	0.2710 ± 0.0144	0.8682 ± 0.1425
1.53	1.25	-0.4	157.5	0.1956 ± 0.0122	0.8039 ± 0.2846
1.53	1.25	0.0	157.5	0.2057 ± 0.0133	0.4283 ± 0.1530
1.53	1.25	0.4	157.5	0.1799 ± 0.0122	0.7118 ± 0.2059
1.53	1.25	0.8	157.5	0.2045 ± 0.0127	0.5677 ± 0.2024
1.53	1.25	-0.8	157.5	0.2944 ± 0.0152	0.7736 ± 0.0999
1.53	1.25	-0.4	157.5	0.2082 ± 0.0127	0.8909 ± 0.1748
1.53	1.25	0.0	157.5	0.1688 ± 0.0120	0.9724 ± 0.2394
1.53	1.25	0.4	157.5	0.1658 ± 0.0117	0.7233 ± 0.2340
1.53	1.25	0.8	157.5	0.2249 ± 0.0134	0.9572 ± 0.2734
1.53	1.25	-0.8	112.5	0.2262 ± 0.0132	0.6626 ± 0.1419
1.53	1.25	-0.4	112.5	0.1599 ± 0.0109	0.8584 ± 0.1614
1.53	1.25	0.0	112.5	0.0951 ± 0.0088	0.9308 ± 0.2323
1.53	1.25	0.4	112.5	0.0916 ± 0.0085	0.3962 ± 0.2330
1.53	1.25	0.8	112.5	0.1828 ± 0.0121	0.5187 ± 0.1674
1.53	1.25	-0.8	67.5	0.2704 ± 0.0144	0.6297 ± 0.1082
1.53	1.25	-0.4	67.5	0.2168 ± 0.0127	0.9929 ± 0.1948
1.53	1.25	0.0	67.5	0.1700 ± 0.0117	0.6796 ± 0.1563
1.53	1.25	0.4	67.5	0.1607 ± 0.0115	0.8294 ± 0.2158
1.53	1.25	0.8	67.5	0.2101 ± 0.0130	0.5432 ± 0.1640
1.53	1.25	-0.8	22.5	0.3498 ± 0.0163	0.5834 ± 0.1002
1.53	1.25	-0.4	22.5	0.3055 ± 0.0152	0.6538 ± 0.1078
1.53	1.25	0.0	22.5	0.3174 ± 0.0164	0.8666 ± 0.1335
1.53	1.25	0.4	22.5	0.2896 ± 0.0155	0.7289 ± 0.1428
1.53	1.25	0.8	22.5	0.3254 ± 0.0162	0.6349 ± 0.1359

W(GeV)	$Q^2(GeV^2)$	$cos(\theta^*_\eta)$	ϕ^*_η	Correction	$\frac{d\sigma}{d\Omega^*_\eta}$
1.56	0.75	-0.8	22.5	0.1736 ± 0.0070	0.9836 ± 0.1044
1.56	0.75	-0.4	22.5	0.1669 ± 0.0072	1.0593 ± 0.1244
1.56	0.75	0.0	22.5	0.1820 ± 0.0074	0.8293 ± 0.1307
1.56	0.75	0.4	22.5	0.1952 ± 0.0075	0.6993 ± 0.1279
1.56	0.75	0.8	22.5	0.1813 ± 0.0070	0.7251 ± 0.1739
1.56	0.75	-0.8	67.5	0.1220 ± 0.0059	1.1095 ± 0.1477
1.56	0.75	-0.4	67.5	0.0654 ± 0.0045	1.1990 ± 0.2202
1.56	0.75	0.0	67.5	0.0609 ± 0.0043	0.7618 ± 0.1769
1.56	0.75	0.4	67.5	0.0561 ± 0.0040	0.8259 ± 0.2627
1.56	0.75	-0.8	112.5	0.1036 ± 0.0055	1.0530 ± 0.1780
1.56	0.75	0.8	112.5	0.0417 ± 0.0033	0.3399 ± 0.2619
1.56	0.75	-0.8	157.5	0.1430 ± 0.0064	1.4226 ± 0.1451
1.56	0.75	-0.4	157.5	0.0781 ± 0.0050	1.3647 ± 0.2754
1.56	0.75	0.8	157.5	0.0698 ± 0.0044	0.9350 ± 0.5348
1.56	0.75	-0.8	157.5	0.1519 ± 0.0066	1.1425 ± 0.1399
1.56	0.75	-0.4	157.5	0.0681 ± 0.0047	1.2406 ± 0.2189
1.56	0.75	0.8	157.5	0.0858 ± 0.0048	0.3548 ± 0.2296
1.56	0.75	-0.8	112.5	0.1170 ± 0.0058	0.8219 ± 0.1336
1.56	0.75	0.8	112.5	0.0410 ± 0.0033	0.7915 ± 0.5023
1.56	0.75	-0.8	67.5	0.1503 ± 0.0066	0.9688 ± 0.1301
1.56	0.75	-0.4	67.5	0.0794 ± 0.0050	1.3207 ± 0.2273
1.56	0.75	0.0	67.5	0.0517 ± 0.0040	1.2927 ± 0.2225
1.56	0.75	0.4	67.5	0.0607 ± 0.0041	0.5814 ± 0.1775
1.56	0.75	-0.8	22.5	0.2046 ± 0.0077	0.8447 ± 0.1054
1.56	0.75	-0.4	22.5	0.1825 ± 0.0076	1.0551 ± 0.1425
1.56	0.75	0.0	22.5	0.1850 ± 0.0075	0.9775 ± 0.1424
1.56	0.75	0.4	22.5	0.1929 ± 0.0075	0.7978 ± 0.1418
1.56	0.75	0.8	22.5	0.1867 ± 0.0071	0.6809 ± 0.1238

W(GeV)	$Q^2(GeV^2)$	$cos(\theta^*_\eta)$	ϕ^*_η	Correction	$\frac{d\sigma}{d\Omega^*_\eta}$
1.56	1.25	-0.8	22.5	0.3033 ± 0.0180	0.6847 ± 0.1240
1.56	1.25	-0.4	22.5	0.2545 ± 0.0159	0.8646 ± 0.1144
1.56	1.25	0.0	22.5	0.2462 ± 0.0164	0.8570 ± 0.1678
1.56	1.25	0.4	22.5	0.3503 ± 0.0199	0.4522 ± 0.1062
1.56	1.25	0.8	22.5	0.3518 ± 0.0197	0.2912 ± 0.0671
1.56	1.25	-0.8	67.5	0.2242 ± 0.0154	0.8653 ± 0.1467
1.56	1.25	-0.4	67.5	0.1384 ± 0.0115	0.7438 ± 0.1913
1.56	1.25	0.0	67.5	0.1448 ± 0.0127	0.7028 ± 0.2403
1.56	1.25	0.4	67.5	0.1461 ± 0.0127	0.6036 ± 0.1962
1.56	1.25	0.8	67.5	0.1814 ± 0.0139	0.6393 ± 0.2475
1.56	1.25	-0.8	112.5	0.2273 ± 0.0153	0.7782 ± 0.1193
1.56	1.25	-0.4	112.5	0.0813 ± 0.0090	0.6860 ± 0.2283
1.56	1.25	0.0	112.5	0.0699 ± 0.0087	0.5688 ± 0.3069
1.56	1.25	0.4	112.5	0.1021 ± 0.0106	0.8843 ± 0.2666
1.56	1.25	0.8	112.5	0.1155 ± 0.0108	0.1982 ± 0.1700
1.56	1.25	-0.8	157.5	0.2520 ± 0.0163	0.6543 ± 0.1242
1.56	1.25	-0.4	157.5	0.1182 ± 0.0108	0.7416 ± 0.2994
1.56	1.25	0.0	157.5	0.0760 ± 0.0092	0.2893 ± 0.3565
1.56	1.25	0.4	157.5	0.0607 ± 0.0081	0.6174 ± 0.3604
1.56	1.25	0.8	157.5	0.1935 ± 0.0144	0.4185 ± 0.2173
1.56	1.25	-0.8	157.5	0.2815 ± 0.0173	0.5821 ± 0.1333
1.56	1.25	-0.4	157.5	0.1592 ± 0.0127	0.4490 ± 0.3977
1.56	1.25	0.0	157.5	0.0883 ± 0.0099	0.3331 ± 0.2909
1.56	1.25	0.8	157.5	0.1902 ± 0.0144	0.4200 ± 0.2219
1.56	1.25	-0.8	112.5	0.2341 ± 0.0155	0.6729 ± 0.1117
1.56	1.25	-0.4	112.5	0.0919 ± 0.0094	0.4579 ± 0.1611
1.56	1.25	0.0	112.5	0.0927 ± 0.0103	0.6019 ± 0.2512
1.56	1.25	0.4	112.5	0.0994 ± 0.0105	0.6907 ± 0.2229
1.56	1.25	0.8	112.5	0.1153 ± 0.0108	0.4764 ± 0.3463
1.56	1.25	-0.8	67.5	0.2993 ± 0.0181	0.5846 ± 0.1077
1.56	1.25	-0.4	67.5	0.1868 ± 0.0136	0.5295 ± 0.1409
1.56	1.25	0.0	67.5	0.1620 ± 0.0135	0.6444 ± 0.1646
1.56	1.25	0.4	67.5	0.1717 ± 0.0139	0.6059 ± 0.1592
1.56	1.25	0.8	67.5	0.1928 ± 0.0141	0.2666 ± 0.2168
1.56	1.25	-0.8	22.5	0.3592 ± 0.0198	0.6036 ± 0.1088
1.56	1.25	-0.4	22.5	0.3455 ± 0.0189	0.6297 ± 0.1060
1.56	1.25	0.0	22.5	0.3506 ± 0.0204	0.4835 ± 0.1272
1.56	1.25	0.4	22.5	0.3488 ± 0.0202	0.4773 ± 0.1223
1.56	1.25	0.8	22.5	0.3747 ± 0.0204	0.3918 ± 0.1119

W(GeV)	$Q^2(GeV^2)$	$cos(\theta^*_\eta)$	ϕ^*_η	Correction	$\frac{d\sigma}{d\Omega^*_\eta}$
1.59	0.75	-0.8	22.5	0.1987 ± 0.0092	0.7092 ± 0.1066
1.59	0.75	-0.4	22.5	0.1732 ± 0.0090	0.9245 ± 0.1399
1.59	0.75	0.0	22.5	0.1928 ± 0.0094	0.7460 ± 0.1272
1.59	0.75	0.4	22.5	0.2042 ± 0.0092	0.5692 ± 0.1374
1.59	0.75	0.8	22.5	0.1884 ± 0.0087	0.4487 ± 0.1177
1.59	0.75	-0.8	67.5	0.1199 ± 0.0071	0.8386 ± 0.1418
1.59	0.75	-0.4	67.5	0.0530 ± 0.0049	0.3659 ± 0.1543
1.59	0.75	0.0	67.5	0.0472 ± 0.0046	0.8689 ± 0.2388
1.59	0.75	0.4	67.5	0.0627 ± 0.0051	0.6630 ± 0.2066
1.59	0.75	0.8	67.5	0.0832 ± 0.0058	0.3391 ± 0.1840
1.59	0.75	-0.8	112.5	0.0797 ± 0.0058	0.9649 ± 0.1744
1.59	0.75	0.0	112.5	0.0833 ± 0.0062	1.0170 ± 0.2026
1.59	0.75	0.4	112.5	0.1219 ± 0.0073	0.7944 ± 0.1565
1.59	0.75	0.8	112.5	0.0656 ± 0.0051	0.3957 ± 0.2126
1.59	0.75	-0.8	157.5	0.1353 ± 0.0077	0.9242 ± 0.1365
1.59	0.75	0.4	157.5	0.0483 ± 0.0046	0.7493 ± 0.2236
1.59	0.75	0.8	157.5	0.0439 ± 0.0042	0.3436 ± 0.2959
1.59	0.75	-0.8	157.5	0.1479 ± 0.0080	0.7329 ± 0.1213
1.59	0.75	0.4	157.5	0.0455 ± 0.0045	1.0359 ± 0.3155
1.59	0.75	0.8	157.5	0.0543 ± 0.0047	0.0958 ± 0.1923
1.59	0.75	-0.8	112.5	0.0989 ± 0.0065	0.5215 ± 0.1308
1.59	0.75	0.0	112.5	0.0983 ± 0.0068	0.9137 ± 0.1783
1.59	0.75	0.4	112.5	0.1306 ± 0.0076	0.8116 ± 0.1756
1.59	0.75	0.8	112.5	0.0672 ± 0.0052	0.6070 ± 0.2599
1.59	0.75	-0.8	67.5	0.1552 ± 0.0081	0.6659 ± 0.1117
1.59	0.75	-0.4	67.5	0.0623 ± 0.0053	0.8026 ± 0.1985
1.59	0.75	0.0	67.5	0.0454 ± 0.0045	0.9234 ± 0.2334
1.59	0.75	0.4	67.5	0.0513 ± 0.0047	0.7786 ± 0.2324
1.59	0.75	0.8	67.5	0.0727 ± 0.0054	0.2426 ± 0.1597
1.59	0.75	-0.8	22.5	0.2297 ± 0.0098	0.5975 ± 0.0894
1.59	0.75	-0.4	22.5	0.2149 ± 0.0101	0.6323 ± 0.0949
1.59	0.75	0.0	22.5	0.1994 ± 0.0095	0.7305 ± 0.1221
1.59	0.75	0.4	22.5	0.2141 ± 0.0096	0.6419 ± 0.1053
1.59	0.75	0.8	22.5	0.1971 ± 0.0089	0.2742 ± 0.0802

W(GeV)	$Q^2(GeV^2)$	$cos(\theta^*_\eta)$	ϕ^*_η	Correction	$\frac{d\sigma}{d\Omega^*_\eta}$
1.59	1.25	-0.8	22.5	0.2776 ± 0.0204	0.5145 ± 0.1092
1.59	1.25	-0.4	22.5	0.2474 ± 0.0190	0.6129 ± 0.1462
1.59	1.25	0.0	22.5	0.2914 ± 0.0216	0.4760 ± 0.1139
1.59	1.25	0.4	22.5	0.3499 ± 0.0241	0.2429 ± 0.0820
1.59	1.25	0.8	22.5	0.3297 ± 0.0224	0.0992 ± 0.0672
1.59	1.25	-0.8	67.5	0.1773 ± 0.0165	0.6336 ± 0.1483
1.59	1.25	-0.4	67.5	0.1329 ± 0.0137	0.7767 ± 0.2279
1.59	1.25	0.0	67.5	0.1263 ± 0.0143	0.5326 ± 0.1802
1.59	1.25	0.4	67.5	0.1393 ± 0.0148	0.4348 ± 0.1668
1.59	1.25	-0.8	112.5	0.1330 ± 0.0139	0.5874 ± 0.1978
1.59	1.25	-0.4	112.5	0.0742 ± 0.0102	0.8860 ± 0.2710
1.59	1.25	0.0	112.5	0.1330 ± 0.0148	0.4968 ± 0.1551
1.59	1.25	0.4	112.5	0.1170 ± 0.0135	0.4619 ± 0.2106
1.59	1.25	0.8	112.5	0.1412 ± 0.0147	0.4216 ± 0.1812
1.59	1.25	-0.8	157.5	0.2335 ± 0.0191	0.5594 ± 0.1212
1.59	1.25	-0.4	157.5	0.0886 ± 0.0112	0.4586 ± 0.3063
1.59	1.25	0.8	157.5	0.1065 ± 0.0127	0.2779 ± 0.2248
1.59	1.25	-0.8	157.5	0.2561 ± 0.0199	0.3863 ± 0.0917
1.59	1.25	-0.4	157.5	0.0746 ± 0.0103	0.2147 ± 0.2355
1.59	1.25	0.8	157.5	0.0955 ± 0.0122	0.1568 ± 0.2073
1.59	1.25	-0.8	112.5	0.1925 ± 0.0170	0.2154 ± 0.1045
1.59	1.25	-0.4	112.5	0.0926 ± 0.0113	0.5628 ± 0.2015
1.59	1.25	0.0	112.5	0.1357 ± 0.0149	0.5147 ± 0.1651
1.59	1.25	0.4	112.5	0.1742 ± 0.0167	0.2677 ± 0.1283
1.59	1.25	0.8	112.5	0.1335 ± 0.0142	0.1031 ± 0.1443
1.59	1.25	-0.8	67.5	0.2613 ± 0.0197	0.5083 ± 0.1038
1.59	1.25	-0.4	67.5	0.1739 ± 0.0160	0.3138 ± 0.1154
1.59	1.25	0.0	67.5	0.1441 ± 0.0152	0.2675 ± 0.1244
1.59	1.25	0.4	67.5	0.1575 ± 0.0157	0.4185 ± 0.1486
1.59	1.25	-0.8	22.5	0.3195 ± 0.0219	0.4648 ± 0.1048
1.59	1.25	-0.4	22.5	0.3453 ± 0.0225	0.4236 ± 0.0951
1.59	1.25	0.0	22.5	0.3666 ± 0.0248	0.3431 ± 0.0825
1.59	1.25	0.4	22.5	0.3564 ± 0.0242	0.3858 ± 0.1056
1.59	1.25	0.8	22.5	0.3150 ± 0.0220	0.2480 ± 0.1347

W(GeV)	$Q^2(GeV^2)$	$cos(\theta^*_\eta)$	ϕ^*_η	Correction	$\frac{d\sigma}{d\Omega^*_\eta}$
1.62	0.75	-0.8	22.5	0.1815 ± 0.0106	0.4673 ± 0.1009
1.62	0.75	-0.4	22.5	0.1936 ± 0.0114	0.5796 ± 0.0973
1.62	0.75	0.0	22.5	0.2070 ± 0.0118	0.4715 ± 0.0788
1.62	0.75	0.4	22.5	0.2110 ± 0.0113	0.2587 ± 0.0883
1.62	0.75	0.8	22.5	0.2038 ± 0.0108	0.2003 ± 0.0944
1.62	0.75	-0.8	67.5	0.1052 ± 0.0079	0.6990 ± 0.1415
1.62	0.75	-0.4	67.5	0.0377 ± 0.0050	0.5043 ± 0.1895
1.62	0.75	0.0	67.5	0.0518 ± 0.0058	0.5158 ± 0.1767
1.62	0.75	0.4	67.5	0.0708 ± 0.0065	0.3334 ± 0.1637
1.62	0.75	0.8	67.5	0.0743 ± 0.0065	0.1418 ± 0.1456
1.62	0.75	-0.8	112.5	0.0614 ± 0.0061	0.6079 ± 0.1766
1.62	0.75	-0.4	112.5	0.0552 ± 0.0061	0.5963 ± 0.1645
1.62	0.75	0.0	112.5	0.1461 ± 0.0099	0.3330 ± 0.1013
1.62	0.75	0.8	112.5	0.1171 ± 0.0084	0.1746 ± 0.1303
1.62	0.75	-0.8	157.5	0.1207 ± 0.0087	0.5113 ± 0.1178
1.62	0.75	0.0	157.5	0.0397 ± 0.0051	0.5008 ± 0.2704
1.62	0.75	-0.8	157.5	0.1252 ± 0.0088	0.5609 ± 0.1229
1.62	0.75	0.0	157.5	0.0622 ± 0.0065	0.2309 ± 0.1687
1.62	0.75	-0.8	112.5	0.0700 ± 0.0065	0.5335 ± 0.1519
1.62	0.75	-0.4	112.5	0.0597 ± 0.0063	0.7666 ± 0.2166
1.62	0.75	0.0	112.5	0.1582 ± 0.0104	0.5402 ± 0.1649
1.62	0.75	0.8	112.5	0.0984 ± 0.0075	0.4878 ± 0.4007
1.62	0.75	-0.8	67.5	0.1320 ± 0.0091	0.4023 ± 0.0877
1.62	0.75	-0.4	67.5	0.0721 ± 0.0070	0.3212 ± 0.1132
1.62	0.75	0.0	67.5	0.0537 ± 0.0059	0.5091 ± 0.2051
1.62	0.75	0.4	67.5	0.0780 ± 0.0068	0.2804 ± 0.1379
1.62	0.75	0.8	67.5	0.0742 ± 0.0064	0.1324 ± 0.1349
1.62	0.75	-0.8	22.5	0.2440 ± 0.0124	0.3724 ± 0.0684
1.62	0.75	-0.4	22.5	0.2236 ± 0.0122	0.4038 ± 0.0729
1.62	0.75	0.0	22.5	0.2162 ± 0.0121	0.3357 ± 0.0747
1.62	0.75	0.4	22.5	0.1919 ± 0.0109	0.3141 ± 0.1025
1.62	0.75	0.8	22.5	0.2022 ± 0.0107	0.0989 ± 0.0609

W(GeV)	$Q^2(GeV^2)$	$cos(\theta^*_\eta)$	ϕ^*_η	Correction	$\frac{d\sigma}{d\Omega^*_\eta}$
1.62	1.25	-0.8	22.5	0.2101 ± 0.0207	0.4400 ± 0.1185
1.62	1.25	-0.4	22.5	0.1957 ± 0.0195	0.5532 ± 0.1440
1.62	1.25	0.0	22.5	0.2563 ± 0.0244	0.2066 ± 0.1006
1.62	1.25	0.4	22.5	0.3216 ± 0.0265	0.1679 ± 0.0726
1.62	1.25	0.8	22.5	0.3383 ± 0.0276	0.0703 ± 0.0558
1.62	1.25	-0.8	67.5	0.1739 ± 0.0190	0.4820 ± 0.1302
1.62	1.25	-0.4	67.5	0.1099 ± 0.0148	0.5356 ± 0.1654
1.62	1.25	0.0	67.5	0.1099 ± 0.0160	0.3332 ± 0.2127
1.62	1.25	0.4	67.5	0.1633 ± 0.0190	0.0961 ± 0.1139
1.62	1.25	0.8	67.5	0.1227 ± 0.0161	0.0220 ± 0.3004
1.62	1.25	-0.8	112.5	0.1269 ± 0.0165	0.3163 ± 0.1431
1.62	1.25	-0.4	112.5	0.0801 ± 0.0126	0.2275 ± 0.2170
1.62	1.25	0.0	112.5	0.1570 ± 0.0187	0.0902 ± 0.1539
1.62	1.25	0.4	112.5	0.1933 ± 0.0212	0.0785 ± 0.2265
1.62	1.25	0.8	112.5	0.1470 ± 0.0177	0.1388 ± 0.1480
1.62	1.25	-0.8	157.5	0.1749 ± 0.0193	0.2034 ± 0.1179
1.62	1.25	0.0	157.5	0.0455 ± 0.0102	0.3932 ± 0.2502
1.62	1.25	-0.8	157.5	0.1707 ± 0.0187	0.2095 ± 0.1236
1.62	1.25	0.0	157.5	0.0542 ± 0.0112	0.4174 ± 0.2227
1.62	1.25	-0.8	112.5	0.1580 ± 0.0181	0.3972 ± 0.1325
1.62	1.25	-0.4	112.5	0.1055 ± 0.0147	0.2591 ± 0.1455
1.62	1.25	0.0	112.5	0.1553 ± 0.0191	0.1010 ± 0.1558
1.62	1.25	0.4	112.5	0.1746 ± 0.0198	0.0106 ± 0.1685
1.62	1.25	0.8	112.5	0.1602 ± 0.0183	0.2116 ± 0.1887
1.62	1.25	-0.8	67.5	0.2089 ± 0.0210	0.5441 ± 0.1167
1.62	1.25	-0.4	67.5	0.1682 ± 0.0182	0.2567 ± 0.1055
1.62	1.25	0.0	67.5	0.1378 ± 0.0178	0.1335 ± 0.1195
1.62	1.25	0.4	67.5	0.1493 ± 0.0182	0.1661 ± 0.1436
1.62	1.25	0.8	67.5	0.1204 ± 0.0159	0.2423 ± 0.2525
1.62	1.25	-0.8	22.5	0.2990 ± 0.0253	0.3836 ± 0.0917
1.62	1.25	-0.4	22.5	0.3463 ± 0.0269	0.3410 ± 0.0789
1.62	1.25	0.0	22.5	0.2786 ± 0.0251	0.3131 ± 0.1156
1.62	1.25	0.4	22.5	0.2997 ± 0.0263	0.2054 ± 0.0907
1.62	1.25	0.8	22.5	0.3178 ± 0.0266	0.1184 ± 0.0784

Bibliography

Bibliography

[1] Adams, *et. al.*, to be published in Nucl. Instrum. Meth.

[2] J. C. Alder *et al.*, Nucl. Phys. **B91**, 386 (1975).

[3] C. S. Armstrong *et al.*, Phys. Rev. **D60**, 052004 (1999)

[4] U. Beck *et al.*, Phys. Lett. **B51**, 103 (1974)

[5] P. R. Bevington and D. K. Robinson, *Data Reduction and Error Analysis for the Physical Sciences*, WCB/McGraw-Hill, 1992

[6] F. W. Brasse *et al.*, Nucl. Phys. **B139**, 37 (1978).

[7] F. W. Brasse *et al.*, Z. Phys. **C22**, 33 (1984).

[8] H. Breuker *et al.*, Phys. Lett. **B74**, 409 (1978).

[9] V. Burkert, CLAS Collaboration internal communication (unpublished)

[10] S. Capstick and B. D. Keister, Phys. Rev. **D51**, 3598 (1995)

[11] D. S. Carman *et al.*, Nucl. Instrum. Meth. **A419**, 315 (1998).

[12] C. Caso *et al.*, Eur. Phys. J. **C3**, 1 (1998).

[13] F. E. Close and Z. Li, Phys. Rev. **D42**, 2194 (1990).

[14] H. Denizli and J. Mueller, private communication, CLAS Note to come

[15] J. Denschlag, L. Tiator and D. Drechsel, Eur. Phys. J. **A3**, 171 (1998)

[16] K. Egiyan, CLAS Note 99-007 (unpublished)

[17] F. Foster and G. Hughes, Rept. Prog. Phys. **46**, 1445 (1983).

[18] G. Hohler, PiN Newslett. **14**, 168 (1997).

[19] F. James, CERN Computing and Networks Division, Geneva Switzerland, http://wwwinfo.cern.ch/a sdoc/WWW/minuit/minmain/minmain.html

[20] N. Kaiser, T. Waas and W. Weise, Nucl. Phys. **A612**, 297 (1997)

[21] K. Y. Kim, private communication

[22] G. Knochlein, D. Drechsel and L. Tiator, Z. Phys. **A352**, 327 (1995)

[23] W. Konen and H. J. Weber, Phys. Rev. **D41**, 2201 (1990).

[24] B. Krusche *et al.*, Phys. Rev. Lett. **74** (1995) 3736.

[25] B. Krusche, N. C. Mukhopadhyay, J. F. Zhang and M. Benmerrouche, Phys. Lett. **B397**, 171 (1997).

[26] P. S. Kummer *et al.*, Phys. Rev. B **30**, 873 (1973).

[27] N. C. R. Makins *et al.*, to be published

[28] L. W. Mo and Y. Tsai, Rev. Mod. Phys. **41**, 205 (1969).

[29] L. C. Smith, private communication

[30] L. C. Smith *et. al.*, to be published in Nucl. Instrum. Meth.

[31] E. S. Smith *et al.*, Nucl. Instrum. Meth. **A432**, 265 (1999).

[32] L. Tiator, C. Bennhold and S. S. Kamalov, Nucl. Phys. **A580**, 455 (1994)

[33] T. P. Vrana, S. A. Dytman and T. S. Lee, Submitted to Phys.Rept.

[34] M. Wilhelm, Ph.D. thesis, University of Bonn (unpublished)

[35] Application and Support Group, CERN Computing and Network Support Division, Geneva, Switzerland, March 1995, http://wwwinfo.cern.ch/asdoc/geant_html3/geantall.html